Dendritic Cooling for Nozzle Guide Vanes

Thesis



J.J.R. Batstone

Worcester College



Hilary 2011

ACKNOWLEDGEMENTS

First and foremost I am very grateful to Dr Gillespie for his intellectual input, guidance and patience. Without his support and help this thesis would not exist.

My gratitude must also extend to Prof. Ireland who co supervised me in the early stages of this work.

Thanks also to Ed Romero of Rolls Royce who was always willing and able to help.

The experiments in this work all relied upon the skill and craftsmanship of the members of the workshop; thanks to Gerald, Trev, Leo, Dave, Nigel and Pete for all their help with 'models and rigs'. Thank you also to all the administrative and support staff in the laboratory.

Thanks also to C. Hambidge and L. Ganin for their help with the flat plate experiments.

Finally, thank you to my parents, John and Dorcas, who have always supported me; questioning me throughout my education.

DENDRITIC COOLING FOR NOZZLE GUIDE VANES
ABSTRACT

J.J.R. Batstone, Worcester College, Hilary 2011

This thesis describes the development and characterisation of an entirely new form of gas turbine cooling scheme, in which passages repeatedly branch within the wall of the cooled component. This type of cooling is known as dendritic cooling. Such geometries offer particular performance improvements compared to traditional cooling holes in film-cooling schemes when the external cross flow is low and conventional films have a tendency to lift off the surface. In these regions, improved internal cooling efficiency is achieved while the coolant film is ejected at a low momentum ratio resulting in reduced aerodynamic losses between the film and hot gases and a more effective surface film. By varying the number of branches, it is possible to optimise the internal convective cooling at a particular location whilst maintaining a low overall coolant flow rate and high pressure margin. This makes the system robust against ingestion of hot gases. The low flow rates through the exit holes, resulting from the internal branching structure, allows quasi-transpiration cooling at the external blade surface and thus improved film-cooling effectiveness.

Many potential cooling arrangements have been investigated in the current study, using a mixture of experimental testing and analytical modelling. The research strategy is multi-stranded: a simple analytical model of the metal temperature response to an applied cooling scheme is required to allow the full design space to be explored; in contrast detailed heat transfer coefficient and film-cooling effectiveness distributions are needed as inputs to stressing and lifing models; finally manufacturability of the components must be assessed. In both the former cases large scale, low temperature, tests of models of the cooling systems were used to obtain detailed data. These are suitably averaged to populate the component model. To assess manufacturability metal test components at real engine scale have been manufactured using two manufacturing techniques. Working with a colleague in the Department of Engineering Science, a relatively conservative scheme has been tested at engine scale to confirm improvements in performance.

Two main campaigns of experimental heat transfer testing are reported, characterising the cooling systems' behaviour both within the component wall (internal) and over the external surface. The experiments are conducted in the presence of a representative external crossflow. Local Nusselt number distributions are reported on the internal surfaces of dendritic systems with 1, 2 and 3 internal flow branches at a range of engine representative Reynolds numbers and exit momentum ratios. These data are correlated to the Reynolds number of the flow at the entrance to each dendritic branch, and are shown to be extremely insensitive to the exit momentum ratio. The heat transfer coefficient-area product of the dendritic schemes is shown to be superior to conventional straight cooling passages. The pressure loss associated with these designs is also characterised, and correlated. Interestingly the trend of these results is against initial expectations, but may be explained by the capping of the holes exiting into the mainstream flow.

The film-cooling effectiveness and heat transfer coefficient performance on the external component surface is characterised for two idealised arrays of dendritic systems, using transient and steady-state tests. The film-effectiveness up to 80 hole diameters downstream of the point of injection was determined and correlated. Using the well known superposition model for film-cooling, it is possible to correlate the results such that they are applicable to arbitrarily spaced rows of holes over the component surface. The use of dendritic cooling hole geometries is shown to be better than plain circular holes. A dramatic improvement in film-cooling performance is, however, seen when the hole exits are contoured to form a contiguous spanwise slot at exit, this being achieved in the deliberate absence of flow acceleration in the hole. The benefit is achieved over the full range of blowing ratios tested. These local data allow component lifing to be undertaken.

The implementation of such cooling arrangements is only achievable using new manufacturing processes. At the outset of this research the best candidate process was virtual pattern casting. Casting trials were conducted of thermodynamically feasible cooling geometries specified for a Nozzle Guide Vane (*NGV*) leading edge. The partial success of these trials allowed the proposal of simple design rules for dendritic cooling systems. Subsequently a direct metal laser deposition technique was used to construct engine scale models. While this clearly cannot be used in the formation of a single crystal component, it offers advantage elsewhere in the engine.

The preliminary design flow and heat transfer model is developed based on the well known standard blade model (Holland and Thake, *1980*) including their modification to account for film-cooling. This allows candidate cooling geometries to be compared to other arrangements and the component metal temperature (chordwise averaged temperature distribution) to be obtained. Data are expressed as non-dimenstional coolant flow *vs* metal effectiveness, though more detailed temperature distributions are also presented. This piecewise isothermal wall model allows the effects of varying geometric parameters to be assessed. The model shows that the dendritic schemes are extremely promising, with both a substantial reduction in non-dimensional cooling flow and a significant increase in blade metal effectiveness at engine take off conditions. The performance improvement has been confirmed by a co-worker at the Osney Laboratory who measured the metal effectiveness distribution of metal *NGVs.*

Experimental results on the internal cooling performance have been submitted and accepted for presentation at the 2011 IGTI conference and a patent application has been submitted, covering novel aspects of the dendritic cooling designs. Further papers are in preparation.

Table of Contents

Abstract i

Nomenclature viii

Chapter 1 Introduction 1

1.1 Historical Context 1

1.2 Thesis Overview 4

Chapter 2 Research Motivation 8

2.1 Operating Principles of Gas Turbines 8

2.2 Relationship of pressure ratios to specific work output 10

2.3 Non-ideal cycles 12

2.4 Entropy generation and its relation to temperature 14

2.5 Further justification for higher TET 17

2.6 The Thermodynamics of a Cooled Gas Turbine Cycle 18

Chapter 3 Current Technology and Research 21

3.1 Cooling Exits 22

3.1.1 Loss Generation 22

3.1.2 External Performance 24

3.2 Internal Cooling Performance 26

3.3 Novel Cooling Systems 29

3.4 Conclusion 38

Chapter 4 Dendritic Cooling Designs 40

4.1 Virtual Pattern Casting 40

4.2 Development of Dendritic Geometry 42

4.3 Design Selection for further Investigation 49

4.4 Vane Ready Designs 50

4.4.1 High Density Small Diameter Circular Cross Section Dendrites 53

4.4.2 Large Diameter Circular Cross Section 1-2 Dendrites 54

4.4.3 Large Diameter Dendrites with only Single Splits and Slot Exits 57

4.4.4 *VPC* Casting Trial of a Low Density, Small Diameter Circular Cross Section Dendritic Cooling Scheme 59

Chapter 5 Experimental Methods and Techniques 64

5.1 Experimental Setup 64

5.1.1 Apparatus 64

5.1.2 Data Acquisition 66

5.2 Introduction to Heat Transfer Processing Techniques 68

5.2.1 Introduction to Liquid Crystal Thermography 69

5.2.2 The Transient Liquid Crystal Technique 70

5.3 Film-Cooling Effectiveness Measurement: Steady State Infrared Thermography 76

Chapter 6 Internal Characteristics of Dendritic Passages 80

6.1 Internal Heat Transfer Performance 80

6.1.1 Introduction 80

6.1.2 Experimental Setup 81

6.1.2.1 Test Specimen Geometry and Instrumentation 81
6.1.2.2 Experimental Assembly 83
6.1.2.3 Procedure 85
6.1.3 Heat Transfer Results 88

6.1.3.1 Local Heat Transfer Coefficient Distributions 88
6.1.3.2 Local Heat Transfer in Subsequent Branches 91
6.1.3.3 CFD 'Diagnosis' of Flow Field 94
6.1.3.4 Generalised Internal Heat Transfer Behaviour of Dendritic Systems 96
6.2 Internal Pressure Loss Characteristics of Dendritic Passages 100

6.2.1 Method 100

6.2.2 Data Extraction and Results Processing 101

6.2.3 Pressure Loss Results 102

6.2.4 Effect of Inlet Reynolds Number 103

6.2.5 Effect of Exit Blowing Ratio 104

6.3 Summary 105

Chapter 7 External Film-Cooling Performance and Flow Behaviour 107

7.1 Experimental Geometry 110

7.2 Method – Transient Technique 113

7.3 General Overview of Flat Plate Results 115

7.4 Results Acquired Using the Transient Technique 116

7.4.1 Circular Cross Section Dendrite 117

7.4.1.1 Circular Cross Section Dendrite: Low Blowing Ratio Behaviour 117

7.4.1.2 Circular Cross Section Dendrite: Intermediate Blowing Ratio Behaviour 118

7.4.1.3 Circular Cross Section Dendrite: High Blowing Ratio Behaviour 120

7.4.2 Slot Exit Dendrite 121

7.4.2.1 Slot Exit Dendrite: Low Blowing Ratio Behaviour 122

7.4.2.2 Slot Exit Dendrite: Intermediate Blowing Ratio Behaviour 124

7.4.2.3 Slot Exit Dendrite: High Blowing Ratio Behaviour 125

7.4.3 Comparison and Generalised Behaviour of Heat Transfer Coefficient Results 126

7.5 Method – Steady State Technique 127

7.6 Results Acquired Using the Steady State Technique 130

7.7 Analysis of Results Acquired Using the Steady State Technique 134

7.7.1 Upstream Behaviour 134

7.7.2 Downstream Behaviour 137

7.7.3 A Film Cooling Effectiveness Row by Row Superposition based Correlation 138

7.7.4 Development of Array Specific Correlations 144

7.7.4.1 Development of Upstream Correlations 146

7.7.4.2 Development of Downstream Correlations 147

7.8 Flow Visualisation of Cooling Films 148

7.8.1 Introduction 148

7.8.2 Experimental Modifications and Method 149

7.8.3 Results 152

7.8.3.1 Film Surface Distribution 152

7.8.3.1.1 Straight Cooling Holes 153
7.8.3.1.2 Dendrite with Circular Cross Section 153
7.8.3.1.3 Slot Exit Dendrite 153
7.8.3.2 Film Profile 155

7.8.3.2.1 Straight Cooling Holes 155
7.8.3.2.2 Dendrite with Circular Cross Section 156
7.8.3.2.3 Slot Exit Dendrite 157
7.8.4 Limitations 157

7.9 Chapter Summary 158

Chapter 8 Preliminary Design Dendritic Cooling Model 159

8.1 Introduction 159

8.2 Local Variables 161

8.3 Coolant Flow Rates 162

8.4 Nusselt Number Calculations 162

8.5 Surface Areas 163

8.6 CAD Geometry and Real Prototype Geometry 165

8.7 Cooling System Characteristics 167

8.8 Thermal Equilibrium Calculations 173

8.9 Results 175

Chapter 9 Sector Rig Experiments 183

Chapter 10 Summary and Conclusion 189

References 195

Appendix A Experimental Procedures 201

A.1 Internal Heat Transfer 201

A.2 Loss in Dendritic Passages 203

A.3 Transient technique: External Heat Transfer Coefficient 203

A.4 Steady state technique: Film-cooling effectiveness 204

A.5 Flow visualisation 205

Appendix B Large Scale Dendritic Results 207

B.1 1-2 Dendritic Configuration 207

B.2 1-2-4 Dendritic Configuration 209

B.2.1 Inlet Branch 210

B.2.2 Exit Branch 213

B.3 1-2-4-8 Dendritic Configuration 215

B.3.1.1 Inlet Branch 215
B.3.1.2 Middle Branch 218
B.3.1.3 Exit Branch 221

Appendix C Dendritic Loss Data 224

C.1 3D Surface Plots of Experimental Data 224

C.1.1 1-2 Surface Plot of Discharge Coefficient vs Re vs 1/BR 224

C.1.2 1-2-4 Surface Plot of Discharge Coefficient vs Re vs 1/BR 224

C.1.3 1-2-4-8 Surface Plot of Discharge Coefficient vs Re vs 1/BR 224

C.2 Loss Comparison of the Different Dendritic Configurations Using the Surface Fits 225

C.2.1 Loss in Terms of Discharge Coefficient for Fixed Inverse Blowing Ratios at Uniform Intervals 225

C.2.2 Loss in Terms of Dynamic Head for Fixed Inverse Blowing Ratios at Uniform Intervals 226

C.2.3 Loss in Terms of Discharge Coefficient for Fixed Reynolds Numbers at Uniform Intervals 227

C.2.4 Loss in Terms of Dynamic Head for Fixed Reynolds Numbers at Uniform Intervals 228

C.3 Tabulated Loss Data 229

1-2 Loss Data Matrices 229
1-2-4 Loss Data Matrices 231
1-2-8 Loss Data Matrices 233

C.4 Loss Data Extraction flow chart 235

Appendix D Camera Settings used for the Film-Cooling Effectiveness Experiments 236

Appendix E Flat Plate Test Results 237

E.1 Results Acquired Using the Transient Technique 237

E.1.1 Circular Cross Section Dendrite 237

E.1.2 Slot Exit Dendrite 239

E.2 Results Acquired Using the Steady State Technique 240

E.2.1 Straight Circular Cross Section Holes 241

E.2.2 Circular Cross Section Dendrite 243
E.2.3 Slot Exit Dendrite 245
Appendix F Rolls Royce Trent 500 Data 247
Appendix G Processing Flow Charts 248
G.1 Heat Transfer Coefficient Map Generation 248
G.2 Film-cooling effectiveness Data Generation 249
Appendix H Summary of Film Flow Visualisation Pictures 250

Nomenclature

A	area, m^2
AS	area served, m^2
BR	blowing ratio, $\frac{\rho U_c}{\rho U_m}$
C_d	discharge coefficient, $\frac{\dot{m}}{\sqrt{2\rho\Delta P}\left(A_{inlet}/n\right)}$
C_p	specific heat capacity, J/kgK
d_h	hydraulic diameter, m (with reference to cooling hole)
f	friction factor
h	specific enthalpy, J/kg
h	heat transfer coefficient, W/ m^2K
I	momentum ratio, $\frac{\rho U_c^2}{\rho U_m^2}$
k	thermal conductivity, W/mK
K_{loss}	Loss in terms of dynamic heads, $\frac{1}{C_d{}^2}-1$
L/D	length to diameter ratio in cooling hole passages
M	Mach number
$\dot{m}$	mass flow rate, kg/s
m^*	non-dimensional cooling flow
Nu	Nusselt Number
NS	number of splits in a dendritic geometry
P	pitch, m
P	pressure, Pa
PD	Pipe diameter, m
Q	Energy input/output, J
Re_{md}	Mainstream Reynolds number based coolant hole diameter
Rs	Specific gas constant, J/kgK
r_p	Pressure ratio
rw	Work ratio
s	specific entropy, J/kgK
S	entropy, J/K
t	Time, s
T	Temperature, K
TET	Turbine Entry Temperature, K
T_R	Temperature ratio (*TET* / engine inlet temperature)
U	velocity, m/s
w	specific work output/input, J/kg
W	work output/input, J

Subscript

a	actual
aw	adiabatic wall
b	blade
c	coolant
C	compressor or compression
ce	coolant exit
ci	coolant inlet
D	dynamic
e	expansion
E	engine
f	film
fc	fraction of coolant
i	ideal
in	input
$irrev$	irreversible process
is	isentropic process
m	mainstream
M	model
max	maximum amount
min	minimum amount
net	net amount
out	output
s	stagnation conditions
S	static
t	turbine
T	total
w	wall

Greek

$\alpha = \frac{C_d}{\sqrt{(1-\beta^4)}}$	flow coefficient
$\beta = \frac{dh}{PD}$	orifice diameter ratio
ε	effectiveness
η	efficiency
η_f	film cooling effectiveness
$\eta_{oc} = \frac{T_{ce} - T_{ci}}{T_m - T_{ci}}$	overall cooling efficiency
$\eta_{cc} = \frac{T_{ce} - T_{ci}}{T_w - T_{ci}}$	convective cooling efficiency
μ	dynamic viscosity, Pa s
γ	ratio of specific heats
ρ	density,kg/m^3
$\sqrt{\rho c k}$	thermal product of substrate, W s$^{0.5}$ / m^2 K
$\Delta\varpi$	pressure loss across orifice
ξ	loss coefficient

Chapter 1 Introduction

Gas turbines are used extensively throughout the world, finding applications in power stations, aeroplanes and oil pipeline pumping. Development in aeronautical technology is driven by tight airline financial margins, constrained within increasing environmental pressures imposed by governments. Technological advances are expensive: a recent example is the €200m NEWAC EC Framework 6 programme which considered radical alternatives to conventional engine architecture to achieve the ACARE 2020 target for NO_x and CO_2 reduction. It is notable that the aerospace sector is one of the most research-intensive sectors in Europe, with more than 12% of its turnover spent in Research & Development (Aeronautics and Air Transport, *2010*).

1.1 Historical Context

The first known example of the application of jet propulsion is that of the Aeolipile which was invented by Hero of Alexandria in the 1st century AD (Landels, *2000*). The device consisted of a spherical chamber into which steam was fed. The steam entered through the pivot on which the sphere was mounted and exited through two nozzles arranged opposite one another and perpendicular to the axis. The exiting steam resulted in the rotation of the sphere.

It was almost two millennia before this principle was applied to jet engine design and a further 16 years before a working engine was constructed. The first axial jet engine was proposed by a Frenchman, Maxime Guillaume, who filed a patent for his design in 1921 (Figure 1-1). At the time the design proved too

difficult to build and it wasn't until 1937 that Frank Whittle ran the first jet engine, albeit with a radial compressor.

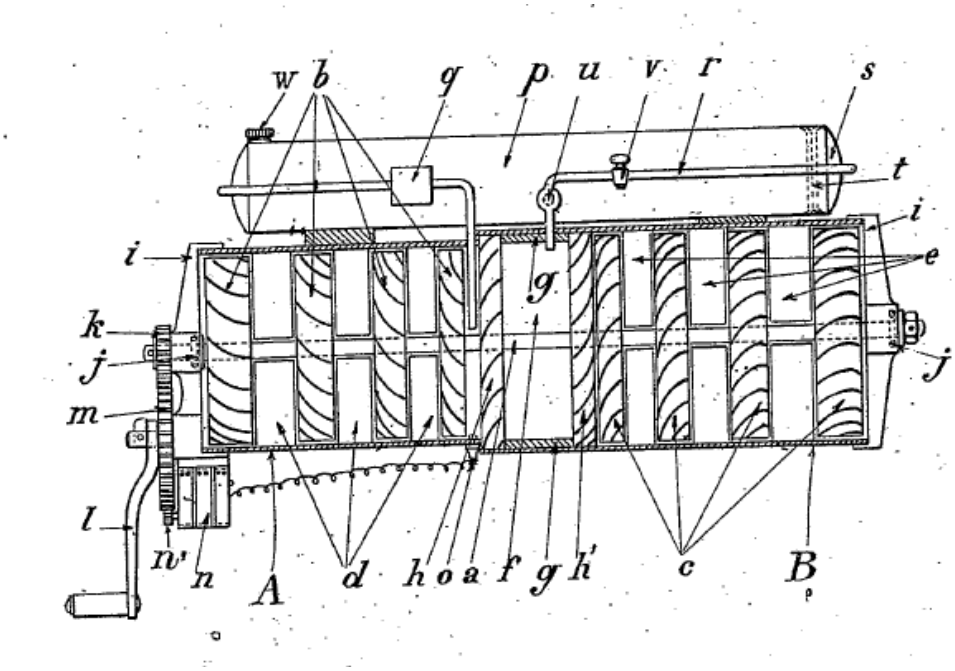


Figure 1-1: A diagram of the first proposed axial jet engine (Guillaume, *1921*)

Running in parallel with Whittle's work was that conducted by Hans von Ohain, who with the help of industrialist, Ernst Heinkel, developed the first jet engine which was used to solely power a plane as shown in Figure 1-2 (Kay, *2002*)



Figure 1-2: The first jet plane, the Heinkel He 178
(http://www.meteorflight.com/waveplus/meteor.nsf/pages/jet_age-he178)

During the infancy of the jet engine, fast development and significant research efforts saw the Gloster Meteor (Figure 1-3), powered by a Rolls-Royce Welland turbojet, deployed in World War II, just two decades after the jet engine concept was first introduced. This intensive research continues today and is nowhere more evident than in the steady rise of the technology's turbine entry temperature (*TET*) (shown in Figure 1-4 for Rolls-Royce engines) which will be shown to be key in the steady fall in its specific fuel consumption (Figure 1-5).

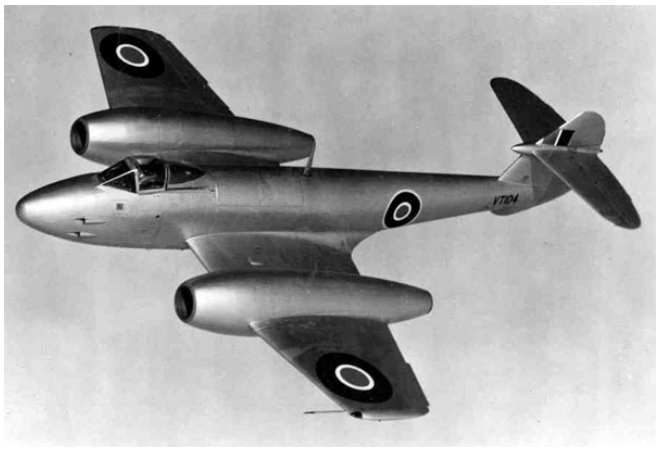


Figure 1-3: The Gloster Meteor, Britain's first operational jet powered fighter aircraft
(http://www.militaryfactory.com/imageviewer/ac/pic-detail.asp?aircraft_id=123&sCurrentPic=gloster-meteor_2.jpg&sCurrentDescriptor=)

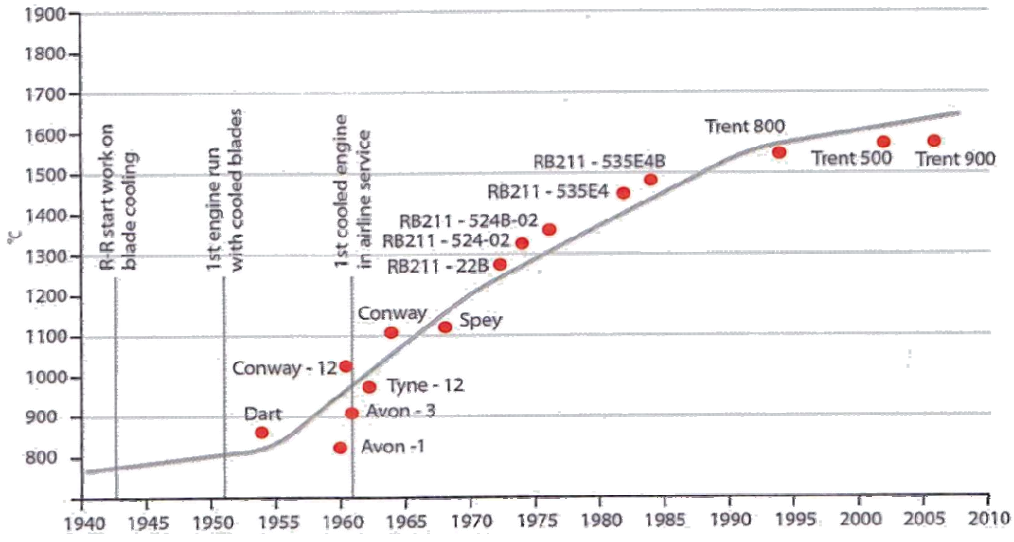


Figure 1-4: The steady rise in the *TET* during the development period of the jet engine (Rolls Royce, *2005*)

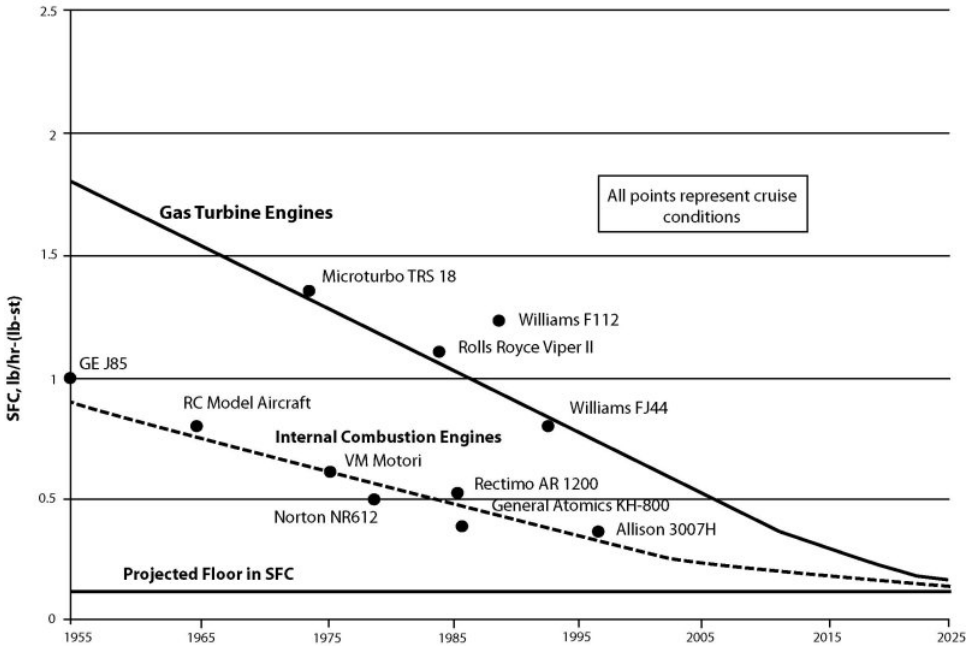


Figure 1-5: The Steady fall in SFC over the development period of the jet engine (Oliver, *2001*)

1.2 Thesis Overview

The research undertaken in this programme aims to reduce the specific fuel consumption (SFC) of aircraft jet engines. A 1% improvement in SFC could allow up to 15 extra passengers to be carried on a typical transatlantic long-haul flight (Steinmetz, *1998*).

Previous research has demonstrated that improvements in the efficiency of gas turbines can be obtained by increasing the TET. Since the development of the first gas turbine there has been a steady rise in TETs to the point where they have far exceeded the metallurgical limits of the turbine vanes and the safe operation of these engines relies upon active cooling of engine components. Whilst the use of coolant permits higher TETs it is also detrimental to turbine performance and results in a reduction in efficiency. With current levels of cooling technology there is little scope for improvement in cycle efficiency by

means of increasing the TET because of the need to increase the cooling flow to prevent engine components melting, so the performance of gas turbines is limited by the current levels of cooling technology and the improvement of cooling performance is a prime candidate for research. Chapter 2 details the drivers of efficiency and fuel burn in the modern jet engine.

In Chapter 3 generally employed cooling schemes are briefly introduced. Current proposals for improving cooling technology beyond the installed state of the art available in the literature are then reported. The review establishes successful characteristics of cooling systems which promote improved cooling performance and reduce aerodynamic losses. As metallurgical developments are stable, better designs of cooling are the key means by which efficiency may be improved in the hot gas path.

In Chapter 4 new concept cooling strategies are developed based on the review and cooling concepts first identified by Mittal (*2006*). The aim of the new designs is to reduce the quantity of cooling air required, and minimise the aerodynamic losses associated with delivering the coolant back into the engine mainstream. These designs are referred to as dendritic cooling: cooling features in which passages repeatedly branch within the wall of the cooled component. Three key terms are regularly used in relation to dendritic geometries in this thesis describing features at differing scale of assembly:

- *A dendritic branch* refers to a passage which splits into two equally sized passages, each of the same cross section as the original.

- A *dendritic system* is formed from a number of dendritic branches. This cooling feature begins at the inner wall of the component and exits at the outer surface and branching internally one or more times in between. Note that a dendritic system may consist of a single dendritic branch.

- A *dendritic array* is a series of dendritic systems arranged to create a cooling scheme for an engine component.

Manufacturable integrated engine designs are proposed. Final designs were developed for the leading passage of the cooling scheme of a Trent 500 NGV. The cost of the cooling system can be reduced by using a design which can be integrally cast into the blade at manufacture, and the designs being used seek to exploit such newly developed manufacturing technology. Results of a casting trial are reported along with the manufacturing design rules resulting from post-casting inspection.

Chapter 5 outlines the principle methods and techniques which underlie the experimental components of this research.

Chapter 6 reports the local internal heat transfer coefficient distributions in a series of dendritic systems along with associated pressure loss measurements. These data are sensibly averaged and correlated. The relative importance of blowing ratio and internal Reynolds number is reported.

In Chapter 7 the external film-cooling performance, an attribute where little information is available either through modelling or existing literature, is investigated using dendritic arrays exiting into a mainstream crossflow. The use

of dimensional analysis allowed the flow conditions to be similar to that of a real turbine. Local heat transfer coefficient distributions are used to find the relative performance of different exit hole configurations, while the film-cooling effectiveness distribution is reported from a series of well-conditioned steady-state tests. Flow visualisation tests were used to infer physical drivers of the flow field.

Chapter 8 details a model created of dendritic systems which can be used accurately to predict their cooling performance. Comparisons are made to conventional cooling designs.

Chapter 9 describes tests performed in near engine annular flow conditions by (Luque*, 2011*). This is a parallel programme being conducted in the Osney lab using parts designed as part of the research programme reported in this thesis. The results are discussed in terms of the modelled flow field.

Finally Chapter 10 summaries the key findings and conclusions of the work conducted and provides suggestion for further work in this area.

Chapter 2 Research Motivation

2.1 Operating Principles of Gas Turbines

The operation of gas turbines is based on the gas power cycle known as the Brayton cycle, first proposed by George Brayton around 1870 (Cengel et al. *1998*). The open cycle consists of three stages as shown schematically in Figure 2-1.

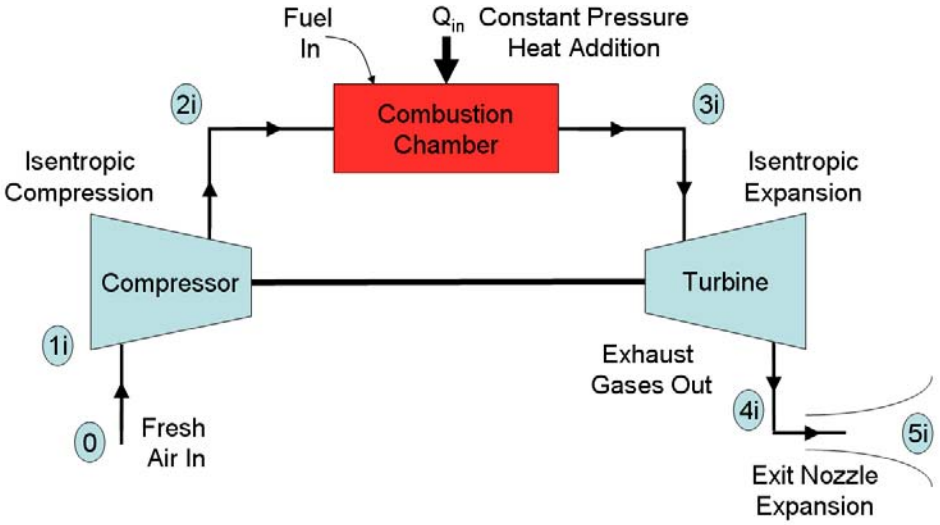


Figure 2-1: The Brayton Gas Turbine Cycle

In the open Brayton cycle the first stage is the compression of fresh air (see Figure 2-1, Figure 2-2 and Figure 2-3). In the ideal cycle this is an isentropic compression (process 1i to 2i). Following this the fuel is burnt in the compressed air at constant pressure (process 2i to 3i). From here the compressed heated air passes into the turbine where it expands isentropically and produces work output (process 3i to 4i). The exhaust gas expands in the turbine, and the power required for the compressor is extracted, the remainder is used for shaft work which for the jet engine consists of powering ancillary

devices and where fitted the engine's fan using an additional turbine. The remainder of the expansion takes place as the gas exits from the engine. The change in momentum of the gas between inlet and outlet producing the forward propulsive force on the airframe.

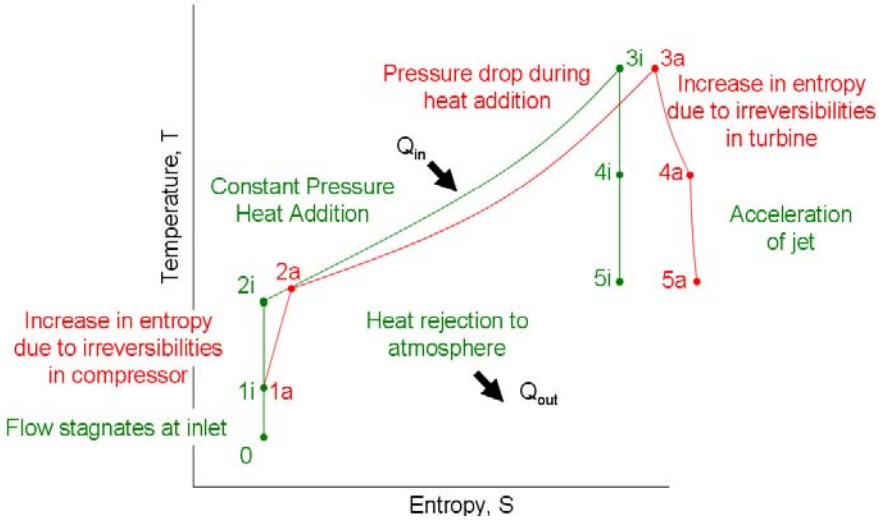


Figure 2-2: Temperature-Entropy Diagram for the Brayton Cycle

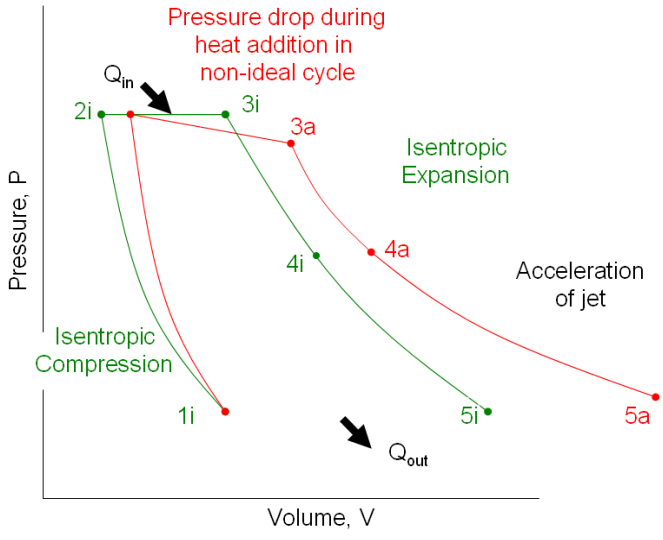


Figure 2-3: Pressure-Volume Diagram for the Brayton Cycle

In the ideal cycle described above it is assumed that there are no losses, all processes are reversible and gas properties are constant. As such the ideal efficiency can be described in terms of key temperatures as set out in Equation 2-1.

$$\eta_i = \frac{W_{out}}{Q_{in}} = \frac{c_p\left(T_{3i} - T_{4i}\right) - c_p\left(T_{2i} - T_{1i}\right)}{c_p\left(T_{3i} - T_{2i}\right)} = 1 - \frac{\left(T_{4i} - T_{1i}\right)}{\left(T_{3i} - T_{2i}\right)}$$

Equation 2-1

Since the process is isentropic it can be shown that:

$$\frac{T_2}{T_1} = \left(\frac{P_2}{P_1}\right)^{\frac{\gamma-1}{\gamma}} = \left(r_p\right)^{\frac{\gamma-1}{\gamma}} = \left(\frac{P_3}{P_4}\right)^{\frac{\gamma-1}{\gamma}} = \frac{T_3}{T_4}$$

Equation 2-2

Therefore the ideal cycle efficiency is given by Equation 2-3.

$$\eta_{is} = 1 - \frac{T_1\left(T_4/T_1 - 1\right)}{T_2\left(T_3/T_2 - 1\right)} = 1 - \frac{T_4}{T_3} = 1 - r_p^{\frac{1-\gamma}{\gamma}}$$

Equation 2-3

From the above relationship it can be seen that the ideal efficiency is dependent only upon the pressure ratio, the maximum efficiency occurring when the maximum pressure ratio is achieved.

2.2 Relationship of pressure ratios to specific work output

The specific work output from the engine is of great importance as it determines the size and weight of the engine required, and thus the drag associated with the engine installation on the wing of the aircraft. For a fixed cycle inlet

temperature, T_1, and TET, T_3, the maximum possible pressure ratio is given by Equation 2-4.

$$r_p = \left(\frac{T_3}{T_1} \right)^{\gamma/(\gamma-1)}$$

Equation 2-4

Whilst using this pressure ratio will result in a cycle with the maximum possible efficiency (for a given set of working temperatures) the net work output would be zero. This is also the case for heat addition without prior compression as demonstrated in Figure 2-4.

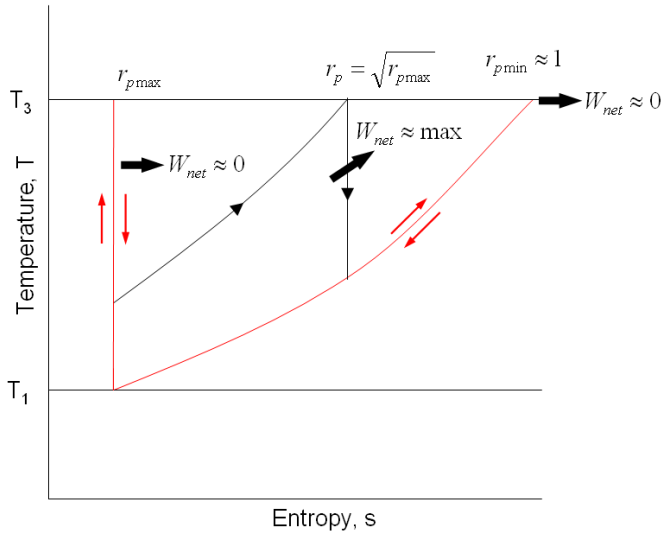


Figure 2-4: Temperature - Entropy Diagram Demonstrating the Optimum Pressure Ratio for Maximum Work Output

The pressure ratio that will give the maximum net work output can be determined by considering the variation of the specific work with pressure ratio.

The specific work output is given by Equation 2-5

$$w = c_p\left(T_3 - T_4\right) - c_p\left(T_2 - T_1\right) = c_p T_3\left(1 - \frac{1}{r_p^{(\gamma-1)/\gamma}}\right) - c_p T_1\left(r_p^{(\gamma-1)/\gamma} - 1\right)$$

Equation 2-5

The pressure ratio at which the work output is, therefore a maximum is the square root of the maximum possible pressure ratio, r_{pmax} (Equation 2-6) marked on Figure 2-4.

$$r_p = \left(\frac{T_3}{T_1}\right)^{\gamma/2(\gamma-1)} = \sqrt{r_{p\,max}}$$

Equation 2-6

In practice an intermediate r_p would be used that gives the best compromise between maximum efficiency and maximum power output for the engine's application. This does not, however, negate the desire to increase the maximum possible r_p and therefore to maximise the temperature ratio T_3 / T_1 which will in turn result in larger possible efficiencies and power outputs. (Rogers and Mayhew*, 1980*)

2.3 Non-ideal cycles

So far it has been assumed that all the processes that take place in the gas turbine cycle are ideal; that they are all reversible; that there is complete heat transfer and there are no losses. In actual gas turbines this is not the case, as demonstrated by the representation of the ideal and actual gas cycle shown in Figure 2-2 and Figure 2-3. Figure 2-5 shows a typical gas turbine where the labels correspond to those in Figure 2-2 and Figure 2-3 with the flow entering on the left and exiting on the right.

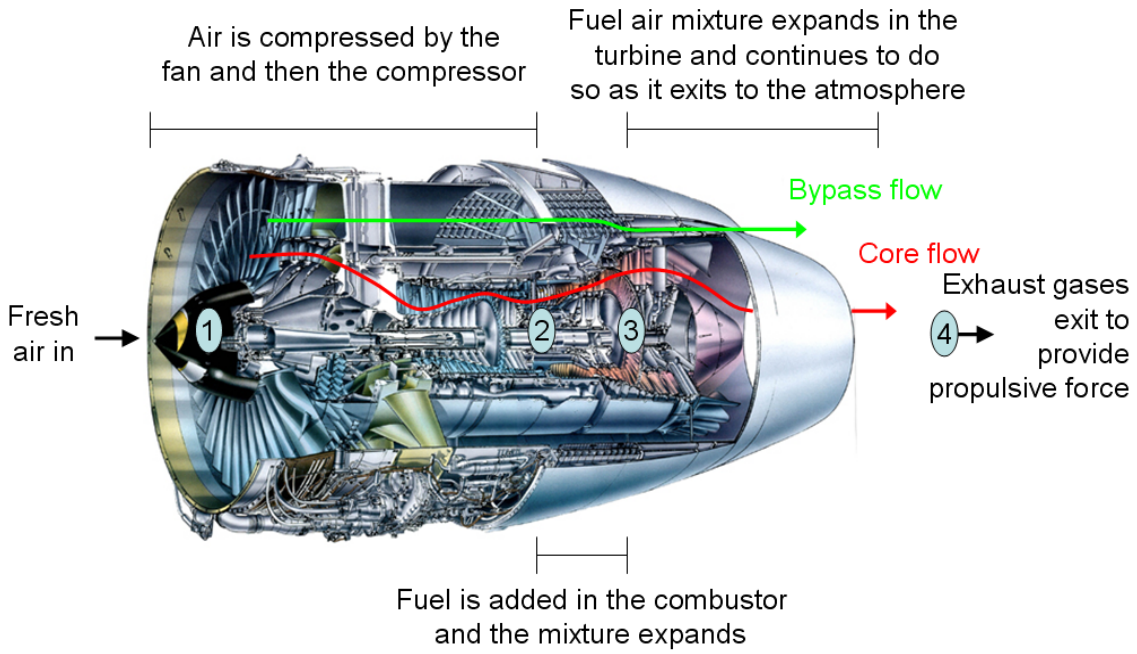


Figure 2-5: Cross Section of a Gas Turbine Engine (http://www.avid.ru/admin/filesru/img/894.jpg)

There are 3 types of loss mechanism that occur in turbomachines (Denton*,1993*); first, viscous effects both in mixing processes and boundary layers; second, non-equilibrium processes such as shock waves and third, heat transfer across finite temperature differences.

Process 1-2 (Figure 2-2, Figure 2-3 and Figure 2-5) is the compression of air that has been drawn into the engine. The losses associated with this include viscous losses, aerodynamic losses which occur when the air flow leaves the profile of the blades, back flow as the high pressure air tries to leak back into the lower pressure regions, tip leakage losses and heat transfer to the casing.

Process 2-3 (Figure 2-2, Figure 2-3 and Figure 2-5) represents heat addition, and is done through the injection of fuel in the combustor where it is mixed with the main gas flow and the mixture is burnt. In actual gas turbines the pressure gradually falls as the mixture passes through the combustor leading to the

process becoming irreversible. The strong mixing of dilution, cooling and combustion air are other factors which make the process non-ideal. There is also considerable heat transfer to the casing.

Process 3-4 (Figure 2-2, Figure 2-3 and Figure 2-5) represents expansion of combustion products. This takes place partly in the turbine, where again there will be losses due to heat transfer, tip leakage, and viscous and aerodynamic losses, and partly as the jet exits where there will be more mixing losses as well as further heat transfer.

2.4 Entropy generation and its relation to temperature

The compression and expansion processes on the T-s diagram of Figure 2-2 are of course not ideal. Isentropic efficiencies of the compression and expansion can be defined by Equation 2-7 and Equation 2-8

$$\eta_C = \frac{W_{ideal}}{W_{compressor}} = \frac{\dot{m}C_p(T_{2i} - T_{1i})}{\dot{m}C_p(T_{2a} - T_{1a})}$$

Equation 2-7

$$\eta_e = \frac{W_{turbine}}{W_{ideal}} = \frac{\dot{m}C_p(T_{3a} - T_{5a})}{\dot{m}C_p(T_{3i} - T_{5i})}$$

Equation 2-8

This leads to revised equations describing the net work from the cycle (Equation 2-9) and the cycle efficiency (Equation 2-10).

$$W_{net} = \dot{m}C_p T_1 \left[\frac{T_3}{T_1} \left(1 - \frac{1}{r_p^{\gamma-1/\gamma}} \right) \eta_e - \frac{r_p^{\gamma-1/\gamma} - 1}{\eta_c} \right]$$

Equation 2-9

$$\eta_{cycle} = \frac{W_{net}}{Q_{in}} = \frac{W_{net}}{\dot{m}C_p T_3 - (W_{compressor} + \dot{m}C_p T_1)} = \frac{\frac{T_3}{T_1}\left(1 - \frac{1}{r_p^{\gamma-1/\gamma}}\right)\eta_e - \frac{r_p^{\gamma-1/\gamma} - 1}{\eta_c}}{\frac{T_3}{T_1} - \frac{r_p^{\gamma-1/\gamma} - 1}{\eta_c} - 1}$$

Equation 2-10

The effect the temperature ratio (Equation 2-13) and the isentropic efficiency of the turbine and compressor is shown in Figure 2-6, Figure 2-7 and Figure 2-8. From Figure 2-6 it is clear that increasing turbine entry temperature (T_3), increases net work and the pressure ratio at which net work is maximised. At the top of an aircraft's climb the pressure ratio may approach 20 (Cumpsty, *1997*).

$$T_r = \frac{T_3}{T_1}$$

Equation 2-11

Figure 2-7 shows that the cycle efficiency is now a strong function of turbine entry temperature, with low temperature ratio leading to a dramatic decrease in cycle efficiency at high pressure ratios. Finally Figure 2-8 demonstrates the importance of the isentropic efficiency of the compressor and turbine components.

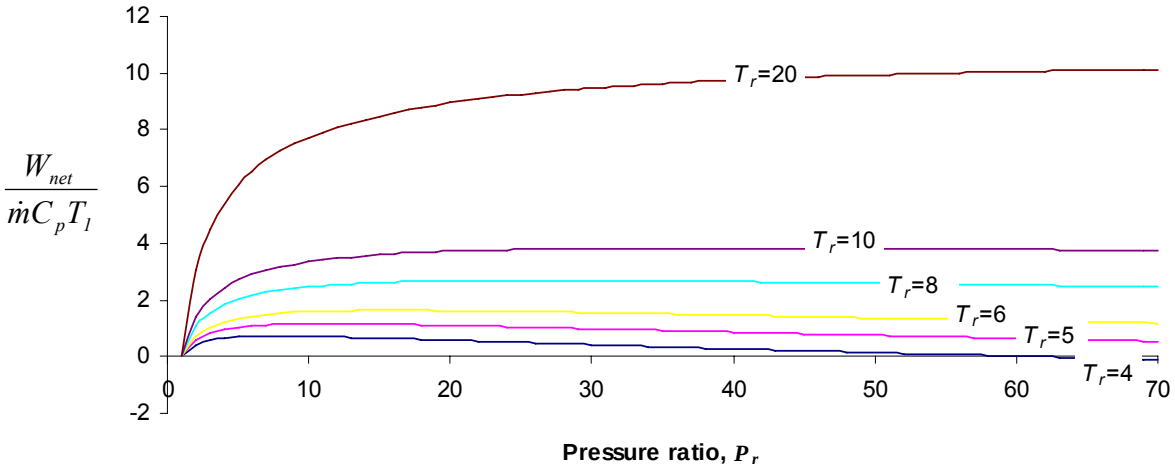


Figure 2-6: Non-dimensional power output for an idealised gas turbine. Demonstrating dependency of power on pressure ratio and temperature ratio for a fixed turbine and compressor efficiency of 0.9

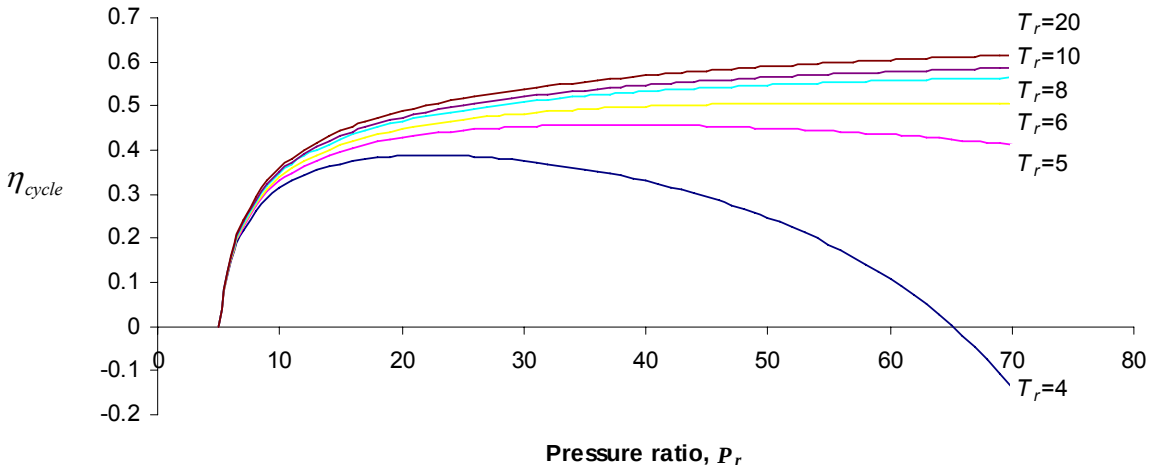


Figure 2-7: Non-dimensional cycle efficiency for an idealised gas turbine. Demonstrating dependency of efficiency on pressure ratio and temperature ratio for a fixed turbine and compressor efficiency of 0.9

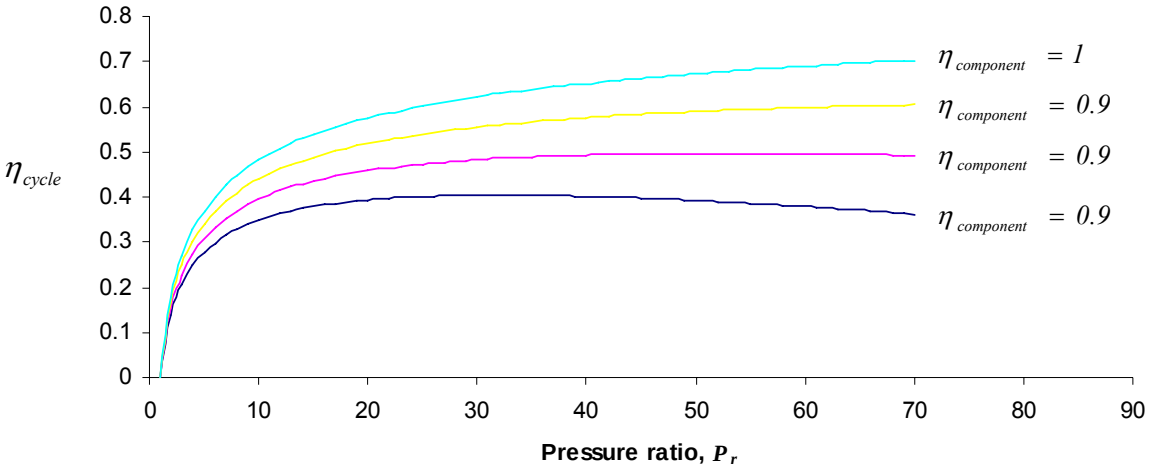


Figure 2-8: Non-dimensional cycle efficiency for an idealised gas turbine. Demonstrating dependency of efficiency on pressure ratio and component efficiencies for a fixed temperature ratio of 6

2.5 Further justification for higher TET

The work ratio, r_w, is a measure of the cycle's susceptibility to irreversibilities; a slight change in either processes' real efficiency will lead to a change in the work ratio. The work ratio is defined in Equation 2-12.

$$r_w = \frac{W_t - W_c}{W_t} = 1 - \frac{W_c}{W_t} = 1 - \frac{c_p(T_2 - T_1)}{c_p(T_3 - T_4)}$$

Equation 2-12

Using Equation 2-12 it is possible to express r_w in terms of r_p, TET (T_3) and the compressor entry temperature, T_1.

$$r_w = 1 - \frac{T_1}{T_3} r_p^{(\gamma-1)/\gamma}$$

Equation 2-13

From Equation 2-13 it is possible to see that not only is the pressure ratio important but also that the ratio T_1 to TET plays a vital role. Whilst there is little control over T_1, since it is determined by the temperature at which air is drawn in, it can be seen that maximising TET will increase the work ratio. A high work ratio would indicate that the irreversibilities associated with a real cycle had been minimised and so the efficiency had been maximised.

It is essential that the TET is maximised. Without any cooling this process is limited by the metallurgical limits of the turbine vanes. It is common practice to use cooled air on parts in the entry region of turbines in order to increase the possible TET of the engine (Rolls Royce*, 2005*).

2.6 The Thermodynamics of a Cooled Gas Turbine Cycle

The effect of cooling can be easily assessed for the case where only turbine cooling is taking place. Cooling air here is compressed air, bled off at the end of the compression process, and is fed into the turbine mainstream during the expansion process (3-4a). There is a subsequent expansion in the uncooled turbine (4a-4b). The exit flow then expands to atmospheric conditions shown here as near isentropic. An enthalpy - entropy (h-s) diagram representing this partial cycle is shown in Figure 2-9.

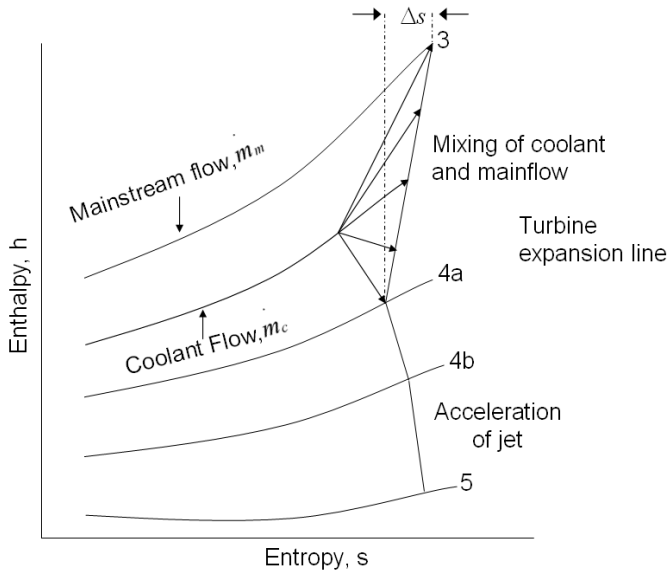


Figure 2-9: Enthalpy - Entropy Diagram for a Cooled Turbine

If it is approximated that only the mainstream ($\dot{m}_m$) contributes to the work output of the turbine and that at any point dQ heat is transferred from the coolant to the mainstream, the actual work output from the turbine may be written as Equation 2-14:

$$W = W_{is} - \int \left(1 - T_{4a}/T\right) dQ - \dot{m}_m \, \Delta s_{irrev}$$

Equation 2-14

The addition of coolant acts to reduce work output in two ways: (a) the middle term represents a reduction in work output because of heat removal from the flow; this is shown by the moving of the expansion line to the left in Figure 2-9; (b) the final term represents the increase in entropy due to the additional viscous effects that occur because of the difference in velocities between the coolant and the mainstream. While the middle term is a function of where the heat transfer to the coolant takes place it is in largely determined by practical

considerations. It will be maximised if it is at the start of the expansion ($T=T_3$) and zero if it takes place at the end. The final term depends upon coolant flow rate and specific coolant exit flow features. Both terms demonstrate that the work output and the overall cycle efficiency is adversely affected by increased coolant flow (Denton, *1993*). As mainflow temperatures become ever closer to the stoichiometric combustion temperature and as there has been little change in allowable metal temperature, the cooling requirement in the NGV increases significantly. In fact this may be so pronounced that the HP rotor inlet temperature falls thus leading to a reduction in the turbine work. (Horlock et al. *2006*).

Horlock et al (*2006*) concluded that with current levels of cooling technology any further increases in TET would require such large levels of cooling flows that the overall efficiency of the cycle would change little or could indeed reduce. Therefore without the introduction of more efficient cooling systems there is little hope of significantly increasing gas turbine efficiencies from their current levels.

Chapter 3 Current Technology and Research

Cooling takes place in both the combustor and turbine in modern jet engines. For the purposes of this study only the cooling in the first stationary stage of the turbine, the high pressure (*HP*) nozzle guide vane (*NGV)* will be considered.

A typical *NGV* from a Rolls-Royce large civil jet engine is shown in Figure 3-1. It can be seen that it is necessary to cool both the end walls of the vane and the external walls. In the case shown the vane internal cooling scheme is split into 2 sections: the leading edge region and the mid span and trailing edge. The leading edge of the *HP NGV* is fed separately from that of the remainder of the vane. In this case, which is typical, the leading edge section is fed from both root and tip, whereas the remainder of the vane is only fed from the hub side where the coolant passes through a serpentine passage and can then exit in one of two ways - through the wall to subsequently form a cooling film or through an impingement plate where it goes on to exit from the trailing edge after passing through a pedestal bank. In the leading edge passage the coolant can only exit through cooling holes in the wall from whence it goes on to form a cooling film. It is the provision of cooling at the leading edge that is of particular interest in this study, however the cooling systems developed could equally be adapted to be used elsewhere in the hot stages of the gas turbine.

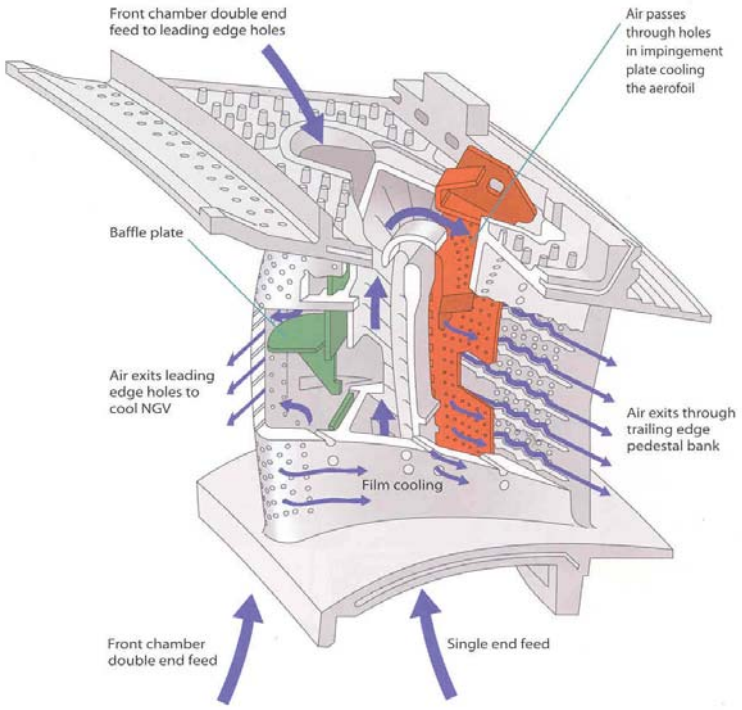


Figure 3-1: *HP NGV* Cooling Flows (Rolls Royce, *2005*)

The flow of coolant through the wall near the leading-edge and its ejection to form a film is now examined in more detail.

3.1 Cooling Exits

There are two metrics by which the overall performance of an external vane cooling strategy may be assessed: first, the loss generated by the exiting coolant and its subsequent mixing, and second, the effectiveness of the cooling film produced and its surface coverage.

3.1.1 Loss Generation

Once the cooling air is ejected through the external surface of the vane surface it should provide a protective enthalpy absorbing film between the hot mainstream and the vane (Rolls Royce*, 2005).* This is the process, outlined in

the previous chapter, by which air used for cooling rejoins the mainstream. The manner in which it rejoins the mainstream can significantly affect the aerodynamic loss associated with the cooling process (Leylek*, 2005*). There are two separate mechanisms driving the aerodynamic loss: mixing losses and wall losses.

Mixing losses tend to dominate the aerodynamic loss and are attributed to the viscous shear between the coolant and mainstream as the coolant mixes with the mainstream (Denton*, 1993*). Shapiro (*1954*) showed that the entropy generation, and therefore the loss associated with the mixing process, increased as the blowing ratio and angle of injection relative to the mainstream increased.

At low blowing ratio, cross flow blockage prevents the coolant flow penetrating the mainstream but at higher blowing ratio the mainstream blockage becomes less significant and the coolant is able to penetrate the mainstream. The jet becomes an obstacle which the mainstream flow must accelerate around. This results in the generation of secondary flows known as horse shoe vortices which give rise to a detrimental increase in the heat transfer coefficient upstream of the hole (Immarigeonk et al. *2006*). For a given blowing ratio the extent to which the jet penetrates the mainstream will reduce as the angle of injection relative to the mainstream is reduced, therefore the extent to which the two streams mix and the obstacle effect of the coolant is reduced.

Aerodynamic losses are the losses that relate to the drag on the turbine. They occur because of the loss in kinetic energy at the boundaries. Aerodynamic losses can take various forms. When coolant is injected there will be an

increase in turbulence; if this results in the initiation of a turbulent boundary layer from a laminar one then this will increase the boundary layer loss for the airfoil. If the injected coolant remains close to the wall it can form a low velocity layer; this will reduce the airfoil wall shear thus reducing loss. Similarly, if the injected coolant forms a high velocity layer this will increase the airfoil shear, thus increasing loss (Denton*, 1993*).

3.1.2 External Performance

As described earlier, blowing ratio has been found to have a large influence on the total loss generated by exiting coolant (Leylek, *2000*), but blowing ratio also has a large effect on how effective the cooling film is (Immarigeonk et al. *2006,* Yuen et al. *2005*). Yuen (*2005*) showed that for a given angle of injection the maximum film-cooling effectiveness, defined as $\eta_f = \frac{T_m - T_f}{T_m - T_{ce}}$, occurred at a blowing ratio of approximately 0.5. It is thought that the film deteriorates at higher blowing ratios because the film separates from the surface (Immarigeonk et al. *2006,* Bogard et al. *2006*). Bogard et al (*2006*) found that film separation, and therefore deterioration in film performance, occurred for a blowing ratio of about 0.65. Strongly related to this is the issue of the angle at which the coolant joins the mainstream. Again Yuen showed that the smaller the angle of the coolant exit relative to the mainstream the more effective the film became.

While many workers merely consider blowing ratio, others (Forth et al. *1986*, Ito et al. *1978*) have shown that in the vicinity of the film-cooling hole exit it is the momentum ratio (Equation 3-1) which determines the initial film trajectory while further downstream it is expected that the mass averaged enthalpy is more

important in determining film-cooling performance and so blowing ratio again becomes important. This said, an increasing momentum ratio is nearly always associated with increasing blowing ratio and the general conclusion set out below can be considered sound over the entire external surface.

$$I = \frac{\rho_{ce} u_{ce}^2}{\rho_m u_m^2}$$

Equation 3-1

Yuen (*2005*) also showed that because stronger jets (higher mass flow rate) travel further downstream before being mixed out, the blowing ratio at which the local maximum effectiveness occurred increased with streamwise distance. This demonstrates the need to consider where the cooling film will be required on the vane surface in the selection of an appropriate blowing ratio.

Immarigeonk (*2006*) showed that the low film cooling effectiveness near the hole exit using a higher blowing ratio could be partly counteracted through the use of a laid back fan exit in the hole design. It was found that this resulted in an increased adherence of the film. It was also found to give improved lateral coverage.

Yuen (*2006*) showed that with smaller pitch the spanwise uniformity and coverage in effectiveness were improved. Likewise Immarigeonk et al (*2006*) found that close hole spacing allows jets to coalesce, and therefore small spacing gives better coverage and better effectiveness. This might be thought to promote designs with many very small holes, however, Zhang et al (*2006*) found that increasing the cooling hole diameter improves film-cooling

effectiveness distribution downstream from the point of injection on both the pressure and suction sides for same amount of cooling mass flow. Furthermore, Walsh et al (*2006*) found that a cooling system's susceptibility to blockage is inversely proportional to hole diameter.

It should be noted that the experiments which the above general guidelines are based upon were all carried out under different test conditions and in different scenarios. It would therefore be ill-advised to use the results directly but rather to use them as guidance in the consideration of the proposed designs. The principal points considered important for a good exit design are set out below;

- Shaped exit hole
- Tuneable system in order to use the optimum blowing ratio to suit conditions at the particular location on the blade
    - In general a low blowing ratio would appear to be ideal
- Minimum angle of coolant exit relative to mainstream flow
- Minimum hole spacing

3.2 Internal Cooling Performance

As well as providing an external film it is intended that the cooling air transfers heat away from the vane by convection as the coolant passes through the internal passages of the vane. From Newton's law of cooling (Equation 3-2) it can be seen that for a given temperature difference and heat transfer coefficient the amount of heat transferred is dependent upon the area of contact between the passage and fluid (Cengel et al. *1998*).

$$\dot{Q} = htcA\Delta T$$

Equation 3-2

For a given passage diameter a longer passage length will result in an increase in heat transfer assuming the mass flow rate and temperature differences remain the same. This was illustrated by Arcangeli et al (*2006*) who showed that the overall cooling effectiveness increased with cooling hole length to diameter ratio (*L/D*). Andrews et al (*1985*) also showed that for a given hole diameter the hole length has a significant influence on the overall heat transfer.

It is also important to consider how the heat transfer coefficient can be maximised within the cooling passage. While laminar flow would maximise the heat transferred per unit pressure drop in the system, it is incapable of removing sufficient heat from the vane with acceptable cooling passage diameters. Thus turbulent flow is promoted in cooling passages (and the performance may be assessed by considering not only Nusselt number, but also NU/f, where f is friction factor).

To further promote internal heat transfer other cooling schemes are often employed along with film-cooling; the most common of these being impingement cooling. Impingement cooling is a process whereby jets of coolant air are projected from a series of nozzles onto the surface of the object to be cooled forming an array of stagnation points. The distance between the nozzle exit and the surface onto which the jet impinges is highly significant in terms of how effective the process is (Dhungel et al *2001*). Brevet et al. (*2002*) quoted the optimum distance as 3 diameters, whereas Jambunatha et al. (*1992*) quote the optimum distance as 2 diameters. The optimum distance can clearly not be

generalised due to its dependence on other factors such as Reynolds number, nozzle geometry and jet confinement. In general the heat transfer is proportional to the Reynolds number, however, a highly turbulent jet can result in dissipation of temperature in the jet and reduced heat transfer (Jambunatha et al. *1992*). For multiple jets the most important factor is the spacing of the jets; Brevet et al. (*2002*) suggest a spacing of 4-5 diameters for optimum performance.

It should be recognised that, from the perspective of convective cooling, the velocity of the cooling fluid through the system needs to be a compromise; from the point of view of cooling efficiency, $\eta_c = \frac{T_{ce} - T_{ci}}{T_m - T_{ci}}$, the flow rate should ideally be as low as possible in order to maximise the heat pick up for a given mass flow rate (J/kg), whereas from an effectiveness point of view the velocity should be as high as possible in order to maximise the quantity of energy taken away by the coolant irrespective of the amount of coolant used.

It would be ill-advised to base any designs directly upon the guidelines set out above, but in general it would appear that again the ability to tune the velocity of the coolant throughout the system would be highly advantageous. Furthermore, maximising the coolant passage lengths along with ensuring turbulent flow through them would be beneficial. Finally if it were possible to incorporate impingement cooling within the system the gains over conventional internal cooling could be maximised.

3.3 Novel Cooling Systems

A review of cooling hole technologies was conducted with particular attention paid to those geometries that imitated the desirable aspects outlined above. The concept of film-cooling known as transpiration cooling (Horlock, *2006*), is theoretically very efficient. It is a process whereby the vane acts as a porous plug allowing the coolant to seep through the wall thus maximising heat pick up before it exits onto the vane surface at very low velocities normal to the surface, thus minimising mixing losses and forming a protective insulating film (Eckert et al*. 1953*). Although this type of cooling strategy would produce the optimum cooling with the coolant available a material has not yet been developed which has the required properties to make such a cooling system viable in engine conditions, and any such system would be prone to sand or volcanic ash blockage.

Effusion cooling is regarded as a step towards transpiration cooling (Battisti, *2006*). In this cooling method micro-holes are used which try to mimic some of the characteristics of transpiration cooling (Arcangeli et al. *2006*). The diameter and spacing of the holes can be varied to suit the variation in pressure difference across the blade (Battisti, *2006*). The main disadvantage of this cooling system is its susceptibility to blockage.

Gillespie (*1996*) and Immarigeonk et al. (*2006*) have presented film-cooling strategies which involve impingement of air through an array of holes integral to the blade wall. In the case of Gillespie the wall is locally and substantially thickened, with two staggered holes in an array impinging into a discrete

passage. The impinging flow is exhausted through 30° film-cooling holes of larger diameter and spanwise pitch (Figure 3-2).

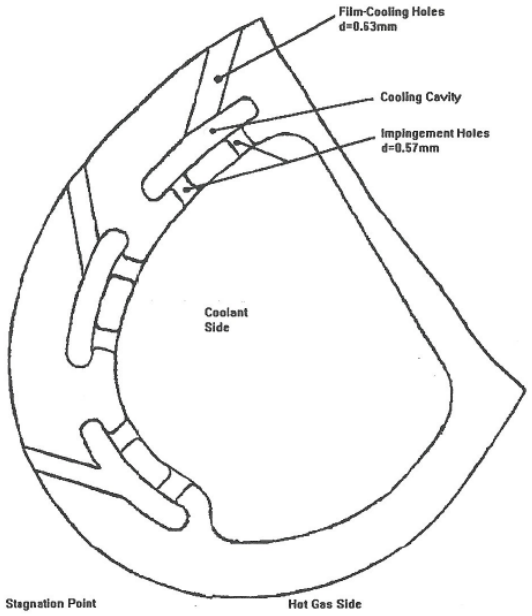


Figure 3-2: Novel geometry with impingement in the blade wall (*Gillespie, 1996*)

Taslim et al. (*2001*, *2009*, *2006*) carried out an extensive study of combined impingement and film-cooling in a leading edge passage. They investigated the inclusion of roughness elements, of shaped impingement holes, and different flow exit strategies. Their method of presentation of results makes it difficult to rank the outcomes from these studies, however, several of the outcomes were highly effective. Immarigeonk et al. (*2006*) present an exit strategy that involves both impingement close to the outside wall and the generation of sharply angled, forward expanding hole exits with pin fins to disperse the flow (Figure 3-3).

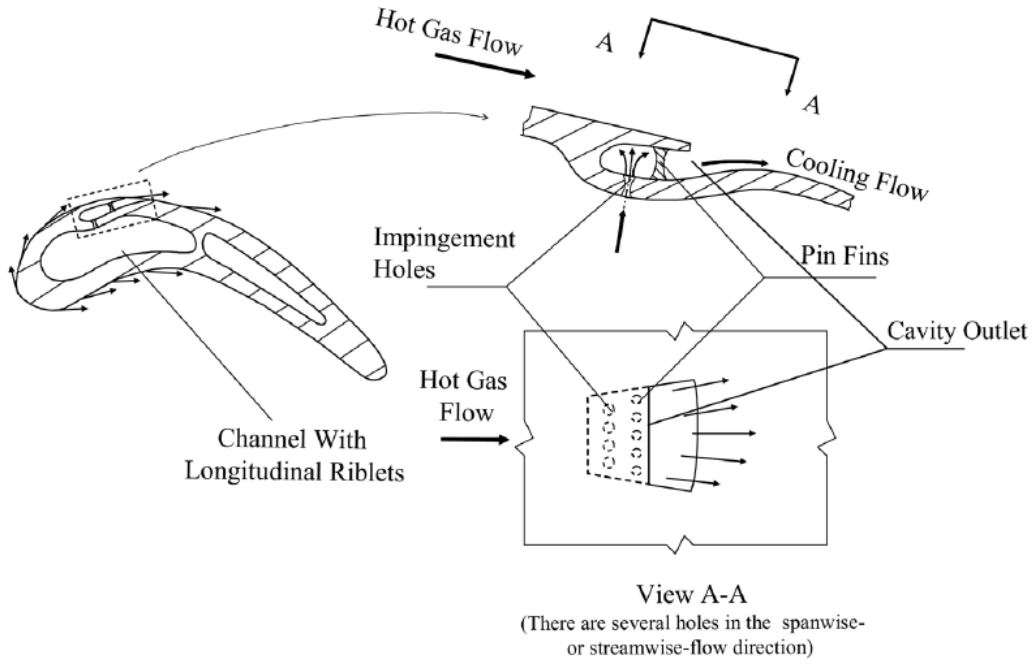


Figure 3-3: Impingement / Film-Cooling Scheme (Immarigeonk et al. *2006*)

This design shows a number of key advantages over a conventional film-cooling strategy; the flared outlet reduces the momentum of the coolant and so gives an improved distribution laterally; the use of pin fins located in the path of the coolant in the louver increase the heat transfer and as the coolant gains momentum with respect to the mainstream, the jet dilution is delayed as more coolant is convected downstream (Immarigeonk et al. *2006)*. However, the scheme appears to create a heavy double wall in the blade or vane, and is most suitable for mid chord applications.

A cooling hole design known as a console is discussed by Sargison et al (*2005*). The geometry aims to achieve similar flow velocity matching using a line of film-cooling holes whose shape is modified such that the exits form a slot. In this case velocity matching is achieved by reducing the passage width in the streamwise direction such that the overall cross-sectional area reduces to

minimise separation of flow in the hole and to accelerate the flow into the mainstream. It offers the mechanical stability of discrete holes, but with high film-cooling effectiveness, η_f, uniform spanwise cooling and reduced aerodynamic loss inside the hole (Sargison et al. *2005*). Figure 3-4 shows a typical console design.

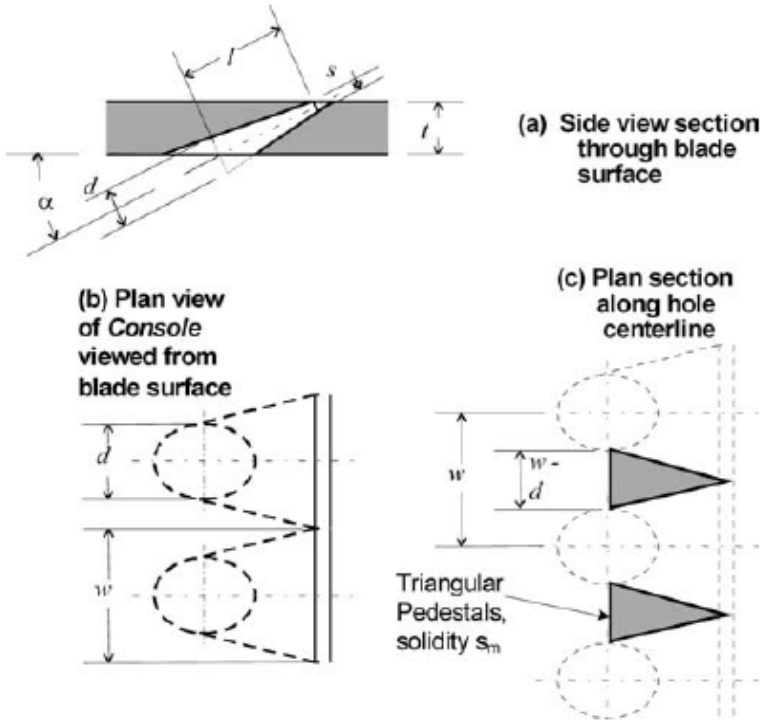


Figure 3-4: Basic Console Configuration (Guo et al. *2005*)

Sargison et al. (*2005*) shows that the jets from the console remain attached to the surface and that the console provides both high levels of cooling and low aerodynamic loss when installed in a NGV. One particularly attractive aspect of this design is its ability to achieve slot-like flow from discrete holes that will remain attached even at high momentum-flux ratios (Sargison et al. *2005*). Again the accelerating flow makes the concept the most applicable to the blade mid chord regions.

Further studies into console geometry were conducted by Liu et al. (*2009)*, who investigated the effect momentum ratio and the console's divergence angle on the film performance. This study found that although far downstream film behaviour was broadly unaffected by the divergence angle, near the slot exit the angle determined the position of peak effectiveness. This study also concluded that at higher momentum ratios film lift-off still occurs and that the optimum momentum ratio with the highest average effectiveness for a console with an inclination of 35˚ was 2.

This study preceded a comparative one, again by Liu et al. *2010*, that presented film-cooling results of both straight holes and consoles arranged around a vane. There were 10 sets of cooling holes with the consoles at a 45˚ inclination. This study found that the consoles performed better at all momentum ratios. On the pressure surface the film performance was found to improve notably with coolant flow, conversely on the suction surface the performance was found to peak, after which it tails off at higher coolant flow rates. The reduction in film-cooling effectiveness was attributed to the separation of the film because of the convex nature of the suction surface.

While such schemes work on the midspan of the vane, at the leading edge ejection of coolant is more problematic, as the momentum ratio of flow exiting is likely to be much greater than unity. The so called Leading Edge Lattice (LEL), which consists of intersecting film-cooling passages arranged around the leading edge, is an example of such a scheme (Nowlin*, 2009*). The LEL scheme (Figure 3-5), utilises high internal loss to prevent ingestion. The high loss makes the system robust against variations in the oncoming flow field and

this results in less cyclical heating and thus potentially a longer component lifespan. Of particular note is the reduction to the stagnation region bulk blade metal temperature and the reduced coolant levels required by using such a scheme compared to conventional films.

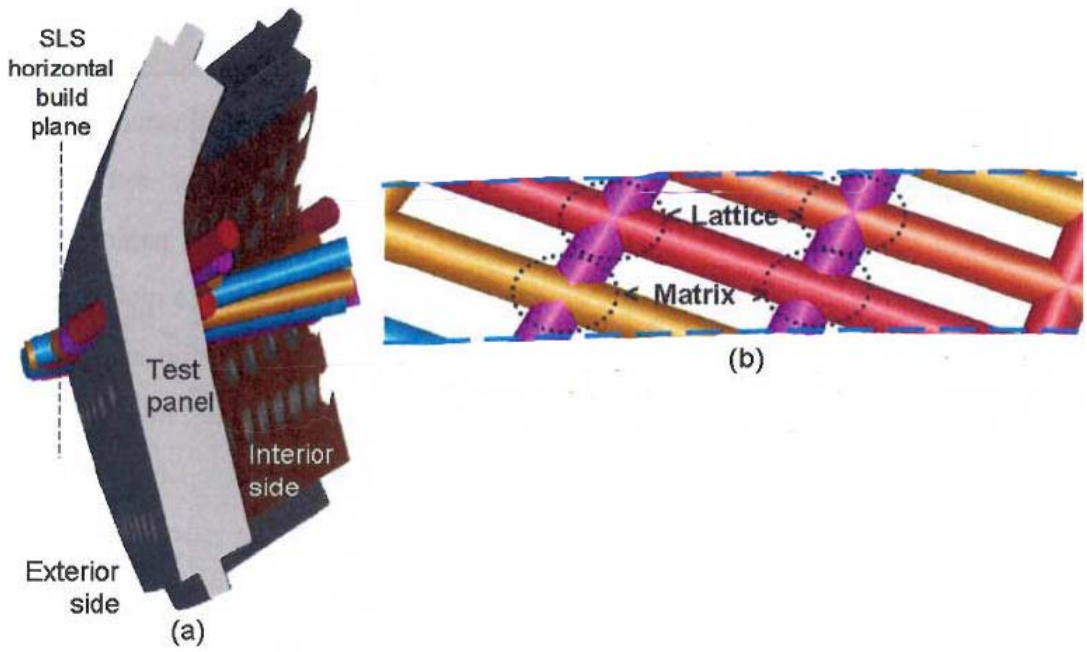


Figure 3-5: CAD detail of the Leading Edge Lattice test panel. Cylinders show cooling passage locations. (a) Span-wise view along Baseline test panel illustrating compound curvature of row paths, (b) view upstream showing wall thickness with wall removed, showing resulting lattice and shallow matrix intersections created by passage alignment within the wall's compound curvature (Nowlin, *2009*)

Dierberger (*1978*) developed a cooling strategy which combines both impingement and transpiration cooling whilst being tuneable to the pressure difference across the vane wall locally. The system (Figure 3-6) consists of chambers within the wall; the inner wall is a variable density impingement plate; the outer wall is a continuous high density array of holes through which the coolant transpires.

The tuning element of the system comes from the ability to vary the ratio of the total area of the impingement holes to the total area of the transpiration holes in each separate chamber.

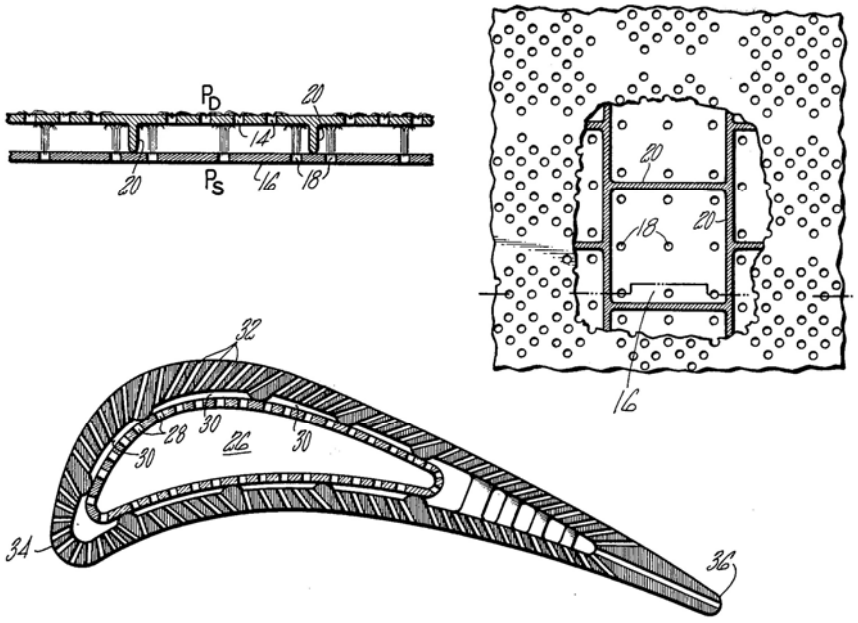


Figure 3-6: Summary of Impingement and Transpiration Cooling System (Dierberger, *1978*)

Before any of the other cooling systems are explained further it is necessary to describe the secondary flow of the coolant exiting a conventional single film-cooling hole. Walters et al (*2000*) showed that the exiting coolant tends to have secondary vortices which are generated by two sources; the streamwise orientated vorticity contained in the film-cooling hole and the friction of the jet with the cross flow. These secondary flows are known as kidney vortices (Kusterer et al. *2006*) and have the effect of entraining the mainstream beneath the cooling jet. This not only means that the hot mainstream flow, which the film is meant to protect the surface from, is able to interact with the surface and cause further heating, but also means that the cooling film is forced to 'lift off'

from the surface. Both these aspects are detrimental to the film-cooling performance. The following novel methods repress the effect of this secondary flow within the cooling flow with the aim of improving η_f (Figure 3-7).

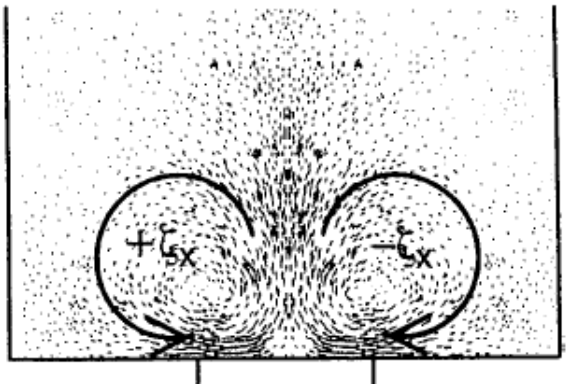


Figure 3-7: Kidney Vortices at a Cross Section Downstream of the Coolant Exit (Walters et al. *2000*)

Kusterer et al. (*2006*) attempted to reduce the effects of kidney vortices through the use of a cooling strategy known as double jet film-cooling (DJFC). The aim was to generate an anti-kidney vortex system in the jet as the major secondary flow phenomenon (Kusterer et al. *2006*). (Figure 3-8)

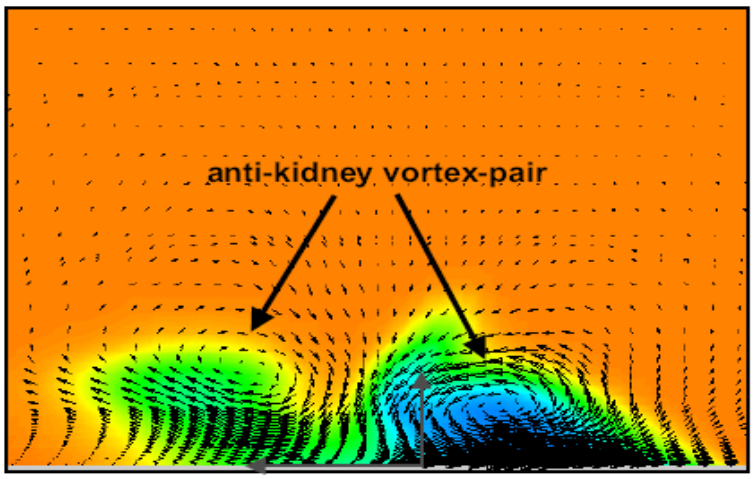


Figure 3-8: A Cross Section of the Flow Field Downstream of the Coolant Injection (Kusterer et al. *2006*)

The principle behind this lay in the use of a second cooling hole with a dominating vortex rotating in the opposite direction to that of the coolant from the original hole (Figure 3-9).

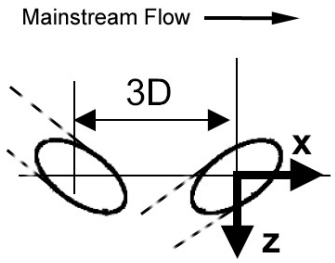


Figure 3-9: Hole Positioning and Alignment for DJFC (Kusterer et al. *2006*)

This was shown to have three benefits; better distribution laterally, improvement in wall contact of jet (thus preventing flow of hot gas under the jet) and reduction in lift off.

Okita et al. (*2007*) developed an arrowhead-shaped cooling hole geometry (Figure 3-10). The geometry was "designed to offer improved film-cooling effectiveness, without increasing the heat transfer coefficient or aerodynamic loss (Okita et al. *2007*).

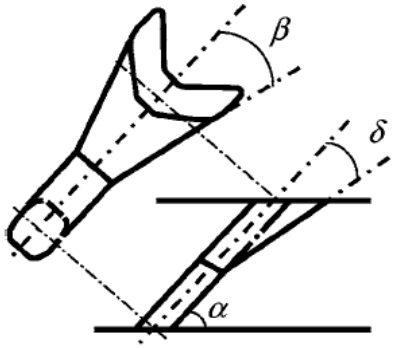


Figure 3-10: Arrowhead-Shaped Hole Geometry (Okita et al. *2007*)

The arrow-shaped cooling holes were shown to exhibit the anti-kidney vortex system which once again reduced both coolant lift off and hot gas entrainment. Results showed greater increases in film-cooling effectiveness at higher blowing ratios and improved lateral coverage.

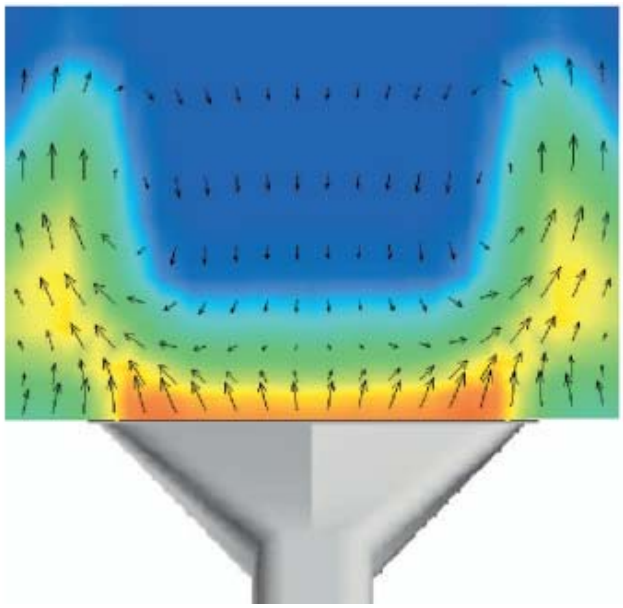


Figure 3-11: Calculated Secondary Velocity Vectors for Arrow-Shaped Cooling Hole (Okita, *2007)*

3.4 Conclusion

The designs and research reviewed in this chapter have highlighted key aspects and parameters of film-cooling designs that significantly affect the system's performance; to achieve an improvement over traditional film-cooling holes in the leading edge region a cooling system should aim to have:

- High internal convective efficiency
- High film-cooling effectiveness (η_f)
- Low external aerodynamic loss
- Ingestion free system robust to fluctuating external pressure field

These aims are addressed by producing a cooling system design strategy with the following capabilities:

- To maximise the cooling hole length to diameter ratio such that the convective cooling efficiency can be increased
- To vary the exit velocity of each cooling row such that the ideal blowing ratio is approached for all hole locations
- To situate impingement of coolant air within the wall as close to the outer surface as possible to maximise its benefit
- To minimise the coolant ejection angle relative to the external flow to reduce mixing of the coolant with the heated flow and to improve film attachment to the surface
- To minimise exit flow velocities near the leading edge to minimise mixing and maximise film coverage.
- To provide sufficient hole length at the cooling hole exit to align the flow with the geometric passage shape
- To generate non-circular exit passages with a high spanwise to streamwise aspect ratio
- To generate turbulent flow within the passages

Chapter 4 Dendritic Cooling Designs

The concept of dendritic cooling was first outlined by Mittal (*2006*). The eventual design aims to address the required capabilities for improved film-cooling whilst exploiting newly available more complex cooling geometry in the wall possible by manufacturing using virtual pattern casting (*VPC*). *VPC* is a technique for the rapid manufacturing of casting cores which is currently under development.

In this chapter, *VPC* casting is first briefly described along with consequences for the heat transfer process found by Mittal (*2006*). Dendritic cooling is next outlined, and modifications made to designs previously proposed to create feasible systems with improved flow or heat transfer characteristics for vane cooling are described in detail. The results of a manufacturing trial of a typical early dendritic test piece are reported along with the design guidelines which resulted from the partial success of the casting process. Finally, a number of dendritic systems have been designed by the author, manufactured using direct metal laser sintering and made available to a co-worker, Mr. S. Luque, in the Osney laboratory for testing in an annular sector rig using real engine parts. These designs are presented.

4.1 Virtual Pattern Casting

The manufacture of cooling systems in the walls of turbine blades and vanes has, until recently been restricted to features which could be drilled or electro-discharge machined into the solid. Only recently has it become possible to add complex features such as bends or branches at reasonable cost with the advent

of a new manufacturing process known as virtual pattern casting (*VPC*). A detailed analysis of the aspects of the processes pertinent to this study are given in Mittal (*2006*) but a brief summary of the process along with the highlights of Mittal's findings is given here.

VPC is a process whereby the ceramic casting mould and core, in this case for an NGV, is created directly from a CAD model. *VPC* is based upon a process called stereolithography. This is a process where a solid part is created using a laser to solidify a photosensitive resin. The fundamental difference between stereolithography and *VPC* is the resin; traditionally an epoxy resin would be used whereas with *VPC* a ceramic resin is used. Ceramic resins can be used at far higher temperatures and therefore offer wider potential applications (Mittal*, 2006*). The motion of the laser is determined by interpretation of the CAD model. There are two important aspects about the nature of the final model which are determined by the sterolithography process; the step size and the growth angle. The step size refers to the size of the layer of sterolith exposed to the laser at each stage as the model is generated. The growth angle refers to the orientation of the model to layers within the model; the base of the model may not be parallel to these layers. Two important conclusions about the nature of the *VPC* passages were drawn from Mittal's 2006 work; i) the nature of the process results in passages having an inherent roughness; this will vary depending upon the angle at which the passages are grown, and ii) the increase in Nusselt Number (Nu) due to friction is proportional to the increase in friction factor over a hydraulically smooth passage. These findings led to the development of a form of cooling which exploited the additional

roughness though the branching of passages, this formed the initial concept of dendritic cooling.

4.2 *Development of Dendritic Geometry*

The basic principle of dendritic cooling is to generate a film-cooling hole passage that continually splits thus facilitating the tuning of coolant flow and the maximisation of heat pick up through extension of passage length for a given vane wall thickness. This relies on the use of small passages (typically less than 1mm in diameter) which repeatedly split along their length. The key point is that the cross sectional area of each subsequent passage remains constant; this effectively means the total exit flow area for a given dendritic system will increase by the ratio exit to inlet at each split. This will in turn result in the inverse ratio in velocity for each split. This is particularly advantageous when considering the control of the exit velocity relative to the mainstream and trying to optimise the film whilst minimising interaction with the mainstream flow.

The first of the designs was a ‘pyramid’ type structure (Figure 4-1). This introduced the basic principle of a splitting cooling passage thus facilitating the tuning of coolant flow and the maximisation of heat pick up through the wall.

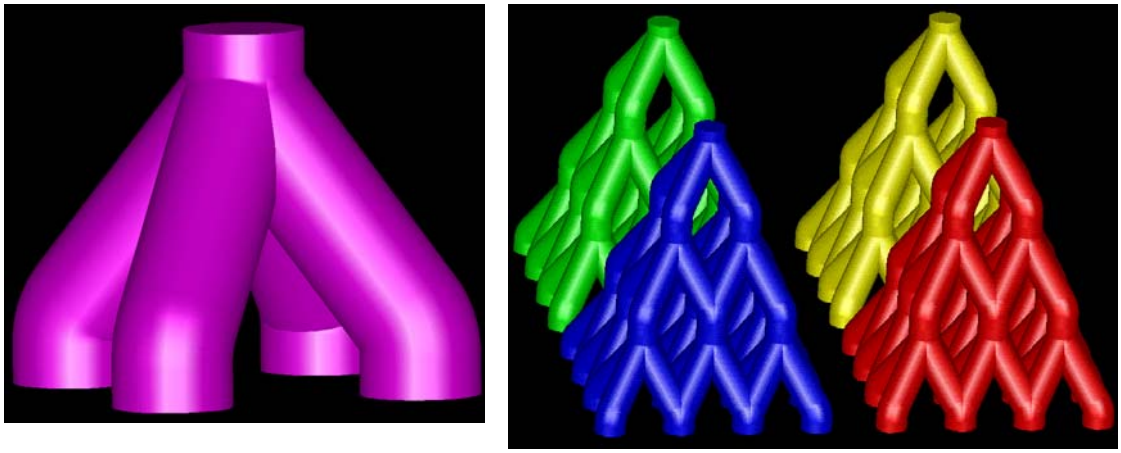


Figure 4-1: Initial dendritic design (Mittal, *2006*)

It was recognised that whilst this design was in principle very promising it was inefficient in terms of packing and that in order to continue the branching system former splits had to merge. As the number of splits increased there was a requirement for an increase in both the spanwise and streamwise dimensions; a single network could potentially experience a large difference in pressure difference from exit to exit and in doing so leave sections of a single cooling network starved of coolant or create a risk of ingestion in the outer branches. This uniform expansion would introduce further problems when trying to apply the design to a vane cooling system scenario where there is significant curvature in the external wall profile.

The first development of this design was to introduce a short connecting passage between exit branches at each split, and to restrict branching to bifurcation. This created an area of impingement heat transfer in each branch. It also allowed the maximum possible number of splits per unit depth of wall to be inclined without the need to recombine branches. By reducing the number of splits per layer to two it was possible to only increase the network in the spanwise direction, making the application of this design to a vane more

feasible (as now exits are all at similar static pressure). The number of splits depends on the required exit velocity. In a vane, where there is a single feed pressure it is possible to achieve spanwise coverage through a series of networks as shown in Figure 4-2. The systems are described by the number of co-flowing passages moving from the inlet to the exit of the dendrite. Thus, the 3 systems show are '1-2', '1-2-4' and '1-2-4-8' systems.

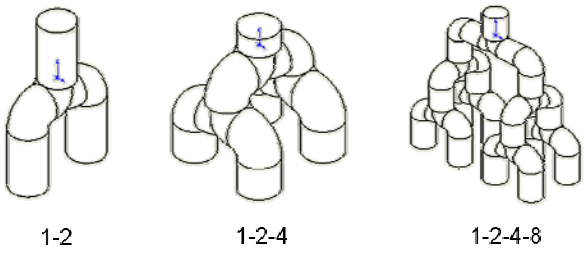


Figure 4-2: Dendritic Geometry Mk I

In order to improve packaging whilst still maintaining full spanwise coverage a skewed version of the original dendritic geometry has been proposed in the current research (Figure 4-3). This was modified to give angled exits (Figure 4-4), which reduce the effective blowing ratio of the exiting flow.

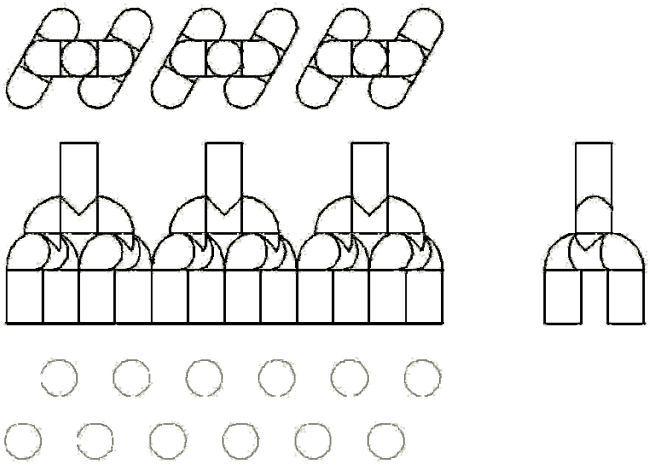


Figure 4-3: Dendritic Geometry MkII

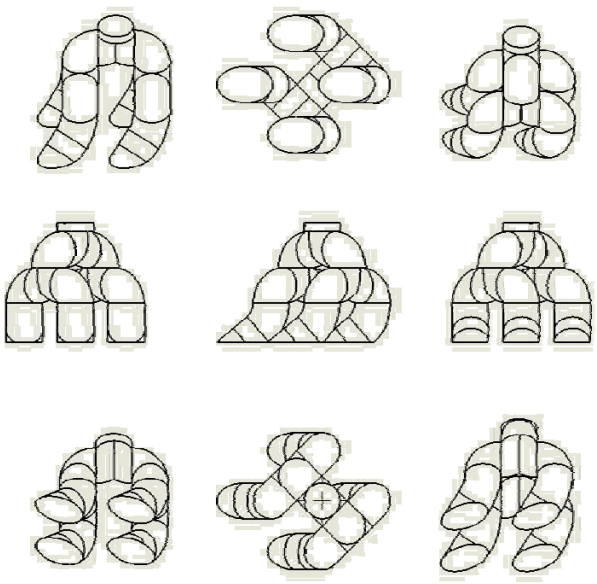


Figure 4-4: Dendritic Geometry Mk III

The Mk III dendritic geometry show in Figure 4-4 presented two problems; in terms of packaging it was not as compact as the Mk II (Figure 4-3) geometry and the angled exits were so short it was thought they would have little effect on the flow. With this in mind the Mk IV geometry was developed (Figure 4-5).

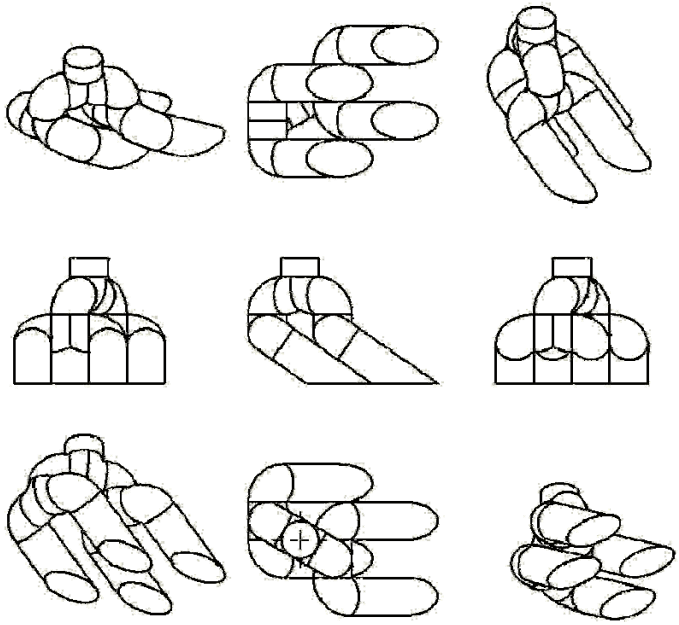


Figure 4-5: Dendritic Geometry Mk IV

Whilst this was an improvement on the previous generations it still did not have any hole fanning which is typical of successful conventional film-cooling designs. A typical design incorporating these features is shown in Figure 4-6.

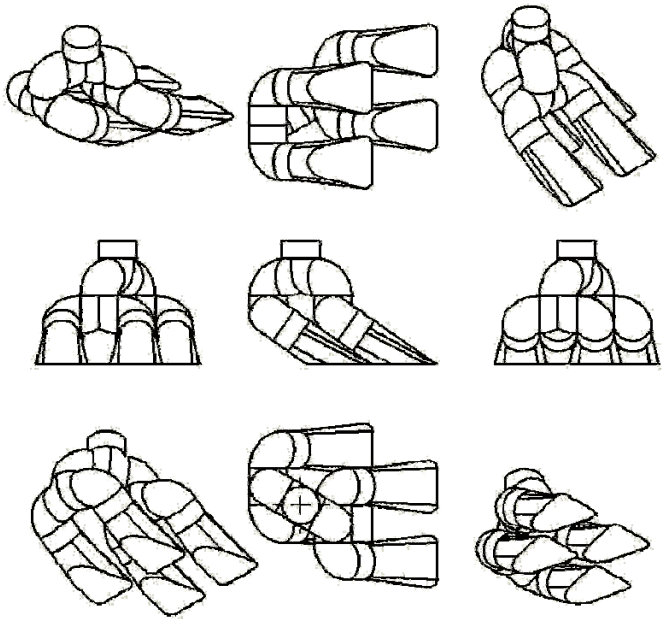


Figure 4-6: Dendritic Geometry Mk V

It was thought that with such large fan exits and such a comparatively short development length the coolant flow would not expand to fill the fan and would exit mainly in the centre. To try to get the coolant flow to fully 'expand' spanwards within the exit, a design similar to the console exit (Sargison et al. *2005*) was incorporated (Figure 4-7). This also had the effect of reducing the tolerances involved with the separation of sections of the dendrite. Importantly the exit here does not converge, but rather is area ruled to maintain constant velocity in the final exit branch.

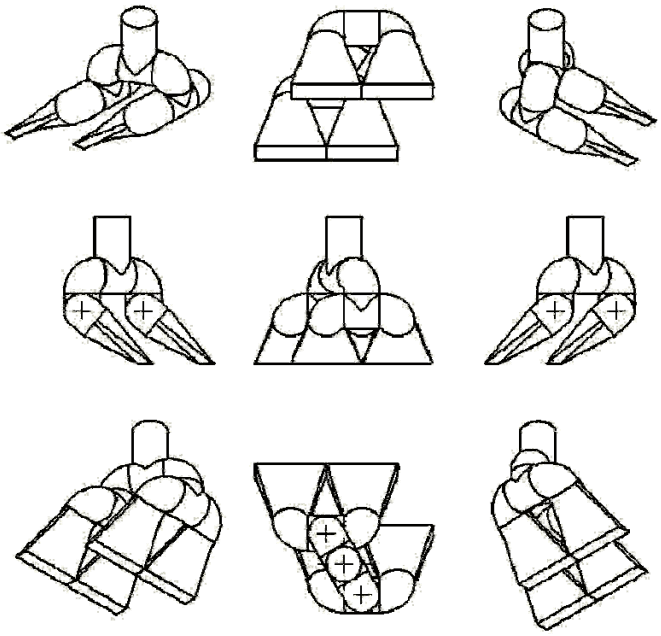


Figure 4-7: Dendritic Geometry Mk VI

Obviously it is possible to incorporate any of the above dendritic designs into either a 1-2, 1-2-4, 1-2-4-8 or even larger systems. In addition to developing designs based upon the dendritic format other designs were also developed by the author. The aim here was to consider what might be possible using *VPC*. The U-bend system shown in Figure 4-8 is loosely based upon the dendritic

geometry but tries to maximise the length of the passages whilst incorporating impingement cooling as close to the heated wall as possible (Figure 4-8).

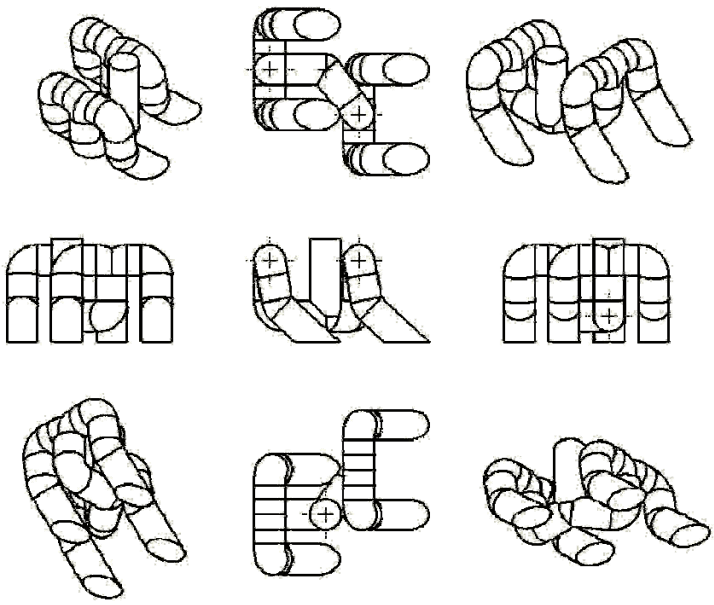


Figure 4-8: U-Bend Geometry

A ‘safe’ geometry in terms of manufacturability risk was also proposed. This was the S geometry (Figure 4-9). This design aimed to maximise the length of the passage whilst giving an angled exit and a high likelihood of turbulent flow by situating bends closely together to enhance heat transfer.

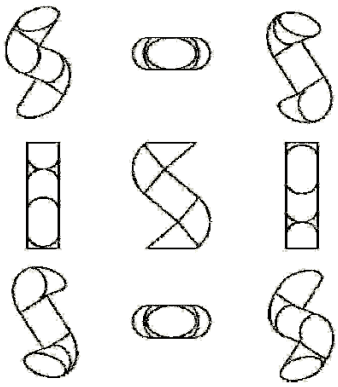


Figure 4-9: S Geometry

4.3 Design Selection for further Investigation

For the remainder of the research reported in this thesis, the design concepts were down selected, with an emphasis on manufacturable designs. Thus two different dendritic designs are considered further in this work; a dendritic system using conventional circular holes, based on, the MkII dendrite, and the more technically adventurous design based on the MkVI geometry. Before testing some of these designs at large scale, as reported in Chapter 6 and Chapter 7, work, reported below, was conducted to verify that such designs could be manufactured and to identify limiting parameters of such processes. Furthermore the Mk IV dendritic design was applied to the leading edge of a Trent 500 NGV. This change was undertaken as more information became available in the project.

The cooling hole diameter was a key parameter that needed consideration before a complete design could be produced. It was decided that the hole diameter should be maintained at that currently used because i) the systems under consideration already push the technological envelope and it was felt that reducing the hole diameter further could unnecessarily jeopardise the programme since susceptibility to blockage is inversely proportional to hole diameter (Walsh et al. *2006*): ii) hole diameters of 0.6mm are those currently used on the Trent 500 NGV which does not experience blockage problems.

Particular attention was paid to the efficient packing of cooling systems into the wall thickness. A geometric compromise had to be found between maximising the number of dendrites and orientating them for optimum cooling performance. Each dendritic system was designed such that it could be neatly incorporated in

to a series of dendrites with the most efficient packaging possible to form a dendritic cooling array.

4.4 Vane Ready Designs

Whilst it is important to understand how a particular cooling system performs in isolation, it is fundamental to know how that system can be applied to real engine geometry and how such a arrays performs under engine representative conditions. With this in mind four alternative dendritic cooling shcemes were designed.

Each scheme was designed such that a single design of dendrite provides cooling over a short streamwise section of the vane, the unit being repeated in the less critical spanwise direction at that streamwise location. This means the variation in pressure between the exits of individual dendrites is small, reducing the likelihood of significantly different flow between a given dendrite's exit passages.

The dendritic structures have longer passage lengths than conventional cooling holes; this means that for one of these systems a section of wall will have lower effective density than in the case of a conventional cooling system. With this in mind, a decision was taken to increase wall thickness in the knowledge that the extra weight associated with the increase would be partly offset by the reduced density, this is advantageous to the inclusion of systems with multiple branches.

All the dendritic proposals were designed for the leading edge of a Trent 500 HP vane. In order to facilitate testing of the cooling arrays, inserts were designed which replaced a section which could be cut from the leading edge of

the vane using a plane EDM cutting tool (Figure 4-10). The inserts were, of course, made from metal of similar conductivity to that of the original blade, and results of testing (not carried out by the author) are reported in Luque (*2011*) and in Chapter 9 of this thesis. As the *VPC* casting technique was much too expensive, the engine scale inserts were manufactured using a process called direct metal laser sintering. This allowed the reproduction of a metal engine scale leading edge with the conventional cooling holes replaced with dendritic systems. This new leading edge could then be transplanted in to an engine NGV on which engine representative tests could be conducted.



Figure 4-10: A vane with leading edge sections removed in preparation for the installation of an insert (right) and as it would have looked before the leading edge section was removed (left)

The size of the insert constrained the region over which the coolant array could be incorporated from approximately 40% of the perimeter from the stagnation point on the pressure surface to 20% of the perimeter from the stagnation point on the suction surface. The portion of the NGV which the insert replaced is show in Figure 4-11. Note that this cooling array must provide film-cooling further downstream on the suction side (up to 30%), and later in this thesis its performance is compared to baseline cooling schemes on that basis (see 7.9).

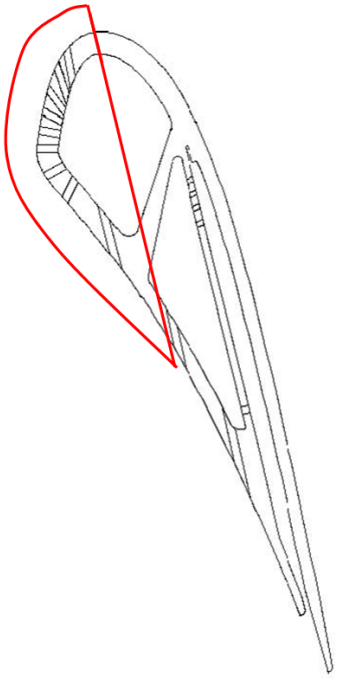


Figure 4-11: Portion of the insert which makes up the *NGV*

For the first two geometries, detailed in section 4.4.1 and 4.4.4, the MkI insert, which is shown in Figure 4-12 on the left, was used. In the subsequent attachment of this type of insert it was discovered that it proved particularly difficult to do so because of the non-parallel edges of the spanwise faces that mate with the cut away section of the NGV. Furthermore it was felt that extending the distance the insert continued in a spanwise direction would minimise any interaction of the joints with the film profile whilst allowing the full width of the aerofoil section to be utilised. To this end the insert detailed in Figure 4-12 on the right was developed for use with the dendritic geometry detailed in section 4.4.2 and 4.4.3.

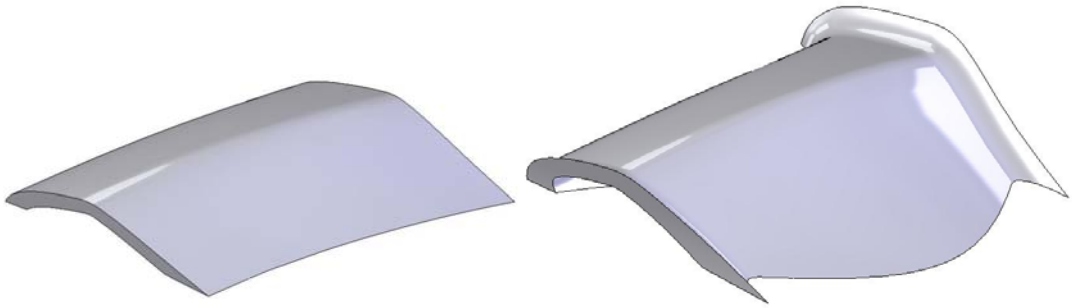


Figure 4-12: Mk I insert (left) and the MkII insert (right)

The MkII insert consisted of a section that whilst only covering a slightly larger region in the streamwise direction extended further in the spanwise direction in to the radiused portion of the end walls. The slight extension in the streamwise direction was beneficial from two points of view: i) the incorporation of a portion of the web section which divides the internal serpentine passages which in turn increases the available contact area for the attachment of the insert, ii) all contact faces between insert and NGV are parallel.

4.4.1 High Density Small Diameter Circular Cross Section Dendrites

The original leading edge dendritic insert was designed such that each row of conventional film-cooling holes was replaced by a row of dendrites. All dendrites were either of 1-2-4 or 1-2-4-8 design. In total there were 9 rows of dendrites all with circular holes, and passage diameter of 0.6mm. The insert is shown in Figure 4-13 and had a wall thickness of 2mm.

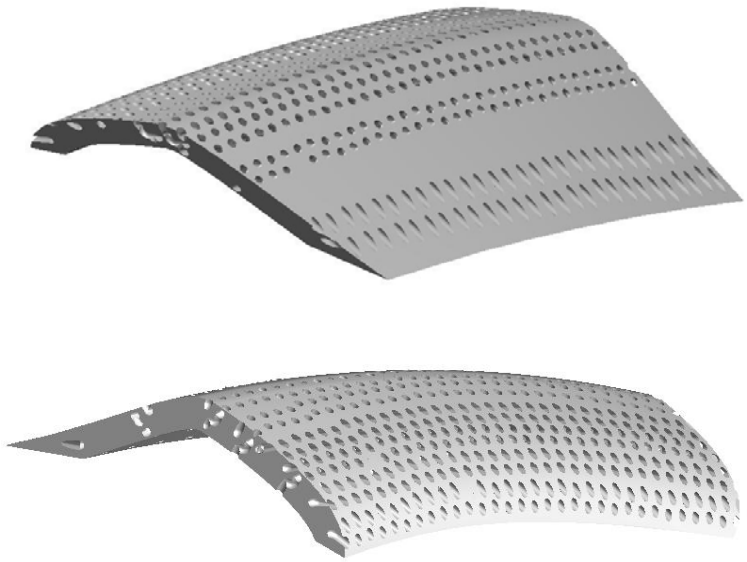


Figure 4-13: Insert with a high density array of small diameter circular cross section dendrites

In this first design particular attention was paid to the external flow around the NGV and how the blowing ratio should be controlled at each exit location to achieve velocity matching to external conditions. The number of branches in each system was high, typically 2-3, in order to achieve a blowing ratio no greater than 1 and ideally no less than 0.5. At this early stage of the research programme the blowing ratio was assessed using a standard pipe work loss model (Fried and Idelchick, *1989*, Miller, *1990*).

4.4.2 Large Diameter Circular Cross Section 1-2 Dendrites

After *VPC* trials described in section 4.4.4 and the subsequent changes in design guidelines, it became apparent that the available wall thickness severely limited the complexity of passages which could be included. Thus, it was decided to focus less on the highly branching systems and instead use simpler systems in combination with a 25% increase in wall thickness from 2mm to

2.5mm. It was felt that such changes would enable subsequent designs to fulfil the initial design brief, while guaranteeing their manufactability.

Thus designs used the design guidelines developed from the earlier casting trial. Unlike 4.3.1-4.3.2 there was no attempt to mirror the position of previous rows of holes. A significant problem of the insert described in 4.4.4 was the extremely low flow rate of coolant which it passed. This in combination with the manufacturing issues of the more complex geometry reinforced the argument to only use the simpler, lower loss, 1-2 dendritic systems. A wall thickness of 2.5mm was maintained in order ensure there would be no break out issues. The sole use of 1-2 dendrites allowed the number of rows of dendrites to be increased whilst satisfying the new design guideline on minimum feature separation. This design had 14 rows of dendrites using a passage diameter of 0.84mm (Figure 4-15 and Figure 4-16). A test piece was manufactured using direct metal laser sintering as shown below. Note that while this technique is not suitable (yet) for engine mainstream components, it may be suitable for sector liners and stationary components in the future. Here it was used for ease of manufacture.

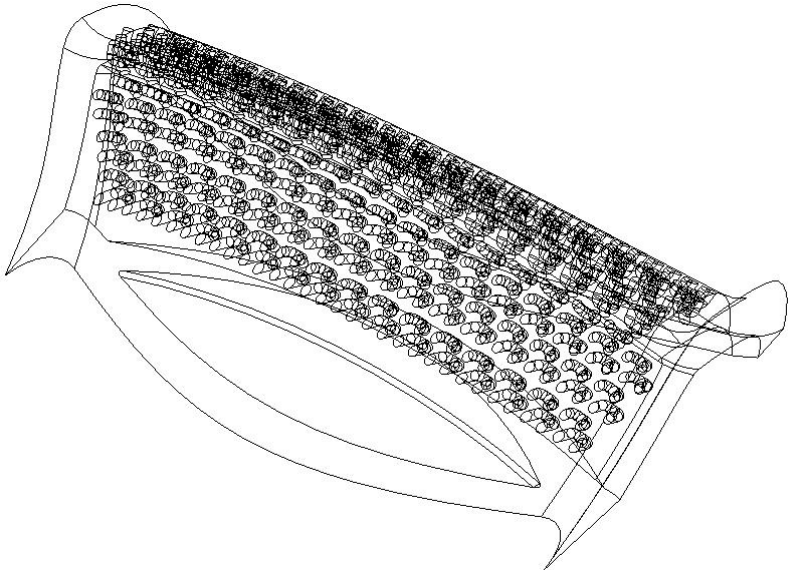


Figure 4-14: CAD picture illustrating the layout and tight packaging of the array of 1-2 circular cross dendrites

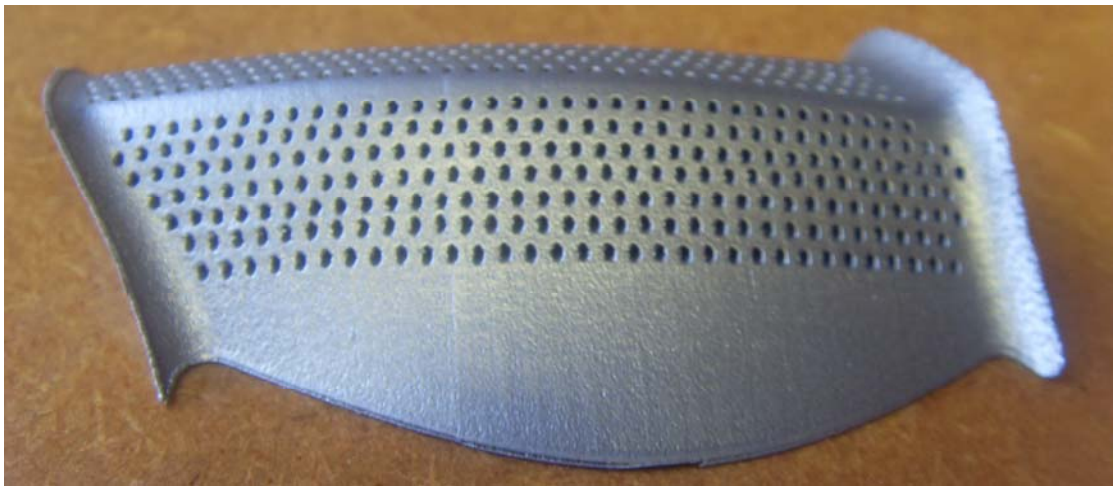


Figure 4-15 A 1-2 circular cross section dendritic cooling array incorporated in to a leading edge insert (pressure surface)

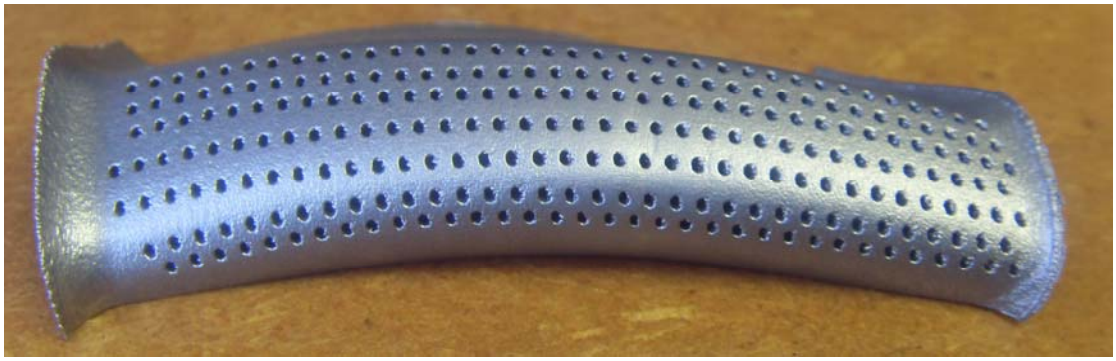


Figure 4-16: A 1-2 circular cross section dendritic cooling array incorporated in to a leading edge insert (suction surface)

As well as the packing, particular attention was paid to the orientation of the dendrites. By angling the dendrite relative to the centreline it was possible to achieve better spanwise coverage by effectively drawing the cooling exits closer together in the spanwise direction.

	Trent 500 leading edge cooling scheme	Leading edge circular cross section dendritic scheme	Leading edge slot exit dendritic scheme
external area served (mm^2)	2750.130	2614.749	2697.057
internal wetted area (mm^2)	2645.699	2185.330	2197.386
hole diameter (mm)	0.728	0.740	0.700
number of passages	238	204	243

Table 4-1 Comparison of geometric design parameters for each cooling design

4.4.3 Large Diameter Dendrites with only Single Splits and Slot Exits

This design was principally based upon the design described in 4.4.2, however rather than using conventional hole exits with a circular cross section this new design used a slot at the exit to give full spanwise coverage for each row (Figure 4-17 and Figure 4-18). Here, it was ensured the area at any cross section through the slot was the same as that at the inlet to the slot. This was to ensure the flow wouldn't accelerate through the passage thus reducing any advantage gained from the reduction in exit velocity created by the splitting of the passage.



Figure 4-17: A 1-2 slot exit dendritic array incorporated in to a leading edge insert (pressure surface)



Figure 4-18: A 1-2 slot exit dendritic array incorporated in to a leading edge insert (suction surface)

In this design particular consideration was given to the maximisation of passage length in order to optimise internal convective heat transfer. It was with this in mind that extended passage design for the final row on the pressure surface was produced Figure 4-19.

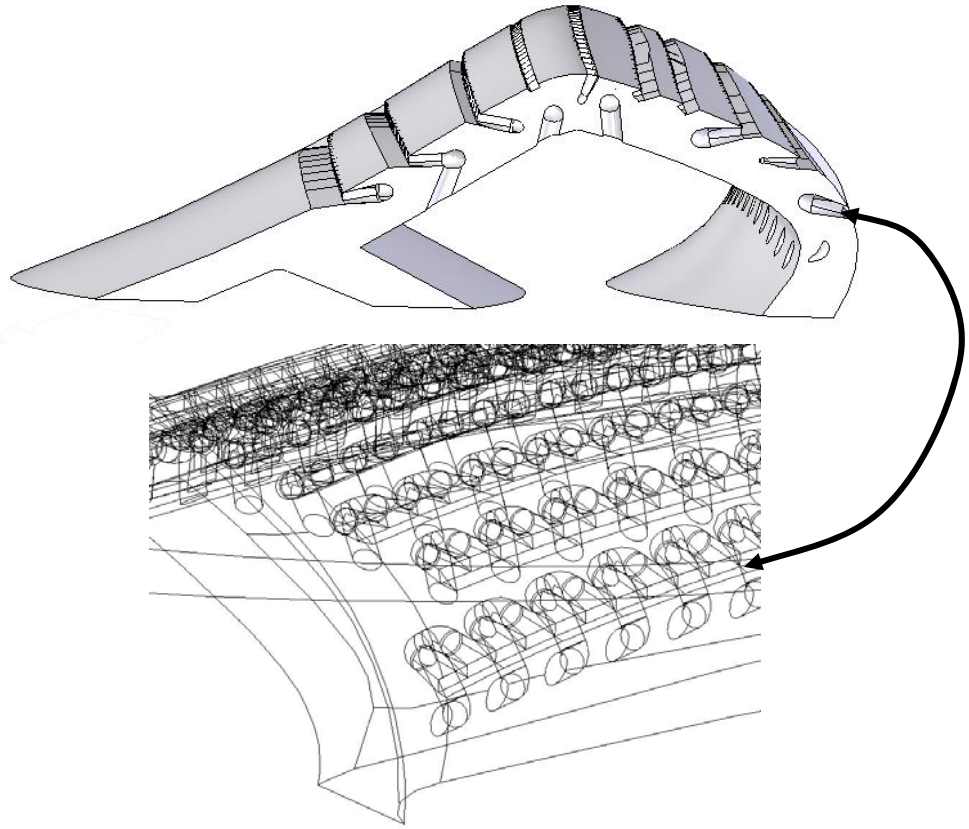


Figure 4-19: CAD picture illustrating the extended passage lengths of the final row of dendrites on the pressure surface

4.4.4 *VPC* Casting Trial of a Low Density, Small Diameter Circular Cross Section Dendritic Cooling Scheme

Demonstrating manufacturing capability is a key aspect to a technology like dendritic cooling if it is to progress beyond this project into real engines. The insert described in section 4.4.1 was used as the basis of a design to be cast in *HP* vane material CMSX4 using the *VPC* manufacturing process pioneered by Rolls-Royce Indianapolis (Frasier, *2010*). This was the first time such a method had been used to produce a part of this type. As such, the limits of the process and how it would deal with such intricate geometry were unknown. To provide the design for a manufacturing test piece a leading edge insert was specified using every other row from the design shown in section 4.4.1 leaving an insert with 5 rows of dendritic systems (Figure 4-20). The wall thickness of the insert

was 2.5mm compared to 2mm for the baseline blade. The casting trial was partially successful; whilst the part formed the desired shape there were some obvious problems with it (Figure 4-21 and Figure 4-22) which are described below.

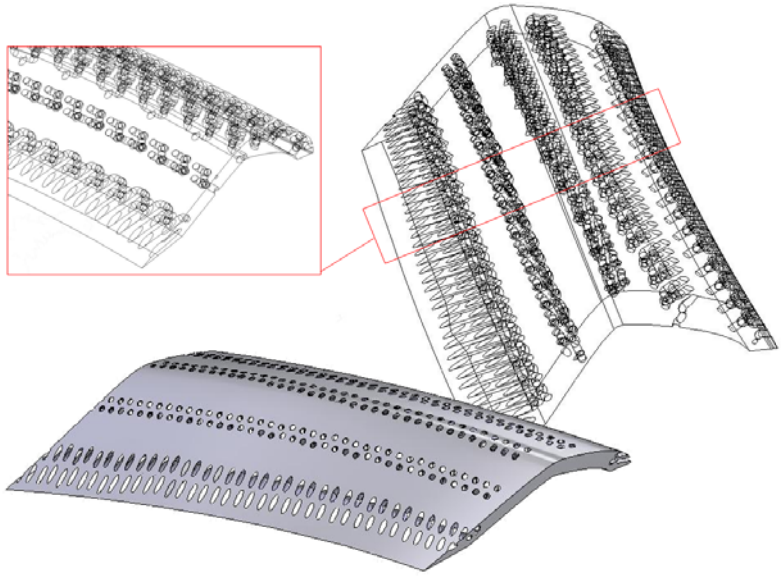


Figure 4-20: A leading edge insert cooling scheme with a low density array of small diameter circular cross section dendrites

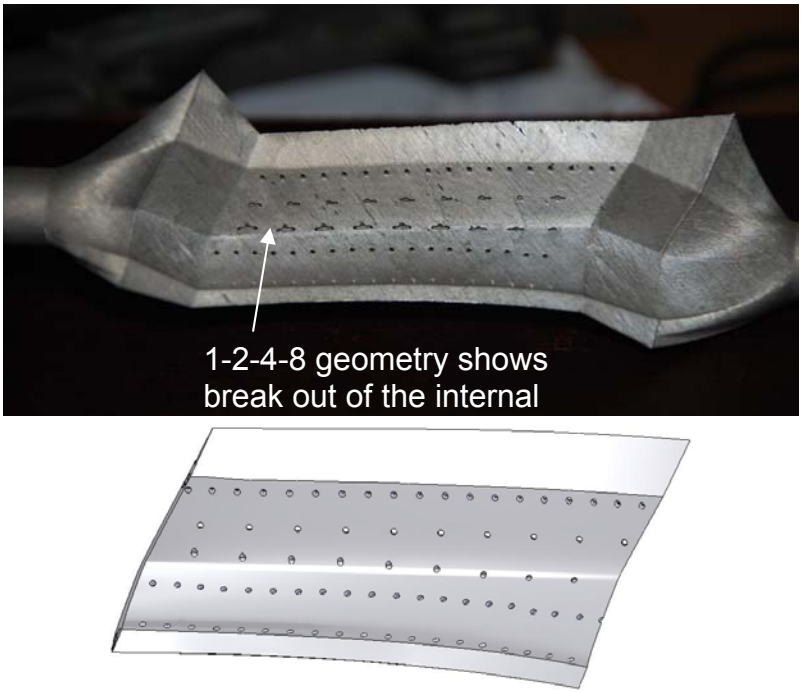


Figure 4-21: A leading edge insert cooling scheme with a low density array of small diameter circular cross section dendrites. Internal view of the actual insert (top) and the CAD model (bottom)

An encouraging and highly significant outcome was that the cast ceramic core which was used to construct the mould from which the insert was manufactured exhibited no cracking along the passage lengths. This therefore meant that the passages were able to fully form and produce a continuous channel capable of passing flow.

Problems encountered were also useful in helping with the formation of design guidelines for future *VPC* leading edge cooling schemes.

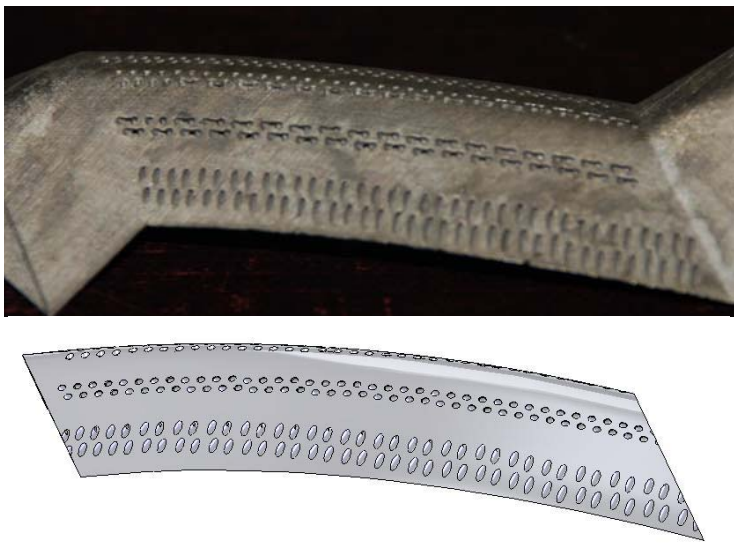


Figure 4-22: A leading edge insert cooling scheme with a low density array of small diameter circular cross section dendrites. Pressure surface view of the actual insert (top) and the CAD model (bottom)

The main problems encountered in the casting trials were a reduction in passage diameter between the initial design and the cast article, the break out of passages near the external surface and the merging of some passages. In the case of reduced hole diameter, it was thought that this discrepancy could be attributed to shrinkage of the part after its initial formation. As such, it was decided that a scale factor should be applied to all passage diameters in order to achieve passage diameters of the desired size.

Passage break out is the situation where the wall surrounding a dendritic system does not completely form and channels were left exposed, at the outside of the insert. It was thought that this occurred as a consequence of the branching members of the passage sitting too close to the wall of the insert. As a result, the surface tension of the metal between the ceramic core and the wall of the casting was too great for the metal to flow and so the passage failed to form leaving the inner part of the passage exposed. In order to avoid such a problem in the future a minimum spacing of one passage diameter (up to 1mm) between the branching passage running parallel to the external wall and the external wall is required.

A similar problem was that of passages merging. In this case adjacent dendrites joined up, forming a single larger system. This is particularly worrying as it is difficult to identify the casing failure, and the void formed is likely to compromise the structural integrity of the component. Again the presence of such passages was put down the proximity of features to one another. It was decided that in order to avoid such a problem in the future a minimum spacing of one passage diameter (for d<1mm) between adjacent dendrites would be adopted in subsequent designs.

After the design and subsequent manufacture of this test piece it became apparent that once new design constraints were implemented space was at a premium. The wall thickness may be locally increased but it is at the expense of weight in the component. It was obvious that the current level of complexity of passages and the space available simply were not compatible. As such it was decided to focus less on the highly branching systems and instead use

simpler systems, designed in this case for a 2.5mm thick wall. It was felt that such a decision would enable subsequent designs to fulfil better the initial design brief. In fact it will be shown later that the additional branches do not significantly affect the loss through the system.

This chapter has shown how the idea of dendritic cooling can be implemented in the cooling schemes of real engine components. Two key dendritic designs which are further investigated in the thesis are set out. These are shown embodied in the leading edge of a modern civil jet engine NGV, and metallic models have been produced at engine scale to allow representative testing to be carried out. Finally a model of a typical system was test cast using the *VPC* technique. The consistent failure of the casting core to yield viable components allowed very simple guidelines to be produced to ensure better performance in future designs, and these rules were immediately implemented in the subsequent designs.

Chapter 5 Experimental Methods and Techniques

All the experimental work conducted by the author which contributed to this thesis centred around the use of a low speed wind tunnel in the OUEL, Osney Laboratory. Furthermore, common techniques were used in the processing and analysis of the results obtained. The wind tunnel and processing techniques are detailed in this chapter.

5.1 Experimental Setup

5.1.1 Apparatus

The wind tunnel used in the experiments is a 500 x 500 mm square working section tunnel. The inlet flow, from atmosphere, passes through a number of screens and a honeycomb section before being accelerated through an area ratio of 4:1. A mesh heater is installed at the entrance to the working section which is able to supply 150 kW of heat to the mainstream flow. The walls of the working section are constructed from Perspex[1], though these may be substituted by Rhoacell[2] parts for adiabatic measurements. Tunnel speeds of up to 27 ms^{-1} can be obtained with the heater installed. The freestream turbulence intensity is very low in the working section $Tu < 0.1\%$. Previous measurements (Nowlin, *2005*) have shown the flow velocity uniformity in the tunnel to be +/- 1% in the first metre of the working section.

[1] ICI trade name for cast Polymethylmethacrylate sheet
[2] A closed pore blown polymethylmethacrylate foam with conductivity similar to that of air.



Figure 5-1: Low Speed Wind Tunnel (Top right: Coolant Plenum and down stream plate coated in liquid crystal, Top Left: Viewing area with DAQ equipment, cameras and coolant exit array)

In the current tests the average flow velocity was measured using a pitot static probe. Data were acquired at 50 Hz from pressure transducers and thermocouples installed on the models and the tunnel. Pressure and temperature data were recorded using a 16 bit A/D convertor on a PC using a Labview driven program. This allowed flow conditions to be set accurately and transient changes in temperature to be recorded.

Models of the cooling system for both the external and internal heat transfer studies were installed in the sidewall of the tunnel, which was fed with regulated dry air. The mass flow rate of air passing through the cooling geometry was fed from an independently regulated supply and measured using a BS1042 orifice meter, installed upstream of a second heater. This allowed independent heating of the coolant representative supply. All experiments were conducted

at low speed in an incompressible flow regime, using air as the driving gas for both mainstream and coolant, as shown in Figure 5-2.

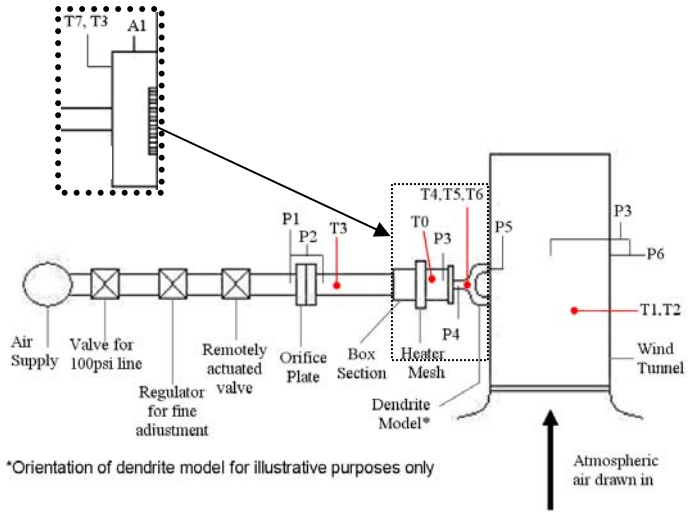


Figure 5-2: Schematic of internal testing experimental setup with typical thermocouple (prefix T) and pressure transducer (prefix P) locations. The insert picture shows the array of dendrites in the configuration used for external heat transfer coefficient and film–cooling measurements

An iris in the far downstream section of the wind tunnel (where the cross section is circular rather than square) was used to alter the mainstream flow velocity and was controlled using a sliding lever that rotated part way round its circumference.

5.1.2 Data Acquisition

In order to accurately understand the performance of the cooling systems, it was necessary to record a number of key pressures and temperatures in the apparatus during the tests performed. This was done using a series of thermocouples and pressure transducers, which were chosen such that values recorded were of the same order as the range of the transducers used. A summary of the transducers used for each wind tunnel configuration is given in the table below.

Pressure Reading Location	Transducer	Range	Non linearity and hysteresis (V)	Long term stability (V)	Output Noise (V)	Temperature effect - combined offset and span (V/°C)		Power supply rejection - offset (V/V)	Power supply rejection - span (V/V)	calibration (Pa/V)	RSS bias error, V	RSS precision error, V	RSS bias error, Pa	RSS precision error, Pa	Total Bias error, V	Total Precision error, V	Total Bias error, Pa	Total Precision error, Pa
Atmospheric pressure	B810 Munro Kew Pattern Barometer	653 - 825mmHg absolute	-	-	-	-		-	-	-					-	-	30	10
Differential across orifice (external experiments)	Sensortechnics HCX001D6H	0-1bar differential	0.045	0.0045		0.001125		0.001125	0.000675	25045	0.045447772	0.003375	1138.239455	42.2634375	0.054	0.003375	1352.43	42.2634375
Differential across orifice (internal experiments)	Sensortechnics BTEL5002D1A	0-2mbar differential	0.015	0.006	9.76563E-05	0.003	offset	0.0015	0.0009	40	0.018792552	0.00450106	0.0141264	0.34987892	0.0306	0.004597656	1.704	0.48390625
						0.0024	span											
Gauge static pressure upstream of orifice	Sensortechnics HCX001D6H	0-1 bar differential	0.045	0.0045		0.001125		0.001125	0.000675	25095	0.045447772	0.003375	1140.511844	84.695625	0.054	0.003375	1355.13	84.695625
Wind tunnel dynamic pressure	Furness Controls Limited FCO44	0 - 200Pa differential	0.05			0.001				44.151							9.8	1.96
Wind tunnel total pressure (gauge)	Sensortechnics HCXPM010D6V	10mbar differential	0.045	0.0045		0.0027		0.001125	0.000675	252.79	0.046496129	0.003375	11.75375642	0.85316625	0.0603	0.003375	15.243237	0.85316625
Coolant plenum pressure (external experiments)	Sensortechnics HCX002A6H	0-2bar differential	0.045	0.009		0.001125		0.001125	0.000675	50375	0.046111278	0.003375	2322.855652	170.015625	0.0585	0.003375	2946.9375	170.015625
Static differential pressure between box section and dendrite inlet	Sensortechnics HCLA02X5PU	0 – 250Pa differential	0.045	0.0045		0.001125		0.001125	0.000675	62.575	0.045447772	0.003375	2.843894347	0.211190625	0.054	0.003375	3.37905	0.211190625
Static differential pressure between box section and dendrite exit	Sensortechnics HCLA02X5PU	0 – 250Pa differential	0.045	0.0045		0.001125		0.001125	0.000675	62.593	0.045447772	0.003375	2.844712407	0.211251375	0.054	0.003375	3.380022	0.211251375

Table 5-1: Summary of the pressure transducers used for the experiments outlined in this work

5.2 Introduction to Heat Transfer Processing Techniques

Because of the complex three dimensional flows associated with these experiments and the large surface temperature gradients which are likely to occur, local temperature data are necessary over the full surface.

A measurement technique which provides detailed spatial resolution of the heat transfer coefficient and local driving gas temperature at the surface as well as being non-invasive is highly desirable. Two possible techniques to measure surface heat transfer coefficient distributions are infrared themography and *TLC*s as they both fulfil these two requirements. Thermochromic liquid crystals exhibit repeatable colour play at known, calibratable temperatures. By coating the wind tunnel wall around the cooling hole exits and the wall downstream with a thermally thin layer of *TLC*s and recording the colour change during a transient heat transfer test, it is possible to obtain the time – temperature history over the surface. Using these data along with gas thermocouple data it is possible to infer the film-cooling effectiveness and heat transfer coefficient distribution (Ling, *2005*).

Infrared thermography may also be used in transient heat transfer testing. Here spatial temperature variation is found through the use of an infrared camera. The principal advantage of infrared thermography is that no surface preparation of the model is required as in *TLC* techniques so long as the emissivity can be considered constant. Therefore, full temperature histories can be obtained during an experiment. In many cases it is necessary for the camera to view the model through a window in the side wall of the test section. Such a viewing window needs to be transparent to the wavelength of infrared light pertinent to

the experiment. This often requires the custom fabrication of windows from zinc selenide (Sargent et al. *1998*). When the heat transfer coefficient is to be determined on the internal surfaces of a complex model, it is unfeasible to create such a window, and so for the majority of heat transfer tests reported, transient liquid crystal techniques were employed and these are described in more detail below. On the external surfaces a steady state infrared thermography technique was used to capture film-cooling effectiveness distributions.

5.2.1 Introduction to Liquid Crystal Thermography

Before describing how *TLC*s are used to evaluate heat transfer coefficient distributions in transient tests it is first necessary to give a brief introduction and explain how they behave in response to changing temperature. *TLC*s exist in a phase between solid and liquid. Their sensitivity to temperature occurs because of the alignment of molecules in planar layers and the extent to which the alignment of molecules is helically angularly offset from layer to layer. In the temperature sensitive region, in which the *TLC*s display colour play, the temperature affects the intermolecular forces and so the angular offset from layer to layer (Figure 5-3). Above this temperature region the substance is liquid like and is optically clear. The distance normal to the surface over which successive molecules rotate through 360˚ is called the pitch, p, and is equal to the wavelength of circularly polarised light which the coating then allows to be selectively reflected from the underlying substrate surface. The temperature bandwidth over which *TLC*s are optically active can be large (20˚C “wideband”) or small (1˚C “narrowband”) (Ireland et al. *2000*). Wideband *TLC*s have the disadvantage that they are subject to varying colour play with changes in the

angle subtended between the viewer and the light source at the coated surface (Ling, *2000*), though they offer greater temperature information if the wavelength of reflected light is appropriately calibrated to surface temperature

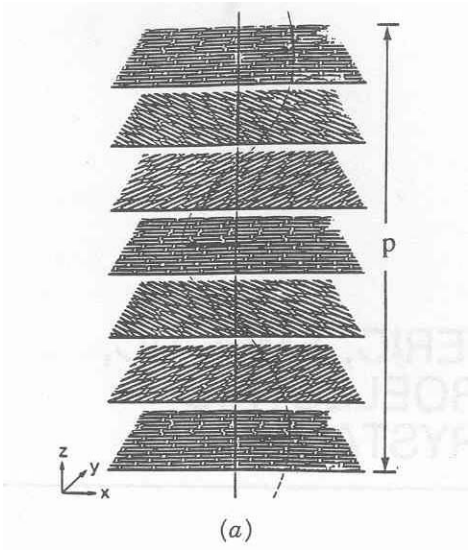


Figure 5-3: The layered Structure and Molecular Alignment of Liquid Crystals (Khoo, *1995*)

Narrow band liquid crystals are more appropriate for complex or curved surfaces. Here the intensity response can be accurately linked to surface temperature and is robust to local viewing angle. When employed as a temperature sensing layer *TLC*s are mixed with an acrylic binder and water in the ratio of 5:1:5. Once dry this mixture, which is applied on top of a black surface to improve colour play visibility, will form a 10 – 30 μm thick coat. The presence of this layer will affect the surface roughness, however the scale of the models to which it is applied in this case means it is effectively hydraulically smooth (Gillespie, *1996*).

5.2.2 The Transient Liquid Crystal Technique

All local heat transfer coefficient distributions were measured using transient liquid crystal techniques. In each case a thermally thin coating of *TLC*s was

used as a full surface thermometer. Two slightly different techniques have been employed; internally where surface curvature is dominant narrow band liquid crystals must be used, but externally where a wide range of asymptotic temperature variation was expected a wide band liquid crystal was used. Each required separate processing techniques. The liquid crystal colour play vs temperature response was calibrated prior to testing.

For the internal heat transfer it is appropriate to base the heat transfer coefficient on the local entry temperature to *each branch* of the dendritic system such that a general correlation can be formed based on the local Reynolds number in each dendrite. This allowed a single correlation for all the branches systems to be determined at the end of testing.

In the case of the narrow band liquid crystals the method involved a processing technique where the 1-D heat conduction equation is solved for a semi-infinite solid, subject to a constant heat transfer coefficient convective boundary condition at the exposed surface, and an arbitrarily changing gas temperature which is at the initial solid temperature prior to the beginning of the test (Neely et al. *2004*). In the current tests it is the coolant representative flow that is heated in order to generate a significant and measurable temperature difference between the flow and the initial temperature of the dendritic model at the start of the test.

For the test surface to behave as a semi-infinite solid, the time taken for the full liquid crystal colour play to occur must be short compared to the time taken for the thermal pulse to travel through the wall of the test rig. Schultz and Jones

(*1973*) showed that the time, t, taken for the thermal pulse to travel across a wall of thickness, x, is calculated using Equation 5-1.

$$t = \frac{x^2}{16\alpha}$$

Equation 5-1

where α is the thermal diffusivity of the material and has a value of 1.08×10^{-7} m^2/s for Perspex. For the internal heat transfer experiments where the minimum wall thickness was 0.010 m and heating from one side only was assumed, the maximum test time was thus calculated to be 60 seconds. In the case of the external heat transfer experiments where the Perspex plate was 15mm thick and again it was assumed that heating took place from one side only the maximum test time was calculated to be 120 seconds.

The solution is formed by modelling the gas temperature as the superposition of a series of offset ramps of slope *m*, such that if the gas temperature distribution is modelled by Equation 5-2

$$T_{gas} = T_{initial} + \sum_{1}^{n} \Delta m_i (t - t_i) \bullet u(t - t_i)$$

Equation 5-2

then a solution exists for the surface temperature of the form:

$$T_{surface} = T_{initial} + \sum_{1}^{n} \Delta m_i (t - t_i) \left(1 - \frac{2}{\frac{h\sqrt{t - t_i}}{\sqrt{\rho ck}}\sqrt{\pi}} + \frac{1 - e^{\frac{h^2 (t - t_i)}{\rho ck}} erfc\left(\frac{h\sqrt{t - t_i}}{\sqrt{\rho ck}}\right)}{\frac{h^2 (t - t_i)}{\rho ck}} \right)$$

Equation 5-3

The narrow band liquid crystals used in the dendritic passages undergo their full colour play over a range of 1 ºC, and are insensitive to both illumination and viewing angle. The liquid crystal colour play was calibrated prior to testing; nominally the two crystals used displayed peaks at 30 °C and 40 °C. The normalised intensity vs temperature correlation is included as Figure 5-5.

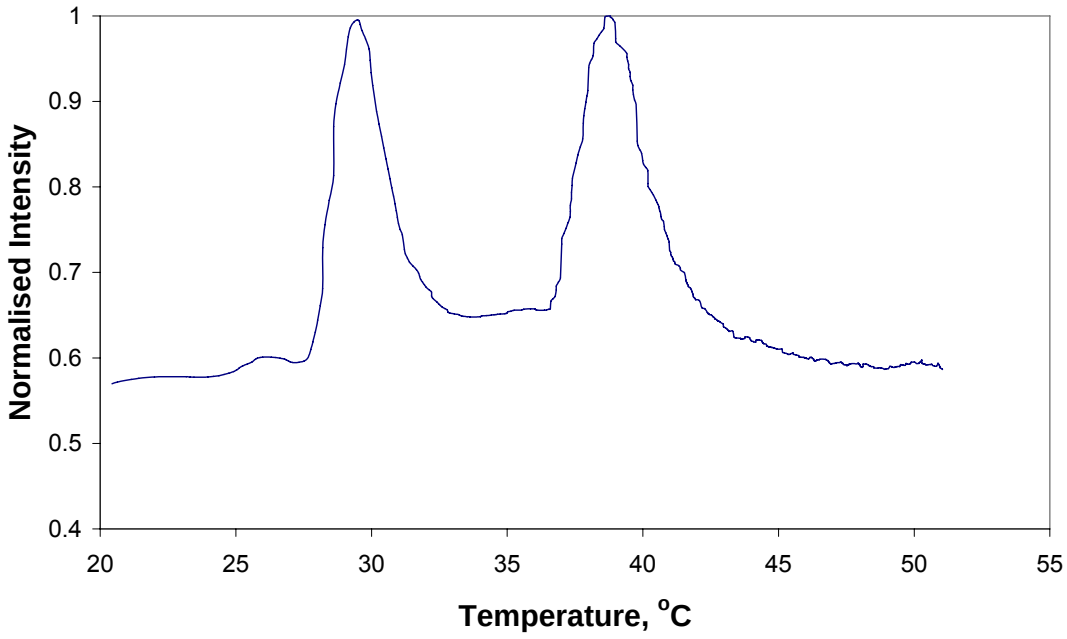


Figure 5-4: Narrowband calibration response

Experimental intensity histories are produced using digital video cameras to capture the crystal colour play at 25 frames per second and resolution of 720 x 576 when the model is subjected to a sudden gas temperature change. To ensure high quality results it was paramount to uniformly illuminate the test section. To do this a combination of fluorescent strip lights and angle poise lights were used; these had a uniform illumination temperature of 5000K. The intensity histories produced were compared to analytical intensity histories generated for a range of heat transfer coefficients; the one with the minimum variance is selected as a solution.

Figure 5-5 shows a typical heat transfer coefficient distribution. Intensity history data are displayed at 3 points on the surface of the branch, representing the full range heat transfer coefficients measured in a single test. Excellent agreement is noted between the analytical and measured intensity data. The use of the full intensity signature ensured redundancy in the data used to create the fitted results. Using this technique results in uncertainty of 7.7 - 7.9% in the local *heat transfer coefficient* reported (Gillespie et al. *1998*).

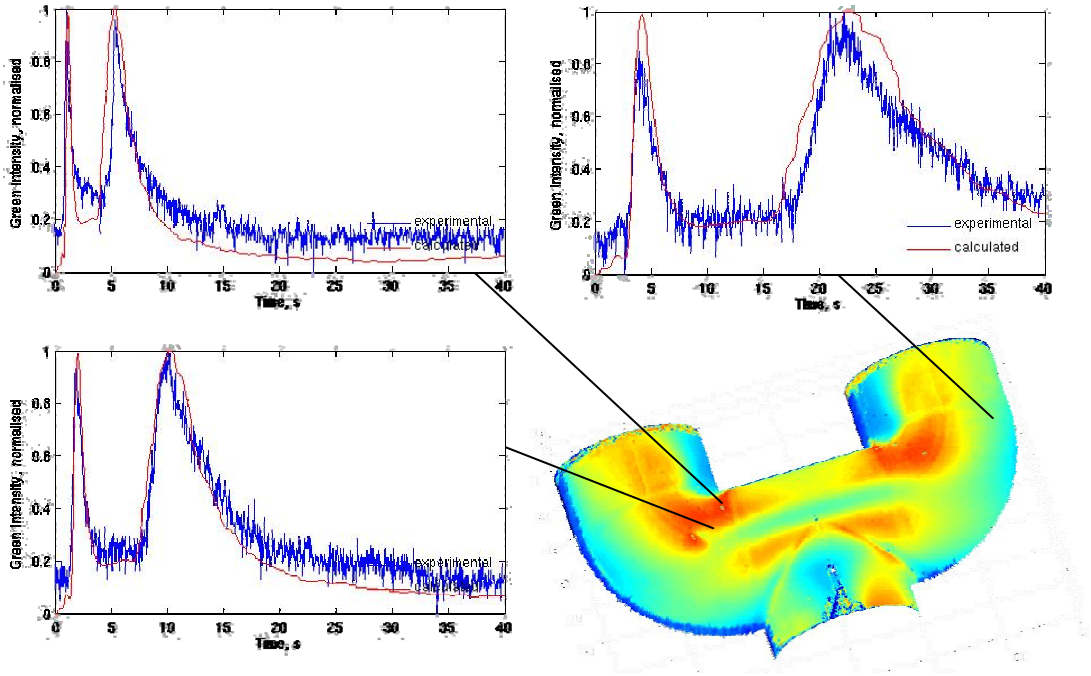


Figure 5-5: Experimental time-intensity fits, narrow band liquid crystal technique

For the external *heat transfer coefficient* measurements a single wide band liquid crystal was used, displaying colour play between 20°C and 40°C (Hallcrest BM/R20C20W/S-40). The normalised hue vs temperature correlation is included as Figure 5-6. Note that in the optically inactive region the colour (hue) response to temperature was not coherent and has been removed. Units of hue are arbitrary. Two PAL video cameras were used to capture the full external surface downstream of the exiting flow. Here a method of solution first

used by Gillespie et al. (*1998*) was used, though an updated global minimisation strategy was employed, which improved the accuracy.

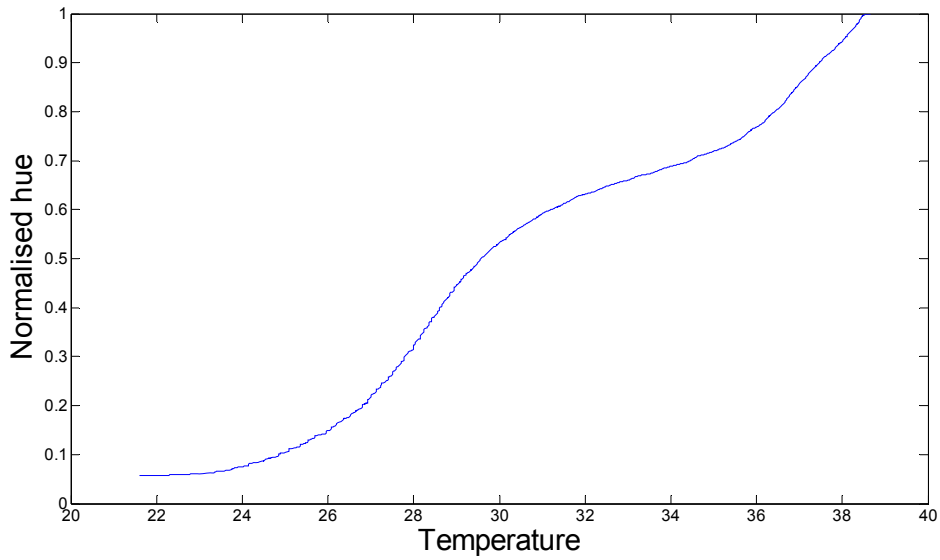


Figure 5-6: Wideband calibration curve

Here hue vs time histories are compared to analytical intensity histories generated for a range of heat transfer coefficients; the one with the minimum variance is selected as a solution (Figure 5-7). The full method of solution of the narrow band transient liquid crystal technique employed in this study is described in Talib et al. *2003*.

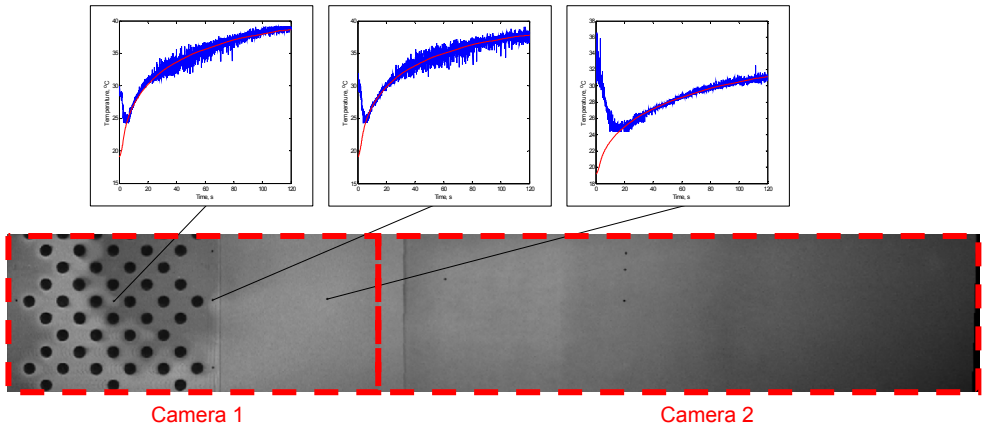


Figure 5-7: Experimental time-intensity fits, wide band liquid crystal technique

Using this wide band liquid crystals technique results in an error of 7.7 - 7.9% in the local heat transfer coefficient reported using the method of Moffatt (*1982*).

5.3 Film-Cooling Effectiveness Measurement: Steady State Infrared Thermography

For the purposes of this research infrared thermography is used to determine the externally film-cooling effectiveness of different cooling systems. In considering the cooling of an NGV there are three temperatures of primary interest; the blade metal temperature, T_b, the temperature of the hot mainstream, Tm and the temperature of the coolant as it exits the cooling hole, T_{ce}, (Figure 5-8) (Eckert, *1953*).

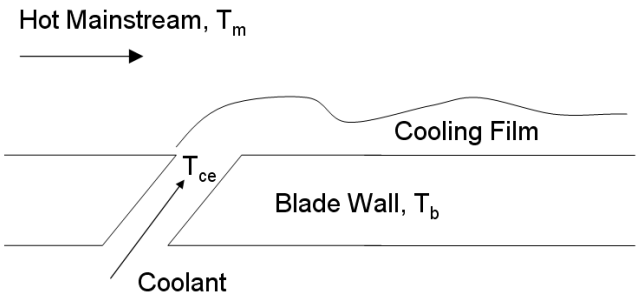


Figure 5-8: The Three Temperature Problem of Film-Cooling (Eckert, *1953*)

The adiabatic film-cooling effectiveness (Equation 5-4) gives an indication of the performance of the film; it is a ratio of the actual to maximum possible temperature difference between the film and the mainstream, when the wall is adiabatic.

$$\eta_f = \frac{T_{aw} - T_m}{T_{ce} - T_m}$$

Equation 5-4

It is similar to the film-cooling effectiveness under isothermal wall conditions which is more representative of engine conditions. Two possible methods of obtaining this parameter were looked considered: a transient and steady-state technique.

It is possible to simultaneously solve the transient heat transfer problem for both heat transfer coefficient and driving gas temperature. To do so it is usual to heat one of the gas streams and to monitor the wall temperature response. In the case of film-cooling there are regions where the heat transfer is entirely driven from one or other of the gas streams – if this is the unheated stream then the solution is very poorly conditioned in this region. Furthermore heat transfer coefficient and Taw must be simultaneously determined, it is quite possible to obtain several combinations of heat transfer coefficient and T_{aw} which provide a similar 'goodness of fit' to noisy experimental data.

In the steady-state technique the wind tunnel wall in the region of interest is constructed from a substance, such as Rohacell, which acts as a near perfect insulator. This means that the period between flow initiation and steady state conditions is short (as there is little heat transfer into the wall). This means that through the use of an IR camera the ratio of the three temperatures (coolant, mainstream and film) relating to film-cooling effectiveness can be instantaneously obtained through the use of a single image. The great benefit of infrared thermography in this case is that temperature representative data can be obtained over the whole surface at steady-state conditions, where as liquid crystals only provide data where they are optically active.

Hence a set of tests were conducted at near steady state conditions in which the η_f was determined independently using a test rig in which the vane representative wall was manufactured from Rhoacell and may be considered non-conducting. The η_f could be established quickly using an infra-red camera which displayed temperature events over the entire surface, at steady state conditions. Note that the dendritic models used were still manufactured from Nylon and thus the test time was still in the order of 15minites per test condition.

Images were recorded by an FLIR A320 infra red camera through a series of zinc selenide ports in the side wall of the tunnel during steady state tests; here the walls were sprayed black to ensure a constant emissivity.

The output from the FLIR A320 IR camera used to monitor the surface is a gray scale, *G*, which is linear with temperature. As it was not important to know the absolute value of the temperature in the η_f experiments, merely the ratio of the temperature differences, wall to coolant and coolant to mainstream, conversion to temperature was not required. Local conditions upstream of the cooling system and inside cooling holes were used to provide grey scale reference values $G_{mainstream}$ and $G_{coolant}$ respectively. The η_f was then simply found using Equation 5-5.

$$\eta_f = \frac{G_{mainstream} - G_{wall}}{G_{mainstream} - G_{coolant}}$$

Equation 5-5

The variance in the gray scale values at the coolant and mainstream temperatures were determined from experimental data. The average of these was applied to the gray scale values on the cooled surface. Using the method

of small perturbations of Moffatt (*1982*) the root sum square uncertainty in the measured adiabatic film-cooling effectiveness was found to lie between 3.68% and 3.88% over its full range, with the maximum worst case error being 6.25%.

Chapter 6 Internal Characteristics of Dendritic Passages

In this chapter the internal heat transfer pressure drop and flow distribution in a circular dendritic system is investigated using a modular large scale model.

6.1 Internal Heat Transfer Performance

Dendritic cooling offers two key benefits: increased convective cooling of the vane / component wall and improved external film-cooling. This section describes experiments carried out to ascertain the heat transfer performance of the internal surfaces of typical dendritic systems using circular cooling passages.

6.1.1 Introduction

The experiments used the low speed wind tunnel detailed in section 5.1 to provide engine realistic crossflow to a single dendrite at large scale. Dimensional similarity was achieved (in part) by matching Reynolds number and blowing ratio between engine and model. The experimental campaign examined 3 alternative configurations (1-2, 1-2-4 and 1-2-4-8 branching designs) of a single dendrite over an engine representative range of both internal and external flow conditions. For a given geometry the range of Reynolds number at the inlet to the dendrite and exit blowing ratios tested were as shown in Table 6-1.

Reynolds Number	Blowing Ratio		Momentum Ratio	
	1	0.5	1	0.25
15000	√	√	√	√
10000	√	√	√	√

5000	√	√	√	√

Table 6-1: Summary of experimental campaign testing conditions

6.1.2 Experimental Setup

In order to obtain detailed internal heat transfer coefficient distributions in the dendritic systems a Perspex model of a single dendrite 33.3 times engine scale was constructed. This single dendrite was designed to be of a modular construction and was fed by the laboratory high pressure air line using a pressure regulator to finely adjust the flow which represented the coolant (see figure 5.2). By taking a modular approach to the design of the apparatus it is possible to reproduce any of the dendritic configurations above. The flow from the dendrite exits flush with the side wall of the wind tunnel into a mainstream flow of known crossflow velocity.

6.1.2.1 Test Specimen Geometry and Instrumentation

The modular blocks were manufactured from 20 mm thick Perspex plate. The Perspex plate was then cut into 80 mm x 40 mm sections and one 120 mm x 40 mm section (used in the 1-2-4-8 system). Each section then had half a 1-2 splitting passage machined into it using a 10mm radius ball nose end milling bit (Figure 6-1). Two blocks are screwed together to form a single module. These modules were, in turn, clamped together to form either a 1-2, 1-2-4 or a 1-2-4-8 dendrite with dowels used to locate the branches relative to one another. A cutaway arrangement of such a configuration is shows as Figure 6-1.

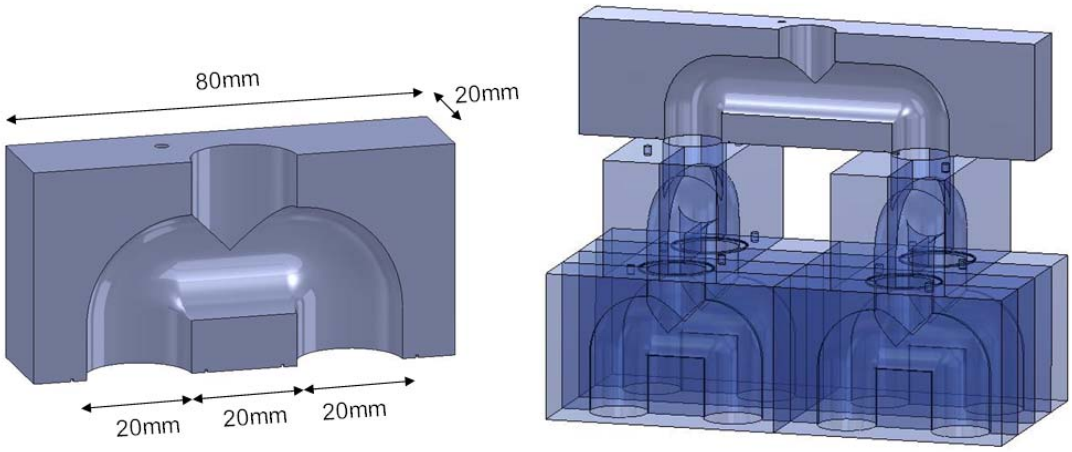


Figure 6-1: CAD model of a single modular dendritic block, and a modular 1-2-4-8 dendritic system. All walls are manufactured from perspex.

Gradations were scribed along straight internal passages at 5mm intervals to aid the interpretation of the heat transfer data and the subsequent superimposing of the data on to the 3D virtual geometry during post-processing. To allow the full surface temperature variation on half of each module to be determined a *TLC* coating was sprayed onto the surface (Figure 6-2). The temperature response of this coating is as detailed in Chapter 5. It should be noted that during testing there was no evidence that the reference markings caused tripping of the flow.

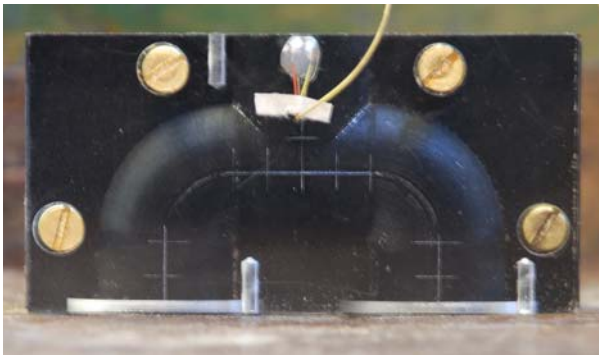


Figure 6-2: Perspex modular dendritic block, coated with liquid crystals and a black ink backing – total thickness ~ 30 μm. Reference makings are visible as is a surface thermocouple used for calibration / validation

6.1.2.2 Experimental Assembly

The modular blocks that create the desired configuration are sandwiched between mounting plates (Figure 6-3) which secure the dendritic system between the wind tunnel and the flange through which the coolant flow is supplied. The flow that is representative of the coolant flow is in fact heated in order to generate a significant and measurable temperature difference between the flow and the initial wall temperature of the dendritic model.

The flow was heated using an inline heater mesh (detailed in Gillespie, *1996*). The power to the heater mesh was adjusted to allow the desired gas temperature rise to be obtained for each test. If the temperature rise is too high the liquid crystal in the entrance region of the dendrite tends to pass through its range of colour play too fast (such that the uncertainty in the time scale is significant), however, if the temperature rise is too low the liquid crystal near the exit experiences little or no colour play and no temperature events can be determined.

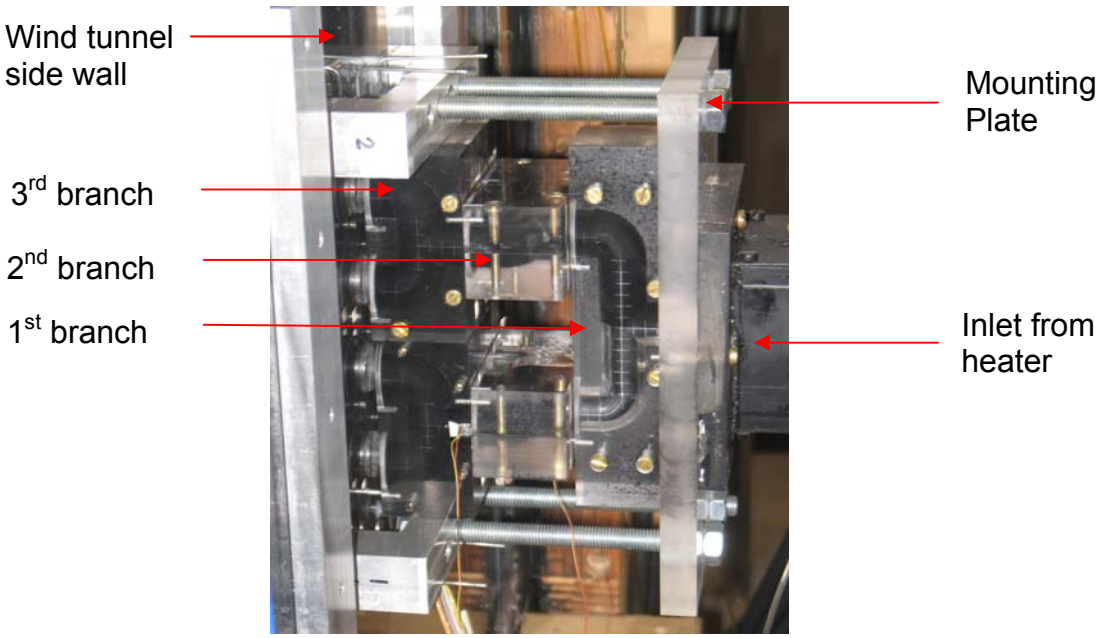


Figure 6-3: Modular dendritic system arrangement

When deciding how to orientate the dendritic systems' exits relative to the mainstream flow it was felt important (and representative of real designs) to ensure that exits from the same branch experienced the same exit pressure if possible. This should minimise the likelihood of flow ingestion. In the wind tunnel this is achieved by locating exits from branches at the same spanwise location. Thus the addition of a branch to a dendritic system requires the reorientation of all upstream branches by 90˚.

Thus for the 1-2 configuration, the dendrite was orientated so that both the inlet and exit passages, which are part of the same branch, can be viewed from a location parallel to the side of the tunnel. In the other two scenarios it was necessary to view the dendrite both from above the working section and from the original location to obtain full surface colour play data necessary to infer the heat transfer coefficient distribution inside the entire dendrite.

Whilst only one camera was required to capture the colour play for the 1-2 configuration, for the other configurations two cameras were required and separate liquid crystal intensity *vs* temperature calibrations were used for each camera. Care was taken to consistently locate the camera as square to the dendrite as possible. The camera used to generate the top view was mounted directly on the working section, fixing its location relative to the model.

An LED was placed in each of the camera's view to synchronise the point at which the heater mesh is switched on in the video with a measured signal recorded by the A/D system. This allowed subsequent matching of colour play data to the pressure and temperature data captured.

Uniform lighting of the test specimens was achieved using strip lights supplemented by additional light sources. These were all 'warm white' florescent tubes. Care was taken to have the lights on for the minimum amount of time required prior to testing. Their location was chosen as a compromise between the optimum lighting set up and the avoidance of heating. A substantial amount of masking was necessary to prevent glare and reflections particularly from the metal structure involved with clamping the dendrite. Stray light was eliminated using a black material to shroud the entire working section.

6.1.2.3 Procedure

A procedure was developed to ensure that all necessary steps were taken to perform the tests successfully. This ensured the validity of the results obtained. The full procedure is set out in Appendix A, and formed a safe means of operation. Prior to the test the coolant and mainstream flow conditions are set such that when heating of the coolant is initiated the desired operating point is obtained. Pressure transducer and thermocouple voltages are recorded along with a synchronisation signal from the heater. Video capture is also initiated. The test begins when power is supplied to the heater.

An LED monitored in the video capture can later be used to synchronise video data to pressures and temperatures. The test finishes when there is no further colour play, or the maximum test time has been reached. The test technique is that set out for narrow band liquid crystals in section 5.2.2.

The processing of experimental data to achieve full surface Nusselt number distributions based on the local inlet temperature to each dendrite branch is complicated. It is implemented through a series of Matlab procedures written by

the author which interface with the existing Osney Narrow Band Liquid Crystal Processing Software, developed by the research group. The outputs from this process are the Reynolds number and blowing ratio of the system; the local Nusselt number and engine scale heat transfer coefficient distributions on all internal surfaces; the perimeter and branch average Nusselt number through each branch of the system.

The flow chart shown in Figure 6-4 gives a detailed summary of steps involved in the generation of the internal heat transfer data.

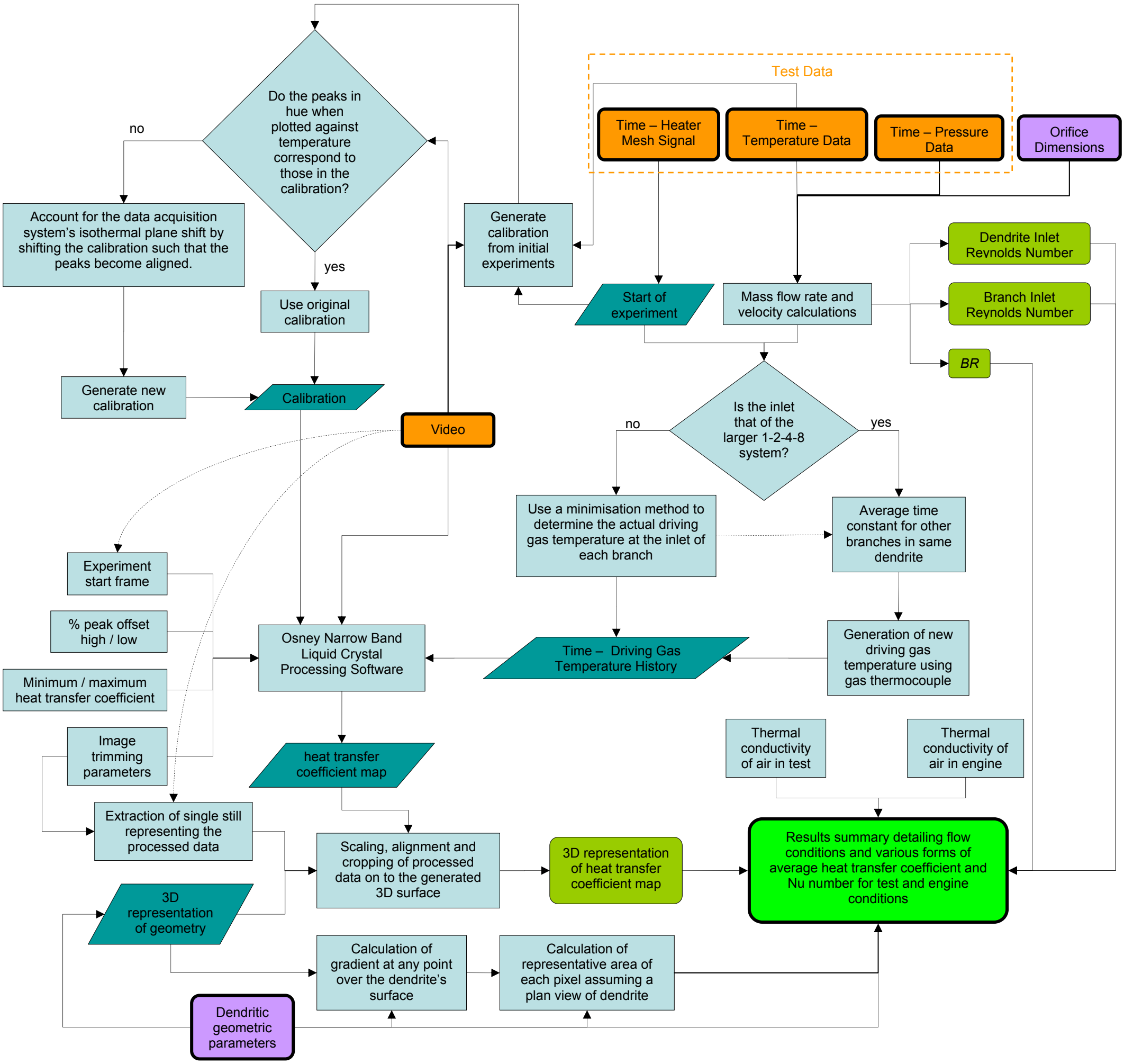


Figure 6-4: A flow chart detailing the steps involved in processing and post processing the internal heat transfer data (orange – test inputs; lavender – prior geometric inputs; light blue – processes; dark green – intermediate output; lime green supplementary outputs, traffic light green – final output)

6.1.3 Heat Transfer Results

Local internal heat transfer coefficient distributions have been produced at each branch for 1-2, 1-2-4 and 1-2-4-8 dendritic configurations. These distributions are very similar if data are presented based on branch inlet Reynolds number (rather than the Reynolds number at the inlet to the configuration). For consistency the heat transfer coefficient is then also based upon the local entry temperature to *each branch* of the dendritic system such that a general correlation can be formed based on the local Reynolds number in each branch.

Inlet Reynolds Number always refers to the dendrite as a whole, whereas *Branch Inlet Reynolds Number* refers locally to conditions at the entrance to each branch of the dendrite (Figure 6-5, Figure 6-8 and Figure 6-9). It should be noted that only one half of each dendritic branch is displayed in the experimental results. For the purposes of scaling the results to engine conditions the following variables were used: 0.066W/(mK) for the thermal conductivity of the coolant air and 0.84mm for the diameter of coolant hole passages, these being correct at engine cruise conditions.

6.1.3.1 Local Heat Transfer Coefficient Distributions

Examples of the local heat transfer distribution as measured under model conditions in each of the branches of the 1-2-4-8 dendrite are shown in Figure 6-5, Figure 6-8 and Figure 6-9 for a single operating condition of exit blowing ratio of 0.5 and Inlet Reynolds number of 15000. Summary graphs showing the local heat transfer coefficient distributions over the full range of operating conditions are included as Figure 6-7 for the inlet branch of this dendrite. These results represent a small part of the main body of work which can be found in

Appendix B. The data in the appendix consists of the remaining distributions for the 1-2-4-8 dendrites as well as the full data set for the 1-2 and 1-2-4 configurations at the range of blowing ratios and Reynolds numbers detailed above.

Several stable repeatable features are visible in the local heat transfer coefficient distributions. There is a characteristic pattern of impingement heat transfer on the branching surface beneath the inlet flow. Here the flow is extremely confined, meaning that there is strong shearing of the flow in the impingement region. At the highest Reynolds numbers this results in the maximum heat transfer coefficient not lying at the stagnation point but in a distorted ring around it, associated, it is thought, with the turbulated flow spraying onto the thin boundary layer. The impingement wall jet wraps around the walls of the downstream branches as shown in the cartoon in Figure 6-6 and is subject to a cross branch pressure gradient. This vortical flow maintains a high heat transfer coefficient in a near horizontal stripe as it is further accelerated towards the exit legs of each dendrite, see Figure 6-5 and Figure 6-6.

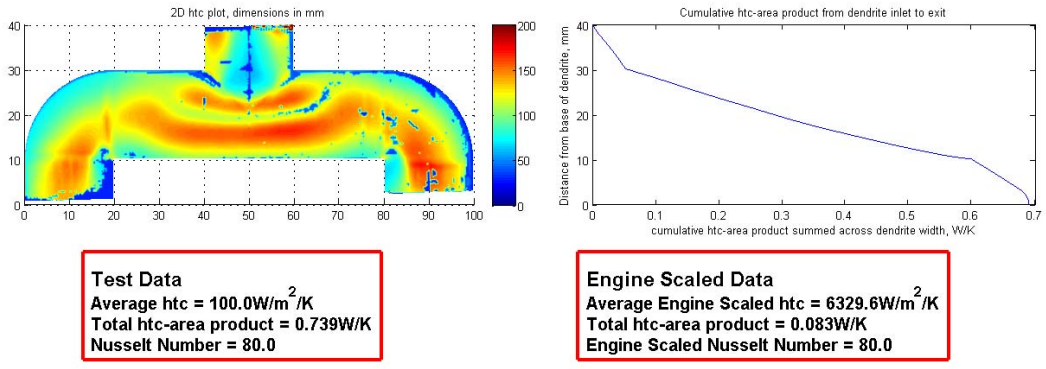


Figure 6-5: Detailed heat transfer coefficient data for the inlet branch of 1-2-4-8 dendrite with an exiting blowing ratio of 0.5 and an inlet Reynolds number of 15000

On the inlet branch of each dendrite there is an unexpected region of low heat transfer, centred at (50,30) on the dendrite in Figure 6-5. It is speculated that this occurs because the flow separates from this surface; it does so because of blockage created by the initial recirculation of the impinging flow (Figure 6-6).

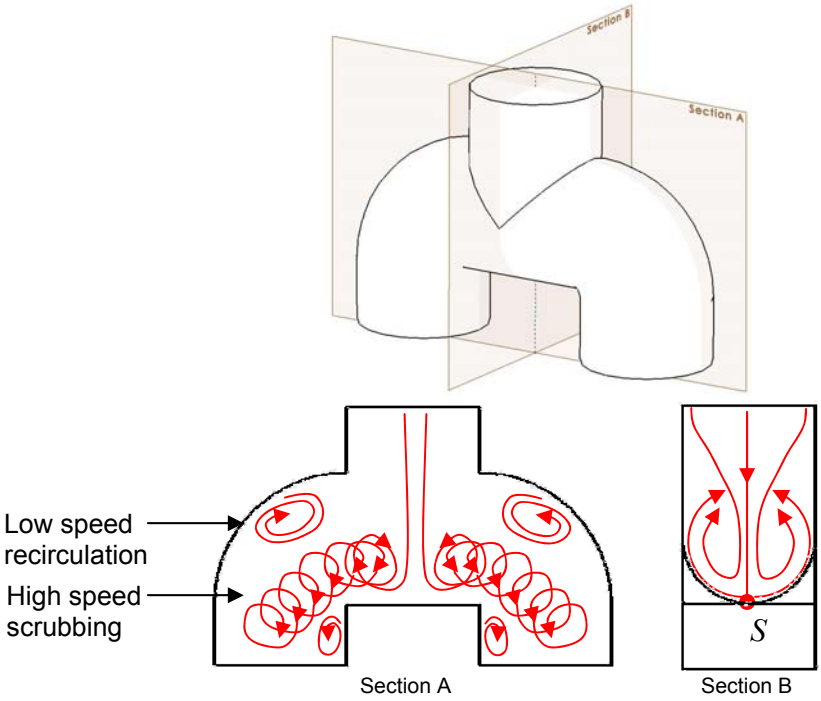


Figure 6-6: Cartoon of flow development from point of impingement

The halving of the average velocity when the flow branches should lead to a drop in heat transfer, but this is only apparent on the outer shoulders of the branch and downstream of the corners where ostensibly that there is insufficient pressure gradient to fully turn the flow round the abrupt corner. The rest of this region benefits from the recirculation set up by the impinging flow as noted above. The effect of blowing ratio and Reynolds number on the local heat transfer coefficient distribution is shown in Figure 6-7, where sensibly over the entire dendrite's surface the heat transfer coefficient increases with increasing Reynolds number. In the inlet branch it is clear that heat transfer coefficient is

a weak function of blowing ratio and in fact this turns out to be the case for all of the dendritic branches investigated.

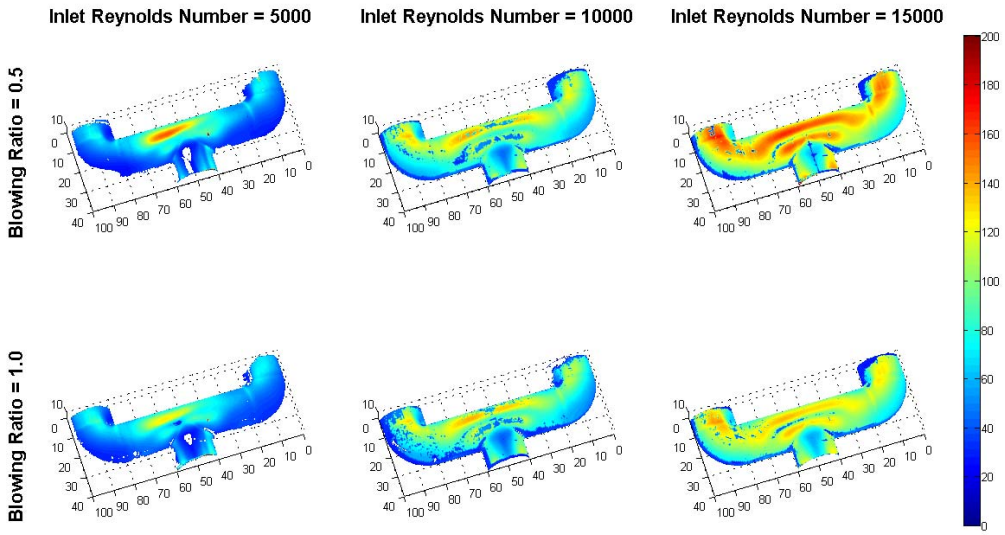


Figure 6-7: Summary of heat transfer coefficient (W/m^2K) distributions for the first branch of a 1-2-4-8 dendritic system

6.1.3.2 Local Heat Transfer in Subsequent Branches

The local heat transfer coefficient distributions in the middle and exit branches of the 1-2-4-8 dendrite are shown in Figure 6-8 and Figure 6-9 at the same dendrite inlet conditions. With each branching of the cooling system the flow rate (branch Reynolds number) is halved and the driving gas temperature is slightly reduced.

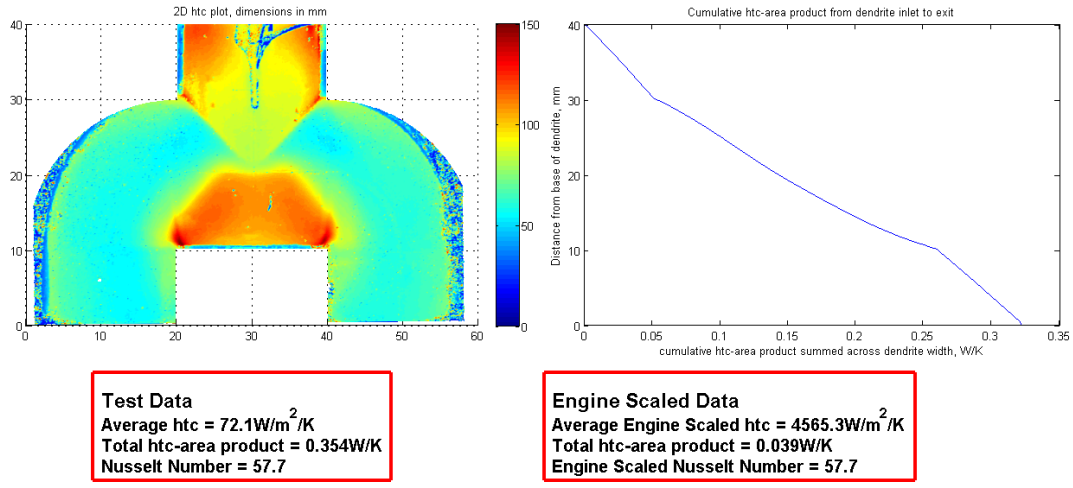


Figure 6-8: Detailed heat transfer coefficient data for a 1-2-4-8 dendrite: middle branch; exiting blowing ratio of 0.5 and an inlet Reynolds number of 15000

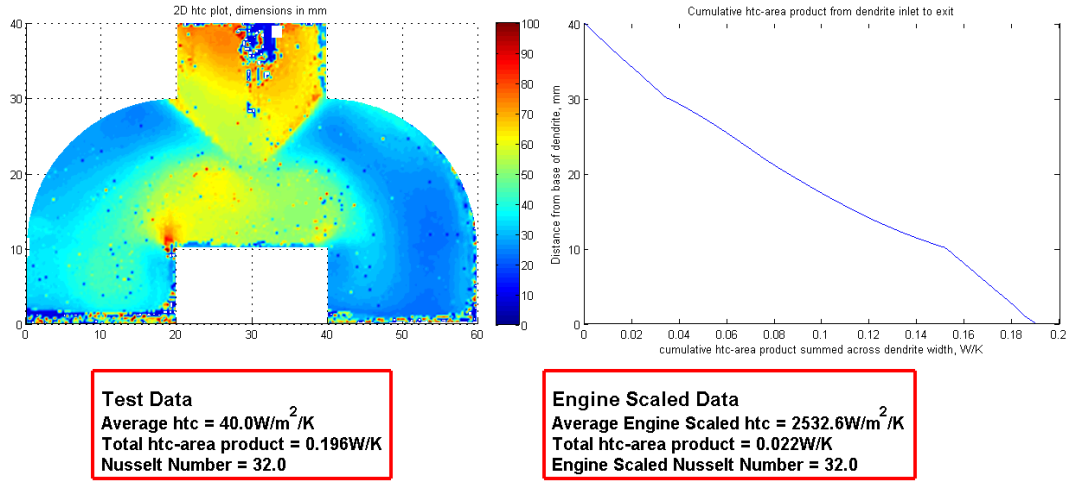


Figure 6-9: Detailed heat transfer coefficient data for a 1-2-4-8 dendrite: exit branch; exiting blowing ratio of 0.5 and an inlet Reynolds number of 15000

It is apparent that the heat transfer coefficient distributions follow a similar form in each branching element with the magnitude sensibly falling from branch to branch. To investigate this further Figure 6-10 shows local Nusselt number distributions in a 1-2-4-8 dendritic system normalised by the average Nusselt number correlation which is presented later in Equation 6-2. Here the inlet Reynolds number to the system is 15,000, and the local Reynolds number local to each branch is used to perform the normalisation. It should be noted that the flow patterns and heat transfer distributions observed at the exit of one branch

do not match the entrance to the subsequent branch in this viewing arrangement because the viewing angle of each is 90 degrees out of phase.

Of particular note in Figure 6-10 is the changed shape of the patch of impingement heat transfer and the lower, normalised Nusselt number in the entrance to the whole system when compared to the entrance of subsequent branches. The former feature was investigated using CFD (see below) and it is inferred that the additional turbulence created in the flow by the first impingement increases the Nusselt number at the entrance to subsequent branches. The enhancement is of similar level in both the entrances to the 2nd and 3rd branches. The level of enhancement in the middle branch of the 1-2-4-8 split appears slightly higher than for the exit branches. The reason for this is not properly understood.

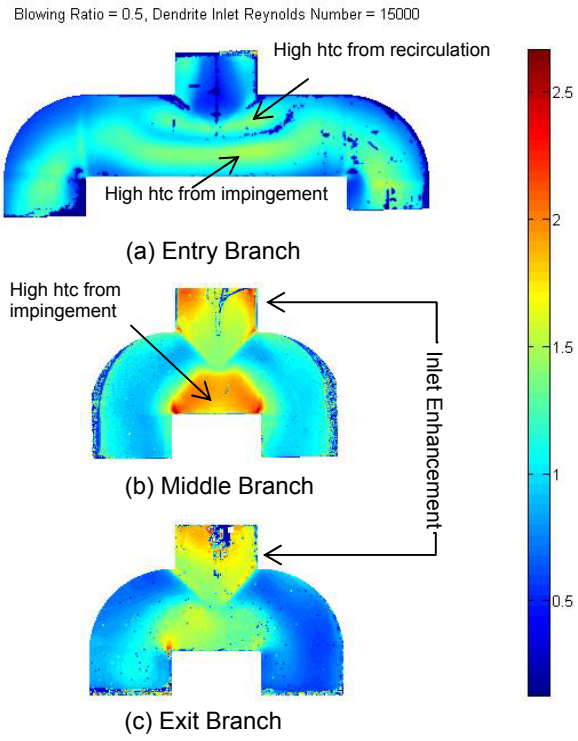


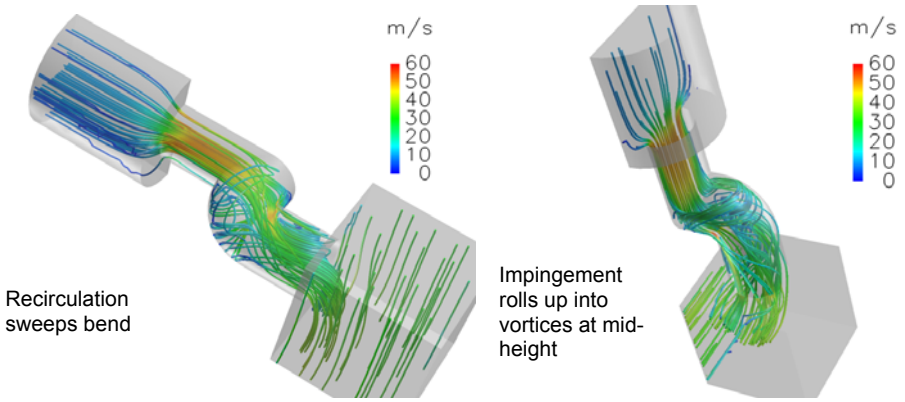
Figure 6-10: Normalised Nusselt number distribution, Nu/Nu_{branch}, for all branches in a 1-2-4-8 dendrite

6.1.3.3 CFD 'Diagnosis' of Flow Field

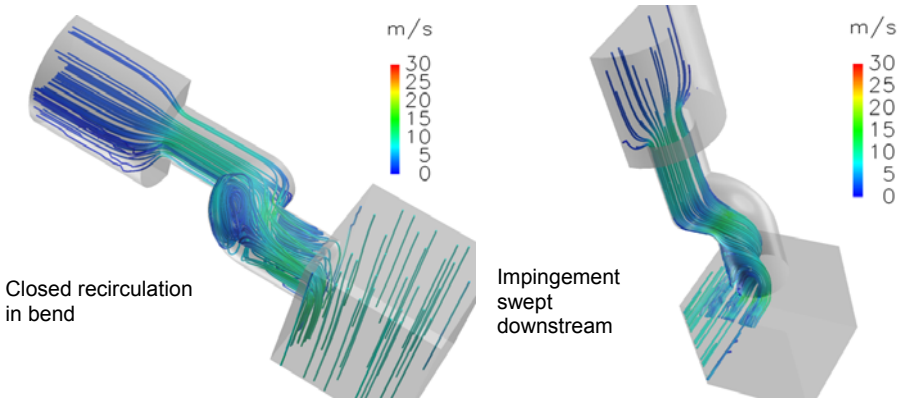
Simple CFD of a 1-2 dendritic system was used to provide diagnosis of the flow field to help explain the heat transfer features seen. A tetrahedral mesh (~600,000 elements) and size functions were used to model the coolant passages, flow was introduced through an inlet plenum and cross flow region at the exit of the branched pattern. The realisable k-ε model was used with standard wall functions. The results confirmed that at high Reynolds numbers the re-circulating flow caused by the wall jet forms a highly shearing flow which scrubs against the side wall of the branch at mid-height before turning towards the exit (see Figure 6-5 and Figure 6-11 (a)). The benefit is seen to be twofold with some of the re-circulating flow from the impingement wall jet sweeping into the shoulder of the branches.

At low Reynolds number the typical impingement features are less pronounced. Here, there was little evidence of this recirculation and the flow from the centreline plane is strongly accelerated into the downstream legs, Figure 6-11 (b). This forms a region of high heat transfer along the bottom surface of the branch as seen in both Figure 6-8 and Figure 6-9. The turning of this flow forms a vortical structure that is confined to the middle of the passage and so generates little improvement in heat transfer in the downstream branches. The other notable difference compared to a high Reynolds number case is that the recirculation in the shoulder region appears much more stable. Thus it can be concluded that the differences seen between Figure 6-5 and Figure 6-8 and Figure 6-9 are largely driven by the branch Reynolds number.

While the CFD solution could not be relied on for accurate heat transfer coefficient levels, the local distribution showed that the local heat transfer coefficient was essentially symmetrical with respect to both geometric planes of symmetry, even in the presence of substantial cross flow (*BR* = 0.3). Thus it was justified to process only one view (half of each dendrite) in the experimental data as presented.



(a) Re~50000



(b) Re~10000

Figure 6-11: Pathlines at high and low Reynolds number 1-2 dendrite, *BR*=0.3, CFD Simulation

6.1.3.4 Generalised Internal Heat Transfer Behaviour of Dendritic Systems

To allow design of dendritic systems averaging has been carried out on the local heat transfer coefficient distributions obtained. The average heat transfer coefficient values quoted are not merely the arithmetic mean of the local heat transfer coefficient data as plotted. This would be unrepresentative because consideration needs to be given to the surface area associated with each location. Rather, a summation of the heat transfer coefficient - area product at each pixel location is calculated and divided by the total area to obtain a truer representation of the average heat transfer coefficient for each branch. To obtain a representative overall heat transfer coefficient-area product for each branch, this average heat transfer coefficient is multiplied by the total surface area of the dendrite. This process effectively assigns the average heat transfer coefficient to areas over which it was impossible to obtain experimental data. Because of passage curvature there is a variation in surface area of each pixel, and this is fully accounted for. These results are presented as a cumulative heat transfer coefficient – area product moving through the wall of the blade and are plotted in Figure 6-5, Figure 6-8 and Figure 6-9, and the figures in the Appendix. In each case it should be noted that they represent a single dendritic branch and that in a full system these would need to be scaled to take into account the doubling of the number of branching systems with each branch.

The data can be further averaged providing a single average Nusselt number for each branch of the dendrite. For each branching section in each of the 3 dendritic system configurations the local branch inlet Reynolds number and the

associated Nusselt number were readily available. Using the 36 heat transfer coefficient distributions and the inlet temperature of the coolant it was possible to calculate the average Nusselt number for each branch. By plotting these two parameters against one another (Figure 6-12) a clear relationship was established (Equation 6-1) that could be used for fast and reliable estimation of the heat transfer taking place given basic flow information and geometry details. While there is some spread in the data as presented in Figure 6-12, there is no systematic variation with blowing ratio and so this is not included as a correlation parameter in Equation 6-1. The generation of such a relationship has allowed the construction of a simple model of a dendritically cooled blade and its comparison to existing cooling designs (7.9).

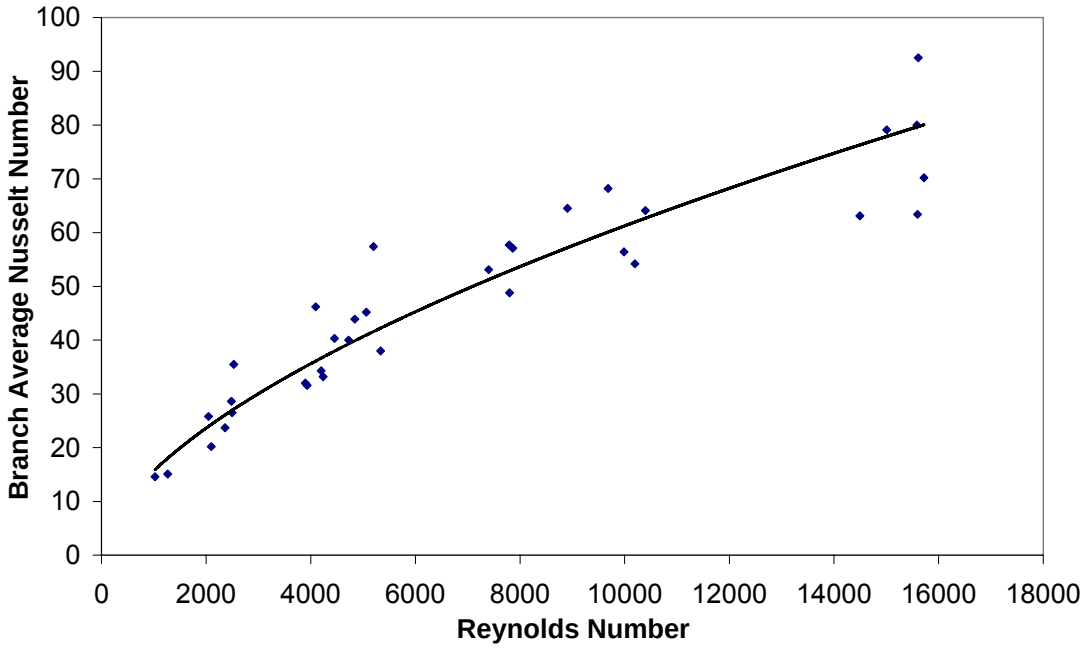


Figure 6-12: Local branch Reynolds number in a dendritic passage plotted against Nusselt number at that point

$$\overline{Nu} = 0.263 Re^{0.5918}$$

Equation 6-1

Using local branch inlet Reynolds number, and normalising the Nusselt number by the Dittus-Boelter correlation for fully developed turbulent flow in smooth pipes, the relationship below was found:

$$\frac{\overline{Nu}}{Nu_{db}} = 13.12\, Re^{-0.21}$$

Equation 6-2

In fact if the Prandtl number dependency of the Dittus-Boelter correlation is assumed Equation 6-1 may be generalised as:

$$\overline{Nu} = 0.302\, Re^{0.591}\, Pr^{0.4}$$

Equation 6-3

Comparison to the work of other researchers is difficult as the wetted passage perimeter increases between the inlet and exit of the system. A comparison is made between the summed product of local heat transfer coefficient and wetted surface area for each dendritic system and the values predicted by the correlation of Metzger and Codaro (*1979*) for short film-cooling holes: this is shown in Figure 6-13. Here the ratio of the summed hA product to two comparable straight hole cooling geometries is presented; these bound the range of possible cooling arrangements available using straight holes of identical diameter. The lower bound of achievable hA is represented by a single straight cooling hole spanning the same overall wall thickness. The upper bound is represented by a number of straight cooling holes, equal in number to the number of exits from each system: again the diameter remains constant. In both cases the mass flow rate is matched to the mass flow rate through the dendritic system. In considering Figure 6-14 it is instructive to also consider the

ratio of the wetted surface area between the dendritic systems and their comparators. This is included as Table 6-2.

Configuration	Wetted area ratio (dendrite / straight)	
	Matched Inlet	Matched Outlets
1-2	1.95	0.98
1-2-4	2.93	0.73
1-2-4-8	4.90	0.61

Table 6-2: Ratio of internal areas assuming the straight equivalents have either the same inlet or outlet cross sectional area

In Figure 6-15 is notable that the highest hA enhancement seen cannot be attributed to the increased wetted surface area alone. The largest ratio of surface areas are created when comparing the 1-2-4-8 configurations. Also notable is that the enhancement factor is greater than 1 for very nearly all the results displayed. It is expected that a single cooling hole would be replaced with a single dendrite in a real engine design, and so these figures of comparison are most instructive. For the highly branched systems (1-2-4) and (1-2-4-8) the comparison to a multiple hole system is necessarily unduly pessimistic. This is because the allowable packing density of such holes spanning the full thickness of the component would be sparser than for a dendritic array. Furthermore, to achieve the comparable mass flow rates used here the pressure ratio would have to be dramatically reduced for the multiple straight holes, and this is unfeasible when flow unsteadiness and possible flow ingestion are taken into account.

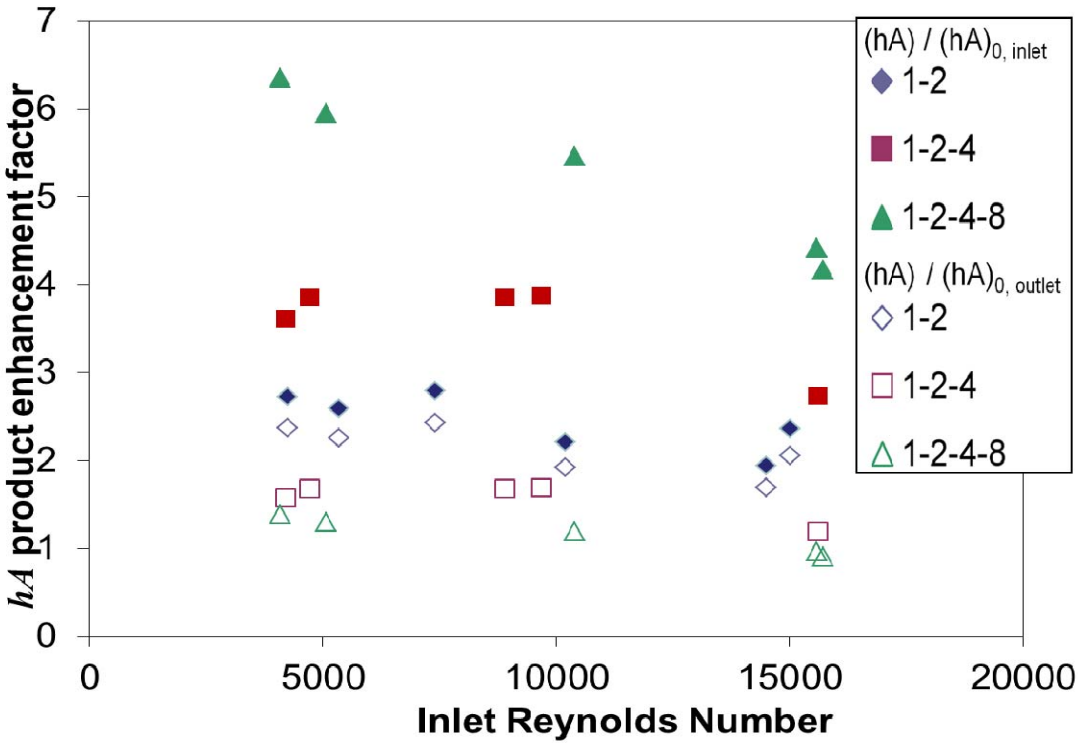


Figure 6-15: Average *hA* Product Enhancement Factor. Mass flow mass flow rate is matched for all ratios.

6.2 Internal Pressure Loss Characteristics of Dendritic Passages

For the geometric configurations described above, the associated pressure loss over the full range of blowing ratios (infinite to approximately 3) and inlet Reynolds numbers (1000 to 15000) has been characterised.

6.2.1 Method

Whilst the apparatus remained the same the coolant flow was not heated as in the heat transfer experiments. The manner in which experiments were conducted was changed to allow a wider range of experimental data to be captured. The mainstream flow of the wind tunnel again remained constant throughout each test run but the coolant mass flow rate was varied such that the Reynolds number at the inlet to the dendritic system increased from 0 to

15000 in small regular increments. After each increment the system was allowed to stabilise and the steady data were collected. Each reading was the average of approximately 100 data points. The procedure used is set out in detail in Appendix A.

Using the method of small perturbations of Moffatt (*1982*) the root sum square uncertainty in the measured total pressure loss in inlet flow dynamic head was found to be 2.05% over its full range, with the maximum worst case error being 4.11%. .

6.2.2 Data Extraction and Results Processing

The pressure loss data can be expressed either as a discharge coefficient or a pressure loss coefficient. For the incompressible conditions tested in the model the discharge coefficient can be expressed as Equation 6-4 and the equivalent loss coefficient K_{loss} is given by Equation 6-5.

$$C_d = \frac{\dot{m}}{\sqrt{2\rho\Delta P}\left(A_{inlet}/n\right)}$$

Equation 6-4

$$K_{loss} == \frac{\Delta P}{\frac{1}{2}\rho u^2}.$$

Equation 6-5

The mass flow rate and velocity of the coolant were determined from the orifice meter installed in the coolant feed line. Once determined the loss data for each dendritic system were correlated as functions of Reynolds number and exit blowing ratio. The data formed a smooth continuous function and while the range of the correlation presented is as described above there is some extrapolation as the full range of test conditions could not be achieved. A full

set of results is presented in Appendix C detailing the 3D surface plots which were used to correlate blowing ratio, Reynolds number and loss; a series of 2D plots at intervals of inverse blowing ratio or Reynolds number plotted against the other variable and loss both in terms of C_d and K_{loss}; and a series of look up tables intended for industrial application. A flow chart explaining the post processing procedure which explains the steps taken to extract the loss data from the raw pressure and temperature data is also included in C.4.

6.2.3 Pressure Loss Results

The data have been correlated as a function of Reynolds number and blowing ratio. The correlations for each configuration are given in equations Equation 6-6, Equation 6-7 and Equation 6-8.

$$C_d = {1.33}/{Re} + 0.361 \times exp(-0.157 \times {1}/{BR}) + 0.00371 \times log({1}/{BR})^2$$

Equation 6-6: Loss correlation for a 1-2 circular cross section dendrite

$$C_d = 0.117 \times exp(-0.000\ 0248 \times Re - 0.109 \times ({1}/{BR})^2) + 0.0582 \times log(Re)$$

Equation 6-7: Loss correlation for a 1-2-4 circular cross section dendrite

$$C_d = \frac{7.7 + {1}/{BR}}{81.54 + 0.000000289 \times Re^2} + 0.0569 \times log(Re)$$

Equation 6-8: Loss correlation for a 1-2-4-8 circular cross section dendrite

In Figure 6-16 these correlations are plotted as K_{loss} vs inlet Reynolds number for each dendritic system configuration and three exit blowing ratios.

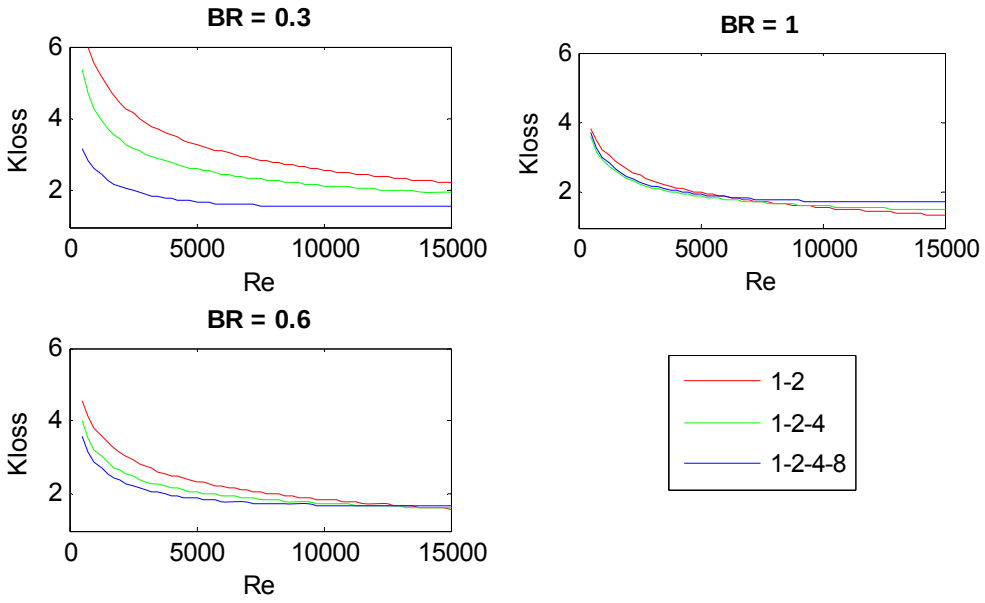


Figure 6-16: Variation in K_{loss} for a range of Re numbers at fixed *BR*s for the 3 dendritic system configurations

6.2.4 Effect of Inlet Reynolds Number

The loss sensibly follows a well known inverse relationship found with inlet Reynolds number in the passage; a higher loss at the lowest Reynolds numbers is associated with laminar flow, while the levelling off of loss at a lower level is typical of fully turbulent flow. This behaviour is consistent over the range of blowing ratios tested. Figure 6-17 confirms that the behaviour follows a sensible pattern, showing the change in discharge coefficient, C_d, with Re_{inlet} for both a 1-2-4 dendrite with constant external crossflow and a straight cooling hole as tested by Hay et al. (*1983*), again with constant external crossflow. As would be expected the loss associated with a dendritic system is significantly greater than that of a conventional straight film-cooling hole, and both sets of data follow the same form. It should be noted that the dendritic system has higher loss *by design*.

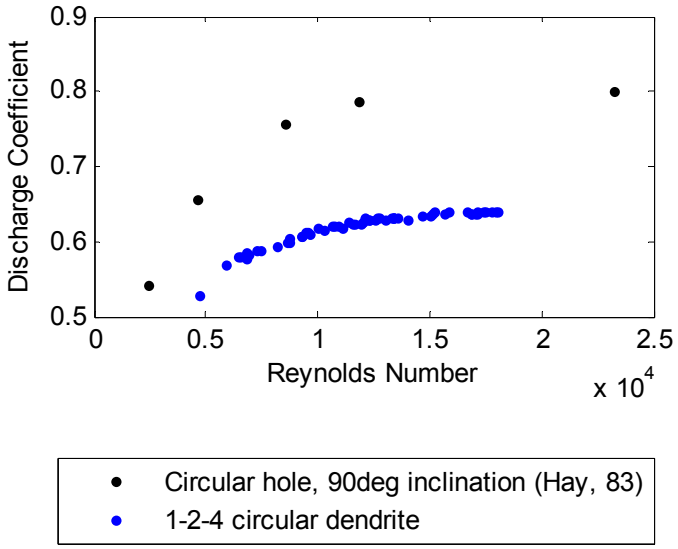


Figure 6-17: C_d data comparison between current work and past studies

6.2.5 Effect of Exit Blowing Ratio

It is clear that as the blowing ratio is increased the loss is reduced for a given dendritic system configuration, and that this change is most pronounced for the single branch dendritic system. More surprisingly the dendritic systems with a higher number of branches have a lower loss at low blowing ratios.

The increases in the loss K_{loss} can be attributed to the capping effect (Rowbury et al. *2001*) of the mainstream flow on the exit of the film-cooling holes. This is a mechanism whereby the mainstream flow effectively reduces the exit area of the hole and partially 'caps' the hole. The extent to which the exit area is reduced, or 'capped', is dependent upon the relative momentum ratios of the two flows involved.

If the momentum of the coolant is high relative to that of the mainstream (high blowing ratio) the coolant exiting cannot be instantaneously turned downstream by the mainstream flow. However at lower momentum ratios this capping mechanism has the effect of reducing the exit area of the coolant holes; with the

flow area reduced and the velocity of the exit flow set by the driving pressure difference, the mass flow rate delivered is reduced. Thus the resultant discharge coefficient is also reduced.

While the proportional reduction in the exit area of the hole is independent of internal geometry at a given blowing ratio (based upon the exit velocity of the coolant), the ratio of the change in area to the throat area in each dendritic system is not. In the case of the 1-2 split, clearly the capping effect is dominant, and the throat must now lie at the exit of the system. However, as each additional branch doubles the exit area, the proportion of the exit area that must be capped to cause a significant flow obstruction increases, and the loss for the 1-2-4-8 split at *BR*=1 is approximately 50% of that for the 1-2 dendrite.

Internally the loss associated with each branch is expected to scale with the local dynamic head, which drops by a factor of 4 with each additional branch. Thus the difference in internal loss between the 1-2, 1-2-4 and 1-2-4-8 dendritic systems would be expected to scale in the ratio 16 : 20 : 21 respectively. At most blowing ratios tested this difference appears to be small compared to the capping effect described above, however, at the highest Reynolds numbers and highest blowing ratios, the relative order of the loss is seen to follow this general pattern, suggesting that the holes are freely flowing into the crossflow under these conditions.

6.3 Summary

A series of tests were conducted to characterise the internal heat transfer and pressure drop performance of dendritic cooling systems. Three dendritic geometries were tested. The local Nusselt number distribution showed clear

signs of flow impingement dominating and enhancing the heat transfer at the point of branching but there were also areas of stable recirculating flow which caused areas of low heat transfer through the systems. The average internal Nusselt scaled sensibly with Reynolds number and was seen to be remarkably insensitive to external blowing ratio. The pressure loss in the system was not as expected. While the effect of Reynolds number was to reduce the loss coefficient, it was found that at engine representative blowing ratios multiple branching systems had lower loss than those with single branches. This is thought to be attributable to the capping effect of external crossflow which is dominant at low blowing ratios. At higher blowing ratios the loss between different configurations was much less pronounced.

Chapter 7 External Film-Cooling Performance and Flow Behaviour

An experimental programme, loosely based on Mittal's (*2006*), was conducted to simulate the internal dendritic flow field and then measure the external heat transfer performance of the resulting cooling film. The aim was to develop characteristics for both heat transfer coefficient and film-cooling effectiveness.

Dimensional analysis of the system suggests that Reynolds number based upon the cooling hole diameter, Re_{md}, blowing ratio and momentum ratio, I, should be matched. However, without the use of a foreign gas or the correct pressure and temperature ratios it is not possible to simultaneously match momentum and blowing ratios. This is because the density ratio in the engine is approximately 2.2:1 but in the current tests is close to unity. To overcome this problem a pair of tests were conducted to model a single engine flow condition: in one test the momentum ratio is matched while in the other the blowing ratio is matched. In the area immediately around the cooling hole a momentum balance governs the penetration of the coolant jet into the mainstream: hence matching the momentum ratio here is critical. Downstream mass weighted mixing processes take place and in order to achieve the correct mixed out film temperature it is necessary to match the blowing ratio. The results should be viewed in this light.

The major difference between Mittal's *2006* study and this is that whereas in the former only the exit pattern of the geometry was replicated, here the internal geometry of the systems being tested has also been reproduced. It was felt necessary to reproduce the internal geometry because of the effects on the

secondary flow in the exiting coolant that this geometry will have. Heidmann et al. (*2000*) use a similar argument when justifying the need to generate the internal geometry of cooling holes when assessing their film-cooling performance. Figure 7-1 shows the wind tunnel in the configuration used for this study, a detailed description of which can be found in Chapter 5.



Figure 7-1: Low Speed Wind Tunnel (Top right: Coolant Plenum and down stream plate coated in liquid crystal, Top Left: Viewing area with DAQ equipment, cameras and coolant exit array)

As noted above setting a blowing ratio between the coolant and the mainstream is not sufficient to model fully the engine test conditions. The range of experimental tests conditions was based on the conditions experienced in a modern civil aeroengine NGV showerhead. The tests conditions used are set out in Table 7-1 below. It should be noted that for the required engine blowing ratios of 0.45 and 1, model blowing ratios of 0.3 and 0.6 approximately match the engine momentum ratios respectively.

Test Blowing Ratio	Test Momentum ratio	Engine Blowing Ratio	Engine Momentum Ratio
0.30	0.09		
0.45	0.20	0.45	0.08
0.50	0.25	0.50	0.10
0.60	0.36		
1.00	1	1.00	0.39

Table 7-1: Cooling Hole Exit Running Conditions

Before any tests could be conducted it was necessary to calculate the required mainstream velocity of the flow through the wind tunnel. This was found by scaling a Reynolds number in the mainstream based upon the cooling hole diameter Re_{md}. To find the required Re_{md} the average Mach number for the flow around the leading edge of a Trent 500 NGV was calculated from data supplied by Rolls Royce (Appendix F). This was used to find the average velocity of fluid flowing around the NGV using Equation 7-1.

$$U_{mE} = M\sqrt{\gamma R T_{mE}}$$

Equation 7-1

The average velocity was found to be near 150m/s. Using this velocity it was possible to find the engine's mainstream Reynolds number based upon the cooling hole diameter using Equation 7-2. This was found to be approximately 10,000.

$$Re_{md} = \frac{\rho U d_h}{\mu}$$

Equation 7-2

From Equation 7-2, the circular cooling hole diameter of 10mm and atmospheric air properties, the required mainstream velocity was found to be 13.34m/s.

Two alternative methods were used to analyse the external performance of different cooling hole geometries: transient heat transfer experiments and adiabatic film-cooling effectiveness experiments.

The first set of results was obtained using a transient technique which employed liquid crystals to give the heat transfer coefficient over the exit area of the holes and the surface downstream. The second, a steady state method, gave only the adiabatic film-cooling effectiveness over the same area and used an infrared camera.

7.1 Experimental Geometry

The cooling hole configurations to be tested were created using interchangeable nylon plates which were populated by a series of cooling hole arrays through which the coolant was fed. The plates were designed using SolidWorks and produced using the Department of Engineering Science sterolithography machine. The first plate to be tested contained an array of 1-2-4 Mk I dendrites as previously described in Figure 4-2. Figure 7-2 shows a third angle projection engineering drawing of the plane with a series of cutaways showing internal detail. An array of 22 1-2-4 dendrites exit normal to the surface, each set of a dendrite's 4 exits forming a diamond configuration relative to the crossflow. In this test specimen it is notable that one possible site for a dendrite has not been populated. This was done to allow liquid crystal calibration and determination of the thermal product of the nylon test piece. Otherwise the array of dendrites form a uniform and dense pattern of holes at the exit, with two half density rows of exits lying in between: the spanwise spacing of the holes being $2\sqrt{2}d$, chosen to ensure a minimum *1d* solid

material between neighbouring branches. The second plate that was tested consisted of an array of 20 1-2-4 MkVI dendrites as first shown in Figure 4-7. Figure 7-3 shows a projected image of the test piece, viewing the exit plane. In this instance the four exits of each dendrite align to form two spanwise pairs which join together at the exit to form a contiguous slot. These two slots in turn form two, larger continuous spanwise slots with adjacent dendrites. The inlets to each dendrite, shown in light grey, lie upstream of both the exit slots it feeds. This maximises the internal surface area of the dendrite. In both Figure 7-2 and Figure 7-3 the mainstream flow runs from left to right. Assuming that engine film-cooling holes would have a hole diameter of 0.6mm the plates are approximately 17 times larger than engine hardware.

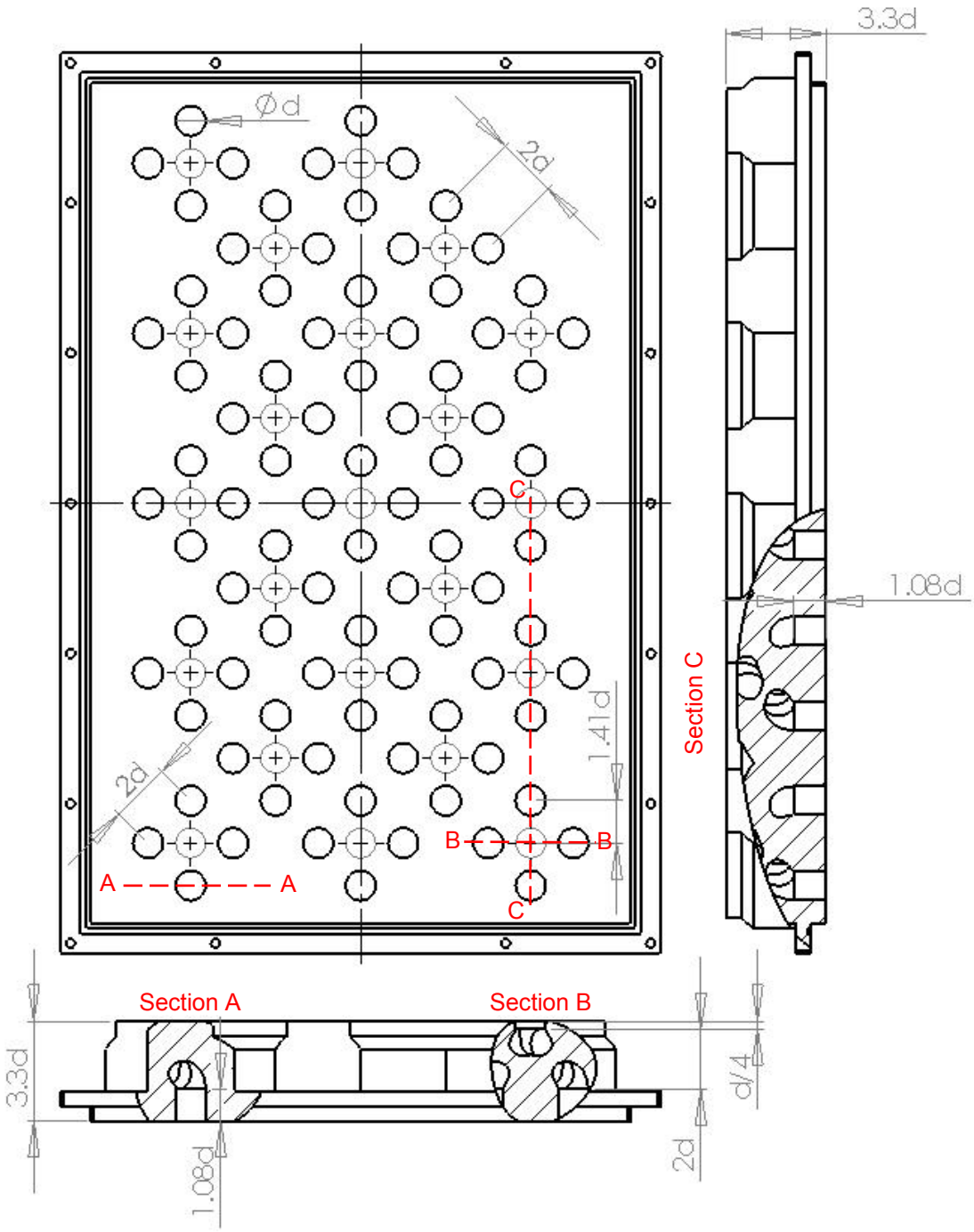


Figure 7-2: Film-Cooling Plate with Mk I Dendritic Geometry (Figure 4-2). Equivalent to a 2mm thick wall with 0.6mm diameter holes. Mainstream flow is from left to right. All dimensions are in mm.

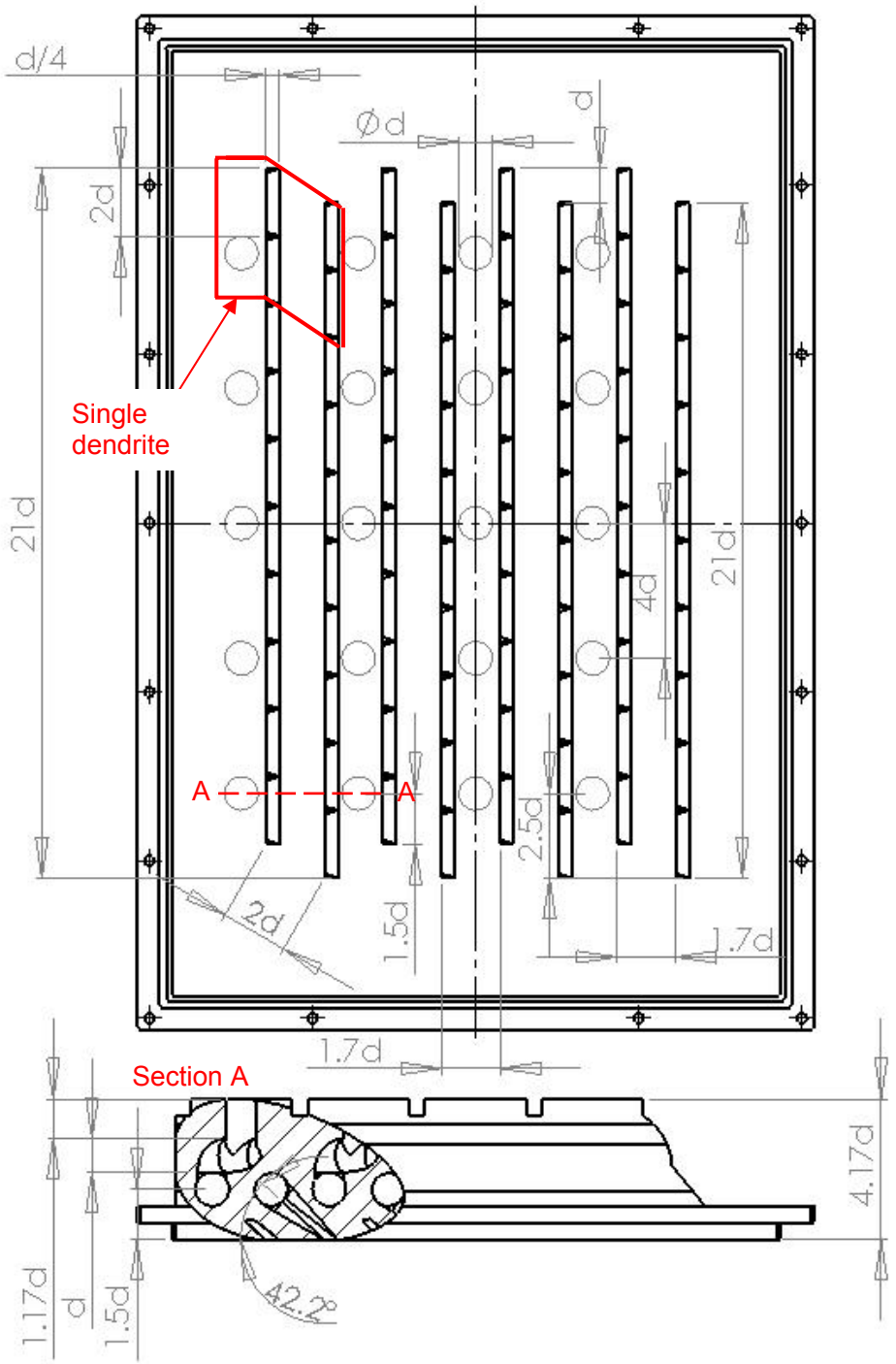


Figure 7-3: Film-Cooling Plate with Mk VI Dendritic Geometry (Figure 4-7). Equivalent to a 2.5mm thick wall with 0.6mm diameter holes. Mainstream flow is from left to right. All dimensions are in mm.

7.2 Method – Transient Technique

The experiment was originally designed such that it should mirror the scenario in an engine where the mainstream flow is hot relative to the coolant flow. However during the processing of the initial circular dendritic cooling hole

results it was discovered that the region immediately downstream of the holes experienced very little colour play and little noteworthy or reliable information could be determined about this region. This was because the coolant film created prevented any interaction of the mainstream flow with the wall. However because the analysis technique relied upon merely a temperature difference to drive heat transfer it was possible to reverse which of the flows was heated without any significant changes being made to the processing technique or resulting flow field. Initially it was assumed that for each blowing ratio / momentum ratio two tests would be required; a test with heated coolant and a test with heated mainstream, however it soon became apparent that all of the region of interest experienced sufficient colour play to obtain worthwhile results with only coolant being heated.

Power was supplied to the smaller mesh heater used to heat the coolant supply using a portable power supply which created little noise in the data acquisition system.

Particular care was taken to ensure that there were no leaks in the coolant supply system, and that reflections on the Perspex plates were eliminated.

The testing procedure for these tests was similar to that described for the narrow band liquid crystal tests conducted in Chapter 6. Each test then is a transient test, with test times limited to 120seconds. See Chapter 5 for details of the analytical approach taken. The benefit of the use of the wideband liquid crystal technique in this series of tests is that areas of low and high film-cooling effectiveness are likely to show temperature events (liquid crystal colour play) during a single test. As the surface is flat and the lighting diffuse, the hue-

temperature calibration is considered constant across the active surface. Heat transfer coefficient maps were produced from the processing of 2 video cameras' images; these were pieced together to obtain full surface maps of heat transfer coefficient. A detailed flow chart describing this procedure is included in Appendix G. Particular care was taken to eliminate pre-test cooling of the model using air from the laboratory compressed air supply. This was achieved by pre-setting the heater mesh power supply and mass flow rate several hours before the tests were to be run. The test was then initiated by the switching of flow to the coolant, followed almost instantly, by the instigation of heat to the model.

Each experiment followed the same routine; the procedure is given in detail in Appendix A.

7.3 General Overview of Flat Plate Results

The results presented in this chapter detail information about the heat transfer coefficient and film-cooling effectiveness over the exit area of the holes and up to approximately 700mm downstream (DS) of the leading row of holes. The main body of results can be found in Appendix D, but examples of typical results at a low, intermediate and high blowing ratio are shown in this section.

As well as presenting a map of the heat transfer coefficient and effectiveness data over one half of the external surface, the region within 7 hole diameters of the streamwise centreline is used to calculate the spanwise average variation in the two parameters.

It was reasoned that this central region was indicative of the film characteristic that would occur in a continuous spanwise implementation of the cooling scheme and in the notional absence of the wind tunnel sidewalls. This latter reasoning was supported by Emery et al. (*1979*) who measured typical secondary flow paths in a square duct, showing migration of the flow on the tunnel wall towards the centreline on that wall as shown in Figure 7-4.

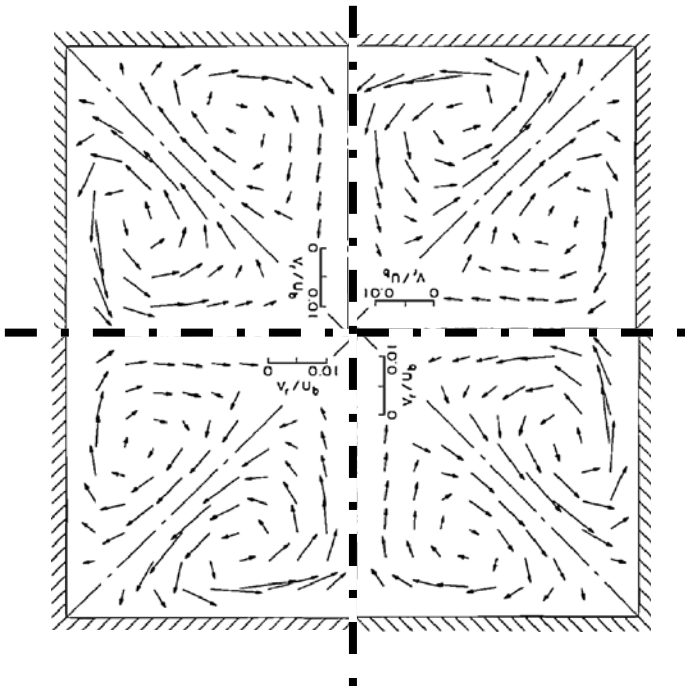


Figure 7-4: Secondary flow paths for flow along a square duct (Emery et al. 1979)

It can clearly be seen that the presence of secondary flow would tend to dilute the edge of the film-cooling flow at its spanwise outermost edges.

7.4 Results Acquired Using the Transient Technique

Using the transient technique it was possible to produce information about the heat transfer coefficient over the test section. As such each set of results

includes a heat transfer coefficient map and the corresponding mean heat transfer coefficient for the central 70mm wide streamwise strip.

7.4.1 Circular Cross Section Dendrite

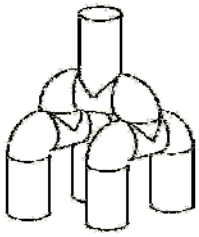


Figure 7-5: 1-2-4 dendrite as used in the flat plate tests

The first set of results presented in this chapter relates to the heat transfer coefficient distribution for a dendritic array constructed from 1-2-4 dendrites with circular cross section passages as shown in Figure 7-5.

7.4.1.1 Circular Cross Section Dendrite: Low Blowing Ratio Behaviour

At all blowing ratios the region surrounding the hole exits exhibits an increase in heat transfer coefficient compared to the duct immediately upstream. In the case of low blowing ratio coolant, this increase does not take place immediately, but does so gradually with streamwise distance over the surface; plateauing out by the fourth row at approximately 100 W/(m^2K). The heat transfer coefficient then gradually falls from about the seventh row until the downstream extent of the cooling hole array. From this position the downstream heat transfer coefficient is essentially invariant, at a constant level of approximately 40 W/(m^2K). There is no evidence of turbulence induced by the presence of the cooling flow in the downstream portion of the working section. This low blowing ratio behaviour is demonstrated in Figure 7-6 by the heat transfer coefficient

data for a blowing ratio of 0.3. It should be noted that the data is unreliable within 1 mm of the hole edges because of 3D conduction effects, but essentially this does not change the pattern observed.

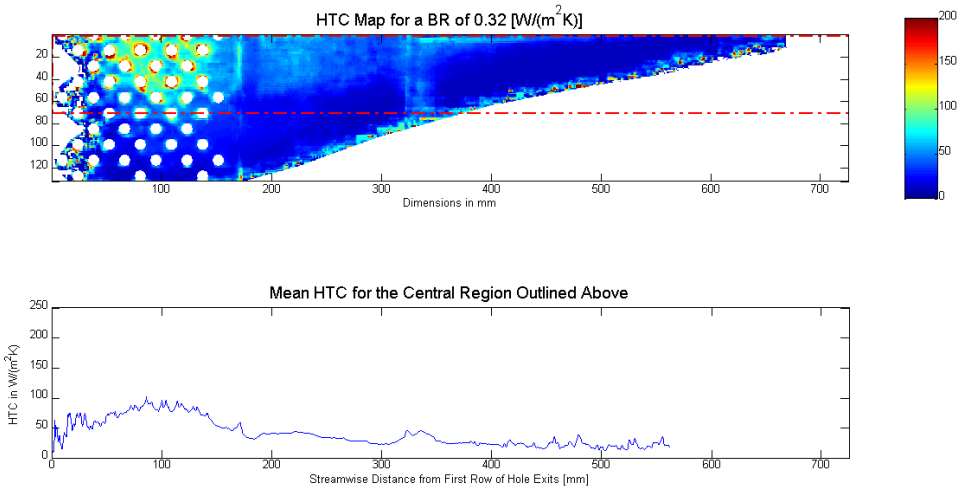


Figure 7-6: heat transfer coefficient distribution over the test section subject to the film generated by an array of 1-2-4 dendrites with circular cross section at a *BR* of 0.3 (Figure 7-3 and Figure 7-5)

7.4.1.2 Circular Cross Section Dendrite: Intermediate Blowing Ratio Behaviour

In a manner similar to the lower blowing ratio scenario, here (*BR* = 0.69) there is only a very small initial change in the heat transfer coefficient over the first two rows, however in contrast to that case there is a sharp rise in heat transfer coefficient beyond this peaking at a level of approximately 170W/(m^{2}K). Such a rise can be attributed to the turbulation of the mainstream flow as it interacts with the coolant flow. It is surmised that here the coolant acts like a virtual cylinder and the mainstream flow forms a horseshoe vortex, scrubbing the surface with increased driving temperature gas. This rapid rise in heat transfer coefficient is followed by a sharper fall in the heat transfer coefficient. This fall

is again to approximately 40 W/(m^{2}K), suggesting that this is the background level expected at the tunnel flow velocity. The level of heat transfer coefficient is surprisingly low and would suggest coherent film build up after the initial turbulent interaction of coolant with mainstream crossflow. This notably is level of heat transfer coefficient found in the far downstream region of the low blowing ratio test and would be expected to persist in the remainder of the downstream region of the plate. A second peak which is visible at about 150 mm can be attributed to the high heat transfer coefficient downstream of the hole closest to the centreline in the final row of the array, the effect of which is exacerbated because it dominates the region for which the spanwise average is taken. This intermediate blowing ratio behaviour is demonstrated in Figure 7-7 by the heat transfer coefficient data for a blowing ratio of 0.69.

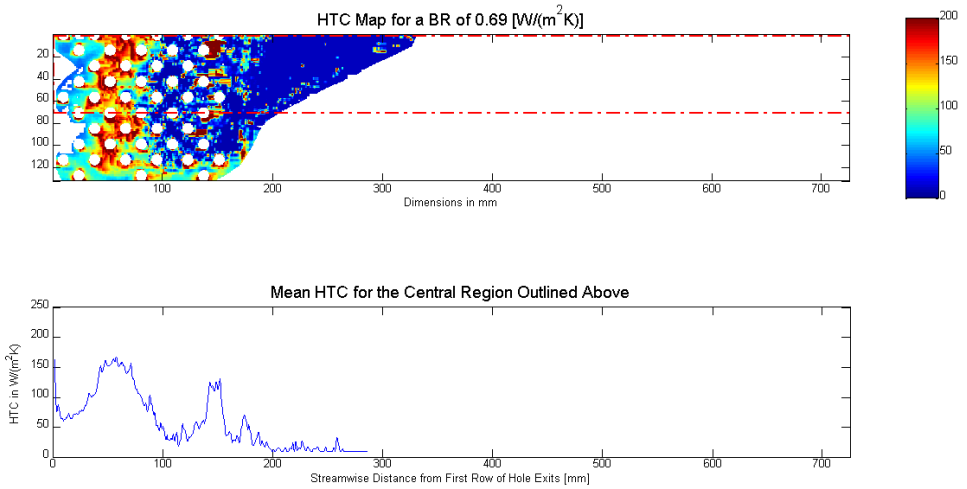


Figure 7-7: heat transfer coefficient distribution over the test section subject to the film generated by an array of 1-2-4 dendrites with circular cross section at a *BR* of 0.69 (Figure 7-3 and Figure 7-5)

7.4.1.3 Circular Cross Section Dendrite: High Blowing Ratio Behaviour

The heat transfer coefficient distribution behaviour of the highest blowing ratio tested in this study follows an almost identical pattern to that of the intermediate blowing ratio above: there is the initial region of low heat transfer coefficient where there is little disruption of the cross flow followed by the region of high heat transfer coefficient created by the interaction of the coolant with the mainstream, finally leading to the region of lowest heat transfer coefficient as the coolant flow floods the area near the external wall and forms a coherent film. In this case however, as was the case in going from the lowest to the intermediate blowing ratio the level of heat transfer coefficient has risen with the peak being almost 200 W/(m^2K). Interestingly it is clear that the behaviour at the edge of the array is very different from that near the centreline. It is unclear to what extent this behaviour would be expected at the edge of an array on a turbine blade as it is impossible to uncouple this behaviour from the proximity of the wind tunnel sidewalls. This high blowing ratio behaviour is demonstrated in Figure 7-8 by the heat transfer coefficient data for a blowing ratio of 0.96.

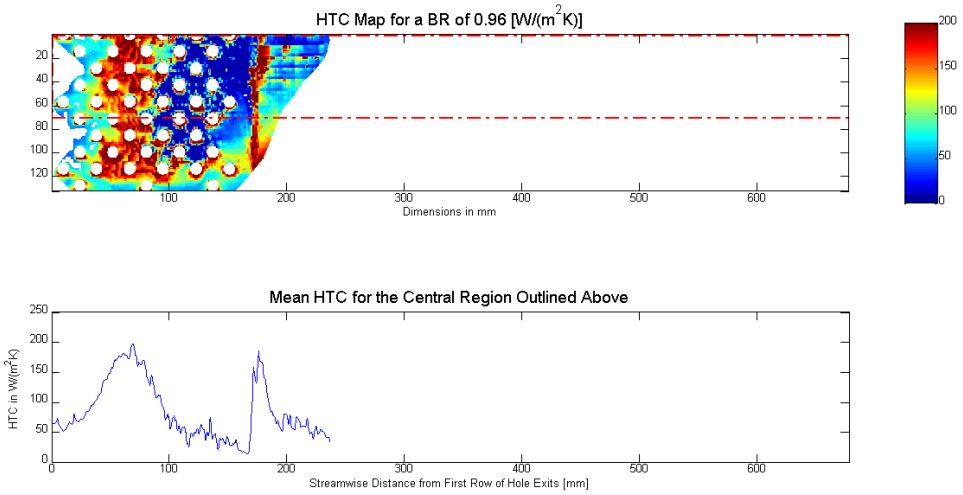


Figure 7-8: heat transfer coefficient distribution over the test section subject to the film generated by an array of 1-2-4 dendrites with circular cross section at a *BR* of 0.98 (Figure 7-2 and Figure 7-5)

The second region of high heat transfer, identified by the second peak in the mean streamwise plot of Figure 7-8, coincides with the edge of the cooling hole array plate where it interfaces with the wind tunnel wall; the plate appears to have turbulated the flow at this location, and there may be very minor leaks, though this was not apparent from the measured adiabatic wall temperature. The presence of this high heat transfer coefficient region is therefore an artifice of the experiment rather than a true characteristic of such a cooling system at these conditions.

7.4.2 Slot Exit Dendrite

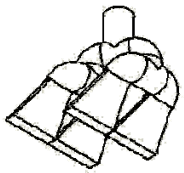


Figure 7-9: 1-2-4 dendrite with slot exit as used in the flat plate tests

The second set of results presented in this chapter relates to the heat transfer coefficient data for an array of 1-2-4 dendrites with slot type exits as shown in Figure 7-9.

7.4.2.1 Slot Exit Dendrite: Low Blowing Ratio Behaviour

For the case of a blowing ratio of 0.3 two separate tests were conducted; the first at a blowing ratio of 0.28 and the second at a blowing ratio of 0.31. As demonstrated by the two streamwise plots in Figure 7-10 there is little variation between the two results. This not only adds confidence to the reliability of these particular results, but also the heat transfer coefficient results presented in this section and the method used to acquire them.

At a low blowing ratio the array of slot exit dendrites experiences a particularly high heat transfer coefficient of over 200 $W/(m^2K)$ around the exits of the cooling holes. This rapid rise in heat transfer coefficient takes place at approximately the second row downstream of the first row of exits. The surprisingly high heat transfer coefficient in this region is an indication of strong interaction between coolant and mainstream flow. Such a high heat transfer coefficient, particularly when viewed in relation to the distributions of such a scheme at higher blowing ratios, could indicate that when the blowing rate is low there is insufficient flow to fill the exit passages and form a contiguous stream of layer of coolant near the surface. Thus the coolant acts in a manner similar to the circular holes at this blowing ratio. It will be seen later however, that this high level of heat transfer coefficient is associated with high film-cooling effectiveness and so is in fact beneficial to the blade temperature. This high heat transfer coefficient continues to the edge of the cooling hole array. Beyond

this, downstream of the cooling hole array, the level of heat transfer coefficient falls to a level below that of the dendritic array with circular cooling hole exits at the same blowing ratio. This behaviour is demonstrated in Figure 7-10. In practice the high heat transfer coefficient in this region would present less of a concern than in a downstream location; the internal cooling provided by the cooling passages is sufficient to cool the metal in this region even if the film-cooling effectiveness were low. This is, of course, the conditions pertaining in many existing cooling designs near the leading edge.

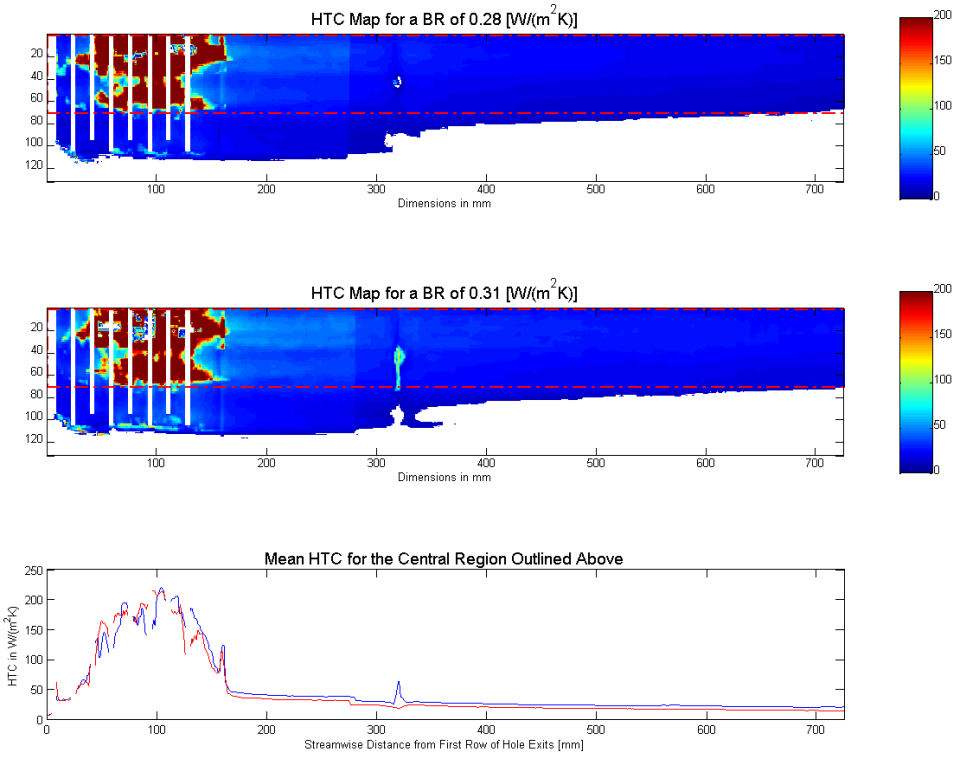


Figure 7-10: Heat transfer coefficient distribution over the test section subject to the film generated by an array 1-2-4 dendrites with slot exits at a blowing ratio of 0.28 (red line) and a blowing ratio of 0.31 (blue line) (Figure 7-3 and Figure 7-9)

The small peak in heat transfer coefficient just beyond 300 mm downstream of the first row of holes in the streamwise average plot a blowing ratio of 0.31 coincides with the interface between the upstream and downstream wind tunnel

walls and is therefore thought again to be an artifice of the experiment rather than a direct result of the cooling hole geometry. This assertion is further supported by the absence of such a peak in the equivalent streamwise plot for a blowing ratio of 0.28.

7.4.2.2 Slot Exit Dendrite: Intermediate Blowing Ratio Behaviour

In a characteristic seen in the array of circular cross section dendrites the general level of heat transfer coefficient over the working section has increased in going from a low to intermediate blowing ratio. Contrary to the behaviour seen with the circular cross section dendritic geometry the level of heat transfer coefficient has fallen significantly over the exit hole region in going from a low to intermediate blowing ratio with a peak level of about 150W/(m^2K). The rise in heat transfer coefficient over the array is also more gradual and no significant rise takes place until approximately the third row of cooling exits. The high level over the region of the hole exits again indicates some interaction of the coolant with mainstream cross flow. In this case once the introduction of coolant to the mainstream is complete the coolant forms a thick coherent film which has a much lower heat transfer coefficient associated with it. This intermediate blowing ratio behaviour is demonstrated in Figure 7-11 by the heat transfer coefficient data for a blowing ratio of 0.44.

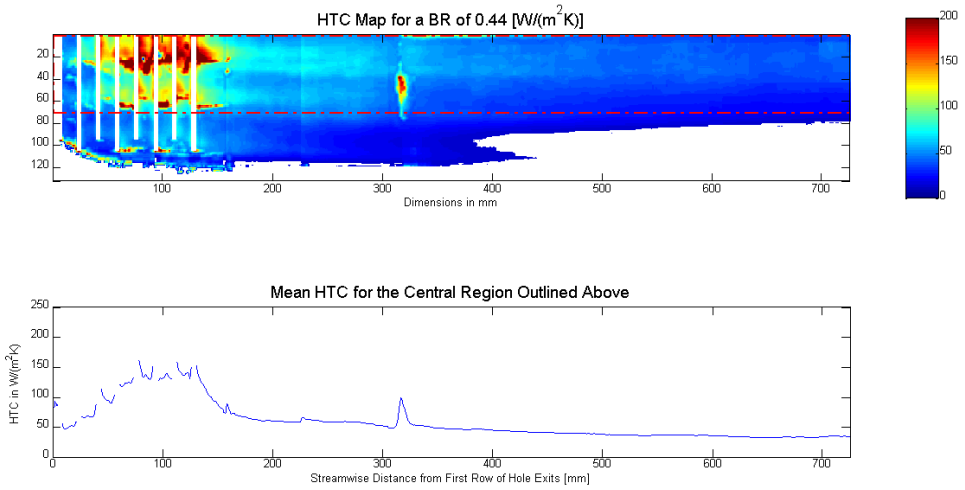


Figure 7-11: Heat transfer coefficient distribution over the test section subject to the film generated by an array 1-2-4 dendrites with slot exits at a *BR* of 0.45 (Figure 7-3 and Figure 7-9)

7.4.2.3 Slot Exit Dendrite: High Blowing Ratio Behaviour

In increasing the intermediate blowing ratio to the highest, little difference is seen between the downstream levels of the heat transfer coefficient. Immediately downstream of the cooling hole array a slight increase in the level of heat transfer coefficient is seen from a mean spanwise value of approximately 60W/(m^{2}K) to 75W/(m^{2}K). Such an increase is driven by the higher blowing ratio and the resulting coolant flow having a more significant interaction with the mainstream cross flow which persists further downstream. Unlike in the case of going from a low to intermediate blowing ratio, an increase is seen in the level of heat transfer coefficient in the region of the hole exits, although its peak of 185W/(m^{2}K) remains below that of the low blowing ratio case. This is likely to be because of the increased interaction of the coolant with the mainstream generating turbulated flow and in turn increasing the heat transfer coefficient in that region. Its distribution, however, stays almost identical to that of the intermediate blowing ratio heat transfer coefficient distribution.

This high blowing ratio behaviour is demonstrated in Figure 7-12 by the heat transfer coefficient data for a blowing ratio of 0.6.

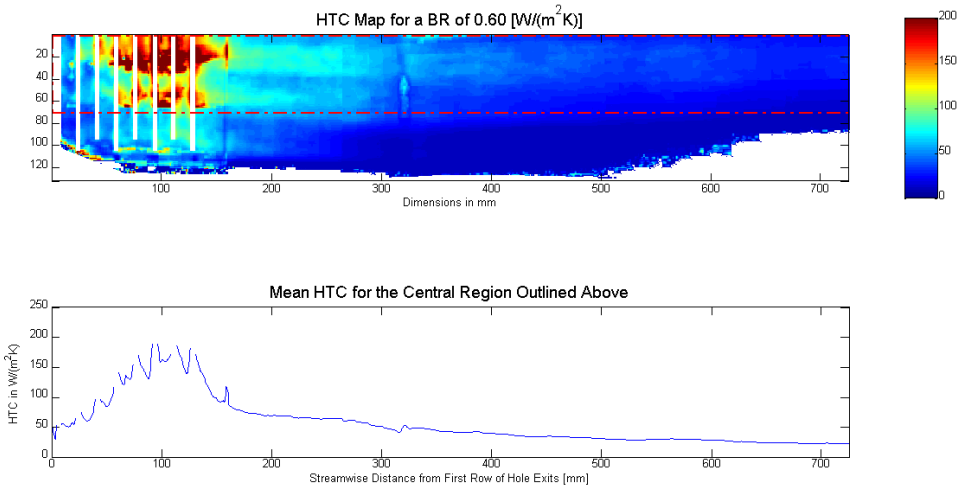


Figure 7-12: Heat transfer coefficient distribution over the test section subject to the film generated by an array of 1-2-4 dendrites with slot exits at a *BR* of 0.45 (Figure 7-3 and Figure 7-9)

7.4.3 Comparison and Generalised Behaviour of Heat Transfer Coefficient Results

It is clear from the data presented that the results are poorly conditioned, particularly for the array of circular dendrites; they are included here in order to gain an overall picture of dendritic cooling array performance. Nevertheless, some key points can be drawn; in the case of the circular cross section dendrites, there is a general increase in heat transfer coefficient with blowing ratio, particularly in the region of the hole exits. Similarly, in the case of the slot exit dendritic array an increase in blowing ratio corresponds to an overall increase in the heat transfer coefficient over the entire working section. In the region of the slot exits this is not entirely true with low blowing ratios resulting in a higher than expected heat transfer coefficient in that region.

Without film-cooling effectiveness data gained at equivalent conditions it is impossible to conclude which system has better performance, but the generally lower heat transfer coefficient of the slot injection would suggest that it is likely to perform better.

7.5 Method – Steady State Technique

While the initial intention of the author was to simultaneously determine the heat transfer coefficient and film-cooling effectiveness in the transient liquid crystal experiments, it became apparent that that this was an inherently poorly conditioned experiment. Thus an additional set of experiments using a modified test-rig were conducted to directly determine adiabatic film-cooling effectiveness. As these were supplementary tests, a key point was to match flow conditions to the transient heat transfer tests.

As well as the testing of the two cooling hole configurations tested in the heat transfer coefficient transient tests a third straight cooling hole array was also tested using the steady state technique.

The testing involved multiple experimental runs to cover the desired range of conditions. While similar to those of the transient heat transfer coefficient tests, here it was possible to conduct additional tests to confirm that the film-cooling effectiveness was a weak function of the mainstream flow Reynolds number. The final testing schedule is set out in Table 7-2 below.

Mainstream Velocity	*BR*s to be tested for each configuration
9.0	0.3,0.45,0.6,1

13.4	0.3,0.45,0.5,0.6,1
17.9	0.3,0.45,0.6

Table 7-2:Testing Schedule

Whilst in the transient tests it was possible to view the liquid crystal colour play through the Perspex wall of the wind tunnel this wasn't possible for the steady state test because the Perspex absorbs IR radiation. A solution to this problem was to view the test section through a Zinc-Selenide window, a material transparent to IR radiation (of constant transmissivity over the temperature range considered). This meant the wind tunnel wall remained sealed whilst the tests were conducted.

To determine the film-cooling effectiveness it was not necessary to know the absolute value of the temperatures involved, merely the ratio of the temperatures relative to one another. Therefore, it was not necessary to conduct an in-situ calibration of the IR camera. The temperature range of the IR camera was, therefore, set to be close to the range of temperatures expected and the output selected to be a gray scale value which is linear with pseudo-temperature over the range of interest. The side wall of the wind tunnel, which as noted in Chapter 5 was constructed from Rhoacell for these tests was sprayed black to create a surface of constant emissivity, this was assumed to be $\varepsilon=0.8$ as it produced a good match between surface thermocouples and the camera output at a known temperature of $45^{\circ}C$.

Pseudo temperature, gray values were easily obtained from the image snap shots. It was possible to achieve near steady-state conditions because the Rhoacell wall is nearly adiabatic and it can be assumed after a short run time

that the temperature of the wall is the same as that of the gas next to it. The mainstream temperature value (the gray scale value assigned by the IR camera) was obtained from a region of the image that represented part of the test section that didn't interact with the coolant flow (i.e. upstream of the insert or the spanwise far field), likewise the coolant temperature value was obtained from regions within the coolant hole / slot exits.

Within the camera's menu system there were various parameters that needed to be set with respect to the experimental conditions to obtain results consistent with the requirements above. A summary of these settings and the rational for them is given in Appendix D.

To eliminate extremely time consuming manual processing required to accurately orientate, scale and join the upstream and downstream images a single viewing window which was moved from upstream to downstream ports was mounted into a machined aluminium frame which was secured to the tunnel wall using two quick release clips. The camera was then mounted to this frame such that the outer rim of the camera lens sat square to the window and the window was flush with the sidewall of the tunnel. By doing this the camera locations were made consistent between tests, and the joining of the images could be entirely automated without the need for any user input.

Window locations on the tunnel side wall opposite the test plate were chosen to ensure the two views taken had a small overlap, captured the hole array, and maximised the view downstream. A blanking plate was used to plug whichever viewing port was not in use.

A detailed flow chart describing the image processing procedure is included in Appendix G. Each experiment followed the same routine; the procedure is given in detail in Appendix A.

7.6 Results Acquired Using the Steady State Technique

The steady state method produced information about the film-cooling effectiveness of each cooling scheme (see section 5.3). The following sets of results detail a map of the film-cooling effectiveness over the test section along with a plot of the mean effectiveness of a 70 mm wide strip in the streamwise direction.

Unlike the transient set of results both the flow passing through the dendritic array of cooling passages as well as the velocity of the mainstream flow was varied. Again, a full set of results for each set of conditions can be found in Appendix D but for illustrative purposes a set of results for each geometry is presented here (Figure 7-13, Figure 7-14 and Figure 7-15), each at approximately the same flow conditions.

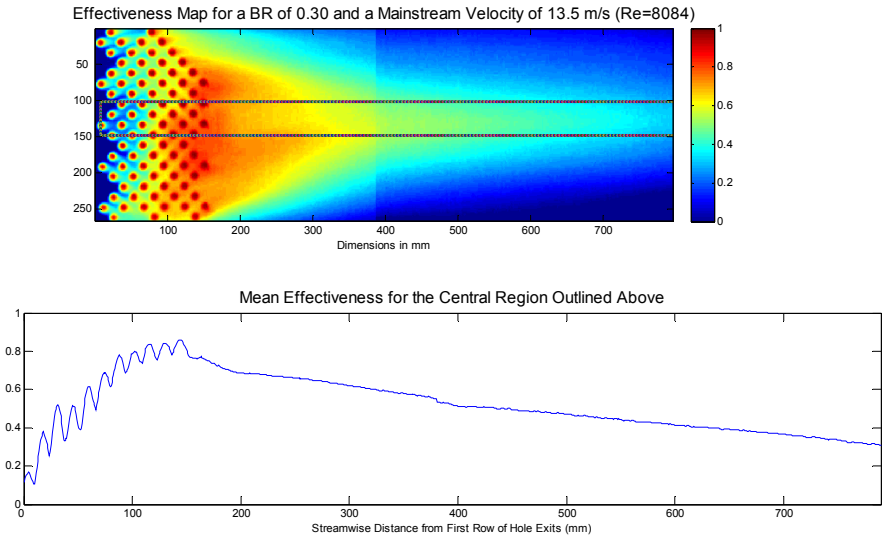


Figure 7-13: Film-cooling effectiveness data for an array of straight, circular cross section holes at a *BR* of 0.3

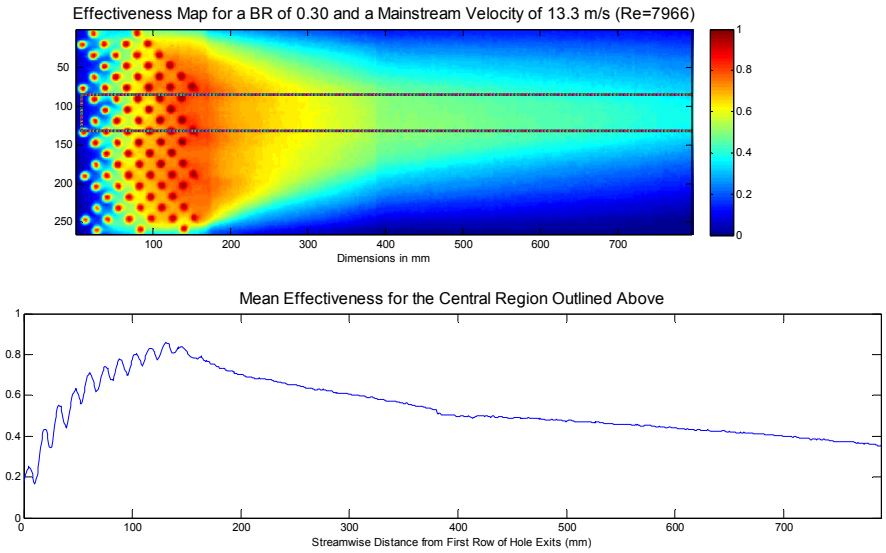


Figure 7-14: Film-cooling effectiveness data for an array of circular cross section dendrites (Figure 7-2 and Figure 7-5)

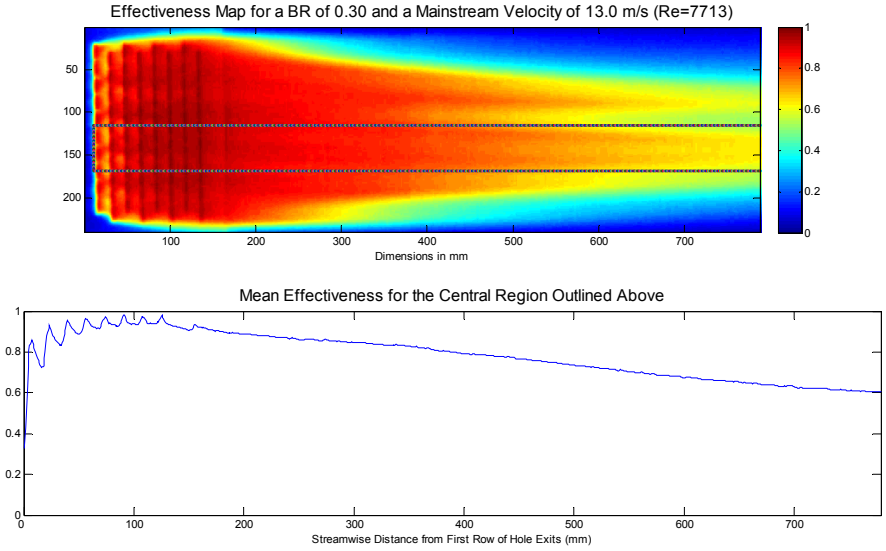


Figure 7-15 Film-cooling effectiveness data for an array of circular cross section dendrites with slot exits (Figure 7-3 and Figure 7-9))

Figure 7-16, Figure 7-17, Figure 7-18 and Figure 7-19 summarise the film-cooling effectiveness data obtained from the 36 steady state tests. The spanwise mean film-cooling effectiveness for a central region (dotted on the local distributions above) over the exit area of the holes and a region up to 80 inlet diameters downstream (DS) of the leading edge row of holes is presented

for the three different geometries. As expected, the variation in film-cooling performance for a given blowing ratio over the range of mainstream velocities tested was negligible, therefore for each blowing ratio the average film-cooling effectiveness for the mainstream velocities is presented, and the decision to collect heat transfer coefficient data at a single mainstream velocity justified.

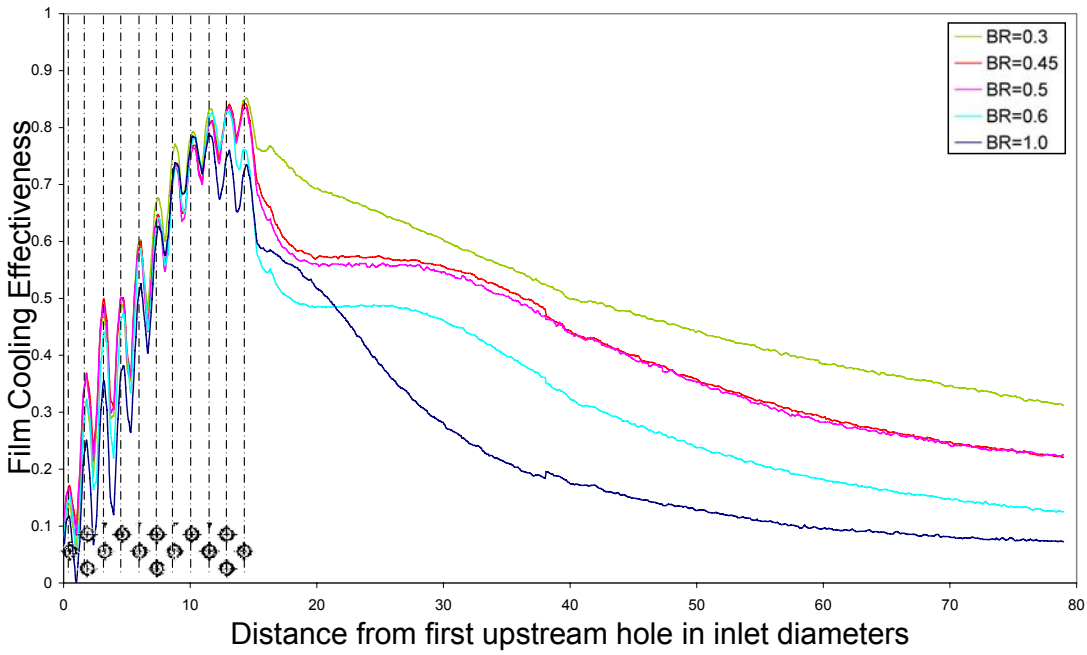


Figure 7-16: Summary of film-cooling effectiveness data for the array of straight film-cooling holes

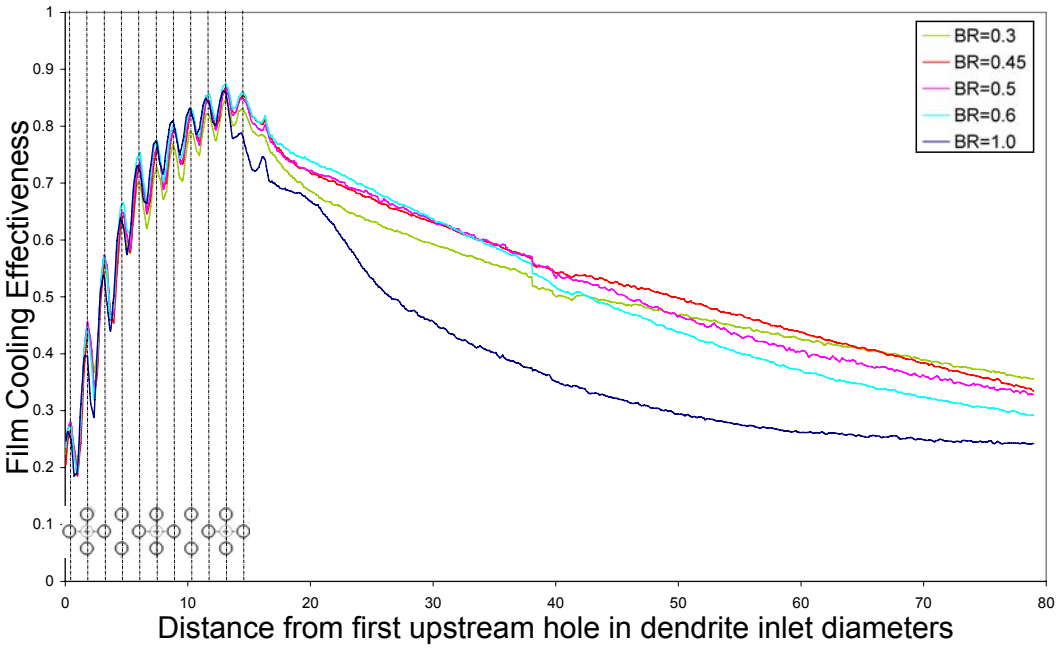


Figure 7-17: Summary of film-cooling effectiveness data for the array of circular cross section dendrites

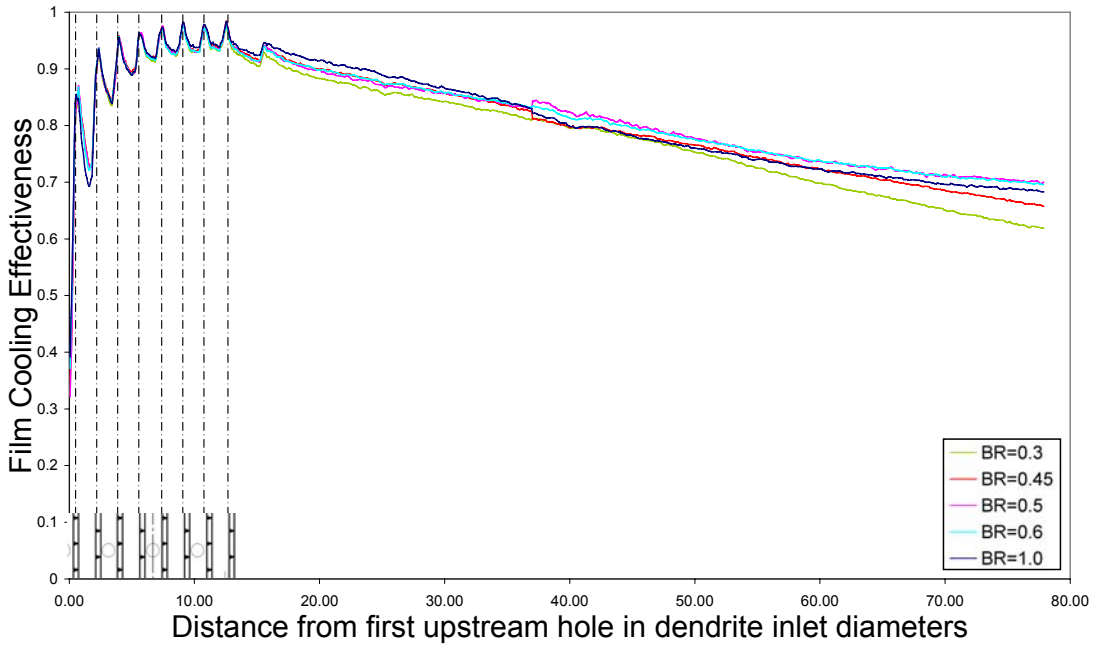


Figure 7-18: Summary of film-cooling effectiveness data for the array of circular cross section dendrites with slot exits

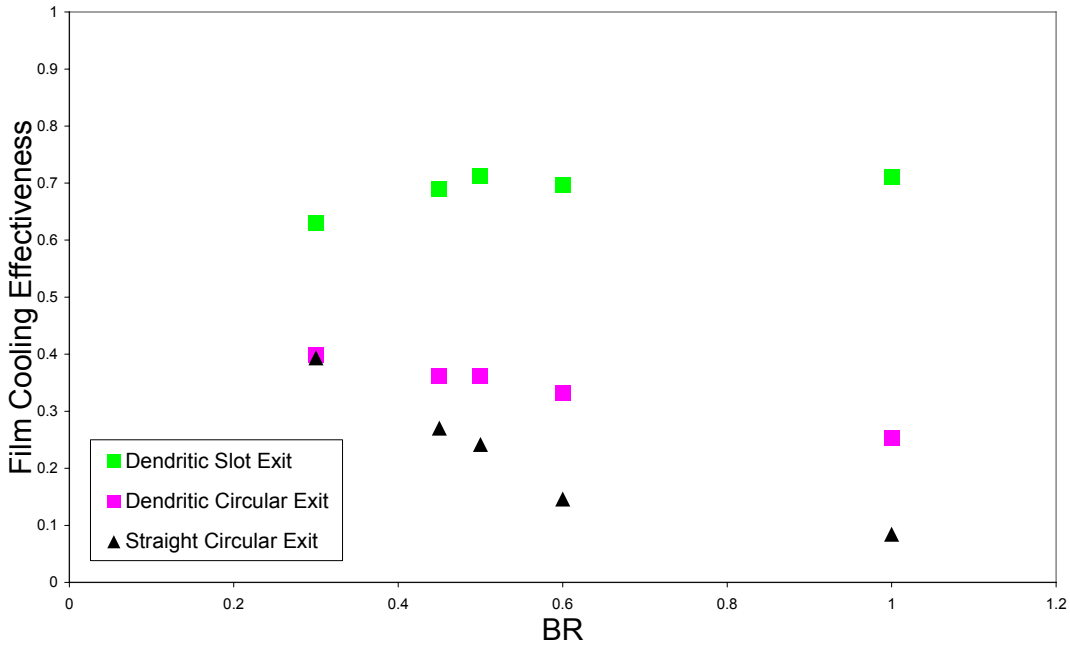


Figure 7-19: Film-cooling effectiveness variation with *BR* 70 inlet diameters downstream of the first row of cooling holes

Figure 7-19 details the behaviour of the film-cooling effectiveness for the three different geometries over a range of blowing ratios 70 inlet diameters downstream of the first row of cooling holes. The behaviour of the slot exit

dendrite is quite different from the other two geometries indicating exceptionally good attachment of the film in the downstream region despite higher blowing ratios. This type of behaviour for console geometry was noted in the study by Liu et al. (*2009*), but is seen again here in spite of the non-converging nature of the exit slots.

It is clear that despite the same mass flow rate and the same hole exit distribution the circular hole dendritic array performs markedly better than the conventional straight cooling holes, although the improvement is less pronounced, than that of the slot exits.

7.7 Analysis of Results Acquired Using the Steady State Technique

7.7.1 Upstream Behaviour

For all cooling arrangements, the film-cooling effectiveness in the region of the hole exits steadily increases due to the cumulative effect of coolant build up in the streamwise direction. The manner in which this rise takes place and its periodic behaviour in the points between the hole exits is dependent upon both the geometry of the cooling holes and the blowing ratio.

In the case of the **straight cooling hole configuration** the cooling film's performance at lower blowing ratios is marginally better than that at higher blowing ratios. This can be partially attributed to the angle through which the bulk flow can be turned by the mainstream as it is ejected onto the external surface. The governing factor here is the momentum ratio between the flows. When the blowing ratio (momentum ratio) is high, the total pressure of the

coolant is substantially higher than the mainstream and little turning takes place. This leads to film detachment. At lower blowing ratios, the momentum of the exiting flow is less and the interaction with the oncoming flow is sufficient to create substantial coolant flow curvature: promoting attachment onto the wall of the wind tunnel. Therefore locally the cooling film produced by a low blowing ratio flow would be expected to perform better because the coolant is able to remain closer to the surface.

Because there are discrete streamwise locations where the film-cooling holes exit the pattern of build up in effectiveness is a series of exponential rises followed by decay in film-cooling effectiveness level due to mixing. A further complication arises in the case of the circular exits from the first and last row of film-cooling hole exits which have double the spanwise pitch compared to the other rows. This is simply modelled by halving the rate of rise for these rows. Conversely because there are in effect more rows of circular exit holes than there are rows of slots the film is more regularly refreshed in the streamwise direction than in the case of the slot exits

For the **circular cross section dendritic array** there are 11 rows of exits supplied by 5 rows of inlets. In effect each row of inlets supplies 3 rows of exits which overlap with exits fed from inlets in other rows. This is because of the diamond breakout pattern adopted. In between these 11 rows there are troughs in the effectiveness where the film-cooling effectiveness is reduced through mixing with the mainstream. In comparison to the straight cooling holes it can be seen that in general the film-cooling effectiveness of the circular cross

section dendritic passage rises more quickly with less fluctuation in film-effectiveness between the rows of hole exits.

Although the maximum effectiveness reached with the two systems is approximately the same, the reduced drop in effectiveness between the rows of hole exits can only be attributed to the secondary flows induced in the coolant flow because of the internal branching of the dendritic geometry. The similarity in the maximum effectiveness of the two systems isn't surprising given the identical exit pattern and the calculation of blowing ratio based upon exit mass flow rate.

It also appears that by a small margin the maximum film-cooling effectiveness is now reached at a blowing ratio of 0.6 rather than at 1 as was previously observed in the case with straight cooling holes. Again this can only be attributed to the secondary flows induced into the flow because of the internal branching of the dendritic geometry.

It can be speculated that at higher blowing ratios the film performs better in between hole exits because the coolant has a greater tendency to break out in to the mainstream providing a barrier from the hot mainstream to the area immediately downstream of the hole exit.

In the case of the **dendritic array with slot exits** there is a very sharp rise in film-cooling effectiveness with streamwise distance over the array of hole exits compared with the same region in the other cases. The effectiveness also reaches a higher maximum and does so with much reduced troughs in effectiveness between rows, again compared to the other two cases, even though there are fewer rows in this case. It is likely that the reduction in the

trough is down to the better alignment of the exiting coolant flow with the surface imparted by the angled exits of the slot. This means the exiting coolant would be closer to the surface immediately downstream of the cooling hole. This is confirmed by the flow visualisation below.

7.7.2 Downstream Behaviour

It can be speculated that the mechanism by which the film is degraded is different not only for alternative geometries but also for the various blowing ratios.

In the case of the film generated by the slot there is a clear distinction between the behaviour exhibited at blowing ratios above 0.6 and that exhibited below 0.6. When looking in detail at Figure 7-18 it can be seen that the behaviour of the films downstream for the various blowing ratios are dissimilar. In the case of a blowing ratio of 0.6 or above the film-cooling effectiveness appears to reach a plateau below which it does not fall regardless of how far downstream the point in question is. Conversely in the case of a blowing ratio of 0.3 the film-cooling effectiveness continues to diminish with streamwise distance from the coolant holes.

In order to understand this it is important to first understand the process by which a cooling film is eroded. This is a mechanism of mixing between mainstream and film where there is mass exchange between the two streams. The extent to which the mixing process and therefore the mass exchange take place is dependent upon the relative streamwise velocities of the two flows. A large difference in the two velocities results in a high shear force between the two and therefore an increase in the extent of mixing. In contrast if the two

flows have the same streamwise velocity there would be little to no shear force between the layers and any film depletion would have to rely on heat transfer in the form of radiation rather than advection.

The same behaviour can be observed in the case of the circular hole dendrites. Whilst the relative ranking of the various blowing ratios is reversed it is clear that at higher blowing ratios rather than continuing to diminish the film-cooling effectiveness plateaus out.

Although the two arrays have an identical exit pattern and the calculation of the blowing ratio is based upon mass flow rate the dendritic array performs better downstream.

7.7.3 A Film Cooling Effectiveness Row by Row Superposition based Correlation

The film-cooling effectiveness distribution of multirow arrays of film cooling holes can be modelled by the suitable superposition of single row film-cooling behaviour.

For a single isolated row the associated film-cooling effectiveness may be expressed by an arbitrary fitting function. The author has chosen a function which is a product of an exponential rise and decay:

$$\eta_f = A\left(1 - e^{-x/B}\right) \times e^{-x^D/C}$$

Equation 7-3

where x is the distance relative to the point of injection of the film in to the mainstream, measured in hole inlet diameters, and the constants A, B, C and D are a simple linear functions of the blowing ratio, BR, such that

$$A = A_o + BR \times A_1 \qquad etc.$$

Equation 7-4

For an array consisting of multiple rows (as shown in **Error! Reference source not found.**), the film formed by upstream rows means that the film-cooling effectiveness of a row of holes ejecting coolant into already existing external film must now be defined with reference to the local external film temperature: i.e. whereas

$$\eta_{f\,1} = \frac{T_m - T_{f,1}}{T_m - T_c}$$

Equation 7-5

for the first row,

$$\eta_{f\,i+1} = \frac{T_{f,i} - T_{f,i+1}}{T_{f,i} - T_c}$$

Equation 7-6

for the $i+1^{th}$ row.

If the film-cooling effectiveness from contributions of all upstream rows is expressed with reference to the mainstream temperature as

$$\eta'_{f_i} = \frac{T_m - T_{f,i}}{T_m - T_c}$$

Equation 7-7

then

$$T_{f,i} = \left(1 - \eta'_{f_i}\right)T_m - \eta'_{f_i}T_c$$

Equation 7-8

Thence from Equation 7-6 and Equation 7-8 it follows that

$$T_{f,i+1} = \left(1 - \eta'_{f_i} - \eta_{f_{i+1}} + \eta'_{f_i}\eta_{f_{i+1}}\right)T_m - \left(\eta'_{f_i} + \eta_{f_{i+1}} - \eta'_{f_i}\eta_{f_{i+1}}\right)_i T_c \equiv \left(1 - \eta'_{f_{i+1}}\right)T_m - \eta'_{f_{i+1}}T_c$$

Equation 7-9

Now the film-cooling effectiveness downstream of the i+1th row can be expressed in a general form for film-cooling effectiveness at any given location over the surface, given by Equation 7-10.

$$\eta'_{f_{i+1}} = \eta'_{f_i} + \eta_{f_{i+1}} - \eta_{f_{i+1}} \times \eta'_{f_i}$$

Equation 7-10

In Equation 7-10 $\eta'_{f_{i+1}}$ is the film-cooling effectiveness based on the mainstream and coolant exit temperatures between the $i+1^{th}$ and $i+2^{th}$ rows. For a series of uniform rows of holes $\eta_{f_{i+1}}$ describes the film-cooling effectiveness of a single row of holes exiting into the freestream at the $i+1^{th}$ location. The underlying assumption here is that the rate of decay of upstream films is unaffected by the injection of additional coolant onto the external surface.

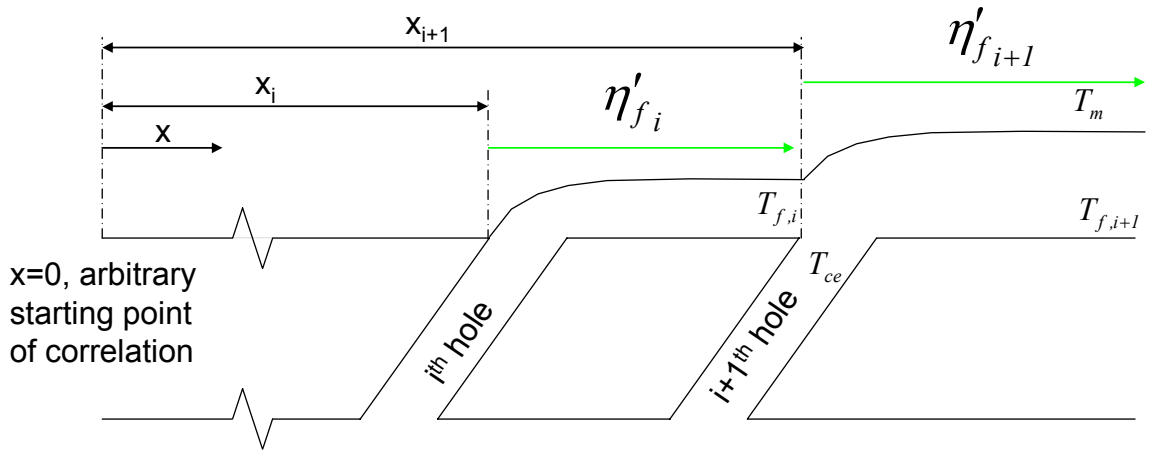


Figure 7-20: Schematic detailing build up of film-cooling from multiple rows and the scheme used for superposition.

For the three different geometries considered in the steady state tests, the superposition model was applied and a least squares regression was found to determine the constants A_0 to D_1. Note that while no data were available for an isolated row of holes, it is possible to infer the correlations for film-cooling effectiveness for an isolated row (Equation 7-3) and these are detailed in Table 7-3 below.

Constant	Straight cooling holes		Dendritic cooling holes with circular cross section		Dendritic cooling holes with slot exits	
$A\,[A_o \quad A_1]$	0.342274	-0.06664	0.350255	0.693624	1.599072	-0.52855
$B\,[B_o \quad B_1]$	0.05666	0.000136	0.05	0.08527	0.178004	0.000419
$C\,[C_o \quad C_1]$	2.339657	0.504804	1.542514	-0.70954	0.797838	1.381465
$D\,[D_o \quad D_1]$	0.312365	0.268022	0.292437	-0.01746	0.219794	0.146308
$\eta_f = (A_0 + A_1 BR)\left(1 - e^{-x/(B_0 + B_1 BR)}\right) \times e^{-x^{(D_0 + D_1 BR)}/(C_0 + C_1 BR)}$ for $0 > BR \le 1$						

Table 7-3: Summary of Constants for Single Row Isolated Film-Cooling Effectiveness Correlation

The result of Equation 7-3 can then be used in Equation 7-10 to calculate the film-cooling effectiveness at any point downstream of a row given known details about the contribution to the film-cooling effectiveness of rows upstream.

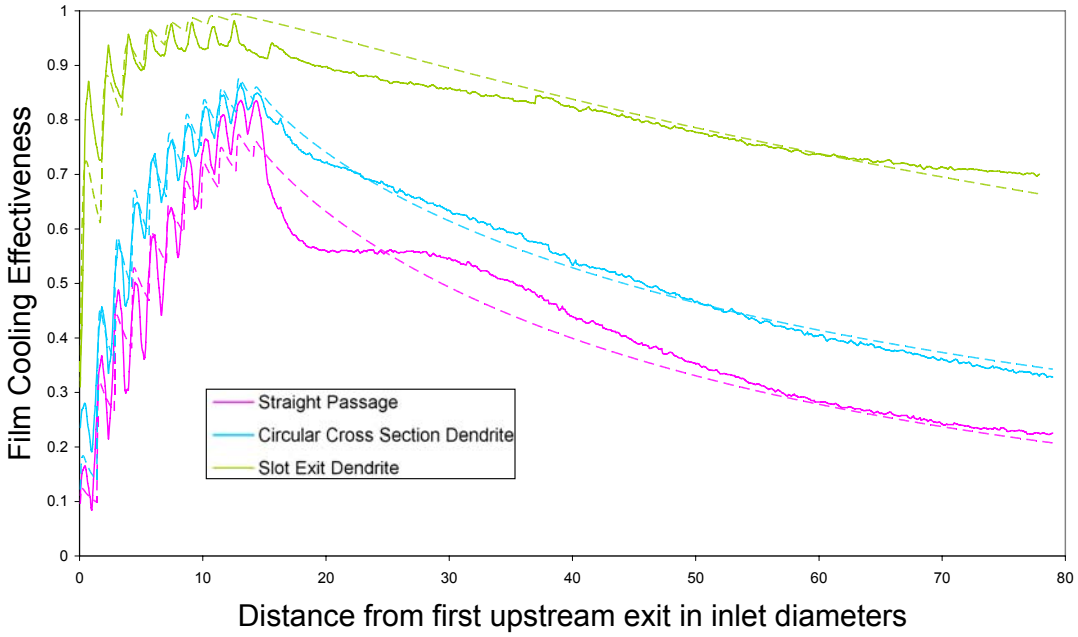


Figure 7-21: Experimental (continuous line) and row summed based correlation (broken line) streamwise film-cooling effectiveness distribution for the 3 tested geometries at a blowing ratio of 0.5

The single row correlations for the three geometries are compared at a blowing ratio of 0.5 in Figure 7-21. Here the difference in film build up between the slot exit and circular holes is again clearly visible, along with the much more stable performance of the slot ejected film downstream. The film-cooling effectiveness distributions and predictions from the correlation for the straight, circular cross section dendritic, and slot exit dendritic cooling arrays are shown in Figure 7-22, Figure 7-23 and Figure 7-24, respectively. Only data and the row summed correlation at blowing ratios of 0.3, 0.5 and 1 are shown for clarity. The fit achieved is good over the entire range of blowing ratios in each case. This

method of film-cooling effectiveness performance prediction clearly provides an excellent match to the original experimental data.

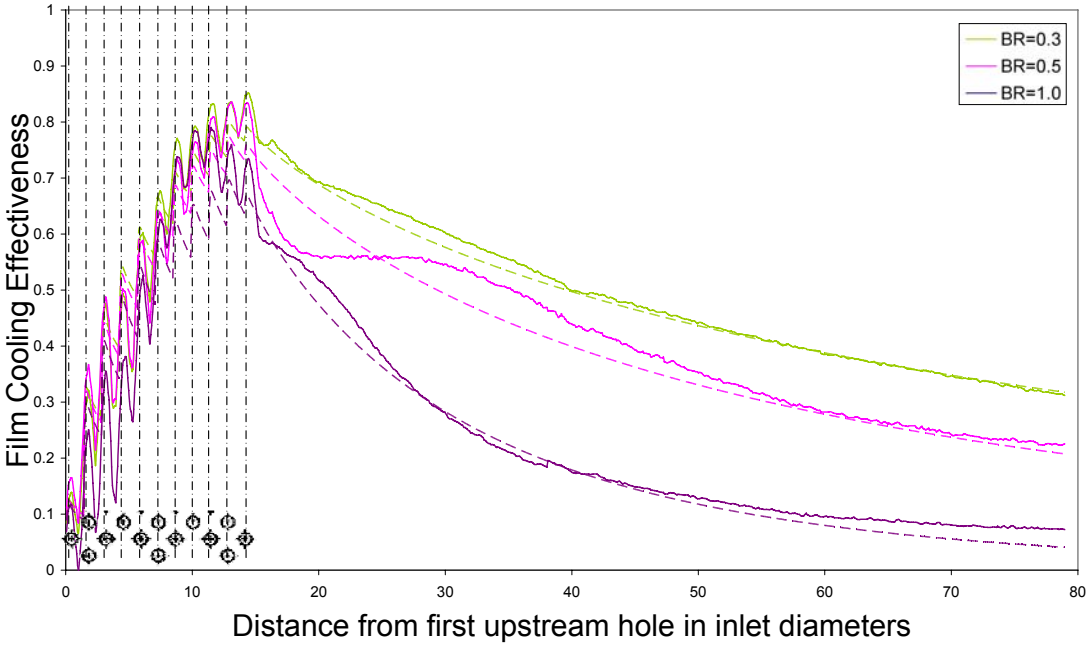


Figure 7-22: Experimental (continuous line) and row summed based correlation (broken line) streamwise film-cooling effectiveness distribution for an array of straight cooling holes

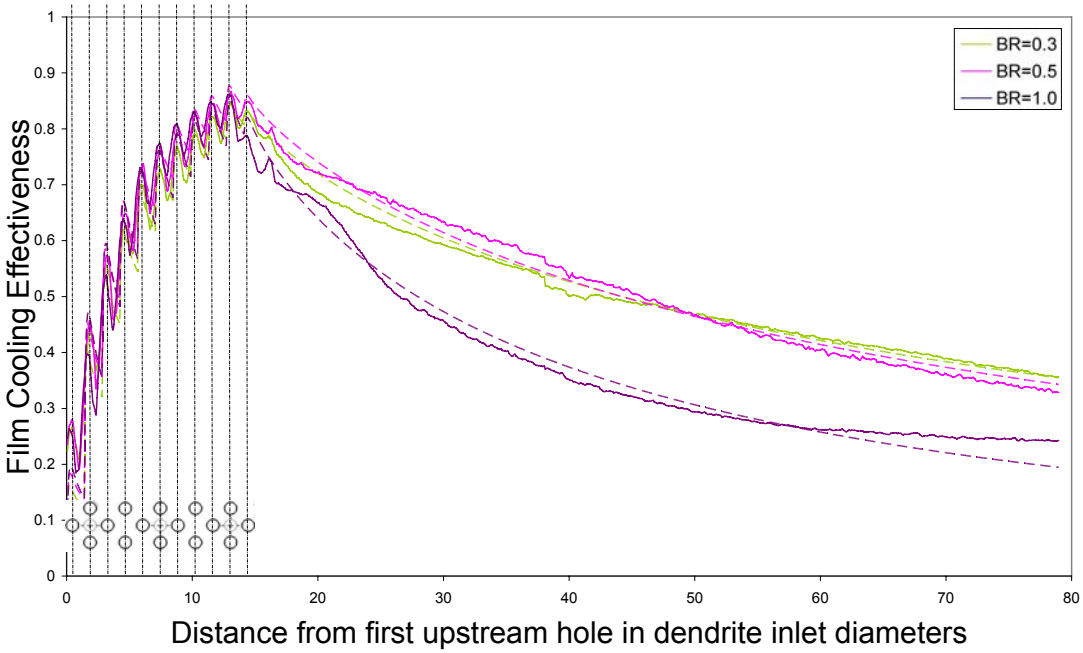


Figure 7-23: Experimental (continuous line) and row summed based correlation (broken line) streamwise film-cooling effectiveness distribution for an array of dendrites with circular cross section

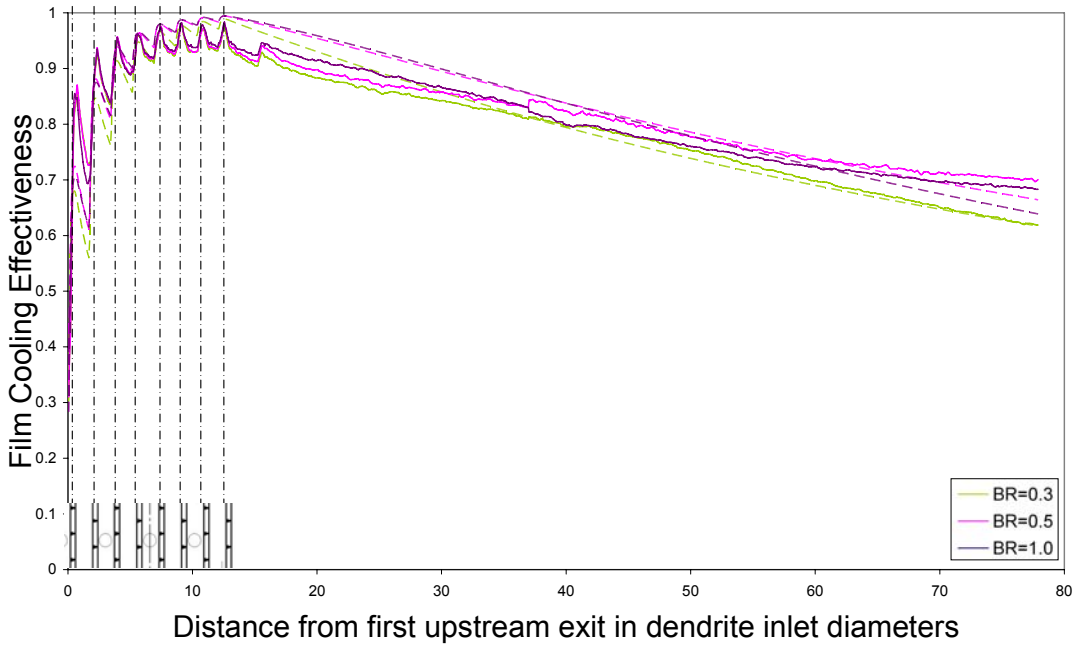


Figure 7-24: Experimental (continuous line) and row summed based correlation (broken line) streamwise film-cooling effectiveness distribution for an array of dendrites with slot exits

Evidently a major advantage of this prediction is that it can accurately account for model geometries with alternative row spacing to that of the original geometry rather than the simple adaptation of the film-cooling effectiveness profiles necessary with the method outlined in section 7.7.4.1 and 7.7.4.2. Furthermore it can accurately model the peaks and subsequent troughs in film-cooling effectiveness in the regions where the coolant is injected, and is consistent with in-house modelling procedures used in engine manufacturing companies.

7.7.4 Development of Array Specific Correlations

Figure 7-25, Figure 7-26 and Figure 7-27 include plots of the generalised relationships for the entire array of film cooling holes explained in detail in section 7.7.4.1 and 7.7.4.2. This set of relationships allows for no variation in the construction of the array of the cooling hole exits and the nature of the correlation changes depending upon the type of geometry and on whether the

point in question is upstream or downstream of the end of the array. It usefully provided a quick means of populating the cooling model in the early stages of its development.

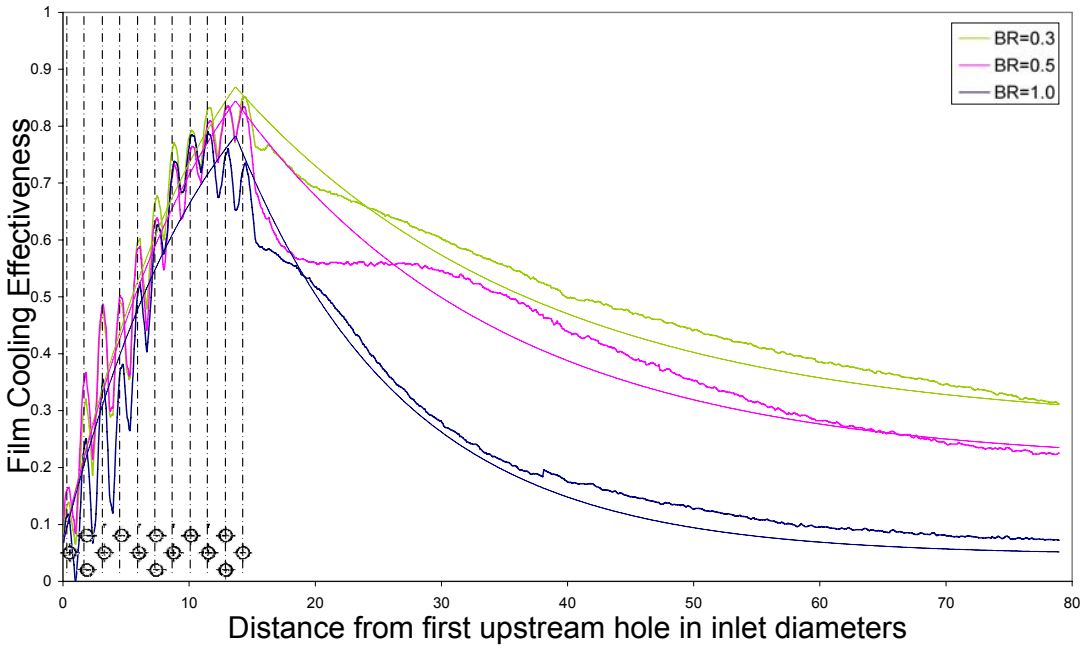


Figure 7-25: Film-cooling effectiveness data (continuous line) and exit array specific correlation (broken line) for the array of straight film-cooling holes

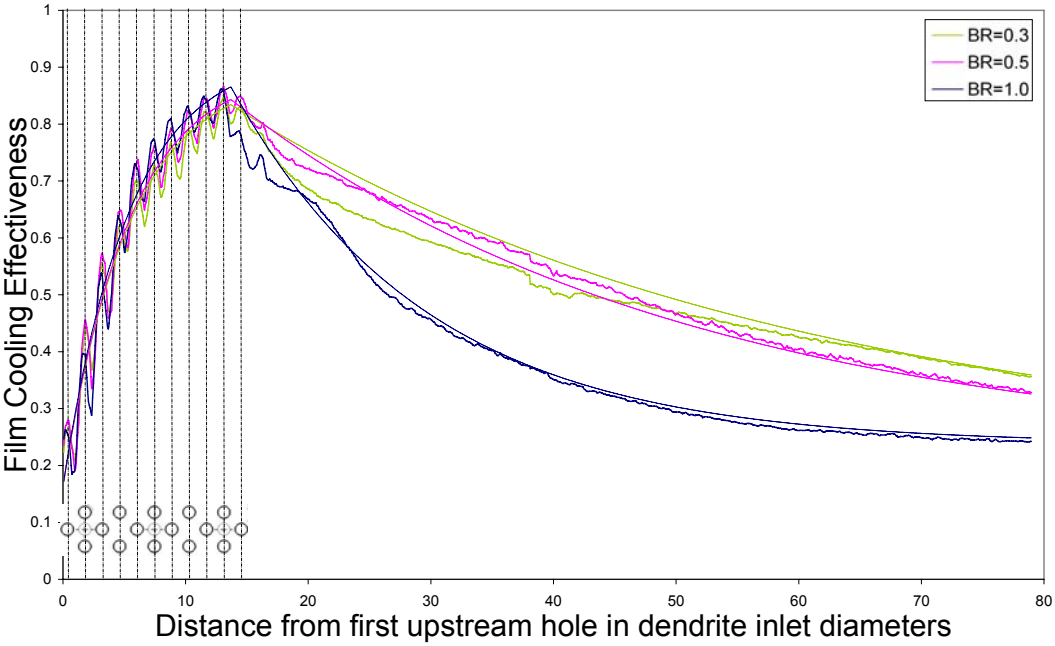


Figure 7-26: Film-cooling effectiveness data (continuous line) and exit array specific correlation (broken line) for the array of circular cross section dendrites

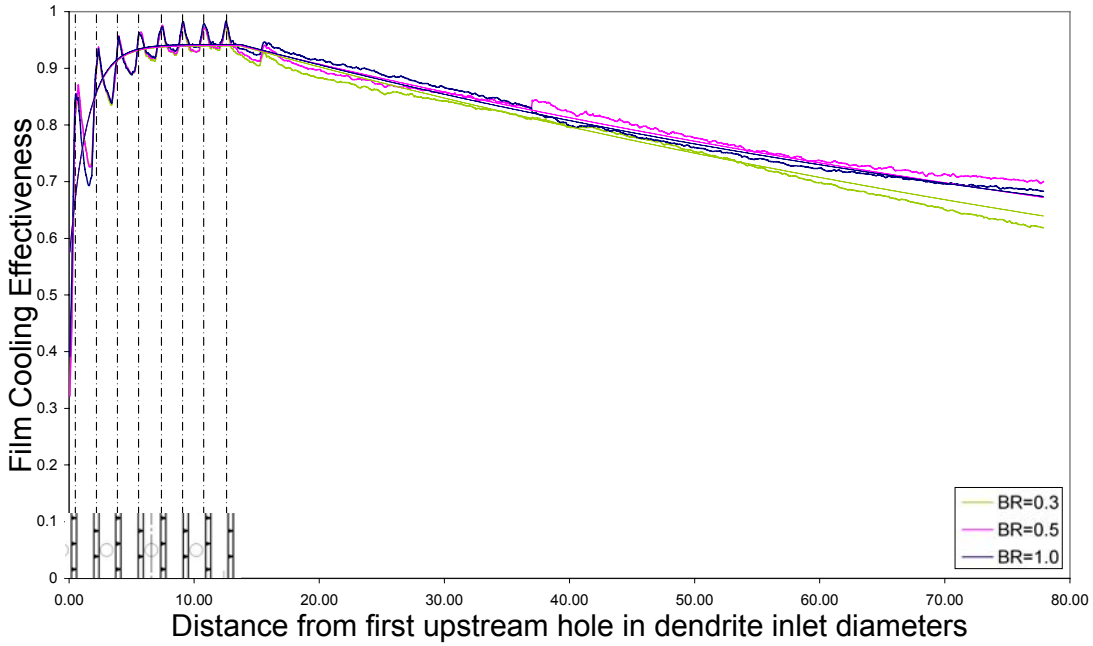


Figure 7-27: Film-cooling effectiveness data (continuous line) and exit array specific correlation (broken line) for the array of circular cross section dendrites with slot exits

7.7.4.1 Development of Upstream Correlations

From the streamwise location of the cooling hole inlets to the final row there is a steady rise in film-cooling effectiveness. It was noted that this rise in film-cooling effectiveness for all three of the configurations tested appeared to take the same form (Equation 7-11).

$$effectiveness = constant + (amplitude\ 1 + amplitude\ 2 \times BR) \times \left[1 - exp\left(\frac{-distance}{time\ constant}\right)\right]$$

Equation 7-11

distance is measured in inlet hole diameters from the upstream edge of the first row of cooling hole exits, and the *constant* is the spanwise averaged value of film-cooling effectiveness at this point.

time constant in this equation actually determines how sensitive the rise is to the distance from the initial point of injection. The maximum effectiveness is determined by the two *amplitude* terms. Clearly *Amplitude 2* is proportional to the blowing ratio.

Parameter	Cooling Hole Type		
	Straight	Circular Dendrite	Slot Dendrite
Constant	0.067	0.163	0.558
Time Constant	11.872	5.378	1.442
Amplitude 1	1.227	0.714	0.380
Amplitude 2	-0.181	0.048	0.004

Table 7-4: Summary of constants

The values assigned to these parameters following least squares regression of the data using Microsoft Excel is shown in (Table 7-4). It can be seen that the film-effectiveness is a very weak function of blowing ratio.

7.7.4.2 Development of Downstream Correlations

A more complicated function was needed to characterise the downstream downstream film behaviour. The region of film considered for the downstream behaviour consists of that immediately after the last row of cooling hole exits, where the film is no longer supplemented with coolant and the effectiveness diminishes with streamwise direction.

In the case of the straight cooling holes and the dendritic passages with circular cross section the same general correlation could be applied to the downstream film generated in both cases (Equation 7-12).

$$effective\,ness = \left(final\ \ upstream\ \ eff - (amplitude\ \ constan\,t + amplitude\ \ ramp \times BR)\right) \times \ldots$$

$$\ldots \left(exp \frac{-distance}{\left(time\ \ constant + time\ constant\ ramp \times BR\right)} \right) + \left(amplitude\ \ constan\,t + amplitude \times BR\right)$$

Equation 7-12

The distance term is measured from the downstream edge of the final hole and again the unit is dendritic system inlet diameters. The 'final upstream effectiveness' gives the value of the film-cooling effectiveness where $distance = 0$. The denominator of the exponential term allows the variation in

decay rate with blowing ratio to be modelled. The equation describing the downstream behaviour of the film generated by the dendritic geometry with a slot exit was modified from Equation 7-12 to take account of the plateauing film-cooling effectiveness at blowing ratios above 0.6 and a continuingly diminishing level with streamwise distance. The correlation used to describe this behaviour is set out in Equation 7-13.

$$effectiveness = \left(final\ \ upstream\ \ eff\ - (amplitude\ \ constant + amplitude\ \ ramp \times BR)\right) * \ldots$$

$$\ldots\left(exp\ \frac{-distance}{\left(time\ \ constant + time\ constant\ ramp\ * BR\right)}\right) + \left(amplitude\ \ constant + amplitude\ * BR\right) \ldots$$

$$\ldots + \left(final\ \ upstream\ \ eff\ - (amplitude\ \ constant + amplitude\ \ ramp \times BR)\right) * \ldots$$

$$\ldots\left(exp\ \frac{-distance}{\left(time\ \ constant + time\ constant\ ramp\ * BR\right)}\right) * amplitude\ \ constant\ 3 * \left(BR\ cutoff\ - BR\right) * distance$$

Equation 7-13

Here it can be seen that the first part of the correlation is identical to that described above; the second part, from line 3 onwards, acts to further reduce the predicted value of the film-cooling effectiveness. The second part again relies on using the same form as the first part but now uses a 3rd amplitude constant in combination with extent to which the blowing ratio was below the cut off limit (0.6) multiplied by the downstream distance to control the extent of the further reduction in film-cooling effectiveness.

7.8 Flow Visualisation of Cooling Films

7.8.1 Introduction

Having conducted the flat plate heat transfer experiments it could be seen that there was what appeared to be some unexplainable behaviour of the film; whilst

the film appeared to perform well downstream its upstream performance immediately around the hole exits seemed questionable. Qualitative flow visualisation tests was undertaken using sublimation of solid CO_2 in hot water to produce a seeded coolant fog to gain better insight into the behaviour of the films.

An experiment and was designed and a test facility built to create the fog and deliver it to the dendrite inlets. The ratio of CO_2 to water as well as the form (pellet or slab) of the CO_2 was used to determine the density of the fog produced. Warm water was used to accelerate the reaction and increase the rate of fog production (Sargison et al. *2005*). The method was based upon that used by Mann *2002* / Sargison *2003* and optimised for this situation. In this previous work a smaller array of exits was tested. This meant that the requirement for fog in this new experiment would be much greater.

7.8.2 Experimental Modifications and Method

In the previous experiments the flow rate was restricted because not enough fog could be generated. It is understood the restriction was because at higher flow rates the coolant wasn't able to mix with the fog successfully. In order to address this issue an in line CO_2 – water – air mixer was designed that could better promote a more complete mixing process. This consisted of a box, in line with the coolant feed, with internal baffles to promote mixing of air with the generated fog see Figure 7-28. The box (capacity approximately 1.5 litres) was filled from above with CO_2 granules (~10mm diameter) and the entrance was sealed. The mixer was designed such that the hot water could quickly be introduced into the box using a gravity feed at the beginning of the experiments

to maximise the fog density. Care was taken to ensure that the box was dry between tests.

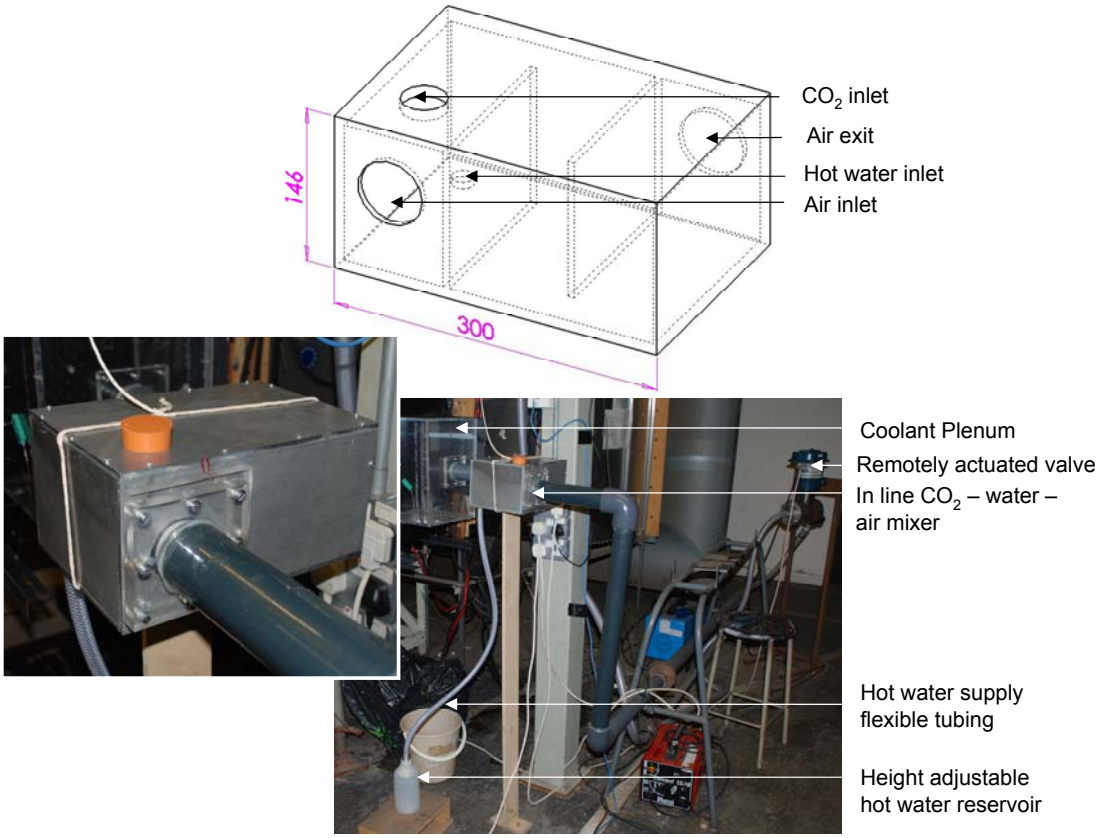


Figure 7-28: Overview of experimental set up

The wind tunnel was run with the 3 flat test specimens installed at a single operating speed, but with blowing ratios of 0.3, 0.45, 0.5 and 0.6. These were set before the introduction of CO_2 to the test rig. The patterns formed by the exiting films were captured using a digital SLR camera and a separate, remotely operated flash.

The coolant plenum temperature was monitored during the injection of fog into the system: temperature rises of about 12 Kelvin were seen which were considered insignificant for these qualitative tests. It was also considered

unnecessary to account for the change in the fluid's density due to the presence of water vapour as this was a small mass fraction of the overall flow rate.

For each blowing ratio and cooling hole configuration the test was repeated up to 10 times to ensure that the images presented in this work were indicative of the flow behaviour under those conditions.

In order to facilitate the viewing of the flow in relation to the hole exits and to see how far downstream the film continued all the edges of the hole exits were highlighted using white paint and a grid with graduations at 20mm intervals was marked on the centre line of the wall downstream of the plate as shown in Figure 7-29. Note that a side view is available because of the installation of a 45° mirror inside the tunnel. As with previous experiments good lighting and elimination of reflections was key to obtaining a good result.

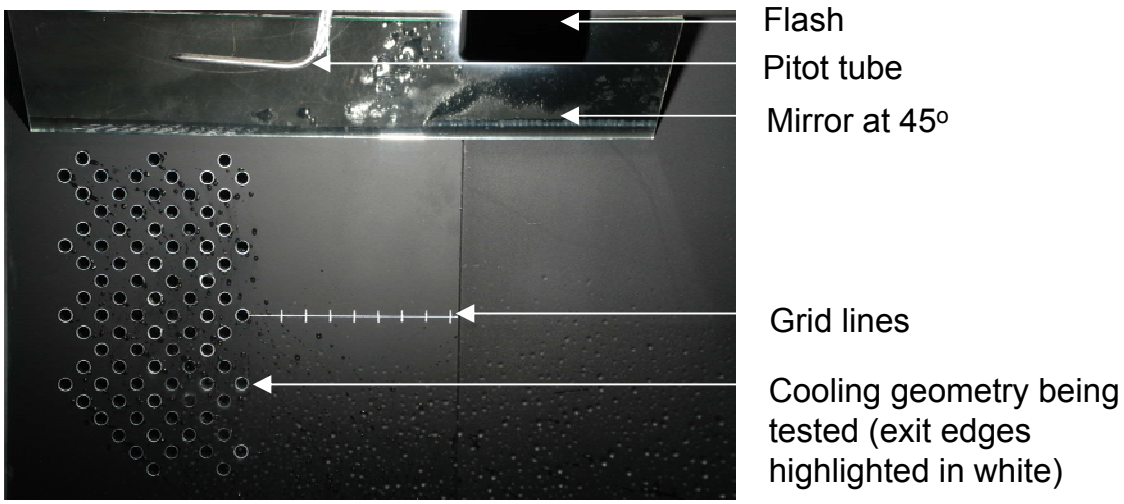


Figure 7-29: Experimental test section

7.8.3 Results

The flow visualisation results are split into two sections; that detailing the film surface distribution (7.8.3.1) and that detailing the film profile (7.8.3.2). A representative set of original pictures are detailed in Appendix H

7.8.3.1 Film Surface Distribution

In the film surface distribution results the series of pictures look in a plane parallel to the surface. This gives a better indication of the film performance in terms of spanwise coverage and how evenly the film is distributed over the surface. The black line denotes the last row of film cooling hole exits in a downstream direction.

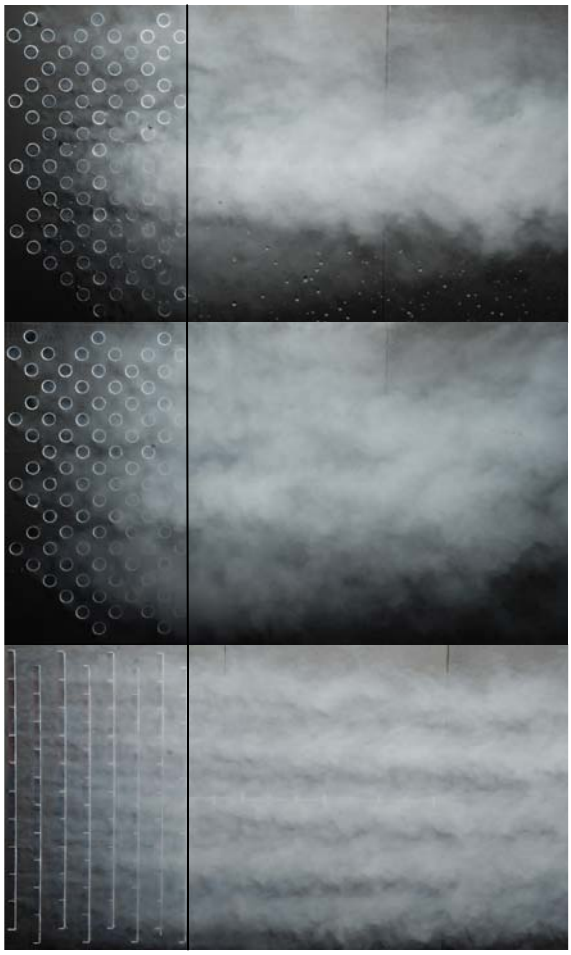


Figure 7-30: Summary of film surface distributions for the 3 different cooling geometry arrays at a blowing ratio of 0.3

7.8.3.1.1 Straight Cooling Holes

On completion of the testing of the straight cooling hole array it was immediately clear that coolant flow through the array wasn't evenly distributed and that there was a higher flow rate passing through the centre of the array. In order to try and obtain a more representative set of results the tests were repeated but this time using a fine mesh inserted across the entire cross section of the coolant plenum to better distribute the flow across the array of hole exits. The use of this mesh had mixed results and whilst the problem of even flow distribution wasn't entirely eliminated it was reduced.

7.8.3.1.2 Dendrite with Circular Cross Section

The film surface distribution for the array of dendrites with circular cross section is more even than that generated by the array of straight cooling holes. This confirms that extra blockage is helpful in generating an even film distribution. It is apparent that the spanwise coverage of the film is reduced with distance downstream from the cooling hole exits; it is also seems that there is dissipation of the film at the extremes of the spanwise coverage at lower blowing ratios.

7.8.3.1.3 Slot Exit Dendrite

It is clear that whilst the coolant film is distributed over the entire span of the cooling array there are distinct regions of higher and lower film density. It can also be seen that the regions of high film density align in spanwise coordinate with entrance to each dendritic system. While this clearly suggests some flow bias, and is possibly a result of the rapidly increasing open area in the internal passages of the system, it could easily be overcome by staggering the spanwise location of the entrance to each system on a row by row basis. While

apparent in the film-cooling effectiveness measurements very near the hole entrance it does not appear to persist downstream.

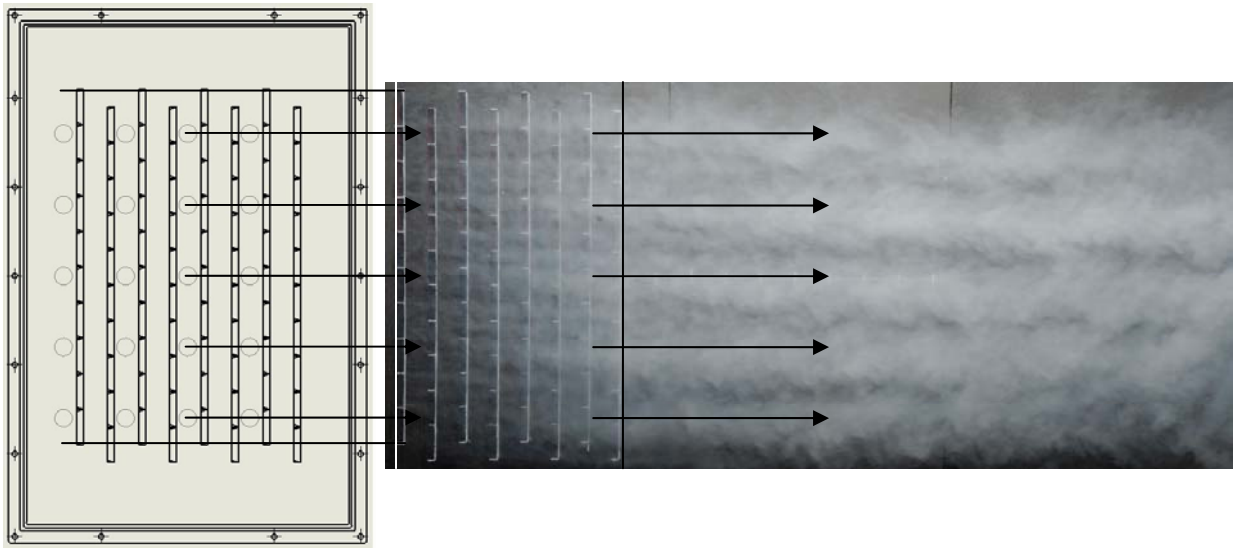


Figure 7-31: Film features and their alignment with the inlets of an array of dendrites with slot exits

Figure 7-31 shows the cooling system's entrances superimposed on the cooling array exit pattern. It can be seen that the horizontal regions of high film density correspond to the vertical location of the entrances of the cooling holes feeding the array.

On first inspection of Figure 7-30 it appears that the absence of these streaks would indicate the presence of a highly uniform well developed film. However, from the results of experiments earlier in this chapter this is known not to be the case and that the dendritic geometry with slot exit produces the superior film. It is speculated that in the case of the straight film cooling holes the lack of streaking can be accounted for by the greater amount of mixing which takes place between the coolant flow and the mainstream. Conversely because of the well behaved film which remains in close proximity to the surface produced

by the slot exit dendritic array there is little scope for spanwise movement other than through the expansion afforded by the area ruled expansion of the slot at the hole exit.

Of particular note with the array of slot exit dendrites is the uniform spanwise coverage which continues for the extent of the working section and shows no degradation of film at its edges. This is contrary to that of the geometry with circular cross section where there is clear degradation at the film's edges.

7.8.3.2 Film Profile

In all of film profile results set out below the series of pictures are looking in a plane perpendicular to the surface. This gives a better indication of the film performance in terms of its thickness and its tendency to remain on the surface. The white line in each picture denotes the first cooling exit and the black line denotes the last in a downstream direction.

7.8.3.2.1 Straight Cooling Holes



Figure 7-32: The film profile for an array of straight film-cooling holes (with a mesh fitted in the coolant plenum)

At all 4 blowing ratios the film rapidly increases in thickness to mix with the mainstream. This is particularly evident at higher blowing ratios where the coolant has mixed with the mainstream to such an extent that it starts to break away from the surface as it moves downstream. Of particular note is the lift off from the surface at the downstream extent of the working section at the highest blowing ratio. Such lift of would result in significant reduction in the film-cooling effectiveness in this region.

7.8.3.2.2 Dendrite with Circular Cross Section

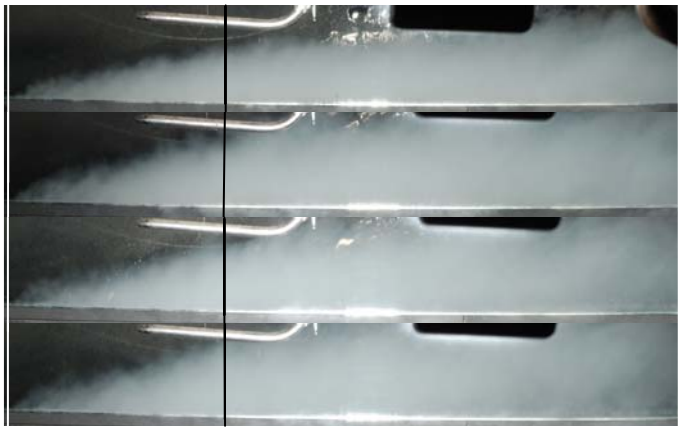


Figure 7-33: The film profile for an array of circular cross section dendritic film-cooling holes

With this setup the cooling film is more controlled with a less rapid increase in film thickness with blowing ratio, there is however still an increase in film thickness with blowing ratio. The cooling film remains closer to the surface throughout the working section and has less interaction with mainstream than in the case of the straight cooling holes. This interaction of the film with the mainstream flow, and therefore the film thickness, will result in a reduction of the film-cooling effectiveness due to the proximity of the diluted mainstream to the surface.

7.8.3.2.3 Slot Exit Dendrite

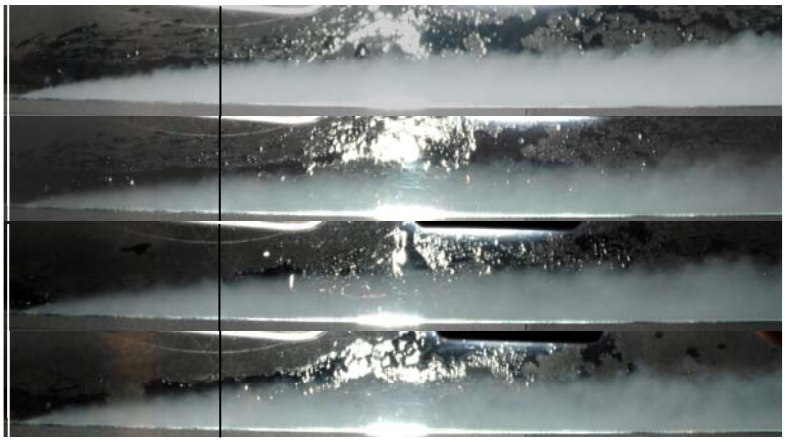


Figure 7-34: The film profile for an array of circular cross section dendritic film-cooling holes with slot exits

It is clear from Figure 7-34 that there is no significant increase in film thickness with blowing ratio like with the previous cooling systems. With the higher blowing ratios however the film more quickly achieves its maximum thickness as it moves downstream. It is worth noting that the film remains attached for the entire viewable region of the working section. It is also worth noting that with this system the film has the least interaction with the mainstream flow. It is also significant that the film appears almost entirely undiluted thus maximising its film-cooling effectiveness.

7.8.4 Limitations

Whilst conducting the experiments it was hard to be consistent with how much water was added per test. In turn this led to variation in the fog density and is in part why up to 10 tests were undertaken per test condition. However, it must be appreciated that the flow visualisation experiments were only ever intended as a means of gaining a qualitative insight into the film-cooling performance of the different geometries and to ultimately allow a fuller picture of the film-cooling performance to be gained.

7.9 Chapter Summary

In this chapter a detailed study has been conducted of the external performance of dendritic geometry using three different experimental techniques. In all three cases it has been shown that both the dendritic geometries have superior performance to that of conventional straight cooling holes.

The film-cooling effectiveness characteristics are seen to be insensitive to the cross flow velocity of the wind tunnel mainstream. Furthermore the film-cooling effectiveness has been characterised for the three different geometries at a variety of blowing ratios. In doing this it has been demonstrated that the dendritic cooling geometries have superior film-cooling performance to that of conventional straight film-cooling holes. Out of the two dendritic arrays studied in this work it has been shown that the film-cooling performance of the dendrite with the slot exit has substantially better performance, particularly in the downstream portion of the working section where internal cooling may be absent. It has also been shown that the characteristics of the film-cooling performance change dependent upon the blowing ratio. A row by row superposition model can accurately be used to predict the film-cooling effectiveness behaviour of each dendritic array.

The data obtained from these experiments are used in the cooling model presented in the following chapter. While the experiments were carried out on flat plates in the absence of pressure gradients they are considered to be sufficiently representative to allow meaningful heat transfer predictions to be made.

Chapter 8 Preliminary Design Dendritic Cooling Model

In this chapter the development of a *Preliminary Design Cooling Model* for a NGV is described. It is applied to designs for incorporation into the leading edge of a Trent 500 NGV. The hole diameters used in the model for assessment of performance of dendritic schemes relate to those achieved in manufactured prototype leading edges (dendritric inserts), one of which has been tested in the Osney laboratory by a co-worker (see chapter 9).

8.1 Introduction

In the construction of a *Preliminary Design Cooling Model* for a NGV a combination of experimental data and theory is used to describe the thermal behaviour of the wall. Using the results from the experiments reported in Chapter 6 and Chapter 7, the key performance parameters can be accurately estimated for different cooling schemes. The basic premise of the model is that the wall is locally isothermal (between cooling features), being a development of the standard blade model of Holland and Thake (*1980*). Three cooling configurations are compared: a current engine build NGV, an NGV with an array of circular hole dendritic systems in 1-2 configuration and an NGV with an array of slot exit dendritic systems also designed solely with a 1-2 configuration. The CAD models described in Chapter 4 (4.4.2 and 4.4.3) were used to provide geometric data in the analysis below.

The model establishes key parameters about the cooling system's characteristics. These are

(i) vane metal temperature, $T_{w,}$ the uniform local temperature of the vane wall;

(ii) vane metal effectiveness, $\varepsilon_b = \frac{T_m - T_w}{T_m - T_{ci}}$ Equation 8-1, where T_m is the mainstream temperature of the gas passing through the engine, and T_{ci} is the temperature of the coolant entering the film-cooling hole;

(iii) convective cooling efficiency, $\eta_{cc} = \frac{T_{ce} - T_{ci}}{T_w - T_{ci}}$ Equation 8-2, where T_{ce} is the temperature of the coolant exiting the film-cooling hole;

(iv) overall cooling efficiency, $\eta_{oc} = \frac{T_{ce} - T_{ci}}{T_m - T_{ci}}$ Equation 8-3;

(v) non-dimension cooling flow, $m^* = \frac{\dot{m} C_{pc}}{h_m AS}$ Equation 8-4, where AS is the external surface area of the component's surface that is being served by mass flow rate $\dot{m}$ of coolant air supplied through the cooling features in question (one or more film-cooling holes or dendritic systems). C_{pc} is the specific heat capacity of the coolant air (this is assumed to remain constant) and h_m is the heat transfer coefficient between the vane surface and the mainstream gas passing over the surface.

The only data comparable with the results of the modelling are those of the metal effectiveness tests carried out in the Oxford Sector Rig (see Chapter 9) for the baseline and circular dendritic design. To make a comparison with those data the model has been applied to a region of the vane ranging from 30% axial chord on the suction side through the stagnation region to 40% axial chord on the pressure side (Figure 8-1). A comparison is also made for the entire blade in the vicinity of the stagnation point.

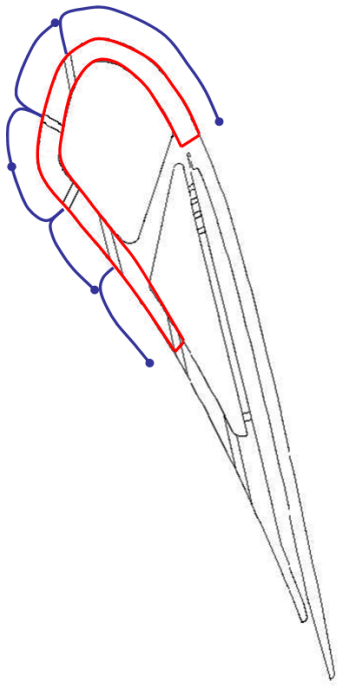


Figure 8-1: A mid-span section through the Trent 500 *NGV* wall showing the axial extent of the blade used for the *m vs effectiveness comparison and the attribution of external surface area served by each row of film-cooling holes. (NB. The blue lines in the figure indicate the *area served* by each hole, not necessarily the direction of flow)**

8.2 Local Variables

A Trent 500 NGV of the build standard described in Appendix F was used as the baseline test geometry for this study. From data provided by Rolls-Royce the local feed pressure and temperature inside the vane, external Mach number, static pressure and blowing ratio at the exit of each row of holes in an existing design Trent 500 NGV were found. Whilst these data could be used directly when estimating the flow and heat transfer parameters of the original Trent 500 leading edge with conventional straight cooling passages, it was necessary to obtain data at locations which fell between those available for the dendritic inserts. Using surface distance as a means of interpolating the values for the locations between original rows allowed calculation of pressures, temperatures and Mach numbers at these new locations.

8.3 Coolant Flow Rates

An early step in modelling heat transfer behaviour is to find the estimated coolant mass flow rate for different cooling system configurations. The work outlined in 6.2 was used for this purpose; the discharge coefficient for each row of dendritic holes being found using the correlations developed therein. As the discharge coefficient correlation is dependent on the exit blowing ratio and inlet Reynolds number, this stage of the model is iterative, with an initial estimate being found assuming isentropic compressible flow. Convergence is fast, and a solution is considered to have been found when the solution changes by less than 0.001% of the output velocity.

For the original Trent 500 conventional straight cooling passages the discharge coefficients at engine conditions were already known and the flow distribution was obtained simply by estimating the ideal velocity for the row in question using compressible flow theory and applying the appropriate discharge coefficient.

8.4 Nusselt Number Calculations

Having established the velocity field through the system it was then necessary to calculate internal heat transfer coefficient distributions. For dendritic geometries the correlation in 6.1 was used to obtain the Nusselt number in each dendritic branch based on the Reynolds number at the entrance to that branch (Equation 6-1). Note that no correction is made to the Reynolds number to account for the heat pick up through the holes, as the change in viscosity is low through the system ($\mathrm{Re} = \frac{4\dot{m}}{\pi\mu d} = \mathrm{fn}(\mu)$). The heat transfer coefficient for that

section is then calculated from the Nusselt number, and the local gas conductivity.

In the case of the existing Trent 500 straight hole cooling passage design the Nusselt number was calculated using a modified version of the Sieder-Tate (Sieder-Tate*, 1936*) relationship (Equation 8-5). This takes accounts of the roughness of the wall; enhancement because of an entry effect; and the reduced influence of the roughness enhancement in the entrance region.

$$Nu = \underbrace{\underbrace{1.3}_{Entry\ Effect}\ \underbrace{(0.8 \times 1.2)}_{Roughness\ Effects}\ 0.27 Re^{0.8}\ Pr^{1/3}\left(\frac{\mu}{\mu_{wall}}\right)^{0.14}}_{Sieder-Tate}.$$

Equation 8-5 (Sieder and Tate, *1936*)

8.5 Surface Areas

Heat is removed from the vane primarily through the internal wetted area of a cooling feature, while heat enters the vane through the external surface. For a particular row of cooling holes an external area must be assigned. It is then essentially the balance of heat transfer coefficient area product between the heated and cooled surfaces which determines the temperature of the vane section in steady state. The external area served can be found and attributed to the cooling hole rows from the location of each set of cooling rows. For the three cooling designs considered the locations of the rows of holes are shown in Figure 8-2 and set out in Table 8-1, Table 8-2 and Table 8-3.

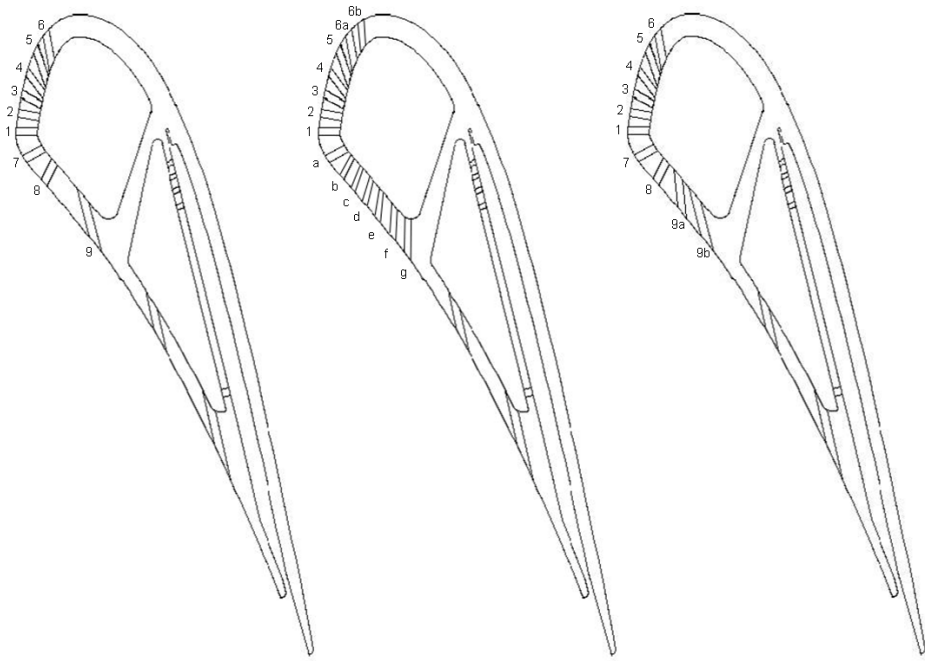


Figure 8-2: Hole location and row naming convention for the original straight cooling rows (left), the 1-2 dendritic geometry with circular cross section (centre) and the 1-2 dendritic geometry with slot exits (right)

The approximate area served by each row is the product of a line joining the point at which the holes break out on to the surface up to the break out point of the next row multiplied by the local spanwise pitch of the holes. The exceptions to this are the first and last rows on each surface. In the case of the first set of rows the area served is from the stagnation point to the break out point of the next row, while for the last set of rows the area served continues to furthest point axially downstream. These are indicated schematically on Figure 8-1. The final values are found on a row by row basis using the product of local surface length and the blade span, correcting these for the breakout area of the film-cooling holes.

The breakout area of the cooling holes reduces the total area requiring cooling; the extent to which the area will change will depend upon the cooling scheme, but may be very significant. In the case of the dendritic geometries the

calculation of the change in external area was trivial, and available from a CAD model. In the case of the baseline Trent 500 geometry a bespoke CAD model was generated from existing industrial drawings, and the surface area of each breakout hole was found. This was done on a row by row basis with the average of three holes being used to give the representative surface area breakout for a hole in a given row. The average of the holes at either end of the span and one in the centre were used for this purpose.

The estimate of the internal surface area of the passages was made from CAD models on a row by row basis. For the dendritic geometries the internal area of the passages at the extremes of the span and in the centre were averaged to give a representative surface area for each row. In the case of the conventional Trent 500 geometry the only CAD geometry available was that with 5 rows of holes in the suction surface region of the leading edge. However, the geometry of row 5 is similar to that of row 6: they both had a '3-into-1' drilled hole configuration and because their locations around the vane were close to one another it was assumed the internal wetted area found for row 5 could be used for row 6. A similar method to that used for the dendritic geometry was used to calculate the internal area on a row by row basis.

The final internal wetted areas and respective external areas served by each row of holes are shown in Table 8-1, Table 8-2 and Table 8-3.

8.6 CAD Geometry and Real Prototype Geometry

The dimensions detailed for the dendritic geometry in this chapter have been found using the CAD models of the designs. However, to allow model validation a decision was made to match as closely as possible the dimensions

used in these tests to those of the prototypes developed for testing by Mr. S. Luque at Oxford.

Due to the variability and inaccuracies of the manufacturing method employed the dimensions specified for the direct metal laser sintering were consistently larger than those obtained in the real geometry. In order to quantify this variation a trial test piece was sectioned along a spanwise centre line and subsequently repeatedly skimmed by a further 0.1mm across this face. This skimming process was repeated 25 times. After each operation a digital photograph was taken in order to build up a 3D image of the geometry and size of the passages intersected by the cut. An example of the data obtained is detailed in Figure 8-3. Using these data it was possible to estimate the hole diameter and hence the required hole geometry scale factor to be 0.83. Note the external geometry was accurately manufactured.

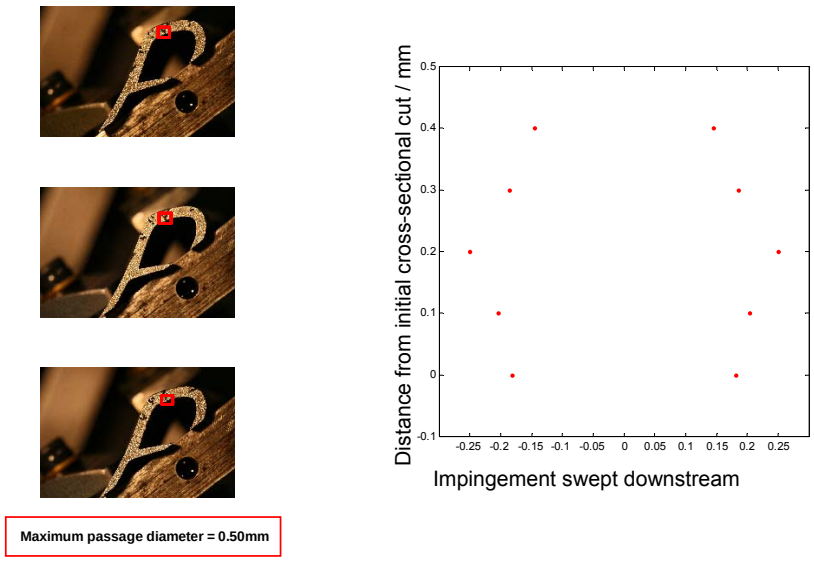


Figure 8-3: An example of the data used to obtain the geometry scaling factor. The three images represent the first, middle and last images in the series used to generate the passage profile detailed on the right (dimensions in mm)

8.7 Cooling System Characteristics

In order to calculate the amount of heat transferred to the vane from the flow around the NGV it is necessary to know both the heat transfer coefficient and film-cooling effectiveness around its surface. This is dependent upon the film characteristics of the cooling scheme being used. The distributions of these two parameters used for the different geometries are shown in Figure 8-5 and Figure 8-6. Single values are used over each discrete area served and this is reflected by the series of horizontal lines plotted.

For easiest prediction of the baseline heat transfer coefficient in the windtunnel, testing would have been conducted using a sharp edged plate with a boundary layer bleed and known trip. This would have allowed the starting point and nature of the boundary layer to be accurately predicted. Rather, a wind tunnel in which there is an inlet contraction followed by a flow restriction in the form of the mesh heater followed by an upstream length (of 200mm) of constant cross section passage prior to the first row of exits from the array was used. This made the application of the absolute values of measured heat transfer coefficient distribution to the NGV unfeasible, however, as the baseline conditions are identical between the slot and circular exit cases, their relative value were superimposed on a reliable reference condition. Suitable data were generated by Eckert (*1983*), who studied an array very similar in configuration to that used in the current study, consisting of 11 rows of circular cross section full coverage film cooling holes. For the circular holed dendritic exit array, the level of the average heat transfer coefficient enhancement above that expected for a turbulent boundary layer on a flat plate was scaled from experimental results to match that seen by Eckert. This enhancement factor ($h / h_{\text{flat plate}}$)

distribution was then superimposed on the uncooled idealised heat transfer coefficient distribution described below to create the cooled external heat transfer coefficient distribution in the presence of cooling. For the slot exit dendritic array, the heat transfer coefficient enhancement factor distribution was scaled using the ratio of the average heat transfer coefficients measured in the holed region between the slot and circular exit dendritic arrays. This was applied to the uncooled htc distribution in the same manner.

The uncooled external heat transfer coefficient distribution (Figure 8-6) is needed to allow film-cooling schemes to be applied. To this end only the Mach number distribution was available around the blade (Appendix F). This was used with a simple turbulent flat plate boundary layer correlation to estimate the heat transfer coefficient distribution over a vane under engine conditions in an uncooled condition. Note that while the uncooled blade would not be fully turbulent at the leading edge, the addition of cooling holes causes immediate transition, justifying the use of such a simplification. At the stagnation point a wedge flow solution was applied. The distribution is very similar to the cooled distribution in regions far from cooling holes.

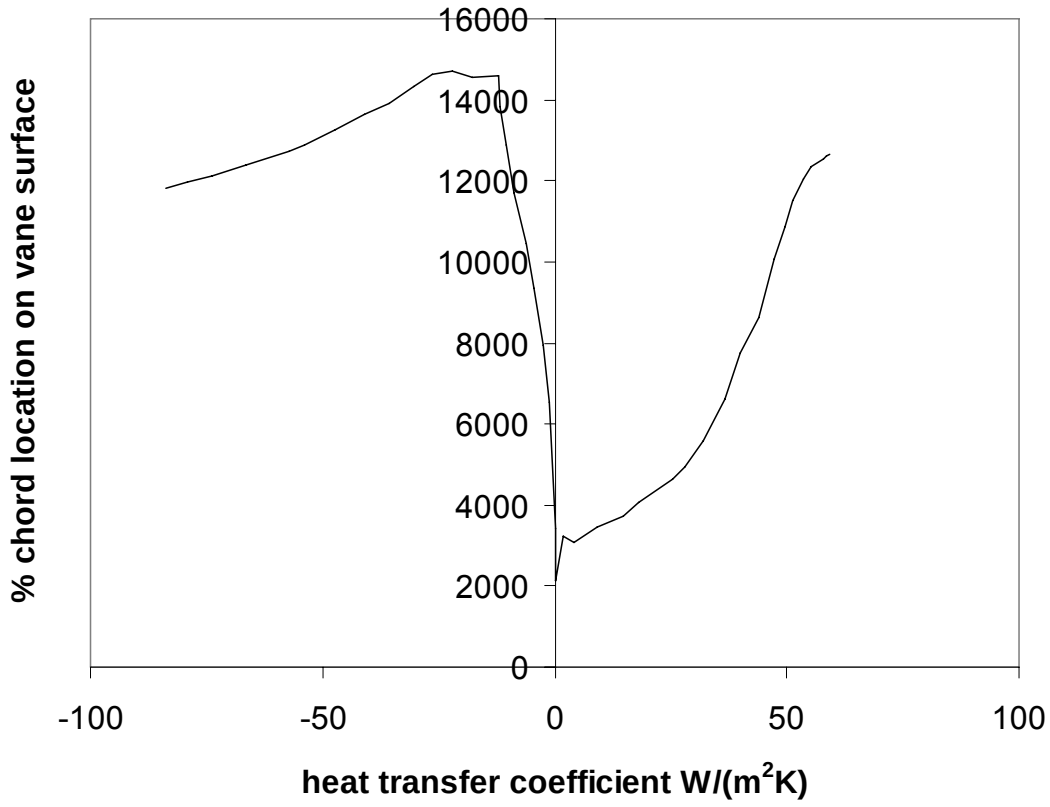


Figure 8-4: Dendritic heat transfer coefficient distribution over the vane without the presence of film cooling

These heat transfer coefficient distributions have been mapped on to the dendrtic insert's hole locations. Using data provided by Rolls Royce over the entire surface of the NGV it was possible to find the same information for the Trent 500 geometry. Figure 8-5 shows the heat transfer coefficient distribution in terms of percentage chord location on the vane surface relative to the stagnation point (based upon hole location and inlet hole diameter); again the piecewise changes in value correspond to the regions served by different rows.

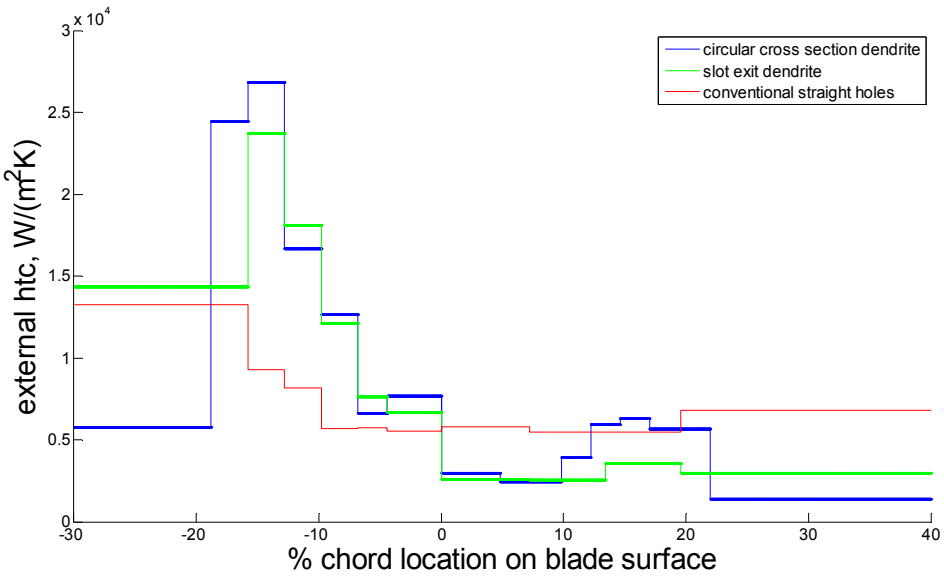


Figure 8-5: The heat transfer coefficient distribution for the three alternative cooling hole arrays mapped on to the hole locations of each geometry over the blade surface (suction surface negative, pressure surface positive)

The row by row superposition based correlation for the film effectiveness distribution (section 7.7.3) was implemented into the model as a separate function that could be called from the main model scripts. This was done in such a way because the blowing ratio was required as an input to the correlation. For any blowing ratios above 1 a blowing ratio of 1 was used in the function, such a simplification was justified because the use of dendritic geometry aims to create coolant flow with low blowing ratios, in general below this cut off. Using this correlation allowed particular array row spacing and the area served downstream of the last row of exits to be accurately accounted for. Figure 8-6 shows the film-cooling effectiveness distribution in terms of percentage location on the vane surface relative to the stagnation point (based upon hole location and inlet hole diameter).

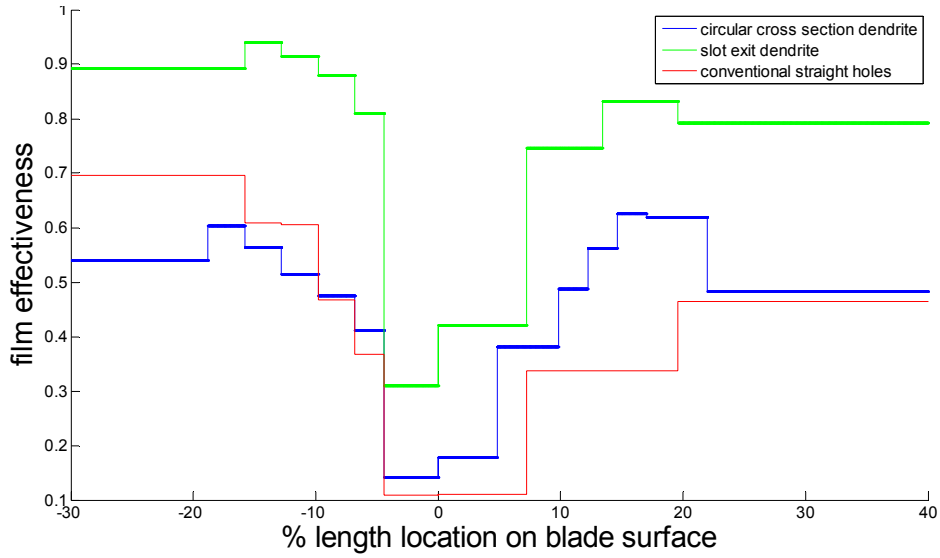


Figure 8-6: The film-cooling effectiveness distribution for the three alternative cooling hole arrays mapped on to the hole locations of each geometry over the blade surface (suction surface negative, pressure surface positive)

For the two dendritic cooling schemes it was possible to establish both the heat transfer coefficient and film-cooling effectiveness distribution over the region which each row served. These values are summarised in Table 8-2 and Table 8-3. A similar method to that used to find the heat transfer coefficient distribution for the Trent 500 geometry above was used to find representative values of the film-cooling effectiveness for the regions served by each row of cooling holes, again using data supplied by Rolls Royce, Table 8-1.

Cooling row ID	1	2	3	4	5	6	7	8	9
internal wetted area per row (m^2)	0.000217	0.000215	0.000226	0.000271	0.000282	0.000294	0.000216	0.000213	0.000251
external area served per row (m^2)	0.000203	0.000094	0.000133	0.000105	0.000095	0.000651	0.000235	0.000408	0.000691
hole diameter (m)	7.50E-04	7.50E-04	7.50E-04	7.50E-04	6.63E-04	7.50E-04	7.50E-04	7.50E-04	7.50E-04
number of passages	22	23	22	24	23	24	22	22	22
angle relative to mainstream (^{o})	91.1	75.05	61.53	46.39	45.7	51.75	99.03	71.97	24.26
external heat transfer coefficient	5534.084	5756.386	5686.617	8200.907	9292.614	13239.52	5795.089	5456.85	6823.656
film effectiveness	0.1094	0.3675	0.4667	0.6056	0.6094	0.6966	0.1107	0.337	0.4647

Table 8-1: The values attributed at each row location to the parameters used to calculate the performance of the conventional straight cooling holes in a Trent 500 at engine conditions

Cooling row ID	1	2	3	4	5	'6a'	'6b'	'a'	'b'	'c'	'd'	'e'	'f'	'g'
internal wetted area per row (m^2)	0.000165	0.000161	0.000160	0.000165	0.000164	0.000142	0.000136	0.000149	0.000147	0.000179	0.000138	0.000177	0.000134	0.000180
external area served per row (m^2)	0.000207	0.000099	0.000139	0.000138	0.000136	0.000137	0.000544	0.000155	0.000156	0.000070	0.000071	0.000071	0.000158	0.000616
hole diameter (m)	0.0007	0.0007	0.0007	0.0007	0.0007	0.0007	0.0007	0.0007	0.0007	0.0007	0.0007	0.0007	0.0007	0.0007
number of passages	18	18	18	18	18	17	17	17	18	18	17	17	16	16
angle relative to mainstream (^{o})	71.35	80.86	69.41	73.71	67.1	79.65	82.6	74.83	63.13	61.59	57.42	57.12	52.88	52.74
external heat transfer coefficient	7720.156	6662.435842	12647.85	16714.17	26869.81	24454.91	5787.162	2965.616	2479.732	3930.09954	5951.345429	6298.323085	5703.31	1391.308
film effectiveness	0.142399	0.412194587	0.474761	0.515606	0.564436	0.603857	0.540477	0.177945	0.382468	0.48767942	0.562783856	0.626572462	0.619505	0.483535

Table 8-2: The values attributed at each row location to the parameters used to calculate the performance of the 1-2 dendrtic insert with circular cross section holes at engine conditions

Cooling row ID	1	2	3	4	5	6	7	'8a'	'8b'	9
internal wetted area per row (m^2)	0.000216	0.000247	0.000279	0.000282	0.000271	0.000294	0.000218	0.000277	0.000291	0.000272
external area served per row (m^2)	0.000207	9.8E-05	0.000139	0.000138	0.000136	0.000694	0.000239	0.000199	0.000199	0.000701
hole diameter (m)	0.000728	0.000728	0.000728	0.000728	0.000728	0.000728	0.000728	0.000728	0.000728	0.000728
number of passages	25	25	24	24	23	24	24	24	23	22
angle relative to mainstream (^{o})	67.33	32.35	39.17	33.3	34.2	38.85	83.63	41.54	32.7	24.57
external heat transfer coefficient	6684.909	7652.556	12148.76	18123.43	23721.6	14341.89	2624.836	2542.647	3545.151	3002.075
film effectiveness	0.310869	0.81006	0.880065	0.914734	0.941148	0.892555	0.421769	0.746446	0.832257	0.792757

Table 8-3: The values attributed at each row location to the parameters used to calculate the performance of the 1-2 dendrtic insert with slot exits at engine conditions

8.8 Thermal Equilibrium Calculations

The *Preliminary Dendritic Cooling Model* solves three expressions which relate the energy going into and being taken away from the metal. These are in balance and the three energy terms are equal (Equation 8-6, Equation 8-7 and Equation 8-8).

$$Energy\ gain\ of\ coolant = \dot{m}_c c_{pc}\left(T_{ce} - T_{ci}\right)$$

Equation 8-6

$$Energy\ extracted\ by\ coolant = \left(hA\right)_{internal}\left(T_w - T_{ci}\right)$$

Equation 8-7

$$Energy\ input\ of\ film = \left(hA\right)_{external}\left(T_f - T_w\right)$$

Equation 8-8

The temperature difference between film and wall in Equation 8-8 can be expressed in terms of the film-cooling effectiveness, η_f, by considering the total enthalpy of the film to be the mass average of its components: the mainstream and coolant exit flows. Assuming the specific heat capacity of the coolant and mainstream to be approximately the same it is possible to write:

$$T_f = \eta_f T_{ce} + \left(1 - \eta_f\right)T_m \Rightarrow \left(T_f - T_w\right) = \eta_f\left(T_{ce} - T_w\right) + \left(1 - \eta_f\right)\left(T_m - T_w\right).$$

Equation 8-9

By then equating Equation 8-7 and Equation 8-8, but using the substitution from Equation 8-9, it is possible to express the coolant exit temperature in terms of the wall temperature (Equation 8-10).

$$T_{ce} = \left[\frac{\left(hA\right)_{internal}}{\left(hA\right)_{external}}\left(T_w - T_{ci}\right) + \left(1 - \eta_f\right)\left(T_m - T_w\right)\right]\frac{1}{\eta_f} + T_w$$

Equation 8-10

Also, by equating Equation 8-6 and Equation 8-7 another expression of coolant exit temperature is derived, again in terms of wall temperature (Equation 8-11).

$$T_{ce} = \frac{(hA)_{internal}(T_{ce} - T_w) + T_{ci}\dot{m}_c c_{pc}}{\dot{m}_c c_{pc}}$$

Equation 8-11

The wall temperature may now be expressed in terms of the known coolant inlet and mainstream temperatures and the heat transfer area products and film-cooling effectiveness:

$$T_w = \frac{T_{ci}\left[1 - \frac{(hA)_{internal}}{\dot{m}_c c_{pc}} + \frac{(hA)_{internal}}{(hA)_{external}\eta_f}\right] + T_m \left(1-\eta_f\right)/\eta_f}{\frac{(hA)_{internal}}{(hA)_{external}\eta_f} + 1/\eta_f - \frac{(hA)_{internal}}{\dot{m}_c c_{pc}}}$$

Equation 8-12

The value of the wall temperature can then be substituted back in to either Equation 8-10 or Equation 8-11 to find the coolant exit temperature.

Now all variables required to calculate the metal effectiveness, film-cooling efficiency and m^*, the non-dimensional cooling flow are available.

It should be noted there are numerous assumptions made in the development of this model: It is assumed that the heat transfer processes relating to the cooling of the vane are in a steady state condition. It is assumed the specific heat capacity of the coolant is the same as that of the mainstream. It is assumed the walls of the serpentine passage in the leading edge are adiabatic. It is assumed each film-cooling passage serves the same surface area over the leading edge. It is assumed, for the dendritic geometries, that film-cooling passages at each end of the row and in the middle are representative of the

internal surface area of the passages in that row. It is assumed the characteristics of the cooling film-cooling effectiveness and heat transfer coefficient distribution are the same for a 1-2-4 dendritic configuration as they are for a 1-2 dendritic configuration. Furthermore it is assumed that the characteristics of the distribution over a flat plate are directly comparable to the 3D surface of a NGV. This final assumption may be justified by the rapid transition to turbulent conditions on the external surface of the NGV in the presence of film-cooling.

8.9 Results

Figure 8-7 demonstrates that at the maximum take off engine conditions modelled, the non-dimensional coolant consumption (m*) for the cooling schemes of dendritic arrays at the leading edge is less than that of the conventional cooling configuration at the same location and equivalent pressure ratio across the holes. This is clearly a significant and positive outcome; both the new geometry's coolant consumption is lower than the conventional geometry's. In the case of the circular dendritic array, where the external hA product is very similar to that of the conventional system (95%), the reduction in m* is directly related to the higher loss in the cooling passages. For the slot exit dendritic array hA is increased by 11% compared to the conventional design, however, there is a dramatic 16% reduction in m*, implying a reduction of 7% in the cooling flow. This is associated with an increase in metal effectiveness in the same region of 0.14 (pressure ratio is maintained). However this comparison should not be viewed in isolation when considering the relative merits of the cooling schemes. It is also necessary to consider the vane metal effectiveness; this is a measure of the cooling performance compared to a

theoretical maximum cooling where the blade would reach the coolant inlet temperature. Once again the superior performance of the dendritic geometry is demonstrated; both the dendritic cooling schemes remove a near equivalent or larger amount of energy from the vane than the conventional geometry operating at the same pressure ratio.

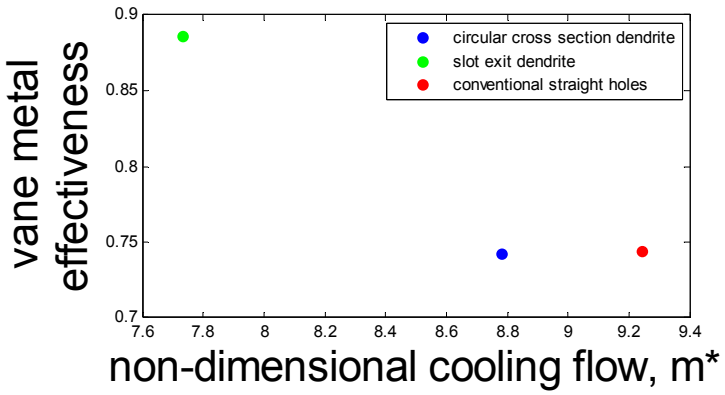


Figure 8-7: Comparative performance of the three cooling geometries

An alternative method of assessing the cooling schemes is demonstrated in Figure 8-8. Here the dendritic systems' hole diameters is incrementally adjusted in steps of approximately 0.007mm until the effectiveness is the same as that of the conventional cooling scheme. This demonstrates how the dendritic schemes could provide the same level of cooling as that of the conventional cooling scheme but with a significant reduction in coolant. As outlined in Chapter 1 any reduction in coolant consumption can ultimately result in an improvement in cycle and therefore engine efficiency. Likewise, the dendritic systems' hole diameters may be incrementally increased in steps of approximately 0.007mm until the non-dimensional cooling flow is the same as that of the conventional cooling scheme as shown by the remaining set of points in Figure 8-8. In this scenario the dendritic cooling schemes prove to be significantly more effective and would therefore result in a lower vane

temperature. This would in turn reduce the thermal loading on the vane which could be used as a cost saving opportunity through reduced service intervals or a change in material. However, this could equally be taken advantage of by increasing the turbine entry temperature, which as described in Chapter 1, would result in an increase in engine efficiency and reduced fuel consumption. It should be noted that in increasing the diameter the change in the arrays' packaging density and spacing was not accounted for, obviously any design looking to take advantage of the increase in hole diameter would have to consider such constraints. Clearly the very striking result here is the enormous reduction in coolant mass flow rate required for the slot exit dendritic scheme.

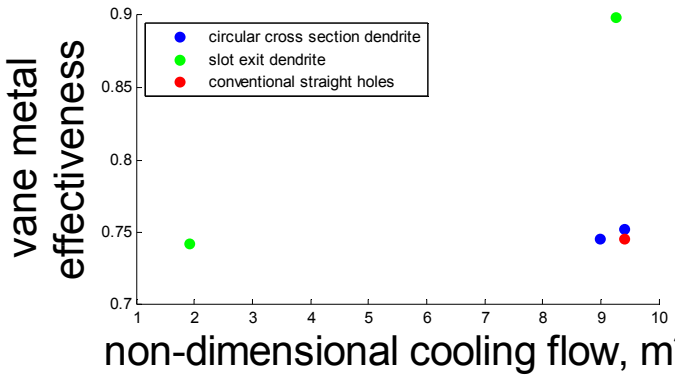


Figure 8-8: Film effectiveness and non-dimensional cooling flow for dendritic cooling schemes matched to conventional cooling geometry performance at engine conditions for the leading edge

As well as considering the entire leading edge cooling scheme array as a single entity the scheme was also considered on a row by row basis to give a distribution of the performance characteristics over the leading edge. Figure 8-9 is a row by row equivalent of Figure 8-7, where the row numbering convention is that from Figure 8-2. It can be seen that the relative magnitudes of vane metal effectiveness of the cooling schemes from Figure 8-7 are in general maintained on a row by row basis.

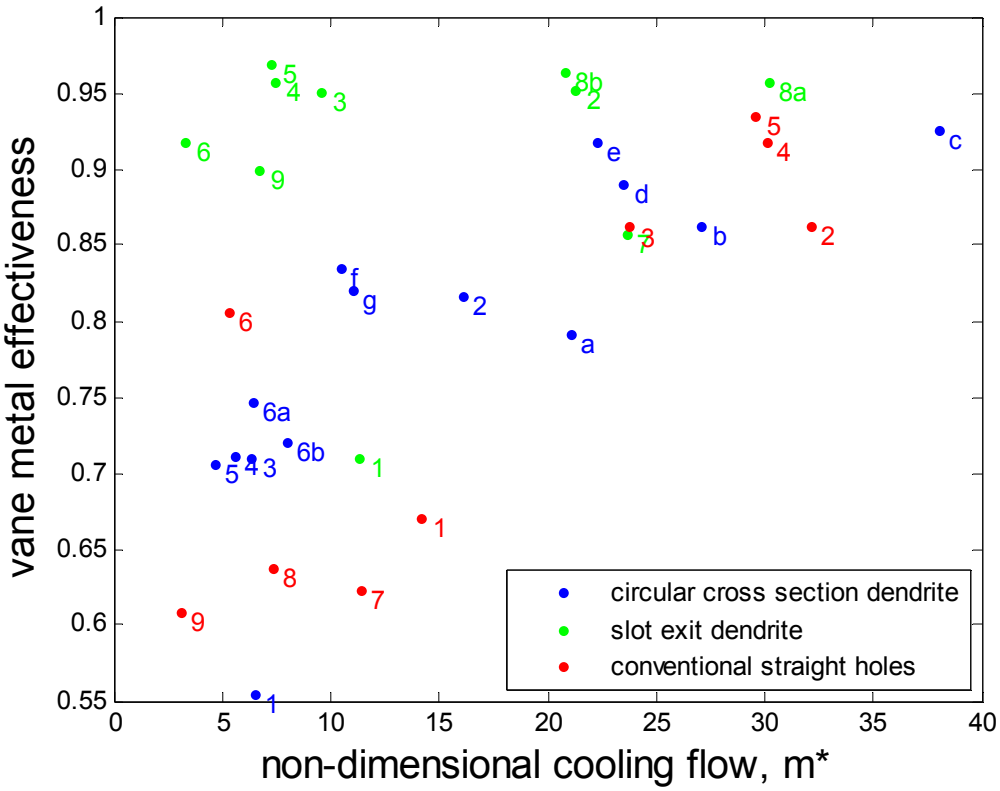


Figure 8-9: Film effectiveness and non-dimensional cooling flow on a row by row basis at engine conditions

The series of vane metal effectiveness values at each row can be translated on to a vane row surface distribution, Figure 8-10. There is a clear drop in the vane metal effectiveness of the circular cross section dendritic array cooling scheme on the suction surface relative to the conventional straight film cooling holes. This relative change in performance is seen in the engine realistic results detailed in Chapter 9, particularly in Figure 9-3. This consistency with real data adds validity to the model but also highlights a region for which further work is required to fine tune the cooling array.

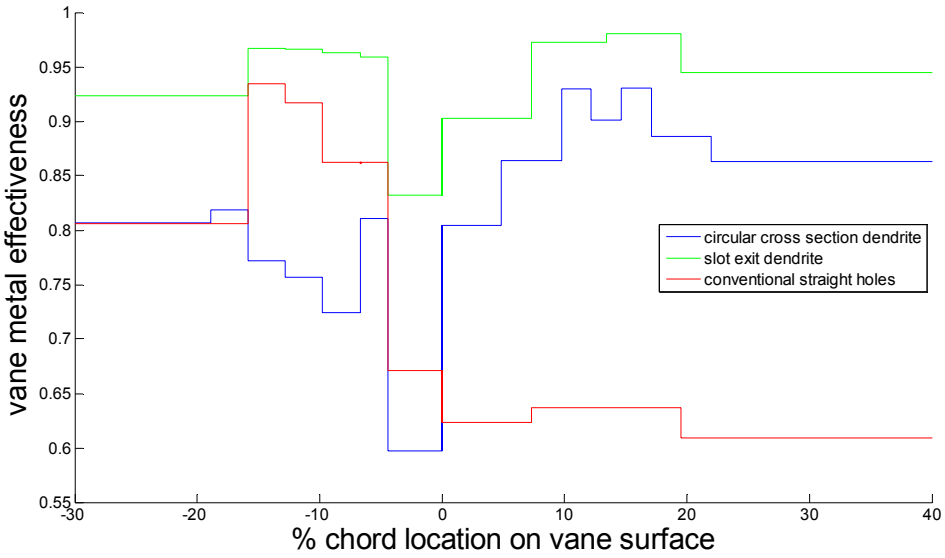


Figure 8-10: Vane metal effectiveness distribution for the three cooling arrays mapped on to the hole locations of each row over the blade surface (suction surface negative, pressure surface positive)

The model has also been able to predict the metal temperature distribution around the vane's leading edge. This is shown in Figure 8-11 from which it is clear the cooling scheme consisting of an array of dendrites with slot exits results in a consistently low vane metal temperature with significantly lower temperature gradients around the vane. Large temperature gradients are particularly bad from a structural integrity point of view and as such a design which minimises such gradients is favourable. As was indicated in the vane metal effectiveness distribution there is what appears to be a relative hot spot on the suction surface. Nevertheless, apart from this, both the dendritic cooling schemes perform better than the conventional cooling schemes: this is borne out by the reduced blade metal temperature compared to the conventional cooling scheme over the majority of the leading edge.

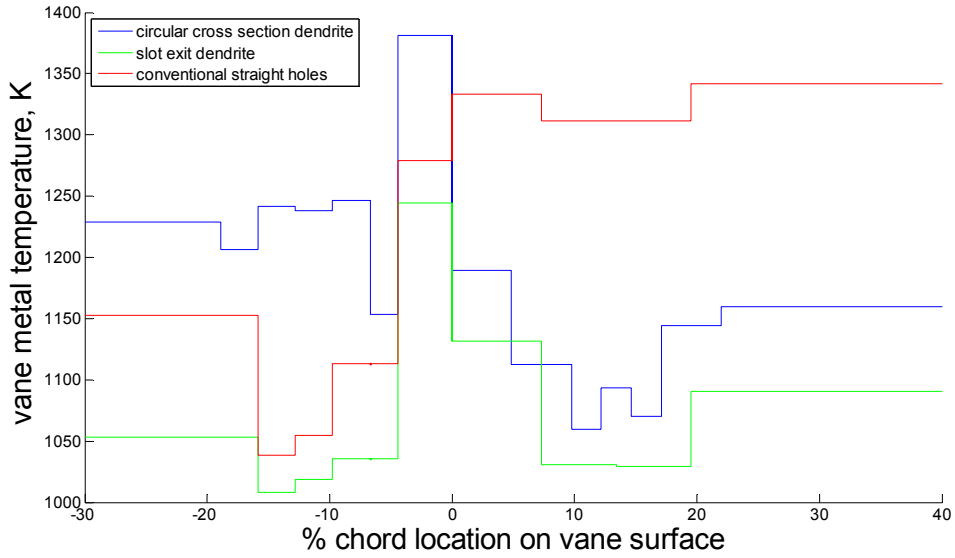


Figure 8-11: Vane metal temperature distribution for the three cooling arrays mapped on to the hole locations of each row over the blade surface (suction surface negative, pressure surface positive)

Figure 8-12 shows the variation in vane metal effectiveness with increasing mass flow rate which is driven by increasing the cooling passage diameter. The dotted lines on the graph indicate the mass flow rate conditions when the original geometry for each cooling scheme is modelled at engine operating conditions.

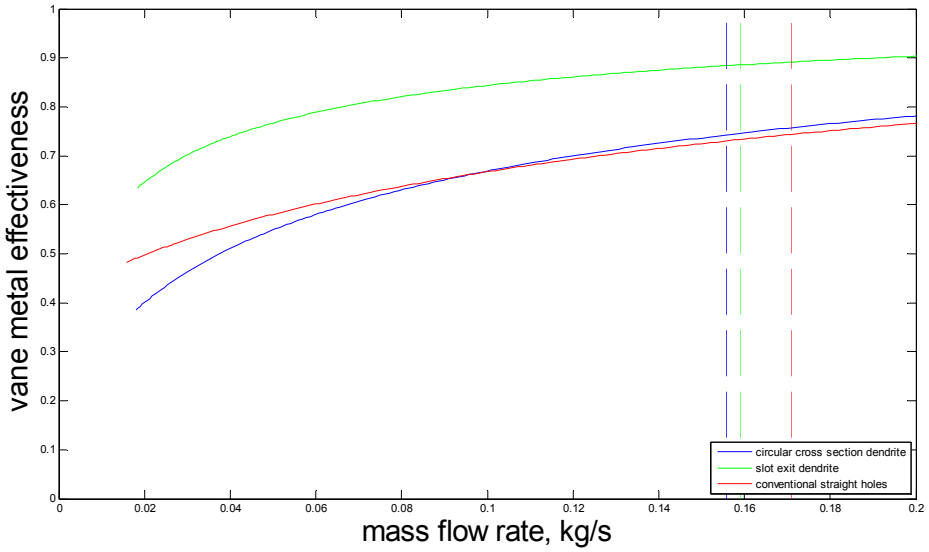


Figure 8-12: Variation in vane metal effectiveness with changing mass flow rate driven by a changing cooling hole diameter at constant pressure ratio distribution

It is clear that with the current level of mass flow rate through the leading edge (approximately 0.17kg/s) there is a significant performance gain to be taken advantage of with the adoption of dendritic geometry with a slot exit. However as the hole diameter (mass flow rate) is increased, the level of performance gain through the adoption of dendritic geometry is reduced. The reduction in performance enhancement with increasing mass flow rate is confirmed by Figure 8-13 where rather than increasing the hole diameter to achieve higher mass flow rates the pressure ratio across the dendritic geometry is increased from an engine condition level of approximately 1.07 up to two. (It should, of course, be noted that whilst it is feasible to achieve a change in mass flow rate by changing the cooling geometry such an increase in pressure ratio would not be because of the existing upstream design constraints.)

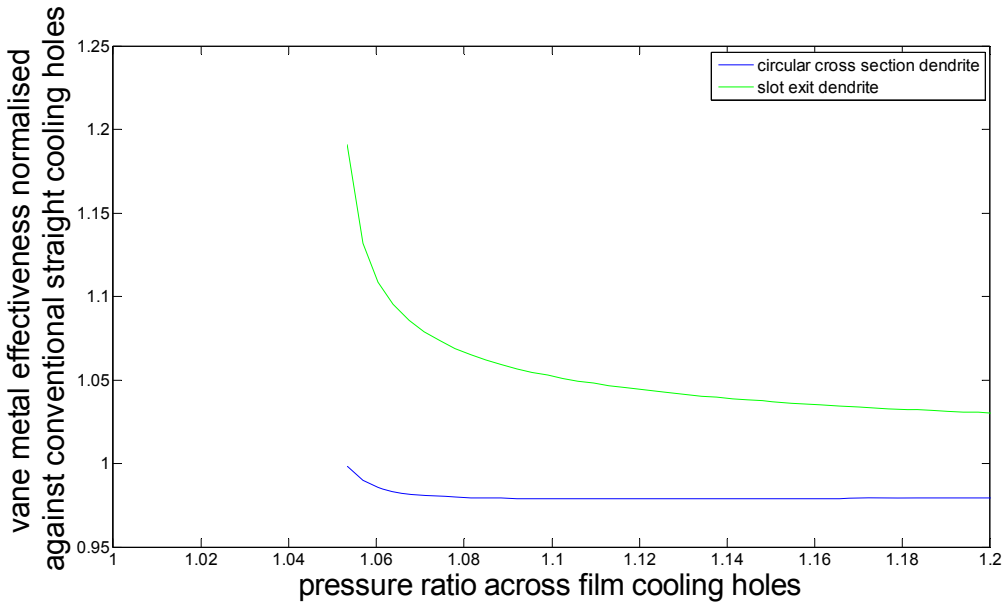


Figure 8-13: Variation in vane metal effectiveness with changing mass flow rate driven by a change in the pressure ratio across the vane wall

In order to gain a fuller picture of the real effect the adoption of a dendritic cooling system at the leading edge would have on the overall performance of an

NGV the model was extended. In order to do this certain assumptions had to be made about the *NGV* geometry and the crucial parameters used to calculate the performance. It was assumed that the remaining rows around the leading edge would be straight holes exactly like those in the Trent 500 configuration. The film-cooling effectiveness and heat transfer coefficient in the region of and downstream of these holes is unaffected by the dendritic geometry at the leading edge and is the same as that in the Trent 500 scenario. In the case of the final row of holes on the suction surface the value of the film-cooling effectiveness used for that portion of the vane is reduced since the deterioration of the film (from the flat plate tests) is accounted for. The value assigned to the heat transfer coefficient remains the same. For all rows area averaged values for the film-cooling effectiveness and the internal and external heat transfer coefficients are used. A cumulative value is used for the mass flow rate, which accounts for the local variation of pressure ratio across the wall at each row location.

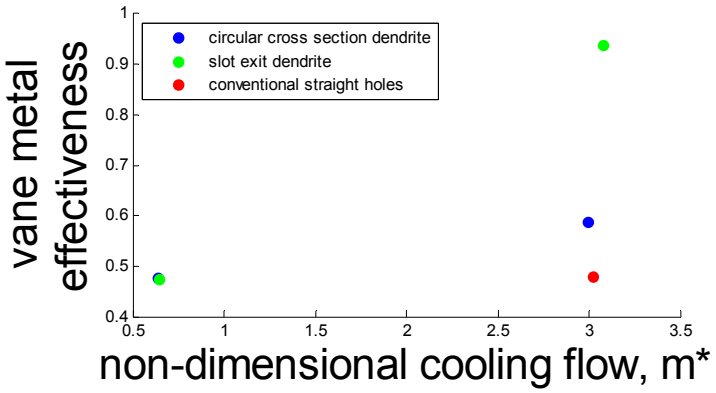


Figure 8-14: Vane metal effectiveness and non-dimensional cooling flow for dendritic cooling schemes matched to conventional cooling geometry performance at engine conditions for an entire vane

Chapter 9 Sector Rig Experiments

The Oxford Annular Sector Rig is a facility that produces results analogous to those created in an engine thermal paint test where accurate measurement of the surface distribution of steady-state metal temperature of an NGV is possible (see Luque et al. *2010*).

The facility consists of a contracting inlet duct, an annular sector of five $HP\ NGV$ passages, a downstream duct formed by the extended NGV hub and casing annuli, two three-dimensionally contoured sidewalls, an annular sector of deswirl vanes and a choke mechanism. This ensures the correct simulation of radial pressure gradients, secondary flow development, coolant flow redistribution and the combined effects of internal convective cooling, through-wall conduction and external film-cooling allowing the useful testing of engine hardware (NGVs). Importantly the mainstream Mach number, Reynolds number and coolant-to-mainstream total pressure ratio are matched to engine conditions.

Air is supplied from a high pressure reservoir at room temperature and delivered to the test section at a constant inlet pressure. Two fast response heater meshes (Gillespie, *1996*) are operated in series and are used to heat the mainstream flow with a maximum temperature rise of 33.5°C. The coolant flow is bled from upstream of the heaters and bypassed through a flow meter into the three central NGV coolant manifolds.

To allow the heat transfer measurements to be performed the surface metal temperatures are measured using IR thermography. From these steady-state

measurements metal effectiveness can be generated. The maximum absolute uncertainty is approximately 0.05. By carrying out a series of tests at different mainstream temperatures careful scaling of the results can be undertaken which allows prediction of the metal effectiveness at engine conditions (Luque, *2011*).

While the author proposed two cooling geometries for testing in the Sector facility (see Chapter 4), at the time of writing it has been possible to test only one of these. Thus there exists data for a large diameter circular cross section with single splits (Figure 9-2). This geometry was tested by S. Luque in the OUEL and compared to the current Trent 500 geometry (Figure 9-1). The results are included here with his kind permission.

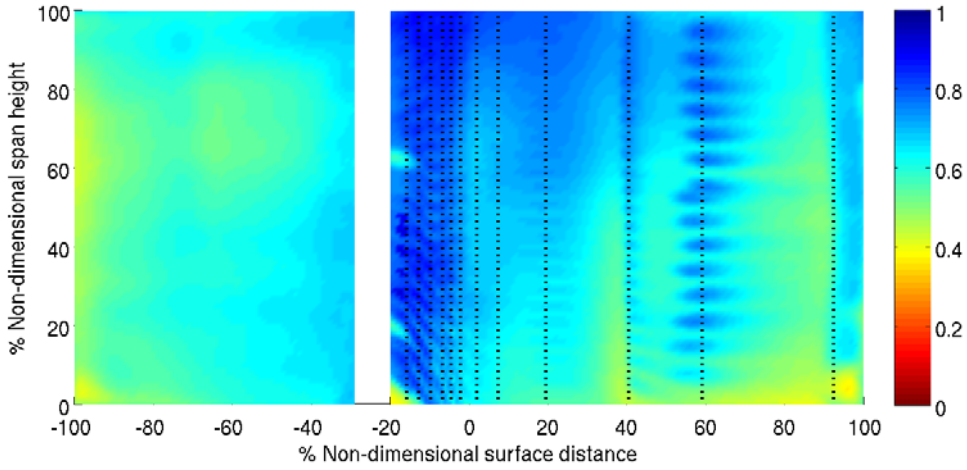


Figure 9-1: Film-cooling effectiveness distribution over the surface of a Trent 500 *NGV* using conventional film-cooling holes

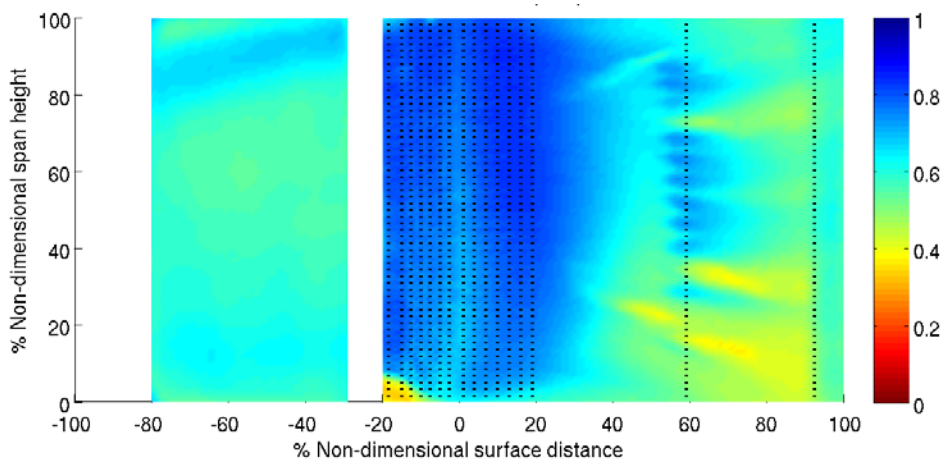


Figure 9-2: Film-cooling effectiveness distribution over the surface of a Trent 500 *NGV* using dendritic film-cooling holes

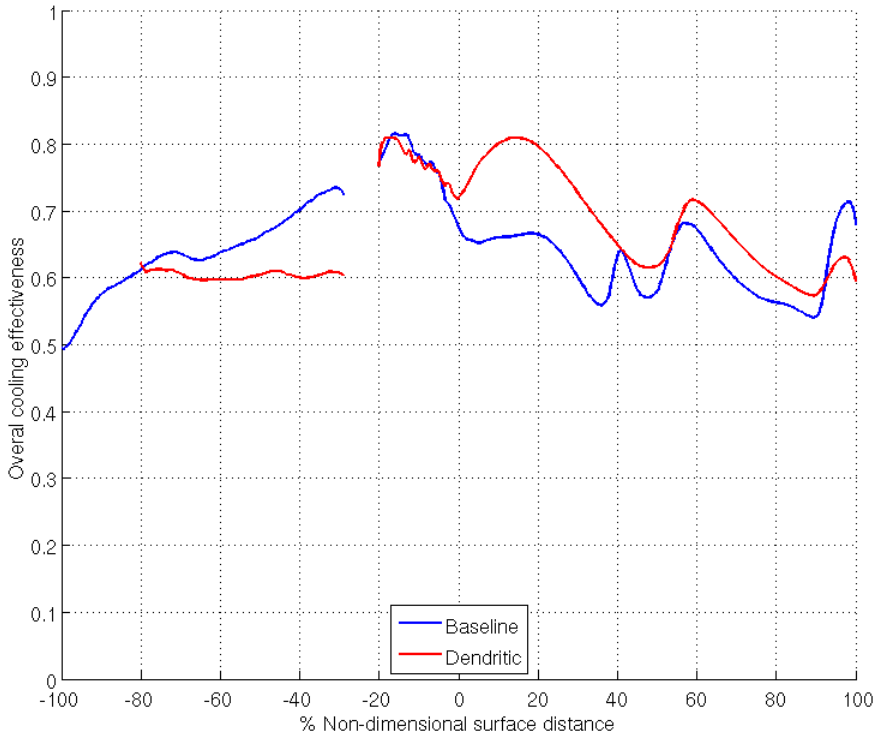


Figure 9-3: Film-cooling effectiveness in a vertical average band between 43 % and 57 % span height

Figure 9-1 and Figure 9-2 show the local metal effectiveness distribution on the outside surface of the NGVs during the steady-state part of a test run. The total mass flow rate through the dendritically cooled NGV is ~10% lower than that of

the conventionally cooled NGV in spite of the addition of 5 additional rows of holes around the leading edge. On the surface the effect of the cooling films are very clearly visible in the leading edge region. The streamwise location of the exits of each row of holes is represented by a dotted line across the span. (The inboard hot spots are a result of the absence of RIDN flows in the experiment).

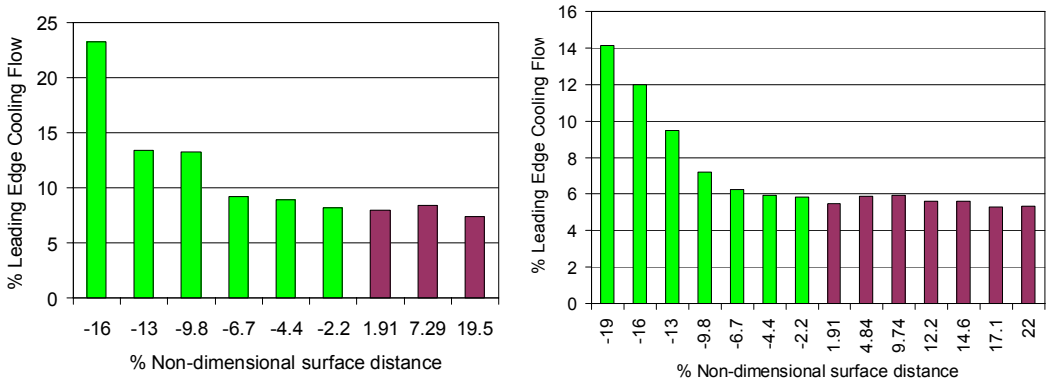
On the pressure surface ($+\,\mathrm{ve}$ non-dimensional surface distance = distance over surface chord) it is clear from Figure 9-3 that in the region of the hole exits the dendritic cooling geometry outperforms the conventional straight film-cooling hole geometry. Midchord on the pressure surface the dendritic geometry significantly outperforms the baseline geometry. This is downstream of the additional rows of 1-2 dendtritic systems and shows that these remain attached. The removal of a row of holes at ~40% chord on the pressure surface is not detrimental to the effectiveness in that location.

By contrast, on the suction surface there is a region (between -30% and -80%) where the conventional system appears to outperform the dendritic system. This is not well understood. Indeed there may be a slight anomaly in the results as there appears to be a sharp contrast in the effectiveness levels seen between the two camera views used at -10% and -30% axial chord. The interesting feature here is the flat metal effectiveness achieved by the dendritic array on the suction side, which shows no decay over the entirety of the region of measurement. It is clear that in the baseline case the effectiveness experiences rapid decay in the downstream direction, which from a design point

of view, is a very unattractive feature because of the large temperature gradients that such a film is likely to induce in the NGV in that region.

The author believes that the dendritic array is probably starved of flow in this region on the suction side, but high metal effectiveness is still achieved near the leading edge because of the excellent internal cooling performance of the dendritic systems. Further downstream the effectiveness, which is somewhat dependent on blowing ratio, while lower, suggests better attached flow as its decay is attenuated.

The flow rate through the rows of film-cooling exits was modelled for the dendritic scheme employed using the data generated earlier in this thesis. The row by row mass flow rates for the films *in the leading edge region* are indicated on the histogram in Figure 9-4. Here the suction side to pressure side flow rate split has been reduced from 76.3 : 23.7 in the case of the conventional arrangement to 60.9 : 39.1 in the case of the circular dendritic array test piece. Taking into account the overall 10% reduction in flow we can estimate a reduction in suction side flow rate in the leading edge region of 28%. The corresponding reduction in average metal effectiveness is just above zero between 0% and 20% and just below 9% between 30% and 80% of the suction side. On the pressure side an increase of 48%. The additional pressure side film in the conventional case would make the latter difference less significant on the late pressure side.



Conventional Cooling Configuration **Dendritic Cooling Configuration**

Figure 9-4: Leading Edge Coolant Mass flow Rate Distribution

It should, however, be noted that the dendritic system tested was designed primarily to ensure ease of manufacture, following a number of earlier manufacture failures, and it was intended that this would be a first iteration. (The development of experimental technique became more of a priority for the programme on the Sector rig and it was not available for further tests of designs created within the current programme).

An alternative design for the leading edge region employing slot exits was developed as described in section 4.4.3. The flow distribution through this system was modelled as above. Here the suction to pressure side coolant flow ratio was found to be 68 : 32, lying midway between the two previous results. It might therefore be expected that for this case, given similar internal performance, but improved film-cooling effectiveness that the metal effectiveness would be improved to an adequate and flat level on the suction surface while the over cooling at pressure side mid span would be mitigated. Given the excellent film cooling effectiveness characteristics of these dendritic systems, the removal of mid-chord film cooling rows is likely with such a design, further reducing cooling requirements.

The results generated by S. Luque from the dendritic test piece designed and manufactured by the author, show potential benefit from the adoption of dendritic cooling. Further testing with refined vane designs created using the tools developed in the course of this research are required to conclusively show the improvements both in the coolant mass flow rate required and the uniformity of external vane temperature and hence oxidation life. Test pieces have been manufactured and are available to the test group for this purpose.

Chapter 10 Summary and Conclusion

An experimental investigation has been carried out into the feasibility of dendritic cooling systems and the technology's application to gas turbines. The internal and external cooling performance of dendritic cooling systems has been characterised experimentally and the results and analysis presented.

Two claimed benefits of dendritic cooling have been demonstrated in comparison to conventional cooling designs: higher internal heat transfer coefficients and improved film-cooling effectiveness. Furthermore, as a consequence of the geometry the exit blowing ratio has been shown to be substantially reduced for a given pressure margin across the vane wall. This pressure loss characteristic is particularly attractive for leading edge applications where there is a direct pay off between hole momentum ratio and cooling film attachment higher loss is important.

In the case of improved internal heat transfer the average Nusselt number has been shown to be a weak function of blowing ratio and has been correlated to the dendritic branch inlet Reynolds number as $\overline{Nu}/Nu_{db} = 13.12Re^{-0.21}$.

Furthermore it has been shown that in comparison to the expected Nusselt number of conventional straight cooling holes, typified by that estimated by Metzger and Cordaro (*1979*), a dendritic system creates significantly higher heat transfer coefficient*s*, in addition to the palpable increase in internal surface area. The product of these two variables is a significant factor in determining the quantity of heat removed internally by a cooling system and therefore an important contributor to the overall performance.

The loss associated with flow passing through various dendritic configurations has been characterised. The loss performance has sensibly been shown to follow the trend with Reynolds number of other cooling hole configurations. More interestingly the variation in loss is a strong function of exit blowing ratio: particularly for dendritic systems with a small number of branches where the capping effect of the mainstream flow has a greater impact on the system's throat. Somewhat unexpectedly the loss does not increase sharply with increasing numbers of branches, and in fact the converse is generally true, with the singly branched dendrites having a higher loss at engine representative Reynolds numbers and blowing ratios. The correlations for the three different configurations investigated are detailed in Equation 10-1, Equation 10-2 and Equation 10-3.

$$C_d = \frac{1.33}{Re} + 0.361 \times \exp(-0.157 \times \frac{1}{BR}) + 0.00371 \times \log(\frac{1}{BR})^2$$

Equation 10-1: Loss correlation for a 1-2 circular cross section dendrite

$$C_d = 0.117 \times \exp(-0.000\ 0248 \times Re - 0.109 \times (\frac{1}{BR})^2) + 0.0582 \times \log(Re)$$

Equation 10-2: Loss correlation for a 1-2-4 circular cross section dendrite

$$C_d = \frac{7.7 + 1/BR}{81.54 + 0.000000289 \times Re^2} + 0.0569 \times \log(Re)$$

Equation 10-3: Loss correlation for a 1-2-4-8 circular cross section dendrite

The external heat transfer coefficient for an array of dendritic cooling holes has been characterised at a variety of blowing ratios. A method has been developed to translate such distributions on to the surface of an engine scale NGV and to scale this distribution appropriately for engine scale conditions.

In the case of the film-cooling effectiveness it has been shown that regardless of blowing ratio a dendrite outperforms a conventional straight cooling hole passage (for the range of blowing ratios tested). Moreover the use of a slot exit further improves the film-cooling effectiveness beyond that of a dendritic system with circular exits. The film-cooling effectiveness was shown to conform to a simple industry standard superposition model which allowed a correlation to be formed for an isolated row of holes. This correlation can be incorporated in an arbitrary manner on the surface of the vane in order to establish the film-cooling effectiveness at any given point given the upstream film-cooling array geometry.

Using the data and correlations developed from experiments detailed in this thesis a MatLab code was developed to model the cooling performance of a dendritic array applied to the leading edge of an NGV at engine realistic conditions. These dendritic cooling passages have been shown to have superior performance in comparison to conventional geometry through the use of this model. The use of an array of dendritic systems with slot exit was shown to drastically reduce the flow requirement at the leading edge to obtain the required metal effectiveness.

Whilst the primary objective of this work was to gain an academic understanding of dendritic geometries and their cooling performance it is of paramount importance to consider how this work will be applied to the design of such cooling schemes in an industrial application. To this end a brief flow chart has been developed to give an overview of the design process involved (Figure 10-1).

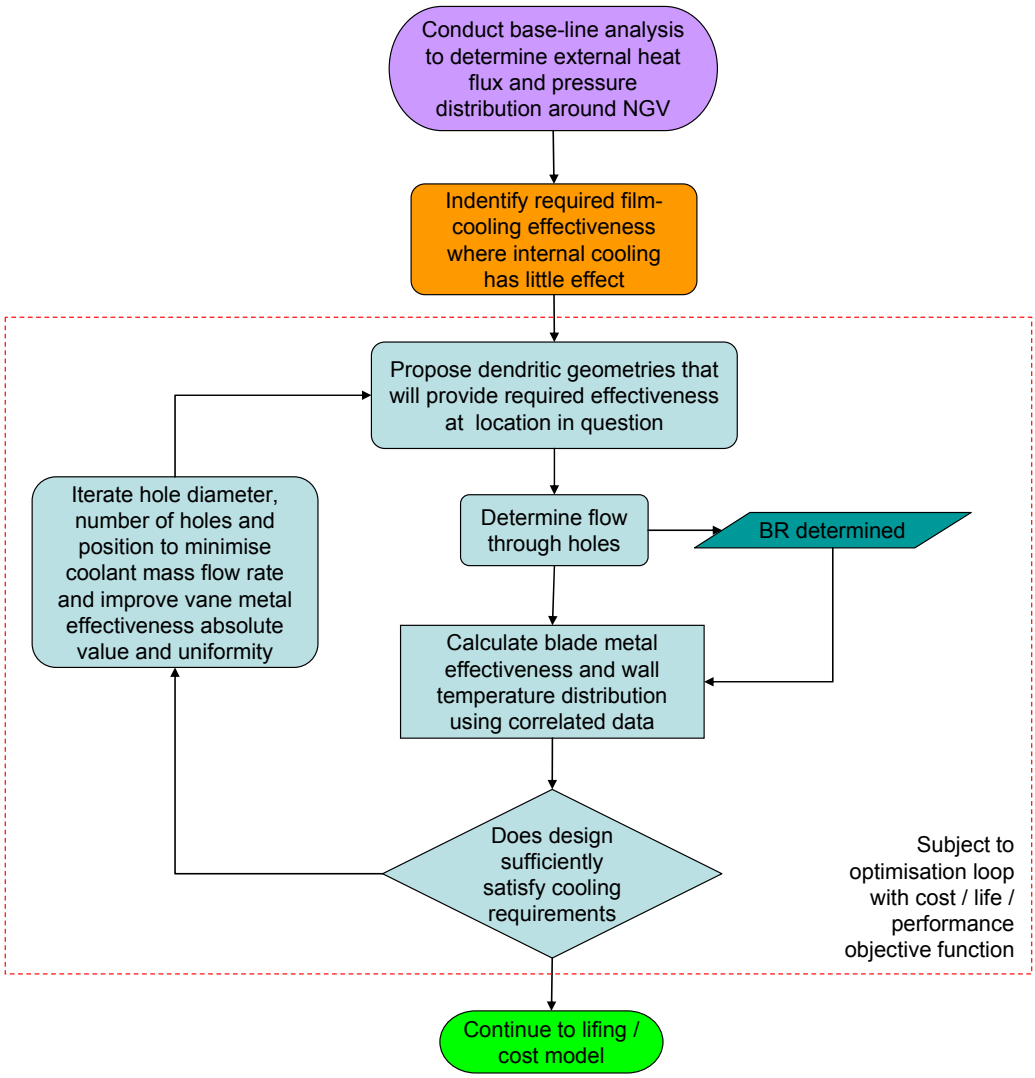


Figure 10-1: Flow chart outlining the design process involved with the application of dendritic geometry to an *NGV* (orange – operation inputs; lavender – prior inputs; light blue – processes; dark green – intermediate output; traffic light green – final output)

Testing of dendritic geometry has been conducted on the sector rig to prove the concept. Such tests are at engine scale with realistically replicated Reynolds

and Mach numbers. Although the concept was successful, as the design tools matured it became obvious that the dendritic geometry used required further refinement.

It has been shown that it is possible to manufacture novel film-cooling geometries of this type with internally branching passages by producing trial metal test pieces for NGV leading edges. Using the knowledge gained from the manufacturing trials design rules have been developed to aid future cooling scheme array development.

Designs for engine realistic cooling schemes were manufactured using both a novel casting technique and a direct laser deposition process. In the former case using super Nickel Alloys this allowed better design rules to be created for the VPC process, though unfortunately the manufacturing process is still some way from allowing commercial production. Direct metal laser sintering processes appear to offer better manufacturing opportunities, though clearly not for single crystal applications.

A potential area of future work is the investigation of components within the engine that would benefit from the application of dendritic cooling. Of particular interest are those components which don't take the thermo-mechanical loading of NGVs and turbine blades and so are not constructed from a single crystal. Such components could be made by direct metal laser sintering and could therefore easily be adapted to incorporate dendritic cooling. One such example is the technology's potential use in the shroudless high pressure blade liner, or in combustor liners.

The main priority in any future work should be to test in the sector rig the already designed and manufactured dendritic slot exit array cooling scheme detailed in Chapter 4. This should not only provide further validation of the model detailed in Chapter 8 but will also provide fast access to another set of valuable performance data for dendritic geometry. Regardless of the success of the slot exit dendritic geometry, which is predicted to out perform the circular cross section dendritic geometry, this geometry should still be further investigated and refined using the data already available from the sector rig tests. Further testing in this rig should allow the external heat transfer coefficient distribution to be determined in a high speed environment.

Further future work should concentrate on the development of dendritic geometry which could have the local wall thickness increased on a row by row basis creating a ribbed internal wall in the component. This increase in wall thickness would allow the use of more highly branched systems which would in turn facilitate better exit flow matching to the external flow conditions and the fine tuning of the system's exit velocity and therefore blowing ratio. Such an alteration would allow the improvement of the film behaviour both in terms of film-cooling effectiveness and its interaction with the mainstream flow. Appropriately applied it could improve internal heat transfer performance.

In the shorter term an improved resolution of external heat transfer coefficient distribution is required, ideally in a high speed environment to capture real mixing processes.

References

ACARE (Advisory Council for Aeronautics Research in Europe) (2010) *Aeronautics and Air Transport: Beyond Vision 2020 (Towards 2050), Background Document.* June 2010 http://www.acare4europe.org/docs/Towards 2050.pdf .

Abu Talib, A.R, Neely, A..J., Ireland, P.T., et al (2003) *A novel liquid crystal image processing technique using multiple gas temperature steps to determine heat transfer coefficient distribution and adiabatic wall temperature*. ASME Journal of Turbomachinery Vol. 126, pp. 587-596

Andrews, G. E., Asere, A. A., Gupta, M. L., Mkpadi, M. C. (1985) *Full coverage discrete hole film cooling: The influence of hole size*. Presented at the Gas Turbine Conference and Exhibition, Houston, March 1985.

Andrews, G. E., Asere, A. A., Gupta, M. L., Mkpadi, M. C., Tirmahi, A. (1986)*Transpiration cooling: Contribution of film cooling to the overall cooling effectiveness.* Presented at the International Gas Turbine Conference and Exhibit, Dusseldorf, June 1986, 86-GT-136.

Andrews, G. E., Bazdidi-Tehrani, F., Hussain, C. I., Pearson, J. P. (1991) *Small diameter film cooling hole heat transfer: The influence of the hole length.* Presented at the International Gas Turbine and Aeroengine Congress and Exposition, Orlando, June 1991.

Arcangeli, L., Surace, M., Tarcho, L., Coutandin, D., Zecchi, S. (2006) *Correlative analysis of effusion cooling systems.* Proceedings of GT2006, ASME Turbo Expo 2006, Power for Land, Sea and Air, Barcelona, May 2006. GT2006-90405.

Aunapu, N. V., Volino, R. J., Flack, K. A. (2000) *Surface flow visualization of a scaled-up turbine blade passage*. Measuring Science and Technology, Vol. 11 (2000), pp 987-991.

Battisti, L., Fedrizzi, R., Cerri, G. (2006) *Novel technology for gas turbine blade effusion cooling.* Proceedings of GT2006, ASME Turbo Expo 2006, Power for Land, Sea and Air, Barcelona, May 2006. GT2006-90516.

Brevet, P., Dejeu, C., Dorignac E., Jolly, M., Vullierme, J. J. (2002) *Heat transfer to a row of impinging jets in consideration of optimization.* International Journal of Heat and Mass Transfer 2002, Vol 45, pp 4191-4200.

British Standards Institution (1981) *Fluid Flow in Closed Conduits: Orifice Plates, Nozzles, and Venturi Tubes Inserted in Circular Cross-Section Conduits Running Full.* London: BSI. BS1042: Section 1.1.

Cengel, Y. A., Boles, M. A. (1998) *Thermodynamics: An Engineering Approach*, 3rd Edition, McGraw-Hill, New York.

Cumpsty, N. A., (1997) *Jet Propulsion; A simple guide to the aerodynamic and thermodynamic design and performance of jet engines.* Cambridge University Press, Cambridge, 2002.

Denton, J. D. (1993) *Loss mechanisms in turbomachines.* Presented at the International Gas Turbine and Aeroengine Congress and Exposition, Cincinnati, May 1993, 93-GT-435.

Dhungel, A., Lu, W., Phillips, W., Ekkad, S.V., Heidemann, J. (2007) *Film-cooling from a row of holes supplemented with anti vortex holes.* Proceedings of GT2007, ASME Turbo Expo 2007, Power for Land, Sea and Air, Montreal, May 2007. GT2007-27419.

Dieberger, J. A. (1978) *Coolable Wall*. United State Patent 4,118,146.

Eastop, T. D., McConkey, A. (1993) *Applied Thermodynamics for Engineering Technologies*, 5th Edition, Prentice Hall, London.

Eckert, E. R. G., Cho, H. H. (1994) *Transition from transpiration to film cooling*. International Journal of Heat and Mass Transfer, Vol 37, Suppl 1, 1994, pp 3 – 8.

Ecker, E.R.G. (1983) *Analysis of Film Cooling and Full Coverage Film Cooling of Gas Turbine Blades*. Proceeding of the 1983 International Gas Turbine Congress. Tokyo, Japan, October, 1983, pp. 109

Eckert, E. R. G., Livingood, J. N. B. (1953) *Comparison of effectiveness of convection-, transpiration-, and film-cooling methods with air as coolant*. National Advisory Committee for Aeronautics, Cleveland, Ohio, July 1953.

Emery, A. F., Neighbor, P. K., Gessner. F. B. (1979) *Computational Procedure for Developing Turbulent Flow and Heat Transfer in a Square Duct.* Numerical Heat Transfer, Vol. 2, pp. 399-416, 1979.

Forth, C.P.J., Jones, T.V. (1986) *Scaling Parameter in Film-Cooling*. Proceeding of the 8th International Heat Transfer Symposium, San Francisco, 1986

Fried, E., Idelchick, I. E. (1989) *Flow Resistance: A Design Guide for Engineers*. Hemisphere Publishing Corporation, New York.

Gillespie, D. R. H. (1996) *Intricate Internal Cooling Systems for Gas Turbine Blading.* D.Phil Thesis, University of Oxford.

Gritsch, M., Schulz, A., Wittig, S. (1998) *Method for correlating discharge coefficients of film cooling holes*. AIAA Journal, June 1998, Vol 36, No 6, pp 976-980.

Guillaume M. M. (1921) *Brevet D'Invention No. 534.801 VI Marine et Navigation 4. Aerostation, Aviation*, Office National de la Propriete, Mai 1921.

Han, J., Dutta, S., Ekkad, S.V. (2001) *Turbine Internal Cooling Chapter 4,* Gas Turbine Heat Transfer and Cooling Technology, Taylor and Francis Group, London, pp 251-413.

Harding, N. (7 December 2010), The Independent, London.

Harrington, M. K., McWaters, M. A., Bogard, D. G., Lemmon, C. A., Thole, K. A. (2001) *Full-coverage film cooling with short normal injection holes.* Journal of Turbomachinery, Vol 123, October 2001, pp 798-805.

Hay, N., Henshall, S. E., Manning, A. (1994) *Discharge coefficients of holes angled to the flow direction*. Transactions of the ASME, January 1994, Vol 116, pp 92-96.

Hay, N., Khaldi, A., Lampard, D. (1987) *Effect of crossflows on the discharge coefficients of film cooling holes with rounded entries or exits.* Proceedings of the ASME Thermal Engineering Conference, Hawaii, 1987, Vol 3, pp 369-374.

Hay. N., Lampard, D. (1995) *The discharge coefficient of flared film cooling holes*. Presented at the International Gas Turbine and Aeroengine Congress and Exhibition, Houston, June 1995. 96GT-492

Hay, N., Lampard, D. (1998) *Discharge coefficient of turbine cooling holes: A review*. Journal of Turbomachinery, April 1998, Vol 120, pp 314-319.

Hay, N., Lampard, D., Benmansour, S. (1983) *Effect of crossflows on the discharge coefficient of film cooling holes*. Journal of Engineering for Power, April 1983, Vol 105, pp 243-248.

Hay, N., Lampard, D., Khaldi, A. (1994) *The coefficient of discharge of 30° inclined film cooling holes with rounded entries or exits.* Presented at the International Gas Turbine and Aeroengine Congress and Exposition, The Hague, June 1994.

Hay, N., Spencer, A. (1992) *Discharge coefficients of cooling holes with radiused and chamfered inlets.* Journal of Turbomachinery, October 1992, Vol 114, pp 701-706.

Heidmann, J. D., Rigby, D. L., Ameri, A. A. (2000) *A three dimensional coupled internal/external simulation of a film-cooled turbine vane*. ASME Journal of Turbomachinery, April 2000, Vol 122, pp 348-358.

Holland, M. J., Thake, T. F. (1980) *Rotor Blade Cooling in High Pressure Turbines.* AIAA Journal of Aircraft, Vol 17, pp 412-418. 1980

Horlock, J. H., Watson, D. T., Jones, T. V. (2001) *Limitations on gas turbine performance imposed by large turbine cooling flows*. Journal of Engineering for Gas Turbines and Power, July 2001, Vol 123, pp 487-494.

Immarigeonk, A., Hassan, I. (2006) *An advanced impingement/film cooling scheme for gas turbines – numerical study.* International Journal of Numerical Methods for Heat & Fluid Flow, Vol 16, No 4, 2006, pp 470-493.

Ito, S., Goldstein, R.J., Eckert, E.R.G. (1978) *Film Cooling of a Gas Turbine Blade.* ASME Journal of Engineering for Power, June 1978, Vol 100 pp 476-481

Ireland, P.T., Jones, T.V. (2000) *Liquid crystal measurements of heat transfer and surface shear stress.* (2000) IOP Publishing Ltd, Meas. Sci. Technol., Vol 11 pp 969-986.

Jambunatha, K., Lai, E., Moss, M. A., Button, B. L. (1992) *A review of heat transfer data for single circular jet impingement*. International Journal Heat and Fluid Flow, June 1992, Vol 13, No 2, pp 106-115.

Kay, A.L. (2002) *German Jet Engine and Gas Turbine Development: 1030 – 1945.* Airlife Publishing Ltd, Shrewsbury, England (2002).

Khoo, I-C. (1995) *Liquid Crystals: Physical Properties and Nonlinear Optical Phenomena.* John Wiley & Sons Inc, New York.

Kim, K-S., Kim, Y. J., Kim, S-M. (2006) *Enhancement of film cooling performance at the leading edge of turbine blade*. Proceedings of GT2006 ASME Turbo Expo 2006, Power for Land, Sea and Air, Barcelona, May 2006, GT2006-90321.

Kusterer, K., Bohn, D., Sugimoto, T., Tanaka, R. (2006) *Double-jet ejection of cooling air for improved film-cooling.* Proceedings of GT2006, ASME Turbo Expo 2006, Power for Land, Sea and Air, Barcelona, May 2006, GT2006-90854.

Ling, J.P.C.W. (2005) *Development of Heat Transfer Measurement Techniques and Cooling Strategies for Gas Turbines.* D.Phil Thesis, University of Oxford.

Landels, J.D. (2000) *Engineering in the Ancient World.* University of California Press (revised edition), Berkeley/Los Angeles, California.

Ling, J. P. C. W., Ireland, P. T., Turner, L. (2002) *Full coverage film cooling for combustor transition sections.* Proceedings of ASME Turbo Expo 2002, Amsterdam, 2002-GT-30528.

Liu, C. L, Zhu, H. R., Bai, J. T., Xu, D. C., (2009) *Experimental research on the thermal performance of converging slot holes with different divergence angles.* Experimental Thermal and Fluid Science, Vol 33, pp 808-817.

Liu, C. L, Zhu, H. R., Bai, J. T., Xu, D. C., (2010) *Film cooling performance of converging slot-hole rows on a gas turbine blade.* International Journal of Heat and Mass Transfer, Vol 53, pp 5232-5241.

Luque, S. (2011) *A Fully Integrated Approach to Gas Turbine Cooling System Design. DPhil Thesis, University of Oxford*

Luque, S., Povey, T. (2010) *A Novel Technique for Assessing Turbine Cooling System Performance*. Journal of Turbomachinery, July 2011, Volume 133, Issue 3, 031013 doi:10.1115/1.4001232

Mann, C., (2002) *Flow visualisation of turbine blade film cooling.* Fourth year project, University of Oxford.

Medic, G., Durbin, P. A. (2002) *Towards improved film cooling prediction.* Journal of Turbomachinery, April 2002, Vol 124, pp 193-199.

Metzter, D. E., Cordaro, J. V., (1979) *Heat Transfer in Short Tubes Supplied from a Cross-Flowing Stream.* ASME, Paper 79-WA/HT-16.

Metzger, D. E., Takeuchi, D. I., Kuenstler, P. A. (1973) *Effectiveness and Heat Transfer with Full-Coverage Film Cooling.* Transactions of the ASME, July 1973.

Miller, D. S. (1990) *Internal Flow Systems*, 2nd Edition, BHRA, Cranfield.

Mittal, V. (2006) *The use of rapid prototyping on turbine blade cooling*. M.Sc. Thesis, University of Oxford.

Moffat, R. J., (1982) *Contributions to the theory of single sample uncertainty analysis.* Journal of Fluids Engineering, 104, pp 350.

Nowlin, S. R., Gillespie, D. R. H., Ireland, P. T., (2005). *A Transient Colorimeter Technique for Determining Regional Heat Tranfer Coefficients in the Three-Temperature Flowfield at a Turbine Airfoil Leading Edge.* Proceedings of 50th ASME Turbo-Expo, Reno, June 2005, Vol 3, pp. 729-738.

Okita, Y., Nishihura, M. (2007) *Film-cooling effectiveness performance of an arrowhead-shaped film-cooling hole geometry*. Journal of Turbomachinery, Vol. 129, April 2007, pp 331-339.

Oliver, D., (2001) *Unmanned Aerial Vehicles Roadmap 2000-2005.* Office of the Secretary of Defense, Washington DC, 2001.

Povey, T., Jones, T. V., Oldfield, M. L. G. (2004) *A new experimental technique for measurement of the steady-state metal temperature distributions of film-cooled NGVs.* Proceedings of the 17th Symposium on Measuring Techniques in Transonic and Supersonic Flow in Cascades and Turbomachines, Stockholm, September 2004.

Rogers, G. F. C. R., Mayhew, Y. R. (1980) *Engineering Thermodynamics Work and Heat Transfer*, 3rd Edition, Longman, London.

Rolls Royce plc (2005) *The Jet Engine,* Rolls Royce Technical Publications, London.

Rowbury, D. A., Oldfield, M. L. G., Lock, G. D. (2000) *A method for correlating the influence of external crossflow on the discharge coefficients of film cooling holes*. Submitted to ASME Turbo Expo 2000, Munich, May 2000.

Rowbury, D. A., Oldfield, M. L. G., Lock, G. D. (2000) *Large-scale testing to validate the influence of external crossflow on the discharge coefficients of film cooling holes*. Submitted to ASME Turbo Expo 2000, Munich, May 2000.

Sargent, S. R., Hedlund, C. R., Ligrani, P. M. (1998) *An infrared thermography imaging system for convective heat transfer measurements in complex flows.* Measurement Science Technology, 9 (1998), IOP Publishing Ltd.

Sargison, J. E., Oldfield, M. L. G., Guo, S. M., Lock, G. D., Rawlinson, A. J. (2005) *Flow visualisation of the external flow from a converging slot-hole film-cooling geometry*. Experiments in Fluids (2005) 38 (3), pp 304-318.

Saumweber, C., Schulz, A., Wittig, S. (2003) *Free-stream turbulence effects on film cooling with shaped holes*. Journal of Turbomachinery, January 2003, Vol 125, pp 65-73.

Shapiro, A. H., (1954) *The Dynamics and Thermodynamics of Compressible Fluid Flows,* Reprinted 1983, Krieger Publishing Corporation, Huntington, New York.

Sieder, E.N., and Tate, G.E., (1936) *Heat Transfer and Pressure Drop of Liquids in Tubes*. Ind. Eng. Chem., 28,1429.

Steinmetz, B.M., Hendricks, R.C., Munson, J., (1998) *Advanced Seal Technology Role in Meeting Next Generation Turbine Engine Goals.* NASA, (TM-1998-206961)

Talib, A., Neely, A. R., Ireland, P. T., (2004) *A Novel Liquid Crystal* I*mage Processing Technique using Multiple Gas Temperature Steps to Determine Heat Transfer Coefficient Distribution and Adiabatic Wall Temperature.* Presented at the International Gas Turbine and Aeroengine Congress and Exhibition, Atlanta, June 2003.

Taslim, M. E., Bethka D. (2009) *Experimental and Numerical Impingement Heat Transfer in an Airfoil Leading-Edge Cooling Channel With Cross-Flow.* Journal of Turbomachinery, Vol. 131, 011021 (2009).

Taslim, M. E., Khanicheh A. (2006) *Experimental and Numerical Study of Impingement on an Airfoil Leading Edge With and Without Showerhead and Gill Film Holes.* Journal of Turbomachinery, Vol. 128, 310 (2006).

Taslim, M. E., Setayeshgar L., Spring S. D. (2001) *An Experimental Evaluation of Advanced Leading Edge Impingement Cooling Concepts*. Journal of Turbomachinery Vol. 123 pg147 – 153 (2001).

Thole, K., Gritsch, M., Schulz., Wittig, S. (1998) *Flowfield measurements for film-cooling holes with expanded exits*. Journal of Turbomachinery, April 1998, Vol 120, pp 327-335.

Walsh, W. S., Thole, J. A., Joe, C. (2006) *Effects of sand ingestion on the blockage of film-cooling holes*. Proceedings of GT2006, ASME Turbo Expo 2006, Power for Land, Sea and Air, Barcelona, May 2006, GT2006-90067.

Walters, D. K., Leylek, J. H. (2000) *A detailed analysis of film-cooling physics: Part 1-streamwise injection with cylindrical holes*. Transactions of the ASME, January 2000, Vol 122, pp 102-112.

Walters, D. K., Leylek, J. H. (2000) *Impact of film-cooling jets on turbine aerodynamic losses.* Journal of Turbomachinery, Vol 122, July 2000, pp 537-545.

Wilcock, R. C., Young, J. B., Horlock, J. H. (2005) *The effect of turbine blade cooling on the cycle efficiency of gas turbine power cycles*. Journal of Engineering for Gas Turbines and Power, January 2005, Vol 127, pp 109-120.

Young, J. B., Horlock, J. H. (2006) *Defining the efficiency of a cooled turbine*. Journal of Turbomachinery, Vol 128, October 2006, pp 658-667.

Yuen, C. H. N., Martinez-Botas, R. F. (2005) *Film cooling characteristics of rows of round holes at various streamwise angles in a cross flow: Part 1. Effectiveness*. International Journal of Heat and Mass Transfer, Vol 48, 2005, pp 4995-5016.

Yuen, C. H. N., Martinez-Botas, R. F. (2005) *Film cooling characteristics of rows of round holes at various streamwise angles in a cross flow: Part 2. Heat transfer coefficients.* International Journal of Heat and Mass Transfer, Vol 48, 2005, pp 5017-5035.

Zhang, L., Moon, H. K. (2006) *Turbine blade film cooling study – the effects of showerhead geometry*. Proceedings of GT2006, ASME Turbo Expo 2006, Power for Land, Sea and Air, Barcelona, May 2006, GT2006-9036.

Appendix A Experimental Procedures

The detailed procedures in this appendix relate to the experiments described in Chapter 6 and Chapter 7.

A.1 Internal Heat Transfer

In general steps, 1-17 were carried out immediately after the previous test in order to minimise down time.

1. Ensure time since previous test is sufficient to allow isothermal wall initial condition to apply.
2. Check previous test's experimental data
   - The temperature rise and the coolant mass flow rate of the preceding test need to be compared to the desired temperature rise and flow rate required in the test in question in order to achieve the best compromise in colour play throughout the test piece.
3. Adjust settings on variable resistor
   - During initial testing it was found that even with the portable power supply on its lowest setting, because of the low coolant mass flow rates associated with this experiment, the temperature rise was too high and the colour play took place too fast. This was overcome through the use of a variable resistor.
4. Connect the power supply to single-phase power supply
5. Check there is nothing inside the tunnel
6. Change iris to required setting before switching on tunnel
   - Each test would require a slightly different wind tunnel speed depending upon blowing ratio and inlet Reynolds number required (Table 6-1). For each test this velocity was checked in combination with the coolant flow rate in order to achieve the correct blowing ratio. The wind tunnel velocity was adjusted using the iris.
7. Set coolant supply to required pressure
   - Immediately after each test the coolant flow rate needed setting for the subsequent test. The reasons for this were two fold; in order for the flow rate to be correct the flow needed to be heated (so that the density change would be accounted for), but from a practical point of view the apparatus needed time to cool before the test run. The time delay required between the setting of the mass flow rate and the experiment taking place became a significant restriction to progress and started to cause the testing schedule to slip. This was particularly the case when it wasn't possible to set up for the next test immediately after the completion of a test. To overcome this, later on in the testing schedule, the facility to manually adjust the coolant temperature was added to the LabView programme. Doing this enabled the pre-setting of the coolant flow rate without the complication of heating as long as the temperature rise could be estimated.
8. Set switch behind tunnel to on
9. Set top box on wind tunnel to X2
10. Set to right wind tunnel
11. Switch on coolant and wind tunnel
12. Switch on the power supply

13. Observe and check settings are correct
14. Turn mesh off and switch off power supply
15. Turn tunnel off
16. Shut coolant valve
17. Repeat steps 1-15 until settings are correct and wait for tunnel and apparatus to cool
18. Make sure data collection period is long enough on DAQ computer
19. Lights on
    - Two fluorescent tubes were mounted in a box with an adjustable shade. This box was then suspended from the metal frame that surrounds the viewing area of the wind tunnel. In addition to this another fluorescent tube was mounted directly on to the wind tunnel at an angle such that it provided illumination for the top view whilst complementing the other light source
20. Video cameras on
    - Primarily the cameras needed to be viewing the passages of the dendrite model. The camera viewing the top of the model had to be particularly finely adjusted so as to get a view through the metal clamping bars whilst still capturing the entire module in question. The side view camera also needed adjustment depending upon which configuration was being tested; for the 1-2 and 1-2-4 configuration only the final branch (the branch closest to the wind tunnel wall) needed to be viewed whilst for the 1-2-4-8 configuration both the first and final branches needed to be viewed. In order to be consistent between tests the location of the tripod was marked and the tripod remained in the same position throughout the experiment. The top camera's custom-made mount and the manner in which it attached to apparatus ensured consistency of its location between tests. It was important that both cameras were in fully manual mode; the focus needed to be adjusted to ensure the features of the holes and colour play could be easily identified. It was important to ensure the white balance was correctly set and was the same for both cameras. Finally, it was vital to ensure an LED was captured by each camera to ensure correct synchronisation at the processing stage.
21. Set switch behind tunnel to on
22. Set top box on wind tunnel to X2
23. Set to right wind tunnel
24. Set data acquisition to get off sets
    - Before any changes in pressure (due to coolant or wind tunnel flow) could be registered the DAQ equipment needed to record any signal from the transducers that was being recorded without any change in pressure taking place.
25. Start wind tunnel using button by wind tunnel viewing window
26. Start recording data – DAQ equipment and cameras on
27. Switch on coolant to establish flow
28. Switch on power supply
    - Mesh is heated and coolant flow runs hot
29. Test run for approximately 1 minute
    - The test period was always slightly longer than 90 seconds but the data that was used was cut to exactly 60 seconds at the processing

stage. Using data beyond the 60 second mark would call in to question its validity because the infinite solid approximation that is assumed at the processing stage would no longer be applicable.

30. Turn mesh off and power down power supply
31. Turn tunnel off
32. Shut coolant valve

A.2 Loss in Dendritic Passages

1. Pre set wind tunnel velocity
   - A range of wind tunnel velocities were required in order to achieve the required range of blowing ratios over the range of Reynolds number at the dendrite inlet
2. Get offsets
3. Switch tunnel on
4. Set DAQ to record pressures
   - Make sure data recording period has been extended - approximately 300 seconds
5. Switch on coolant
   - For each mainstream velocity the coolant pressure was increased in small increments and given sufficient time to stabilise after each increase. The flow was increased such that the dendrite's inlet Reynolds number ranged from 0 to 15000
6. Switch off mainstream
7. Switch off the coolant

A.3 Transient technique: External Heat Transfer Coefficient

In general steps 1-19 were carried out immediately after the previous test in order to minimise down time.

1. Check previous test's experimental data
   - The temperature rise and the coolant mass flow rate need to be compared to the desired temperature rise and flow rate required in the test in question.
2. Adjust settings on portable power supply
3. Connect the power supply to the single-phase power supply
4. Check there is nothing inside the tunnel
5. Change iris to required setting before switching on tunnel
   - For all the transient tests the mainstream velocity was kept at approximately 13.43m/s. For each test the velocity was checked in combination with the coolant flow rate. Any adjustments to the velocity were made with adjustment of the iris.
6. Pre set coolant supply to required level
   - Immediately after each test the coolant flow rate needed setting for the subsequent test. The reasons for this were two fold; in order for the flow rate to be correct the flow needed to be heated (so that the density change would be accounted for), but from a practical point of view the apparatus needed time to cool before the test run.
7. Switch on coolant and wind tunnel

8. Switch on the power supply
9. Observe and check settings are correct
10. Turn mesh off and switch off power supply
11. Turn tunnel off
12. Shut coolant valve
13. Repeat steps 1-12 until settings are correct and wait for tunnel and apparatus to cool
14. Lights on
    - Two fluorescent tubes were mounted above and below the flat plates. They were mounted on brackets which also acted as shades which prevented any glare when viewed from the opposite side of the wind tunnel through the Perspex plates by the cameras.
15. Video cameras on
    - Primarily the cameras needed to be viewing the correct portions of the flat plates, making sure there was overlap between the two images. In order to be consistent between tests the location of the tripod was marked and the tripods remained in the same position throughout the experiment. It was important that both cameras were in fully manual mode; the focus needed to be adjusted to ensure the features of the holes and colour play could be easily identified. It was important to ensure the white balance was correctly set and the same for both cameras.
16. Switch on fan isolator
17. Make sure data collection period is long enough on DAQ computer
18. Set data acquisition to get offsets
    - Before any changes in pressure (due to coolant or wind tunnel flow) could be registered the DAQ equipment needed to record any signal from the transducers that was being recorded without any change in pressure taking place
19. Start wind tunnel using button by wind tunnel viewing window
20. Switch on isolator behind power supply (Down=off, up =on)
21. Switch on Drake front power supply
22. Start recording data – DAQ and cameras
23. Simultaneously power mesh and open valve for coolant supply
24. Run test for over 2 minutes
    - The test period was always slightly longer than 120 seconds but the data that was used was cut to exactly 120 seconds at the processing stage. Using data beyond the 2 minute mark would call in to question its validity because the infinite solid approximation that is assumed at the processing stage would no longer be applicable.
25. Turn mesh off and power down power supply
26. Turn tunnel off
27. Shut coolant valve

A.4 Steady state technique: Film-cooling effectiveness

1. Check the previous setting of the Drake power supply in the log
2. If the voltage is too high make sure no busbars are connected and switch on Drake so that the voltage can be reduced to a level where it can be safely adjusted with the wind tunnel on.

3. Check the drake supply is off, open the switch box and set the busbars to D (the low speed wind tunnel).
4. Adjust the iris of the wind tunnel to achieve the desired velocity.
5. For each test the velocity was adjusted and checked in combination with the coolant flow rate. The velocity was adjusted with the iris.
6. Check there is nothing inside the tunnel
7. Switch on the wind tunnel
8. Adjust the coolant flow rate to achieve the required blowing ratio
9. Take initial pressure and temperature readings
10. Switch the Drake power supply on and manually adjust the voltage to achieve the desired mainstream temperature (ideally above 45°C, but must be less than 50 °C).
11. Take pressure and temperature readings to check the blowing ratio is correct
12. Wait for temperature to stabilise, take snapshots of the upstream and downstream sections using the IR camera
13. Collect steady-state thermocouple data
14. Switch off the Drake power supply
15. Wait for the power supply wires to cool down and repeat steps 6 to 12 for the required range of blowing ratios
16. Switch of the tunnel and adjust the iris to a new position after the motor has stopped rotating
17. Repeat steps 1 to 15 for the required range of tunnel speeds

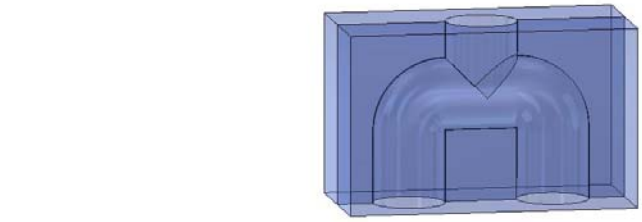
A.5 Flow visualisation

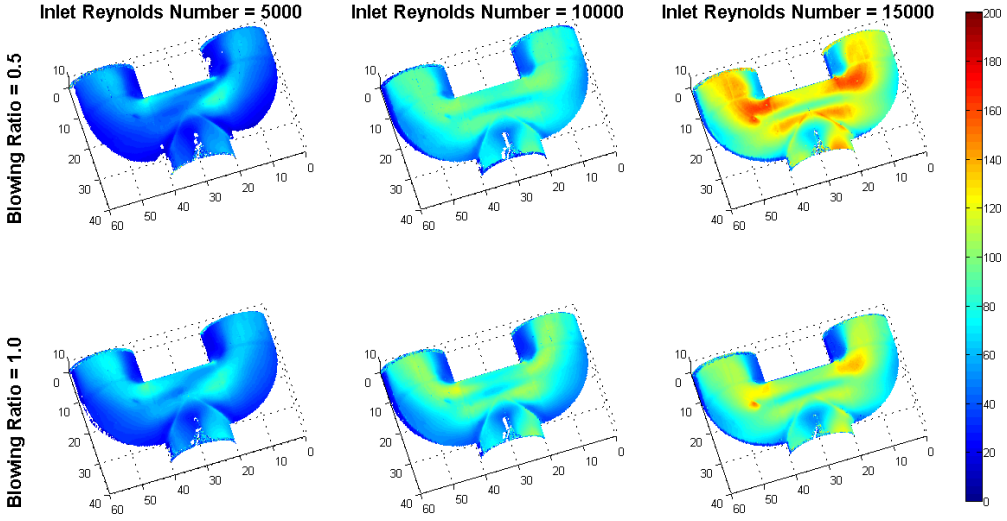
1. Set data acquisition to get off sets
   - Before any changes in pressure (due to coolant or wind tunnel flow) could be registered the DAQ equipment needed to record any signal from the transducers that was being recorded without any change in pressure taking place.
2. Wind tunnel switched on and velocity checked
   - For all the flow visualisation tests the mainstream velocity was kept at approximately 13.43m/s. For each test the velocity was checked in combination with the coolant flow rate. Any adjustments to the velocity were made with adjustment of the iris.
3. Coolant flow switched on and rate adjusted to achieve desired blowing ratio
4. Camera switched on and readied
   - The area of interest was framed as best as possible by adjusting first the camera location and then the focal length. Following this the focus was adjusted (autofocus was switched off and set to manual mode) so that the grid on the wind tunnel wall was sharp. The shutter speed was then set to 1 second and then the aperture was adjusted until the contrast was correct. Finally the flash was switched on (but not fired). A single photo was then taken to instantly verify the settings were correctly adjusted. It was sometimes necessary to reframe the shot in cases where the film extended downstream further than expected or was thicker than anticipated.
5. The coolant flow rate was adjusted to give the desired blowing ratio and then switched off

6. Hot water readied
    - 2 litres of boiling water was readied before each test.
7. Granulated CO_2 added and bung replaced
    - 140ml of dry ice used per shot.
8. Lights switched off
9. Coolant switched on
10. Water added (operator signals that water is being added)
    - $1/3^{rd}$ of a litre of water is used for each shot. The water is added by raising the plastic bottle which holds the water above the mixer. This forces the water to drain into the mixer and to mix with the CO_2 pellets. The time for the flow to become visible is almost instantaneous. There was obviously a time lag between the water being added, the operator signalling and the camera shutter being opened that meant by the time the image was captured the flow was in the period at which it was at its maximum visibility.
11. Shutter opened and flash fired
    - Once the water is added the flow becomes almost instantly visible. The camera shutter is opened for 1second and during that time the flash is fired.
12. Water stops being added and is drained back into plastic bottle
    - The plastic bottle is lowered below the mixer and so the water drains out.
13. Coolant switched off
14. More ice added for repeat runs of the same test set up
    - With the coolant flow rate correctly set and the wind tunnel running at the correct velocity it was only necessary to add more ice and repeat the steps from point 9.

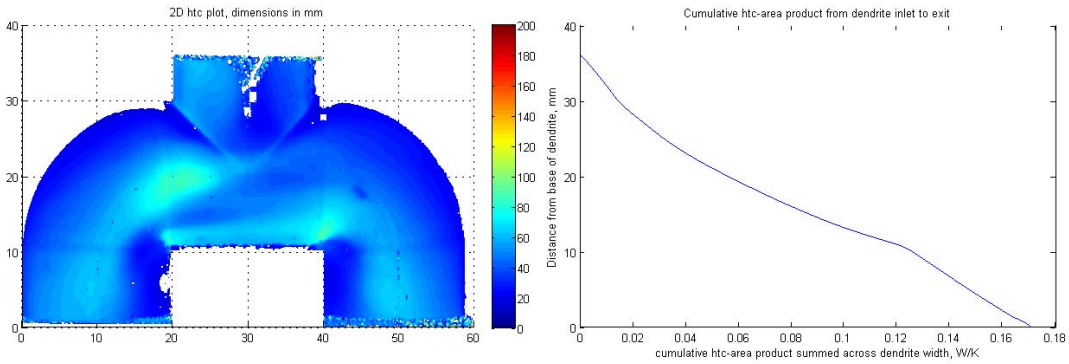
Appendix B Large Scale Dendritic Results

B.1 1-2 Dendritic Configuration





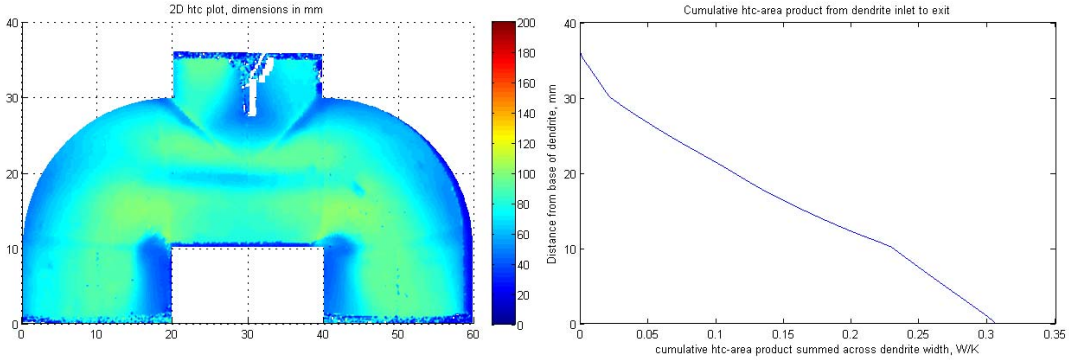
1-2 Inlet: Blowing Ratio = 0.5, Dendrite Inlet Reynolds Number = 5000, Branch Inlet Reynolds Number = 5000



Test Data
Average htc = 41.5W/m^2/K
Total htc-area product = 0.203W/K
Nusselt Number = 33.2

Engine Scaled Data
Average Engine Scaled htc = 2627.0W/m^2/K
Total htc-area product = 0.023W/K
Engine Scaled Nusselt Number = 33.2

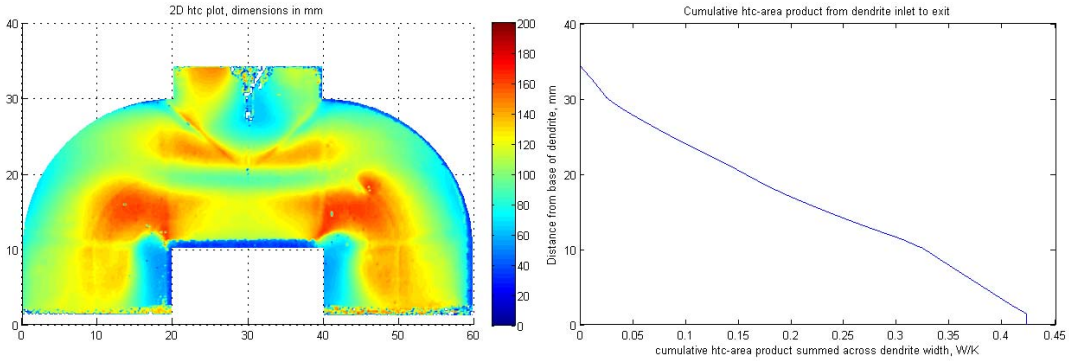
1-2 Inlet: Blowing Ratio = 0.5, Dendrite Inlet Reynolds Number = 10000, Branch Inlet Reynolds Number = 10000



Test Data
Average htc = 67.7W/m^2/K
Total htc-area product = 0.332W/K
Nusselt Number = 54.2

Engine Scaled Data
Average Engine Scaled htc = 4284.7W/m^2/K
Total htc-area product = 0.037W/K
Engine Scaled Nusselt Number = 54.2

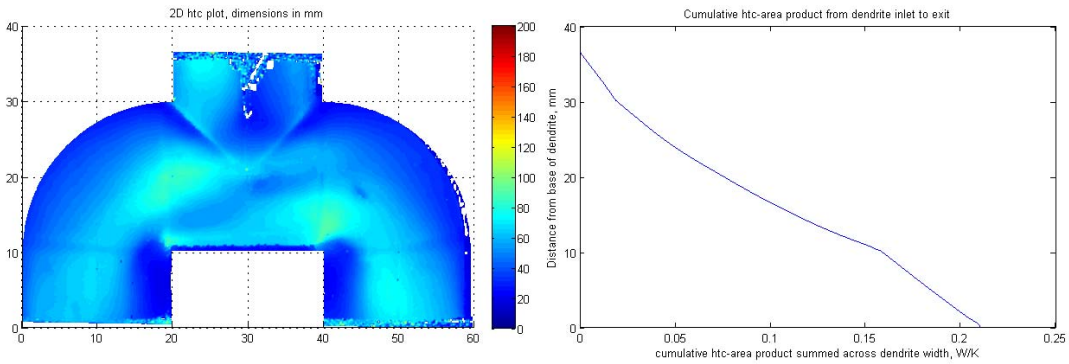
1-2 Inlet: Blowing Ratio = 0.5, Dendrite Inlet Reynolds Number = 15000, Branch Inlet Reynolds Number = 15000



Test Data
Average htc = 98.9W/m^2/K
Total htc-area product = 0.485W/K
Nusselt Number = 79.1

Engine Scaled Data
Average Engine Scaled htc = 6256.5W/m^2/K
Total htc-area product = 0.054W/K
Engine Scaled Nusselt Number = 79.1

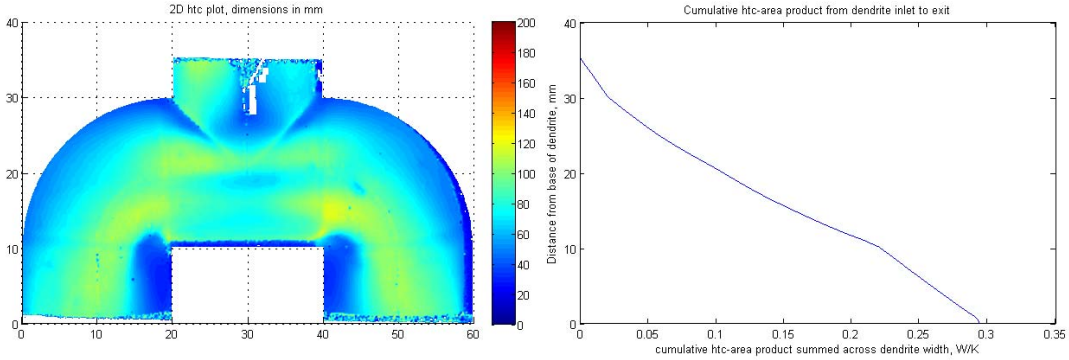
1-2 Inlet: Blowing Ratio = 1.0, Dendrite Inlet Reynolds Number = 5000, Branch Inlet Reynolds Number = 5000



Test Data
Average htc = 47.5W/m^2/K
Total htc-area product = 0.233W/K
Nusselt Number = 38.0

Engine Scaled Data
Average Engine Scaled htc = 3005.3W/m^2/K
Total htc-area product = 0.026W/K
Engine Scaled Nusselt Number = 38.0

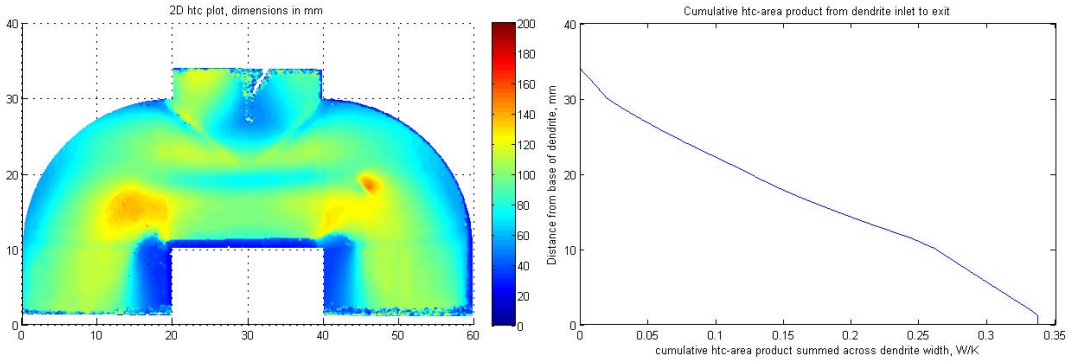
1-2 Inlet: Blowing Ratio = 1.0, Dendrite Inlet Reynolds Number = 10000, Branch Inlet Reynolds Number = 10000



Test Data
Average htc = 66.4W/m^2/K
Total htc-area product = 0.326W/K
Nusselt Number = 53.1

Engine Scaled Data
Average Engine Scaled htc = 4202.9W/m^2/K
Total htc-area product = 0.036W/K
Engine Scaled Nusselt Number = 53.1

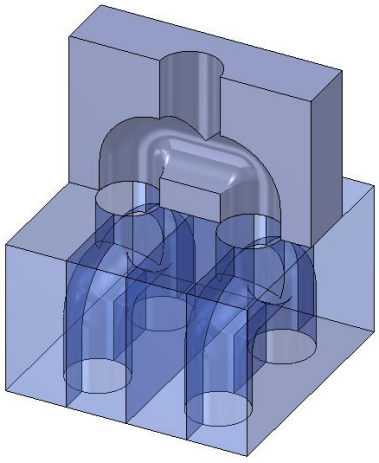
1-2 Inlet: Blowing Ratio = 1.0, Dendrite Inlet Reynolds Number = 15000, Branch Inlet Reynolds Number = 15000



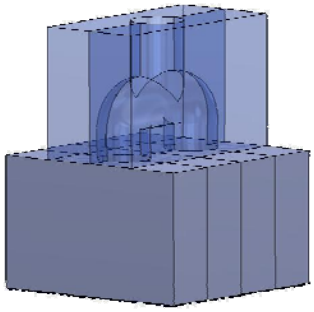
Test Data
Average htc = 78.9W/m^2/K
Total htc-area product = 0.387W/K
Nusselt Number = 63.1

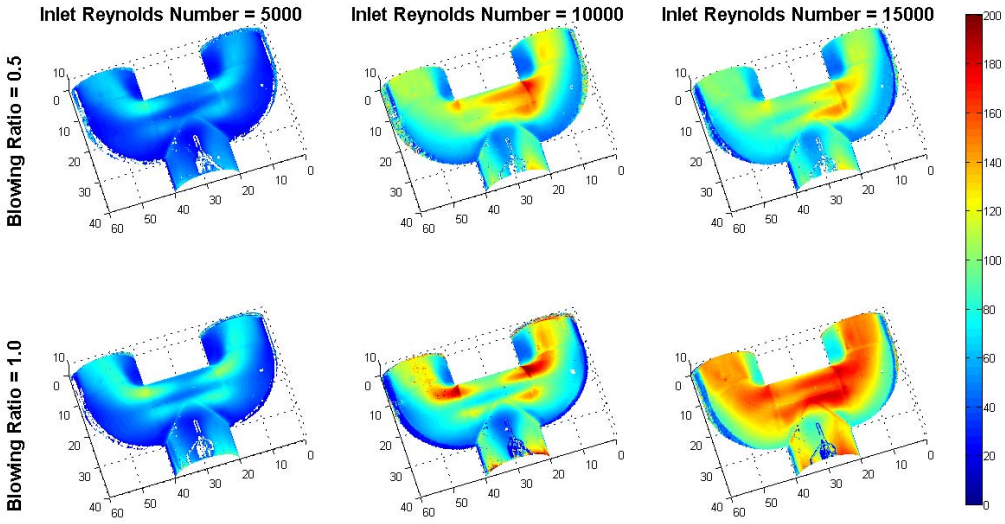
Engine Scaled Data
Average Engine Scaled htc = 4991.0W/m^2/K
Total htc-area product = 0.043W/K
Engine Scaled Nusselt Number = 63.1

B.2 1-2-4 Dendritic Configuration

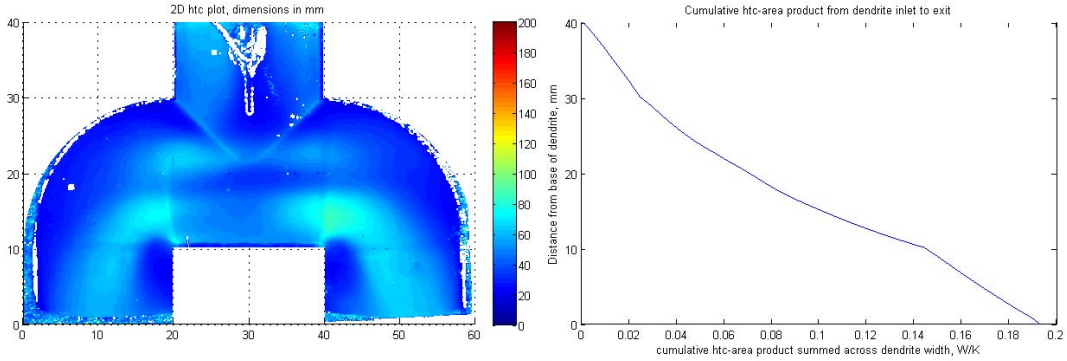


B.2.1 Inlet Branch





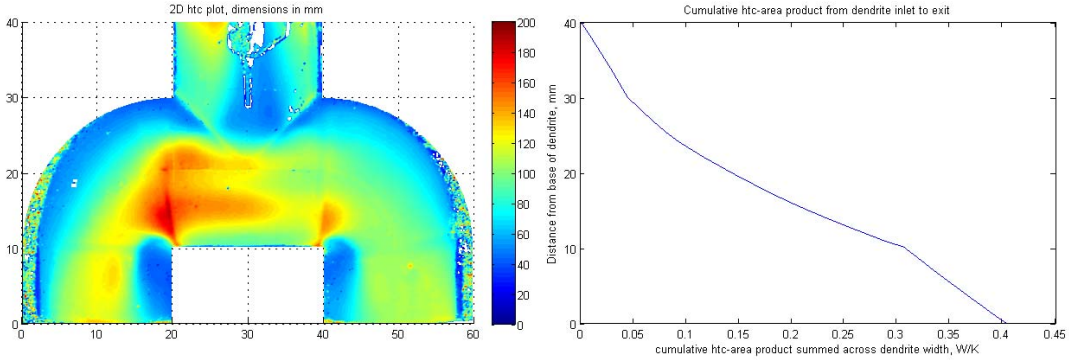
1-2-4 Inlet: Blowing Ratio = 0.5, Dendrite Inlet Reynolds Number = 5000, Branch Inlet Reynolds Number = 5000



Test Data
Average htc = 42.9W/m^2/K
Total htc-area product = 0.210W/K
Nusselt Number = 34.3

Engine Scaled Data
Average Engine Scaled htc = 2712.6W/m^2/K
Total htc-area product = 0.023W/K
Engine Scaled Nusselt Number = 34.3

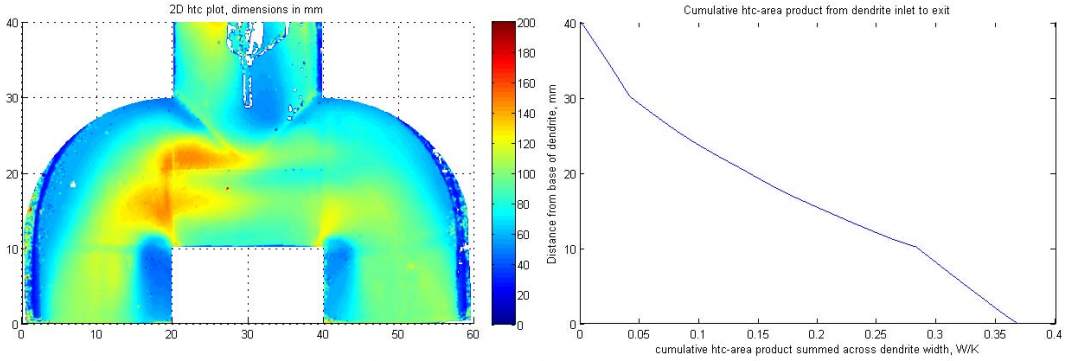
1-2-4 Inlet: Blowing Ratio = 0.5, Dendrite Inlet Reynolds Number = 10000, Branch Inlet Reynolds Number = 10000



Test Data
Average htc = 85.3W/m^2/K
Total htc-area product = 0.418W/K
Nusselt Number = 68.2

Engine Scaled Data
Average Engine Scaled htc = 5396.3W/m^2/K
Total htc-area product = 0.047W/K
Engine Scaled Nusselt Number = 68.2

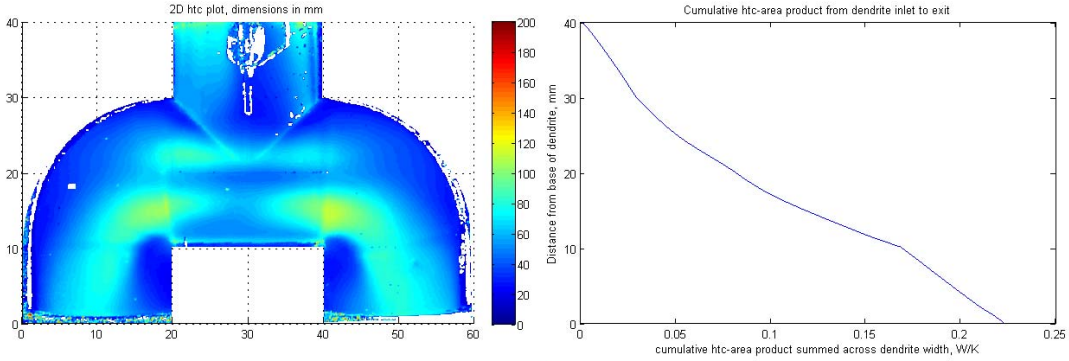
1-2-4 Inlet: Blowing Ratio = 0.5, Dendrite Inlet Reynolds Number = 15000, Branch Inlet Reynolds Number = 15000



Test Data
Average htc = 79.3W/m^2/K
Total htc-area product = 0.389W/K
Nusselt Number = 63.4

Engine Scaled Data
Average Engine Scaled htc = 5016.3W/m^2/K
Total htc-area product = 0.043W/K
Engine Scaled Nusselt Number = 63.4

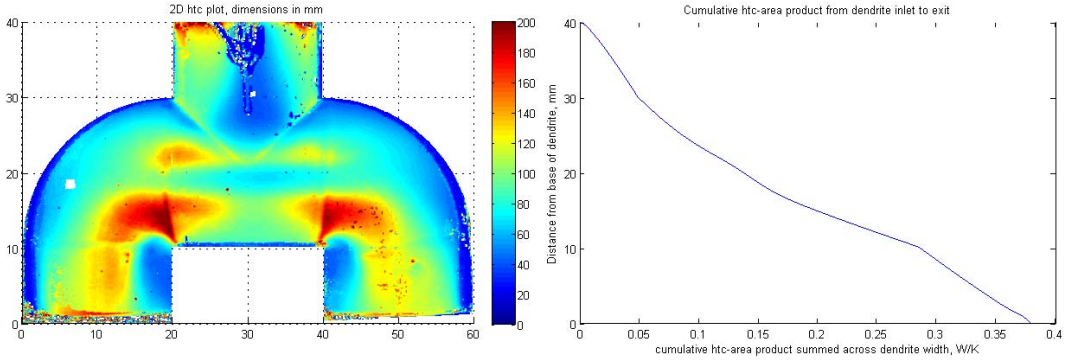
1-2-4 Inlet: Blowing Ratio = 1.0, Dendrite Inlet Reynolds Number = 5000, Branch Inlet Reynolds Number = 5000



Test Data
Average htc = 50.0W/m^2/K
Total htc-area product = 0.245W/K
Nusselt Number = 40.0

Engine Scaled Data
Average Engine Scaled htc = 3164.5W/m^2/K
Total htc-area product = 0.027W/K
Engine Scaled Nusselt Number = 40.0

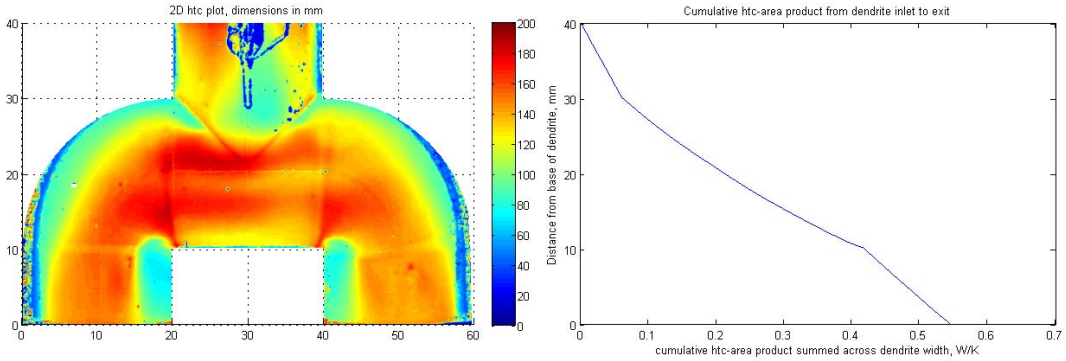
1-2-4 Inlet: Blowing Ratio = 1.0, Dendrite Inlet Reynolds Number = 10000, Branch Inlet Reynolds Number = 10000



Test Data
Average htc = 80.6W/m^2/K
Total htc-area product = 0.395W/K
Nusselt Number = 64.5

Engine Scaled Data
Average Engine Scaled htc = 5101.4W/m^2/K
Total htc-area product = 0.044W/K
Engine Scaled Nusselt Number = 64.5

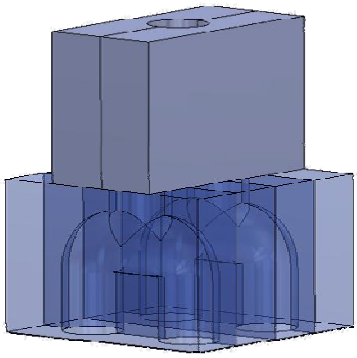
1-2-4 Inlet: Blowing Ratio = 1.0, Dendrite Inlet Reynolds Number = 15000, Branch Inlet Reynolds Number = 15000

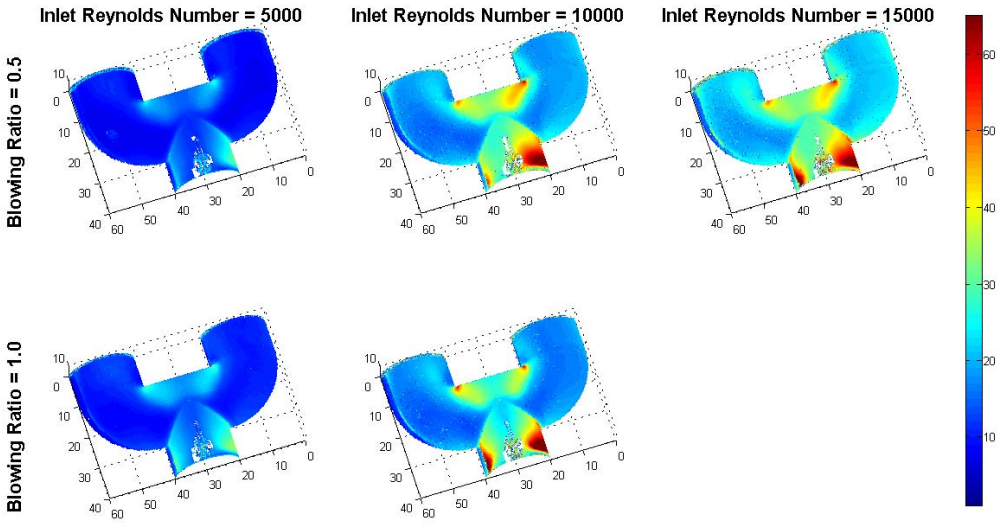


Test Data
Average htc = 115.6W/m^2/K
Total htc-area product = 0.567W/K
Nusselt Number = 92.5

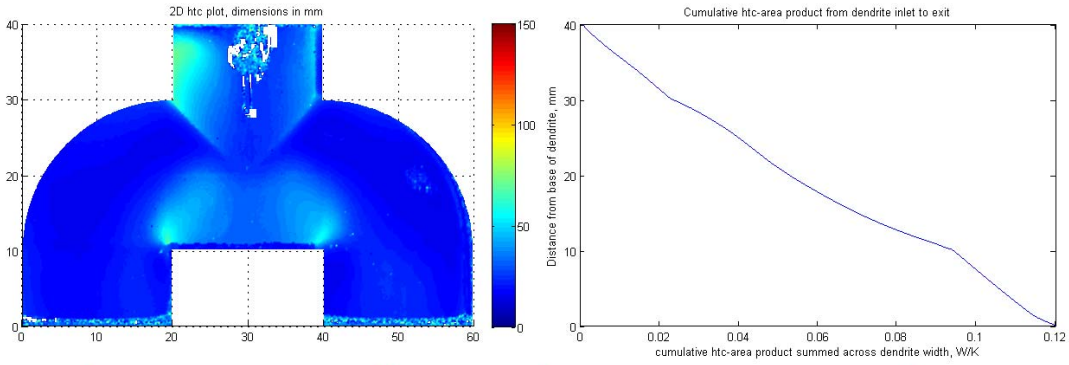
Engine Scaled Data
Average Engine Scaled htc = 7316.4W/m^2/K
Total htc-area product = 0.063W/K
Engine Scaled Nusselt Number = 92.5

B.2.2 Exit Branch





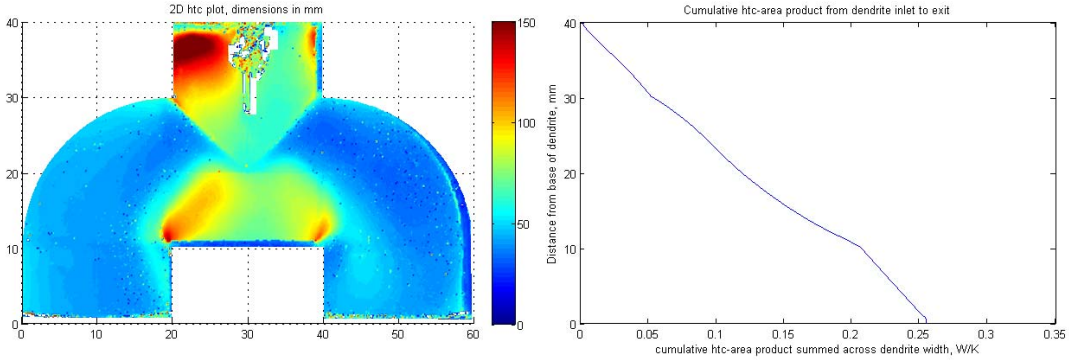
1-2-4 Exit: Blowing Ratio = 0.5, Dendrite Inlet Reynolds Number = 5000, Branch Inlet Reynolds Number = 2500



Test Data
Average htc = 25.3W/m^2/K
Total htc-area product = 0.124W/K
Nusselt Number = 20.2

Engine Scaled Data
Average Engine Scaled htc = 1601.1W/m^2/K
Total htc-area product = 0.014W/K
Engine Scaled Nusselt Number = 20.2

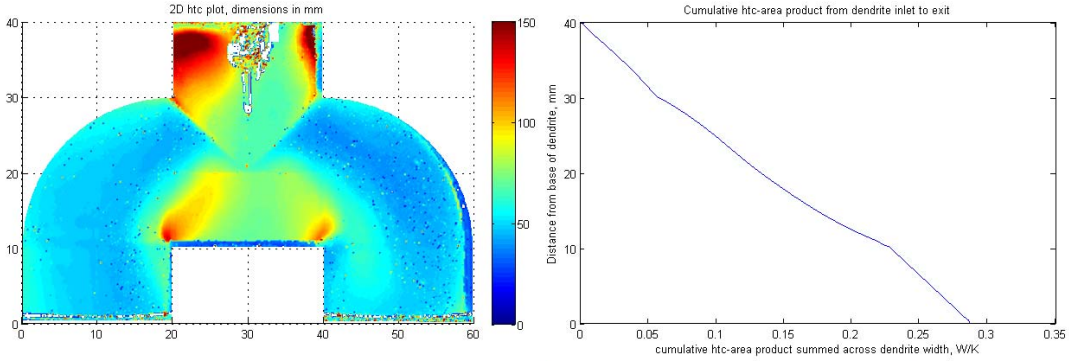
1-2-4 Exit: Blowing Ratio = 0.5, Dendrite Inlet Reynolds Number = 10000, Branch Inlet Reynolds Number = 5000



Test Data
Average htc = 54.9W/m^2/K
Total htc-area product = 0.269W/K
Nusselt Number = 43.9

Engine Scaled Data
Average Engine Scaled htc = 3473.9W/m^2/K
Total htc-area product = 0.030W/K
Engine Scaled Nusselt Number = 43.9

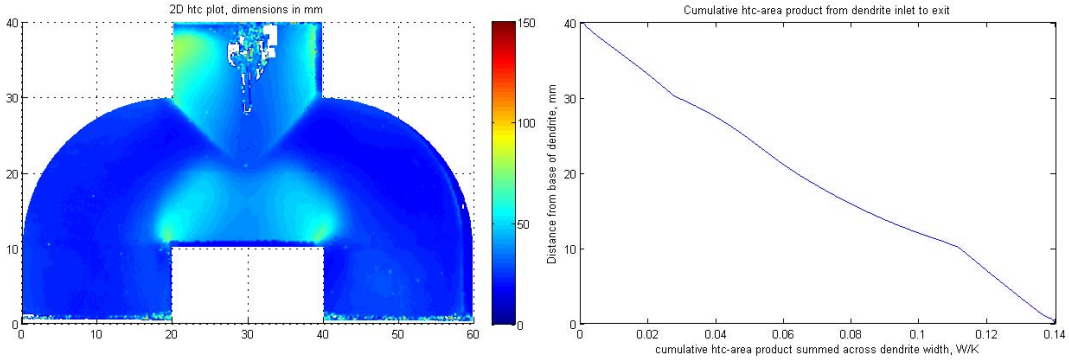
1-2-4 Exit: Blowing Ratio = 0.5, Dendrite Inlet Reynolds Number = 15000, Branch Inlet Reynolds Number = 7500



Test Data
Average htc = 61.0W/m^2/K
Total htc-area product = 0.299W/K
Nusselt Number = 48.8

Engine Scaled Data
Average Engine Scaled htc = 3857.7W/m^2/K
Total htc-area product = 0.033W/K
Engine Scaled Nusselt Number = 48.8

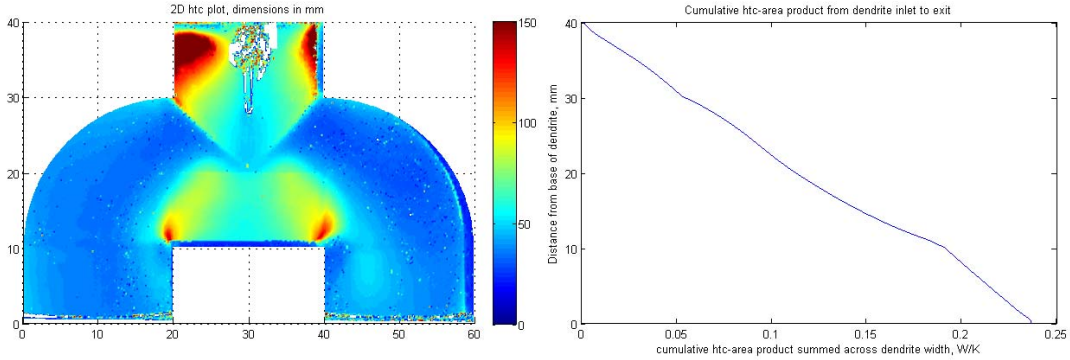
1-2-4 Exit: Blowing Ratio = 1.0, Dendrite Inlet Reynolds Number = 5000, Branch Inlet Reynolds Number = 2500



Test Data
Average htc = 29.7W/m^2/K
Total htc-area product = 0.145W/K
Nusselt Number = 23.7

Engine Scaled Data
Average Engine Scaled htc = 1877.0W/m^2/K
Total htc-area product = 0.016W/K
Engine Scaled Nusselt Number = 23.7

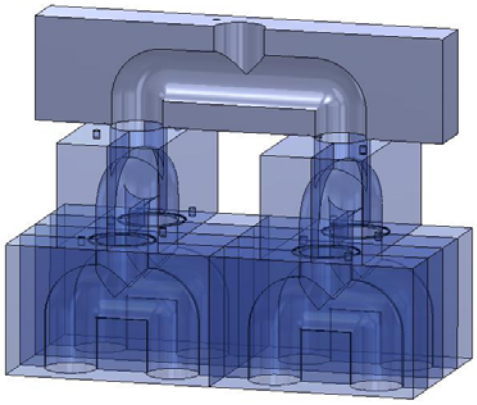
1-2-4 Exit: Blowing Ratio = 1.0, Dendrite Inlet Reynolds Number = 10000, Branch Inlet Reynolds Number = 5000



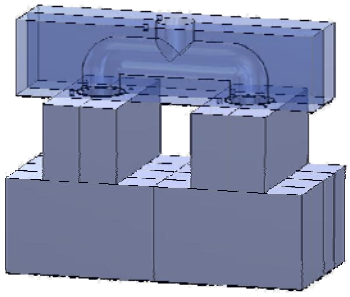
Test Data
Average htc = 50.4W/m^2/K
Total htc-area product = 0.247W/K
Nusselt Number = 40.3

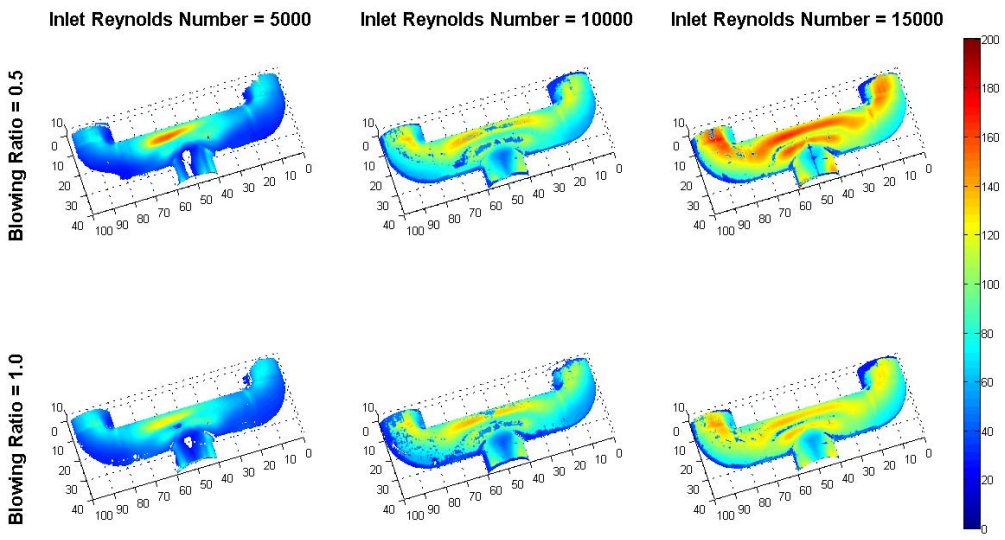
Engine Scaled Data
Average Engine Scaled htc = 3189.4W/m^2/K
Total htc-area product = 0.028W/K
Engine Scaled Nusselt Number = 40.3

B.3 1-2-4-8 Dendritic Configuration

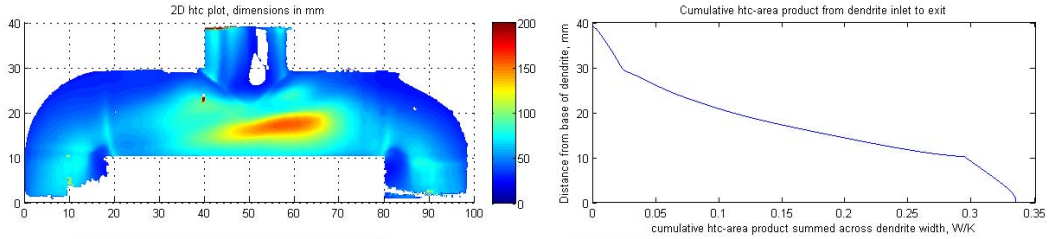


B.3.1.1 Inlet Branch





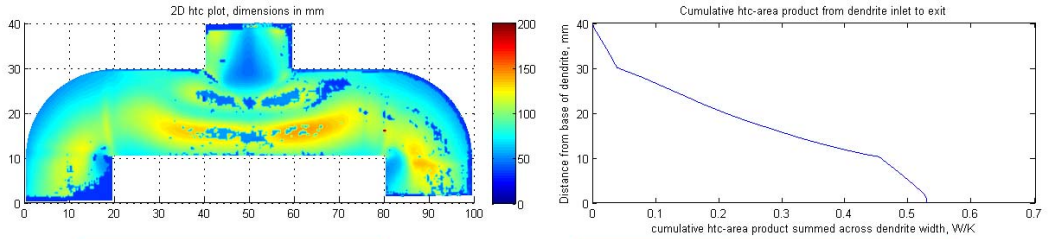
1-2-4-8 Inlet: Blowing Ratio = 0.5, Dendrite Inlet Reynolds Number = 5000, Branch Inlet Reynolds Number = 5000



Test Data
Average htc = 57.7W/m^2/K
Total htc-area product = 0.426W/K
Nusselt Number = 46.2

Engine Scaled Data
Average Engine Scaled htc = 3651.8W/m^2/K
Total htc-area product = 0.048W/K
Engine Scaled Nusselt Number = 46.2

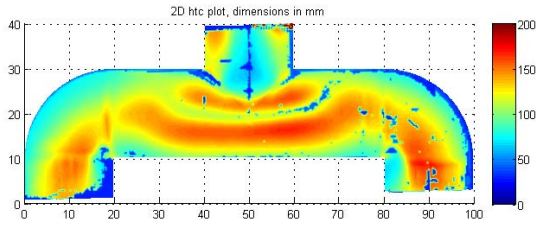
1-2-4-8 Inlet: Blowing Ratio = 0.5, Dendrite Inlet Reynolds Number = 10000, Branch Inlet Reynolds Number = 10000

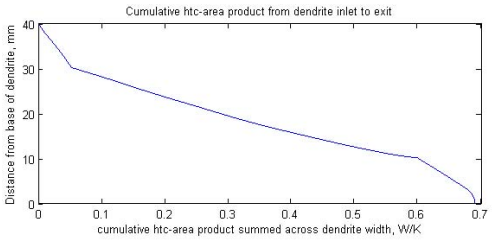


Test Data
Average htc = 80.2W/m^2/K
Total htc-area product = 0.592W/K
Nusselt Number = 64.1

Engine Scaled Data
Average Engine Scaled htc = 5072.4W/m^2/K
Total htc-area product = 0.066W/K
Engine Scaled Nusselt Number = 64.1

1-2-4-8 Inlet: Blowing Ratio = 0.5, Dendrite Inlet Reynolds Number = 15000, Branch Inlet Reynolds Number = 15000

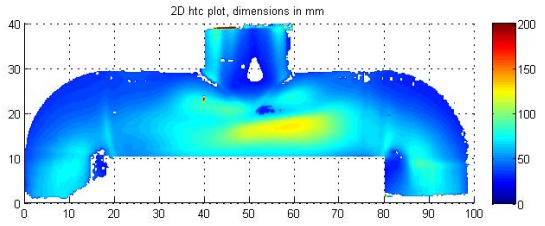


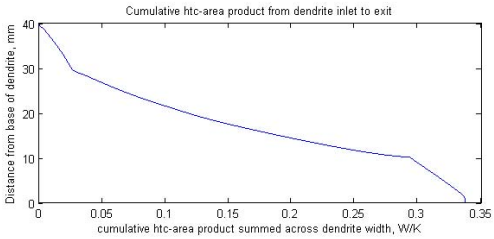


Test Data
Average htc = 100.0W/m^2/K
Total htc-area product = 0.739W/K
Nusselt Number = 80.0

Engine Scaled Data
Average Engine Scaled htc = 6329.6W/m^2/K
Total htc-area product = 0.083W/K
Engine Scaled Nusselt Number = 80.0

1-2-4-8 Inlet: Blowing Ratio = 1.0, Dendrite Inlet Reynolds Number = 5000, Branch Inlet Reynolds Number = 5000

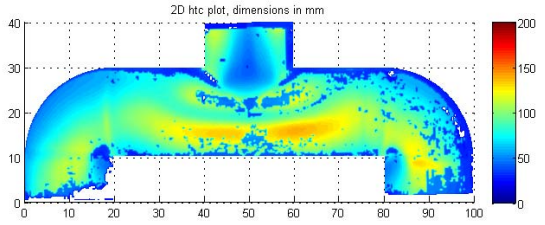


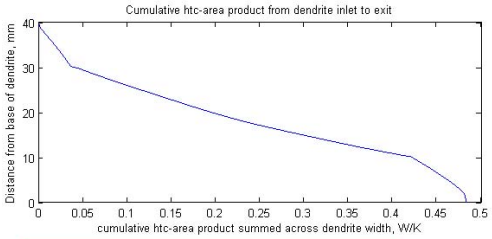


Test Data
Average htc = 56.5W/m^2/K
Total htc-area product = 0.418W/K
Nusselt Number = 45.2

Engine Scaled Data
Average Engine Scaled htc = 3576.1W/m^2/K
Total htc-area product = 0.047W/K
Engine Scaled Nusselt Number = 45.2

1-2-4-8 Inlet: Blowing Ratio = 1.0, Dendrite Inlet Reynolds Number = 10000, Branch Inlet Reynolds Number = 10000

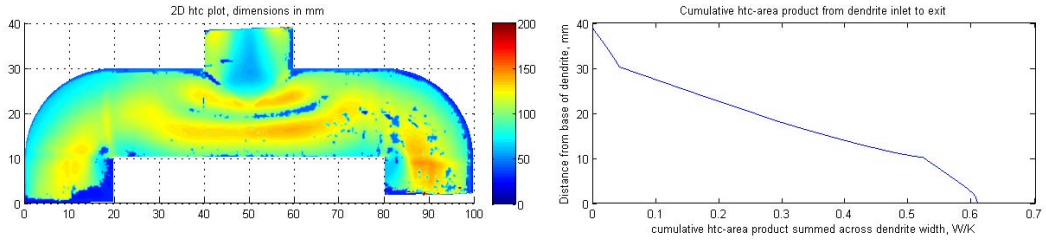




Test Data
Average htc = 70.5W/m^2/K
Total htc-area product = 0.521W/K
Nusselt Number = 56.4

Engine Scaled Data
Average Engine Scaled htc = 4459.9W/m^2/K
Total htc-area product = 0.058W/K
Engine Scaled Nusselt Number = 56.4

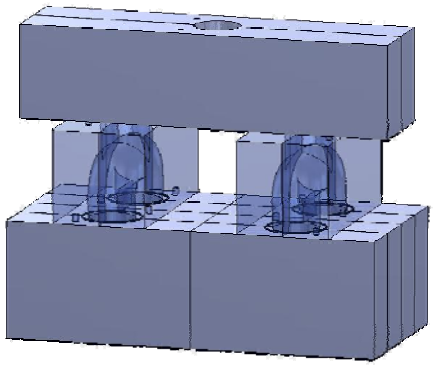
1-2-4-8 Inlet: Blowing Ratio = 1.0, Dendrite Inlet Reynolds Number = 15000, Branch Inlet Reynolds Number = 15000

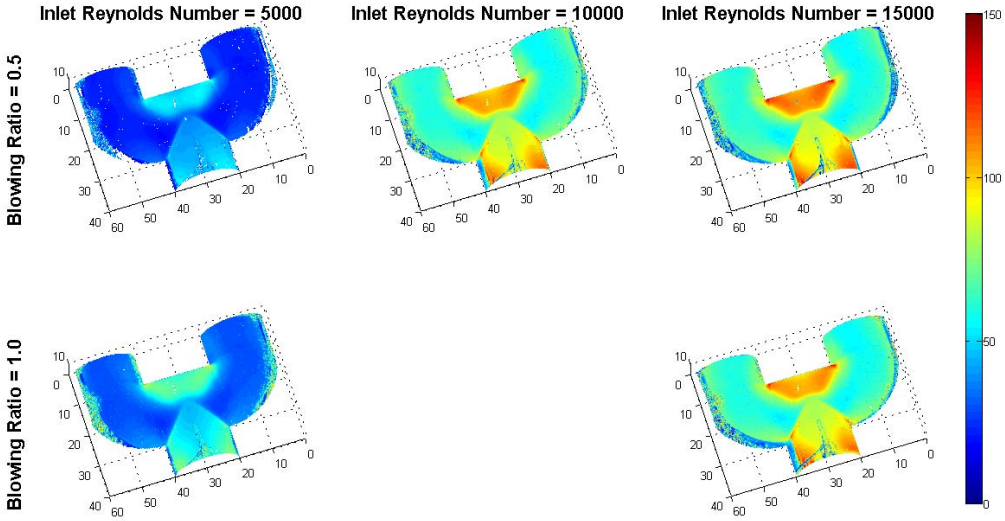


Test Data
Average htc = 87.8W/m^2/K
Total htc-area product = 0.649W/K
Nusselt Number = 70.2

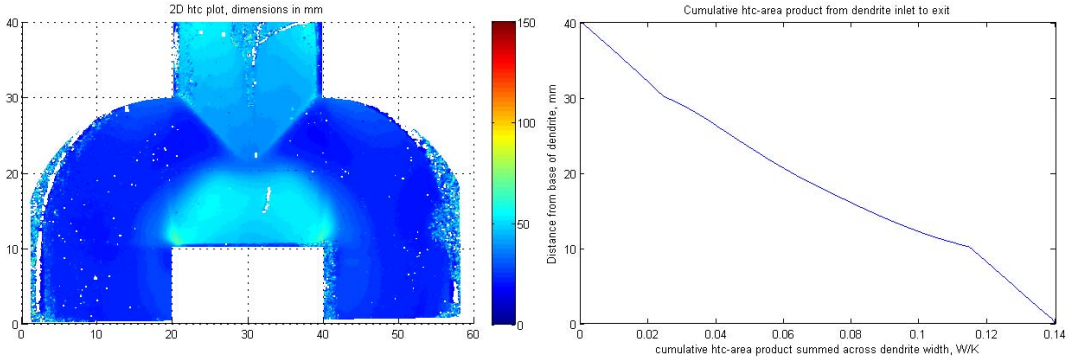
Engine Scaled Data
Average Engine Scaled htc = 5555.9W/m^2/K
Total htc-area product = 0.072W/K
Engine Scaled Nusselt Number = 70.2

B.3.1.2 Middle Branch





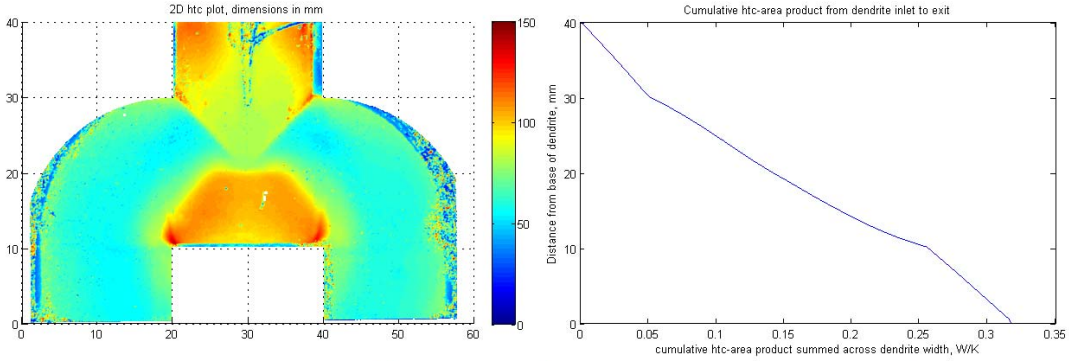
1-2-4-8 Middle: Blowing Ratio = 0.5, Dendrite Inlet Reynolds Number = 5000, Branch Inlet Reynolds Number = 2500



Test Data
Average htc = 32.3W/m^2/K
Total htc-area product = 0.158W/K
Nusselt Number = 25.8

Engine Scaled Data
Average Engine Scaled htc = 2044.4W/m^2/K
Total htc-area product = 0.018W/K
Engine Scaled Nusselt Number = 25.8

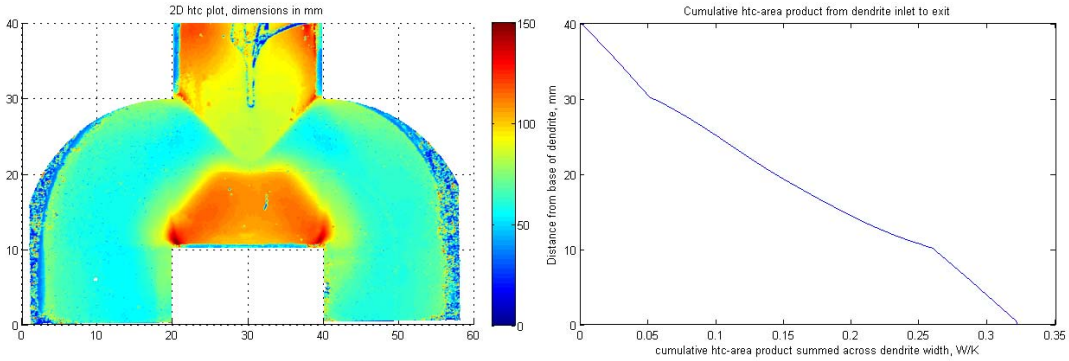
1-2-4-8 Middle: Blowing Ratio = 0.5, Dendrite Inlet Reynolds Number = 10000, Branch Inlet Reynolds Number = 5000



Test Data
Average htc = 71.8W/m^2/K
Total htc-area product = 0.352W/K
Nusselt Number = 57.4

Engine Scaled Data
Average Engine Scaled htc = 4542.2W/m^2/K
Total htc-area product = 0.039W/K
Engine Scaled Nusselt Number = 57.4

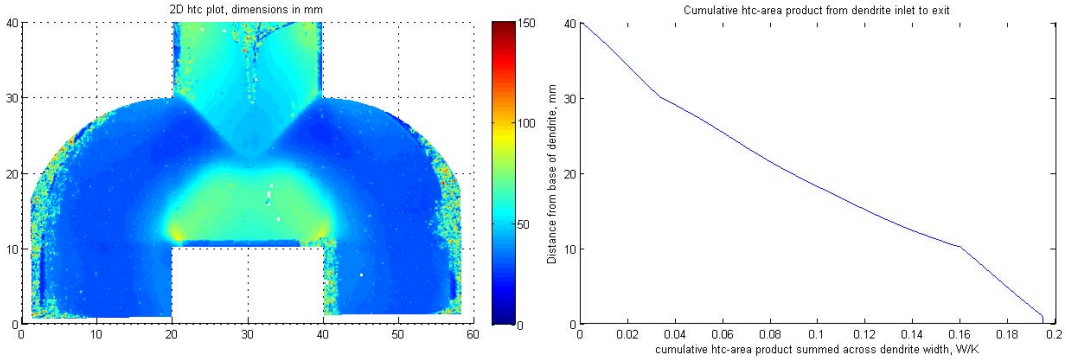
1-2-4-8 Middle: Blowing Ratio = 0.5, Dendrite Inlet Reynolds Number = 15000, Branch Inlet Reynolds Number = 7500



Test Data
Average htc = 72.1W/m^2/K
Total htc-area product = 0.354W/K
Nusselt Number = 57.7

Engine Scaled Data
Average Engine Scaled htc = 4565.3W/m^2/K
Total htc-area product = 0.039W/K
Engine Scaled Nusselt Number = 57.7

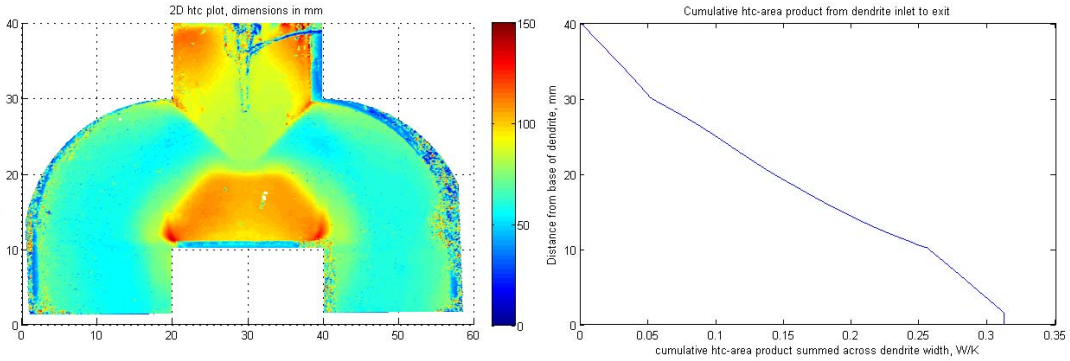
1-2-4-8 Middle: Blowing Ratio = 1.0, Dendrite Inlet Reynolds Number = 5000, Branch Inlet Reynolds Number = 2500



Test Data
Average htc = 44.4W/m^2/K
Total htc-area product = 0.218W/K
Nusselt Number = 35.5

Engine Scaled Data
Average Engine Scaled htc = 2811.8W/m^2/K
Total htc-area product = 0.024W/K
Engine Scaled Nusselt Number = 35.5

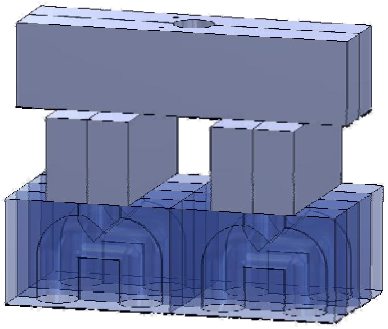
1-2-4-8 Middle: Blowing Ratio = 1.0, Dendrite Inlet Reynolds Number = 15000, Branch Inlet Reynolds Number = 7500

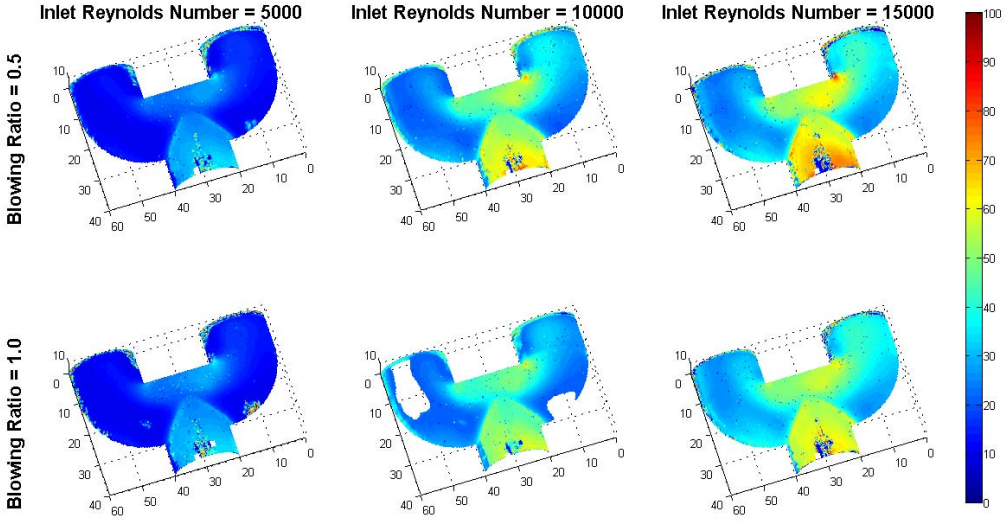


Test Data
Average htc = 71.3W/m^2/K
Total htc-area product = 0.350W/K
Nusselt Number = 57.1

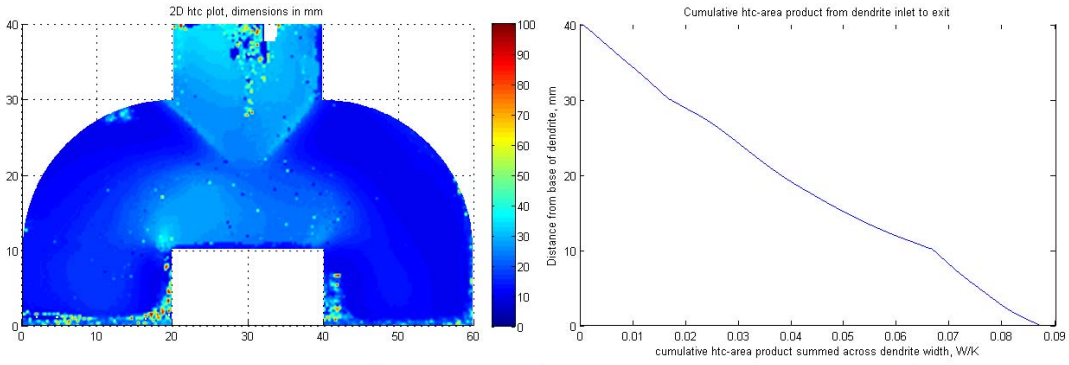
Engine Scaled Data
Average Engine Scaled htc = 4512.8W/m^2/K
Total htc-area product = 0.039W/K
Engine Scaled Nusselt Number = 57.1

B.3.1.3 Exit Branch





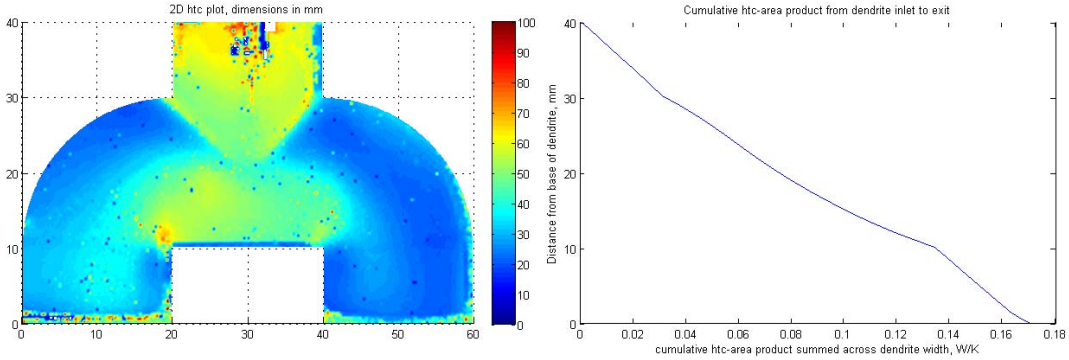
1-2-4-8 Exit: Blowing Ratio = 0.5, Dendrite Inlet Reynolds Number = 5000, Branch Inlet Reynolds Number = 1250



Test Data
Average htc = 18.3W/m^2/K
Total htc-area product = 0.090W/K
Nusselt Number = 14.6

Engine Scaled Data
Average Engine Scaled htc = 1155.9W/m^2/K
Total htc-area product = 0.010W/K
Engine Scaled Nusselt Number = 14.6

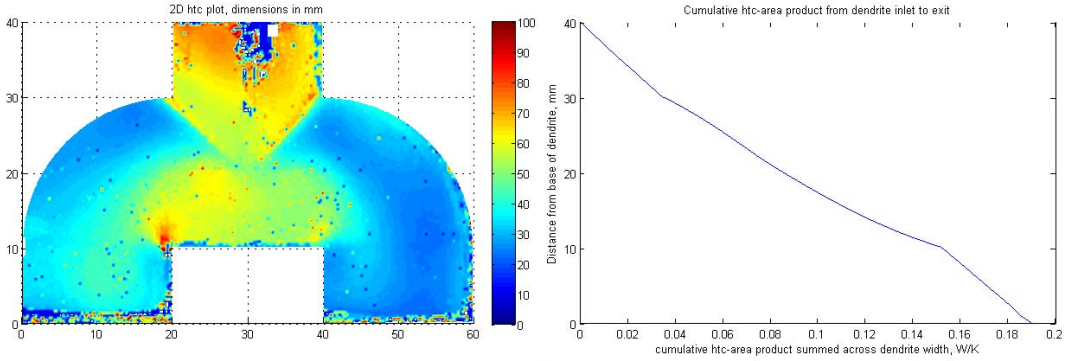
1-2-4-8 Exit: Blowing Ratio = 0.5, Dendrite Inlet Reynolds Number = 10000, Branch Inlet Reynolds Number = 2500



Test Data
Average htc = 35.7W/m^2/K
Total htc-area product = 0.175W/K
Nusselt Number = 28.6

Engine Scaled Data
Average Engine Scaled htc = 2261.4W/m^2/K
Total htc-area product = 0.020W/K
Engine Scaled Nusselt Number = 28.6

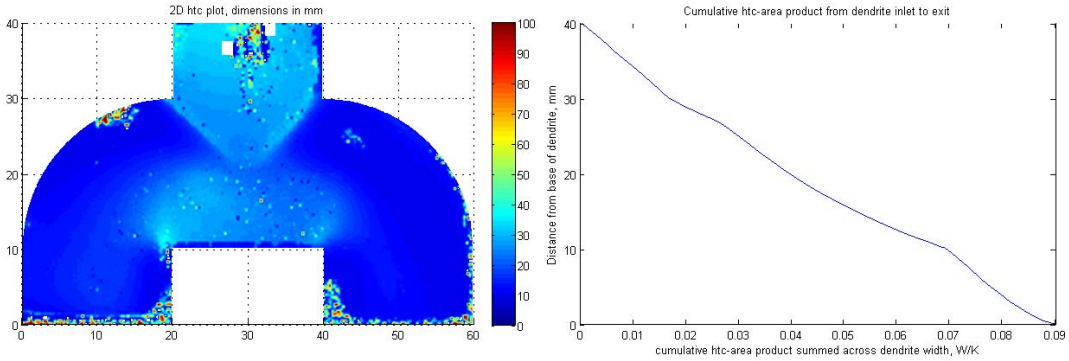
1-2-4-8 Exit: Blowing Ratio = 0.5, Dendrite Inlet Reynolds Number = 15000, Branch Inlet Reynolds Number = 3750



Test Data
Average htc = 40.0W/m^2/K
Total htc-area product = 0.196W/K
Nusselt Number = 32.0

Engine Scaled Data
Average Engine Scaled htc = 2532.6W/m^2/K
Total htc-area product = 0.022W/K
Engine Scaled Nusselt Number = 32.0

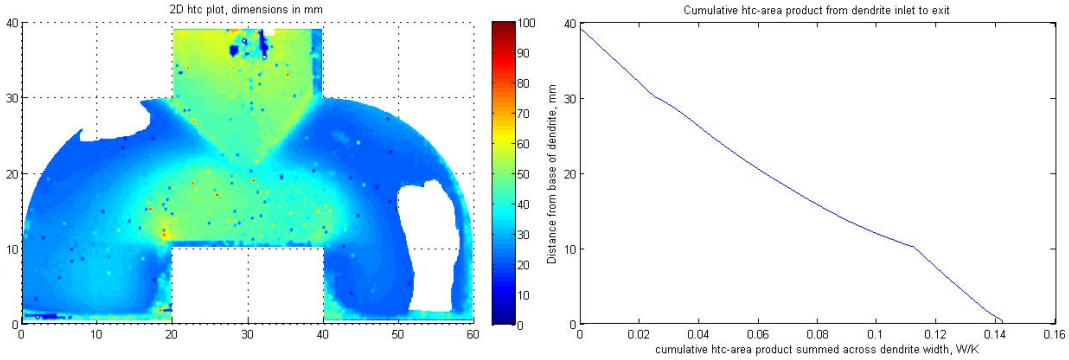
1-2-4-8 Exit: Blowing Ratio = 1.0, Dendrite Inlet Reynolds Number = 5000, Branch Inlet Reynolds Number = 1250



Test Data
Average htc = 18.9W/m^2/K
Total htc-area product = 0.093W/K
Nusselt Number = 15.1

Engine Scaled Data
Average Engine Scaled htc = 1198.1W/m^2/K
Total htc-area product = 0.010W/K
Engine Scaled Nusselt Number = 15.1

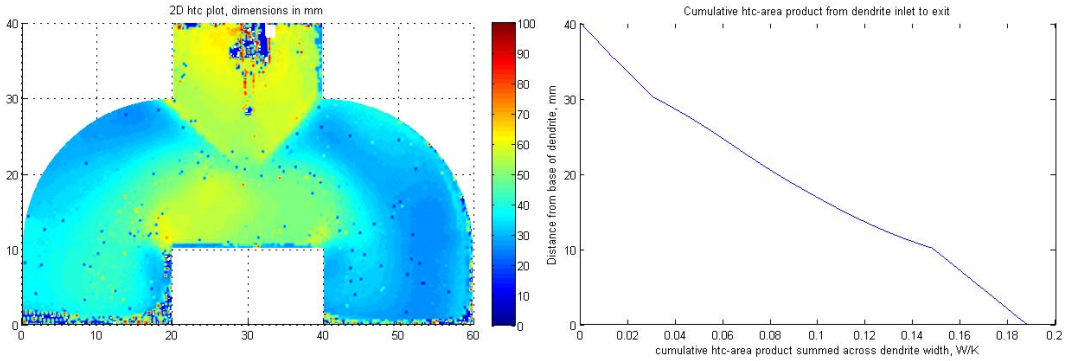
1-2-4-8 Exit: Blowing Ratio = 1.0, Dendrite Inlet Reynolds Number = 10000, Branch Inlet Reynolds Number = 2500



Test Data
Average htc = 33.2W/m^2/K
Total htc-area product = 0.163W/K
Nusselt Number = 26.5

Engine Scaled Data
Average Engine Scaled htc = 2098.9W/m^2/K
Total htc-area product = 0.018W/K
Engine Scaled Nusselt Number = 26.5

1-2-4-8 Exit: Blowing Ratio = 1.0, Dendrite Inlet Reynolds Number = 15000, Branch Inlet Reynolds Number = 3750



Test Data
Average htc = 39.5W/m^2/K
Total htc-area product = 0.194W/K
Nusselt Number = 31.6

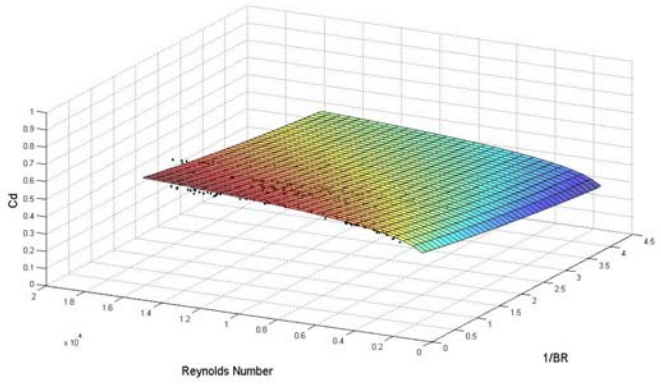
Engine Scaled Data
Average Engine Scaled htc = 2501.1W/m^2/K
Total htc-area product = 0.022W/K
Engine Scaled Nusselt Number = 31.6

Appendix C Dendritic Loss Data

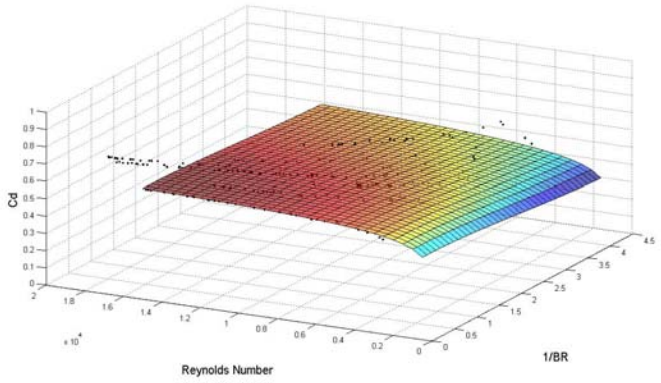
C.1 3D Surface Plots of Experimental Data

In this section the three surface plots used to generate the correlations in section 6.2 are presented

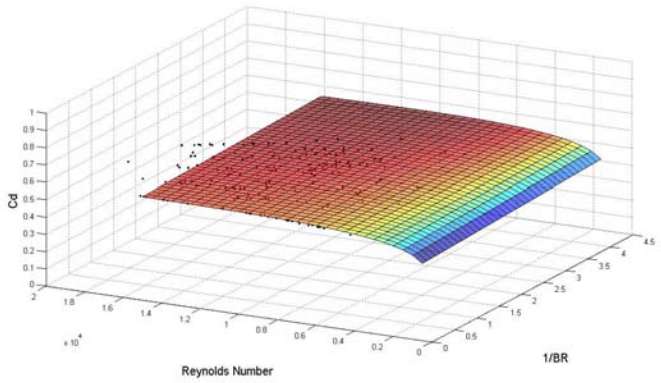
C.1.1 1-2 Surface Plot of Discharge Coefficient vs Re vs 1/BR



C.1.2 1-2-4 Surface Plot of Discharge Coefficient vs Re vs 1/BR

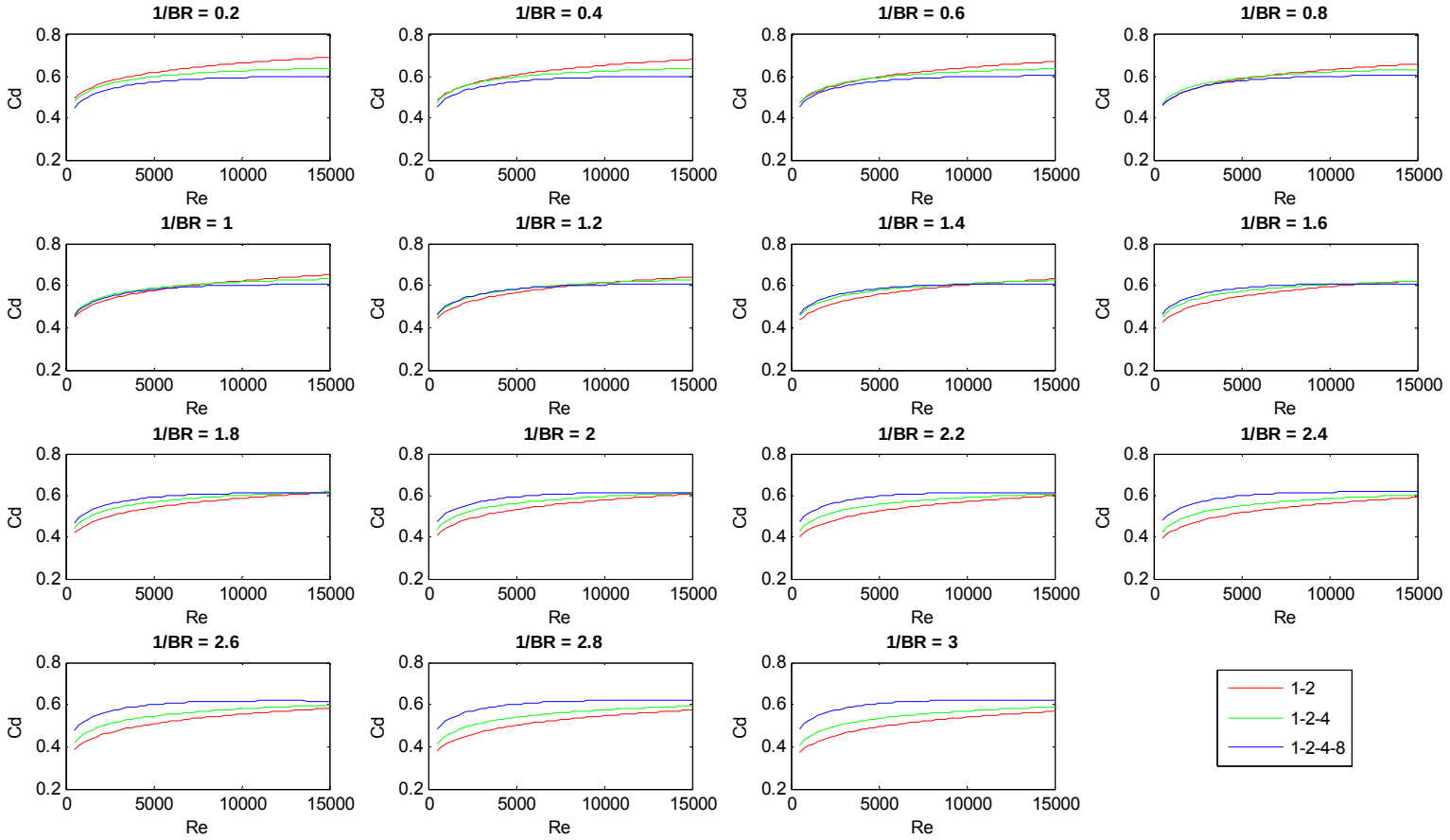


C.1.3 1-2-4-8 Surface Plot of Discharge Coefficient vs Re vs 1/BR

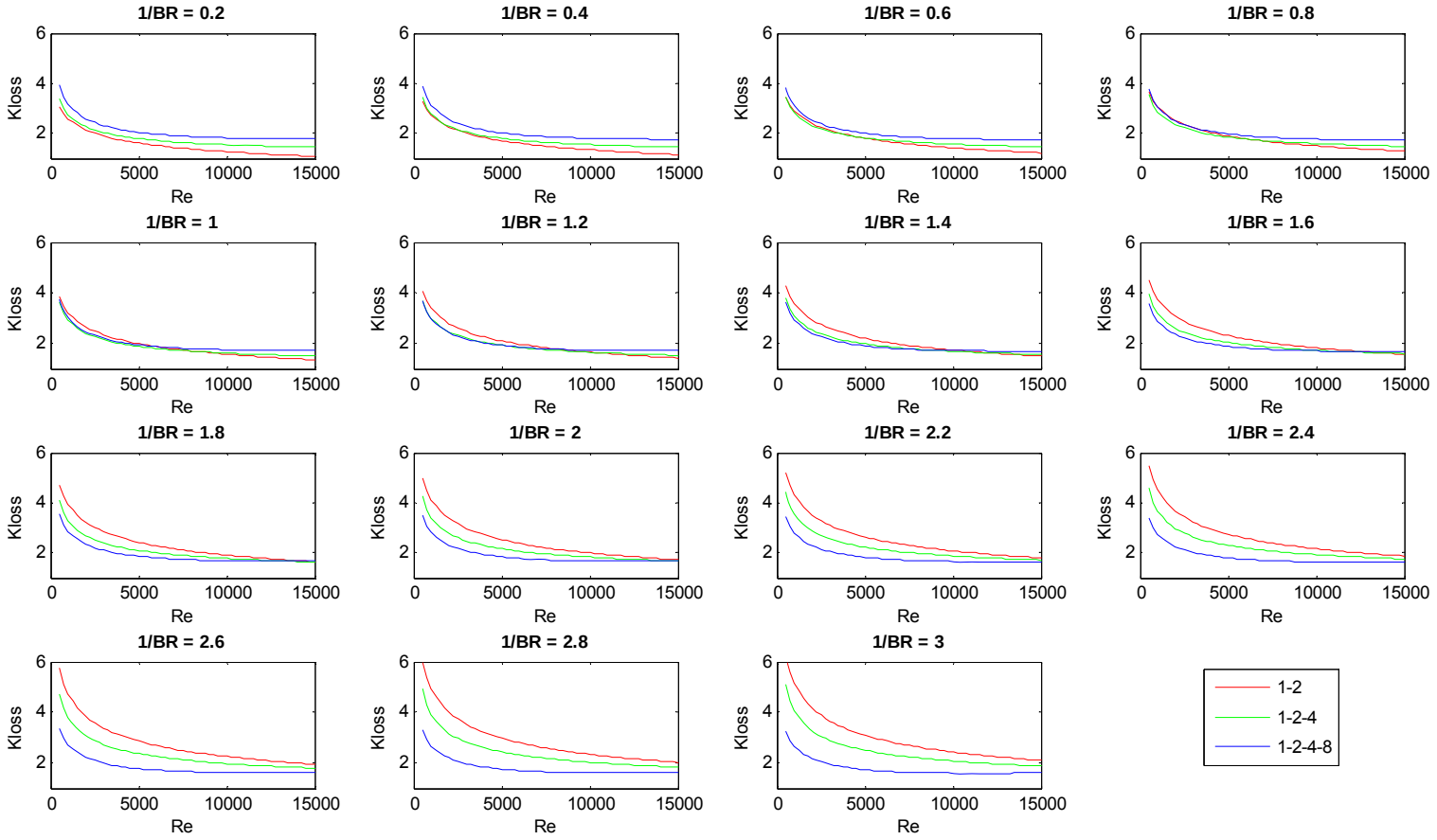


C.2 Loss Comparison of the Different Dendritic Configurations Using the Surface Fits

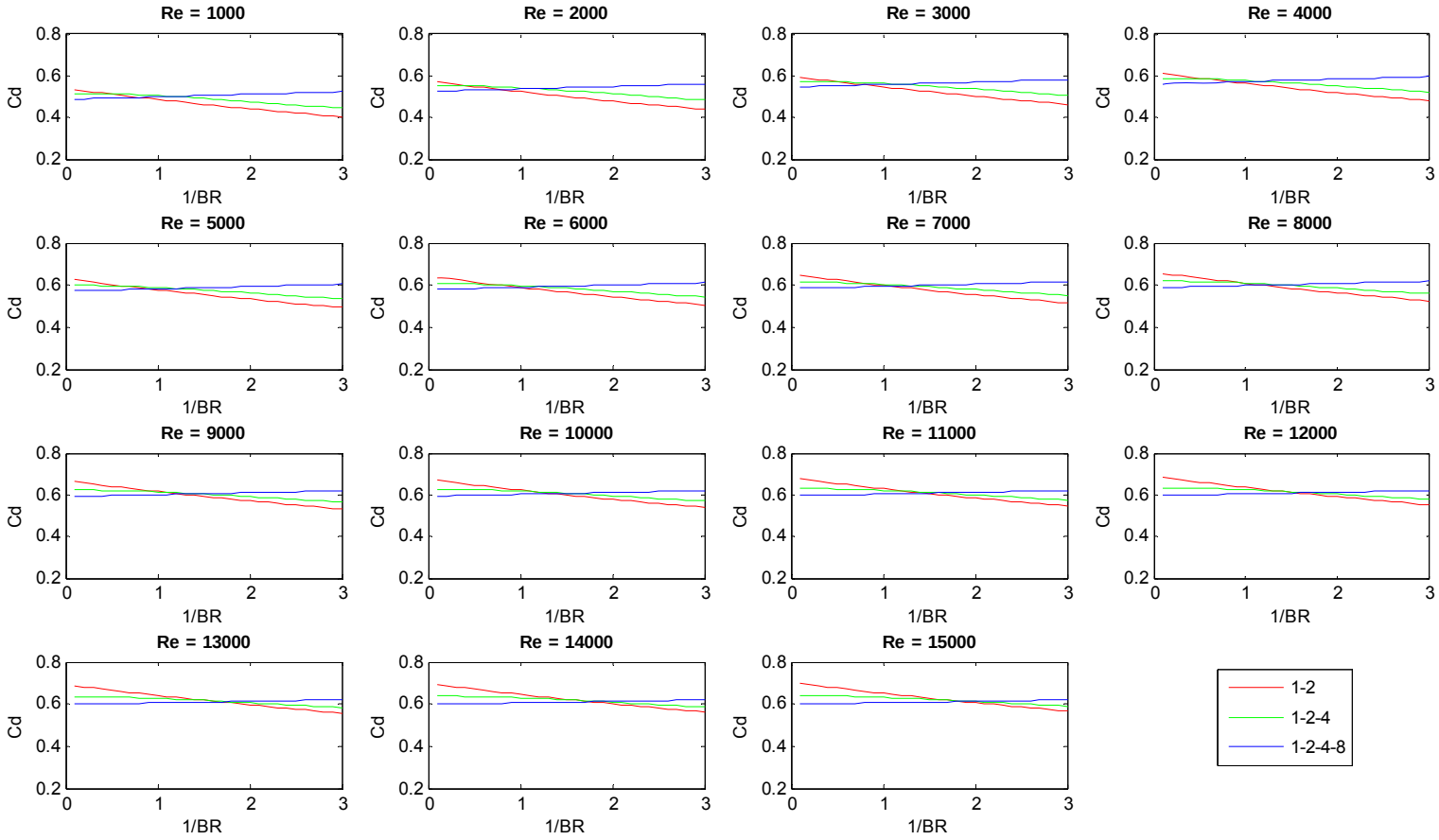
C.2.1 Loss in Terms of Discharge Coefficient for Fixed Inverse Blowing Ratios at Uniform Intervals



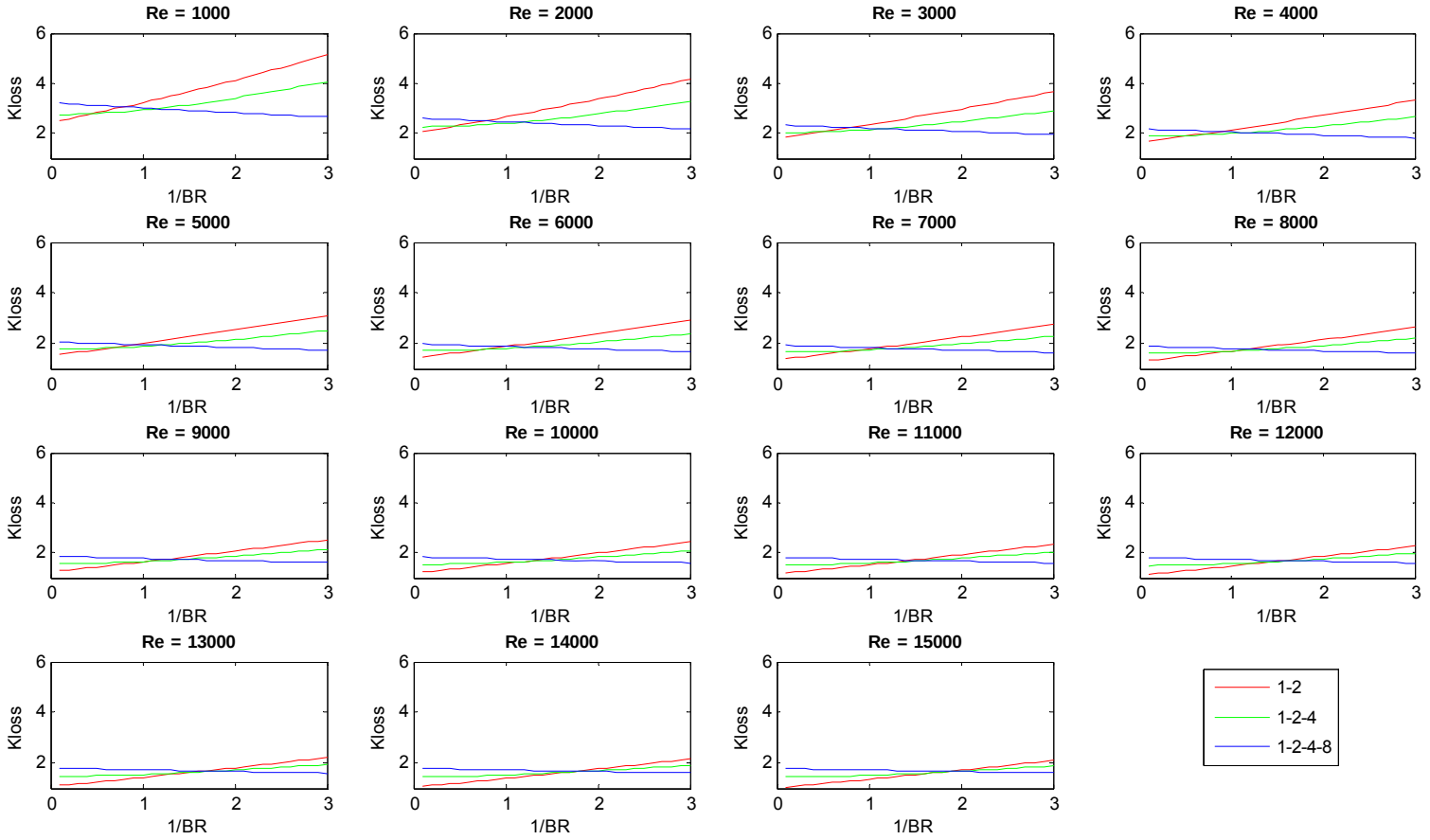
C.2.2 Loss in Terms of Dynamic Head for Fixed Inverse Blowing Ratios at Uniform Intervals



C.2.3 Loss in Terms of Discharge Coefficient for Fixed Reynolds Numbers at Uniform Intervals



C.2.4 Loss in Terms of Dynamic Head for Fixed Reynolds Numbers at Uniform Intervals



C.3 Tabulated Loss Data

For the purposes of implementing the loss data in an industrial application the generation of simple look up tables was felt to be the most appropriate way to format the data. Three sets of tables were generated, each set consisting of two tables; one for the loss in terms of discharge coefficient (the first table in each set) and one for loss in terms of inlet dynamic head (the second table in each set) giving a total of six look up tables.

The loss values which populate the look up tables are generated from the best fit functions outlined in Chapter 6. The values highlighted in red in the following tables represent data outside the range for which experimental data was obtained and as such the loss behaviour in this area is based upon the inferred fit.

1-2 Loss Data Matrices

BR	Reynolds number														
	1000	2000	3000	4000	5000	6000	7000	8000	9000	10000	11000	12000	13000	14000	15000
inf	0.539	0.576	0.599	0.616	0.63	0.642	0.652	0.66	0.668	0.675	0.682	0.688	0.694	0.699	0.704
0.3	0.392	0.428	0.452	0.469	0.483	0.494	0.504	0.513	0.521	0.528	0.535	0.541	0.546	0.552	0.557
0.4	0.422	0.458	0.482	0.499	0.513	0.524	0.534	0.543	0.551	0.558	0.565	0.571	0.576	0.582	0.586
0.5	0.442	0.478	0.502	0.519	0.533	0.544	0.554	0.563	0.571	0.578	0.585	0.591	0.596	0.602	0.606
0.6	0.456	0.492	0.516	0.533	0.547	0.558	0.568	0.577	0.585	0.592	0.599	0.605	0.61	0.616	0.621
0.7	0.466	0.503	0.526	0.544	0.557	0.569	0.579	0.588	0.596	0.603	0.609	0.615	0.621	0.626	0.631
0.8	0.475	0.511	0.535	0.552	0.566	0.577	0.587	0.596	0.604	0.611	0.618	0.624	0.629	0.634	0.639
0.9	0.481	0.518	0.541	0.558	0.572	0.584	0.594	0.603	0.61	0.618	0.624	0.63	0.636	0.641	0.646
1	0.486	0.523	0.546	0.564	0.578	0.589	0.599	0.608	0.616	0.623	0.63	0.636	0.641	0.646	0.651
1.1	0.491	0.528	0.551	0.568	0.582	0.594	0.604	0.612	0.62	0.627	0.634	0.64	0.646	0.651	0.656
1.2	0.495	0.531	0.555	0.572	0.586	0.597	0.607	0.616	0.624	0.631	0.638	0.644	0.649	0.655	0.659
1.3	0.498	0.535	0.558	0.575	0.589	0.601	0.611	0.619	0.627	0.634	0.641	0.647	0.653	0.658	0.663
1.4	0.501	0.537	0.561	0.578	0.592	0.603	0.613	0.622	0.63	0.637	0.644	0.65	0.655	0.661	0.665
1.5	0.503	0.54	0.563	0.58	0.594	0.606	0.616	0.625	0.632	0.64	0.646	0.652	0.658	0.663	0.668
1.6	0.505	0.542	0.565	0.582	0.596	0.608	0.618	0.627	0.635	0.642	0.648	0.654	0.66	0.665	0.67
1.7	0.507	0.544	0.567	0.584	0.598	0.61	0.62	0.629	0.636	0.644	0.65	0.656	0.662	0.667	0.672
1.8	0.509	0.545	0.569	0.586	0.6	0.611	0.621	0.63	0.638	0.645	0.652	0.658	0.663	0.669	0.674
1.9	0.51	0.547	0.57	0.588	0.601	0.613	0.623	0.632	0.64	0.647	0.653	0.659	0.665	0.67	0.675
2	0.512	0.548	0.572	0.589	0.603	0.614	0.624	0.633	0.641	0.648	0.655	0.661	0.666	0.672	0.676
2.1	0.513	0.55	0.573	0.59	0.604	0.616	0.626	0.634	0.642	0.649	0.656	0.662	0.668	0.673	0.678
2.2	0.514	0.551	0.574	0.591	0.605	0.617	0.627	0.636	0.643	0.651	0.657	0.663	0.669	0.674	0.679

2.3	0.515	0.552	0.575	0.592	0.606	0.618	0.628	0.637	0.644	0.652	0.658	0.664	0.67	0.675	0.68
2.4	0.516	0.553	0.576	0.593	0.607	0.619	0.629	0.638	0.645	0.653	0.659	0.665	0.671	0.676	0.681
2.5	0.517	0.554	0.577	0.594	0.608	0.62	0.63	0.638	0.646	0.653	0.66	0.666	0.672	0.677	0.682
2.6	0.518	0.554	0.578	0.595	0.609	0.62	0.63	0.639	0.647	0.654	0.661	0.667	0.672	0.678	0.683
2.7	0.519	0.555	0.578	0.596	0.61	0.621	0.631	0.64	0.648	0.655	0.662	0.668	0.673	0.678	0.683

BR	Reynolds number														
	1000	2000	3000	4000	5000	6000	7000	8000	9000	10000	11000	12000	13000	14000	15000
inf	2.443	2.018	1.788	1.634	1.519	1.429	1.355	1.293	1.239	1.192	1.15	1.112	1.079	1.048	1.019
0.3	5.514	4.447	3.901	3.546	3.289	3.09	2.929	2.796	2.682	2.583	2.496	2.418	2.349	2.286	2.228
0.4	4.623	3.76	3.311	3.018	2.803	2.637	2.502	2.389	2.293	2.209	2.135	2.07	2.01	1.956	1.907
0.5	4.127	3.372	2.976	2.715	2.524	2.376	2.255	2.154	2.067	1.992	1.925	1.866	1.813	1.764	1.719
0.6	3.813	3.124	2.76	2.52	2.344	2.207	2.095	2.001	1.92	1.85	1.789	1.733	1.683	1.638	1.597
0.7	3.597	2.952	2.61	2.384	2.218	2.088	1.982	1.894	1.818	1.751	1.693	1.64	1.593	1.55	1.51
0.8	3.44	2.826	2.5	2.284	2.126	2.001	1.9	1.815	1.742	1.678	1.621	1.571	1.526	1.484	1.446
0.9	3.32	2.73	2.416	2.208	2.054	1.934	1.836	1.754	1.683	1.621	1.567	1.518	1.474	1.434	1.397
1	3.225	2.654	2.35	2.147	1.998	1.881	1.786	1.706	1.637	1.577	1.523	1.476	1.433	1.394	1.358
1.1	3.149	2.593	2.296	2.098	1.953	1.838	1.745	1.667	1.599	1.54	1.488	1.442	1.399	1.361	1.326
1.2	3.087	2.542	2.252	2.058	1.915	1.803	1.711	1.634	1.568	1.51	1.459	1.413	1.372	1.334	1.3
1.3	3.034	2.5	2.214	2.024	1.883	1.773	1.683	1.607	1.542	1.485	1.435	1.389	1.349	1.311	1.277
1.4	2.99	2.464	2.183	1.995	1.856	1.748	1.659	1.584	1.52	1.463	1.414	1.369	1.329	1.292	1.258
1.5	2.951	2.433	2.155	1.97	1.833	1.726	1.638	1.564	1.5	1.445	1.396	1.351	1.312	1.275	1.242
1.6	2.918	2.406	2.131	1.948	1.813	1.707	1.62	1.546	1.483	1.429	1.38	1.336	1.297	1.261	1.228
1.7	2.889	2.382	2.111	1.929	1.795	1.69	1.604	1.531	1.469	1.414	1.366	1.323	1.284	1.248	1.215
1.8	2.863	2.361	2.092	1.912	1.779	1.675	1.589	1.517	1.456	1.402	1.354	1.311	1.272	1.237	1.204
1.9	2.84	2.343	2.076	1.897	1.765	1.662	1.577	1.505	1.444	1.39	1.343	1.3	1.262	1.226	1.194
2	2.819	2.326	2.061	1.884	1.753	1.65	1.565	1.494	1.433	1.38	1.333	1.29	1.252	1.217	1.185
2.1	2.801	2.311	2.047	1.871	1.741	1.639	1.555	1.485	1.424	1.371	1.324	1.282	1.244	1.209	1.177
2.2	2.784	2.297	2.035	1.86	1.731	1.629	1.546	1.476	1.415	1.363	1.316	1.274	1.236	1.202	1.17
2.3	2.769	2.285	2.024	1.85	1.722	1.62	1.537	1.468	1.408	1.355	1.309	1.267	1.229	1.195	1.163
2.4	2.754	2.273	2.014	1.841	1.713	1.612	1.53	1.46	1.4	1.348	1.302	1.26	1.223	1.189	1.157
2.5	2.742	2.263	2.005	1.833	1.705	1.605	1.523	1.453	1.394	1.342	1.296	1.254	1.217	1.183	1.152
2.6	2.73	2.253	1.996	1.825	1.698	1.598	1.516	1.447	1.388	1.336	1.29	1.249	1.211	1.178	1.146

2.7	2.719	2.244	1.988	1.818	1.691	1.591	1.51	1.441	1.382	1.33	1.285	1.244	1.206	1.173	1.142

1-2-4 Loss Data Matrices

BR	Reynolds number														
	1000	2000	3000	4000	5000	6000	7000	8000	9000	10000	11000	12000	13000	14000	15000
inf	0.516	0.554	0.575	0.589	0.599	0.607	0.614	0.619	0.623	0.627	0.631	0.633	0.636	0.638	0.64
0.3	0.436	0.476	0.498	0.514	0.526	0.536	0.544	0.552	0.558	0.563	0.568	0.572	0.576	0.58	0.583
0.4	0.46	0.499	0.521	0.536	0.548	0.557	0.565	0.572	0.577	0.582	0.587	0.591	0.594	0.597	0.6
0.5	0.476	0.514	0.536	0.551	0.563	0.572	0.579	0.585	0.59	0.595	0.599	0.603	0.606	0.609	0.612
0.6	0.487	0.525	0.546	0.561	0.572	0.581	0.588	0.594	0.599	0.603	0.607	0.611	0.614	0.617	0.619
0.7	0.494	0.532	0.553	0.568	0.578	0.587	0.594	0.6	0.605	0.609	0.613	0.616	0.619	0.622	0.624
0.8	0.498	0.536	0.558	0.572	0.583	0.591	0.598	0.604	0.609	0.613	0.617	0.62	0.623	0.625	0.628
0.9	0.502	0.54	0.561	0.575	0.586	0.594	0.601	0.607	0.612	0.616	0.619	0.623	0.625	0.628	0.63
1	0.505	0.542	0.563	0.578	0.588	0.597	0.603	0.609	0.614	0.618	0.621	0.625	0.627	0.63	0.632
1.1	0.507	0.544	0.565	0.58	0.59	0.598	0.605	0.611	0.615	0.619	0.623	0.626	0.629	0.631	0.633
1.2	0.508	0.546	0.567	0.581	0.592	0.6	0.606	0.612	0.617	0.621	0.624	0.627	0.63	0.632	0.634
1.3	0.509	0.547	0.568	0.582	0.593	0.601	0.608	0.613	0.618	0.622	0.625	0.628	0.631	0.633	0.635
1.4	0.51	0.548	0.569	0.583	0.594	0.602	0.608	0.614	0.618	0.622	0.626	0.629	0.631	0.634	0.636
1.5	0.511	0.549	0.57	0.584	0.594	0.602	0.609	0.614	0.619	0.623	0.626	0.629	0.632	0.634	0.636
1.6	0.512	0.549	0.57	0.584	0.595	0.603	0.61	0.615	0.62	0.624	0.627	0.63	0.632	0.635	0.637
1.7	0.512	0.55	0.571	0.585	0.595	0.603	0.61	0.615	0.62	0.624	0.627	0.63	0.633	0.635	0.637
1.8	0.513	0.55	0.571	0.585	0.596	0.604	0.61	0.616	0.62	0.624	0.628	0.631	0.633	0.635	0.638
1.9	0.513	0.551	0.571	0.586	0.596	0.604	0.611	0.616	0.621	0.625	0.628	0.631	0.633	0.636	0.638
2	0.513	0.551	0.572	0.586	0.596	0.604	0.611	0.616	0.621	0.625	0.628	0.631	0.634	0.636	0.638
2.1	0.514	0.551	0.572	0.586	0.597	0.605	0.611	0.617	0.621	0.625	0.628	0.631	0.634	0.636	0.638
2.2	0.514	0.551	0.572	0.586	0.597	0.605	0.611	0.617	0.621	0.625	0.629	0.632	0.634	0.636	0.638
2.3	0.514	0.552	0.572	0.587	0.597	0.605	0.612	0.617	0.622	0.625	0.629	0.632	0.634	0.637	0.639
2.4	0.514	0.552	0.573	0.587	0.597	0.605	0.612	0.617	0.622	0.626	0.629	0.632	0.634	0.637	0.639
2.5	0.514	0.552	0.573	0.587	0.597	0.605	0.612	0.617	0.622	0.626	0.629	0.632	0.635	0.637	0.639
2.6	0.515	0.552	0.573	0.587	0.597	0.606	0.612	0.617	0.622	0.626	0.629	0.632	0.635	0.637	0.639
2.7	0.515	0.552	0.573	0.587	0.598	0.606	0.612	0.618	0.622	0.626	0.629	0.632	0.635	0.637	0.639

BR	Reynolds number														
	1000	2000	3000	4000	5000	6000	7000	8000	9000	10000	11000	12000	13000	14000	15000
inf	2.751	2.26	2.028	1.885	1.786	1.713	1.656	1.61	1.572	1.541	1.515	1.492	1.472	1.455	1.44
0.3	4.259	3.422	3.028	2.782	2.609	2.477	2.373	2.288	2.216	2.154	2.1	2.052	2.01	1.972	1.937
0.4	3.728	3.02	2.684	2.476	2.33	2.22	2.132	2.061	2.001	1.951	1.906	1.868	1.833	1.803	1.775
0.5	3.414	2.778	2.477	2.29	2.16	2.062	1.984	1.921	1.869	1.824	1.786	1.752	1.723	1.696	1.673
0.6	3.225	2.632	2.351	2.177	2.055	1.964	1.893	1.835	1.787	1.746	1.711	1.681	1.654	1.63	1.609
0.7	3.105	2.538	2.27	2.104	1.988	1.902	1.834	1.779	1.734	1.695	1.663	1.634	1.609	1.587	1.567
0.8	3.025	2.476	2.215	2.055	1.943	1.859	1.794	1.741	1.698	1.661	1.63	1.603	1.579	1.558	1.539
0.9	2.969	2.432	2.177	2.02	1.911	1.83	1.766	1.715	1.673	1.637	1.607	1.58	1.557	1.537	1.519
1	2.928	2.4	2.15	1.995	1.888	1.808	1.746	1.696	1.654	1.619	1.59	1.564	1.542	1.522	1.505
1.1	2.898	2.376	2.129	1.977	1.871	1.792	1.73	1.681	1.64	1.606	1.577	1.552	1.53	1.511	1.494
1.2	2.875	2.358	2.113	1.962	1.857	1.779	1.719	1.67	1.63	1.596	1.567	1.543	1.521	1.502	1.485
1.3	2.857	2.344	2.101	1.951	1.847	1.77	1.71	1.661	1.621	1.588	1.56	1.535	1.514	1.495	1.479
1.4	2.842	2.332	2.091	1.942	1.839	1.762	1.702	1.654	1.615	1.582	1.554	1.529	1.508	1.49	1.474
1.5	2.831	2.323	2.083	1.935	1.832	1.756	1.696	1.649	1.609	1.577	1.549	1.525	1.504	1.485	1.469
1.6	2.821	2.315	2.076	1.929	1.827	1.751	1.691	1.644	1.605	1.572	1.545	1.521	1.5	1.482	1.466
1.7	2.813	2.309	2.071	1.924	1.822	1.746	1.687	1.64	1.601	1.569	1.541	1.517	1.497	1.479	1.463
1.8	2.806	2.304	2.066	1.92	1.818	1.743	1.684	1.637	1.598	1.566	1.538	1.515	1.494	1.476	1.46
1.9	2.801	2.299	2.062	1.916	1.815	1.74	1.681	1.634	1.596	1.563	1.536	1.512	1.492	1.474	1.458
2	2.796	2.296	2.059	1.913	1.812	1.737	1.679	1.632	1.593	1.561	1.534	1.51	1.49	1.472	1.457
2.1	2.792	2.292	2.056	1.911	1.81	1.735	1.676	1.63	1.591	1.559	1.532	1.509	1.488	1.471	1.455
2.2	2.788	2.289	2.054	1.908	1.808	1.733	1.675	1.628	1.59	1.558	1.531	1.507	1.487	1.469	1.454
2.3	2.785	2.287	2.051	1.906	1.806	1.731	1.673	1.626	1.588	1.556	1.529	1.506	1.486	1.468	1.453
2.4	2.782	2.285	2.05	1.905	1.804	1.73	1.672	1.625	1.587	1.555	1.528	1.505	1.485	1.467	1.452
2.5	2.78	2.283	2.048	1.903	1.803	1.728	1.67	1.624	1.586	1.554	1.527	1.504	1.484	1.466	1.451
2.6	2.778	2.281	2.046	1.902	1.802	1.727	1.669	1.623	1.585	1.553	1.526	1.503	1.483	1.465	1.45
2.7	2.776	2.28	2.045	1.901	1.8	1.726	1.668	1.622	1.584	1.552	1.525	1.502	1.482	1.465	1.449

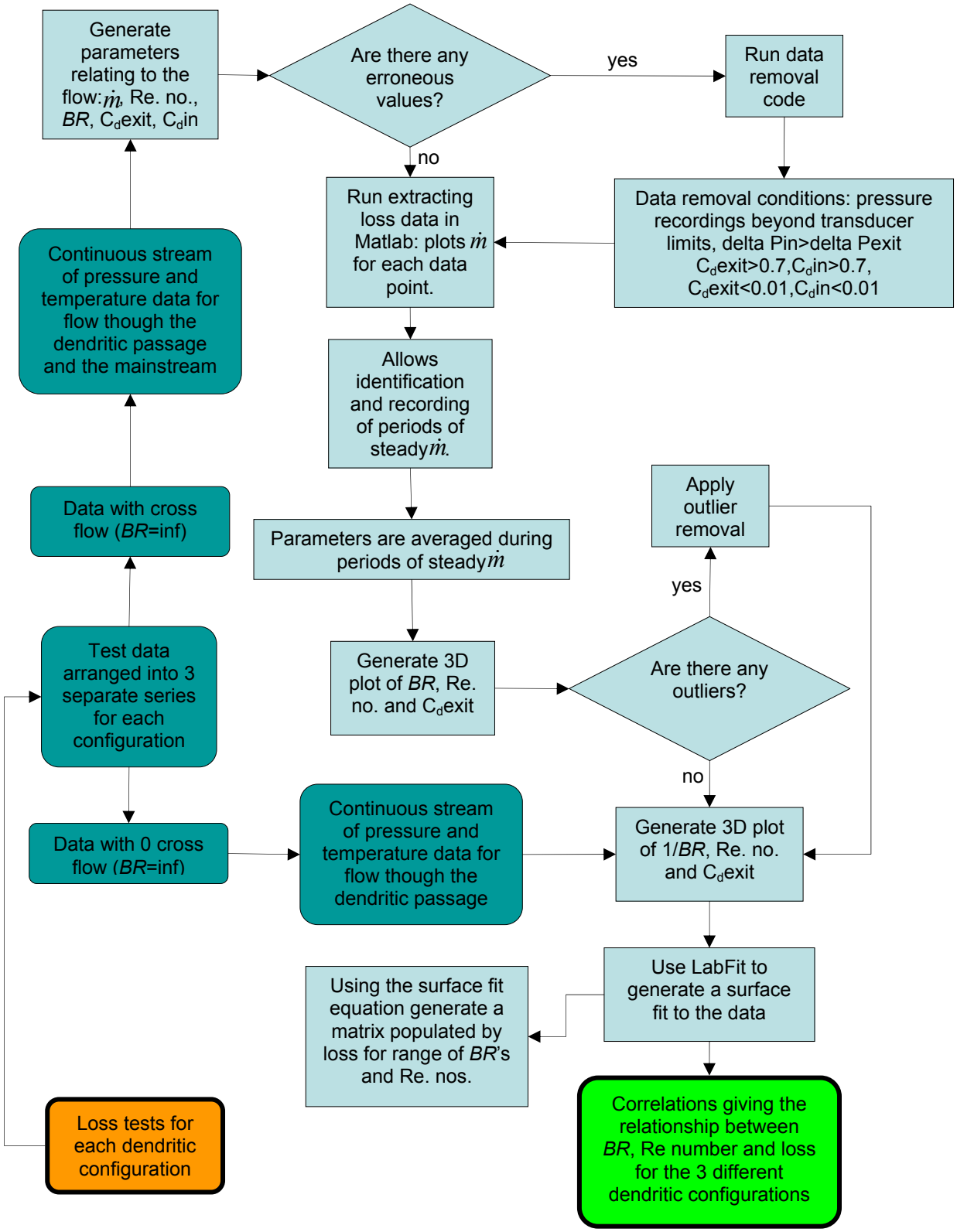
1-2-8 Loss Data Matrices

BR	Reynolds number														
	1000	2000	3000	4000	5000	6000	7000	8000	9000	10000	11000	12000	13000	14000	15000
inf	0.487	0.525	0.547	0.561	0.571	0.578	0.584	0.588	0.591	0.593	0.595	0.596	0.598	0.598	0.599
0.3	0.528	0.565	0.586	0.6	0.608	0.615	0.619	0.621	0.623	0.624	0.624	0.624	0.623	0.623	0.622
0.4	0.517	0.555	0.576	0.59	0.599	0.605	0.61	0.613	0.615	0.616	0.617	0.617	0.617	0.617	0.616
0.5	0.511	0.549	0.57	0.584	0.593	0.6	0.605	0.608	0.61	0.611	0.612	0.613	0.613	0.613	0.613
0.6	0.507	0.545	0.566	0.58	0.59	0.596	0.601	0.605	0.607	0.608	0.609	0.61	0.61	0.611	0.611
0.7	0.504	0.542	0.564	0.577	0.587	0.594	0.599	0.602	0.605	0.606	0.607	0.608	0.609	0.609	0.609
0.8	0.502	0.54	0.561	0.575	0.585	0.592	0.597	0.6	0.603	0.605	0.606	0.607	0.607	0.608	0.608
0.9	0.5	0.539	0.56	0.574	0.583	0.59	0.595	0.599	0.602	0.603	0.605	0.606	0.606	0.606	0.607
1	0.499	0.537	0.559	0.572	0.582	0.589	0.594	0.598	0.601	0.602	0.604	0.605	0.605	0.606	0.606
1.1	0.498	0.536	0.557	0.571	0.581	0.588	0.593	0.597	0.6	0.602	0.603	0.604	0.605	0.605	0.605
1.2	0.497	0.535	0.557	0.571	0.58	0.587	0.592	0.596	0.599	0.601	0.602	0.603	0.604	0.604	0.605
1.3	0.496	0.534	0.556	0.57	0.58	0.587	0.592	0.596	0.598	0.6	0.602	0.603	0.603	0.604	0.604
1.4	0.495	0.534	0.555	0.569	0.579	0.586	0.591	0.595	0.598	0.6	0.601	0.602	0.603	0.604	0.604
1.5	0.495	0.533	0.555	0.569	0.578	0.586	0.591	0.595	0.597	0.599	0.601	0.602	0.603	0.603	0.604
1.6	0.494	0.533	0.554	0.568	0.578	0.585	0.59	0.594	0.597	0.599	0.6	0.602	0.602	0.603	0.603
1.7	0.494	0.532	0.554	0.568	0.578	0.585	0.59	0.594	0.597	0.599	0.6	0.601	0.602	0.603	0.603
1.8	0.494	0.532	0.553	0.567	0.577	0.584	0.59	0.593	0.596	0.598	0.6	0.601	0.602	0.602	0.603
1.9	0.493	0.532	0.553	0.567	0.577	0.584	0.589	0.593	0.596	0.598	0.6	0.601	0.602	0.602	0.603
2	0.493	0.531	0.553	0.567	0.577	0.584	0.589	0.593	0.596	0.598	0.599	0.601	0.601	0.602	0.603
2.1	0.493	0.531	0.552	0.566	0.576	0.583	0.589	0.593	0.596	0.598	0.599	0.6	0.601	0.602	0.602
2.2	0.492	0.531	0.552	0.566	0.576	0.583	0.589	0.592	0.595	0.597	0.599	0.6	0.601	0.602	0.602
2.3	0.492	0.53	0.552	0.566	0.576	0.583	0.588	0.592	0.595	0.597	0.599	0.6	0.601	0.602	0.602
2.4	0.492	0.53	0.552	0.566	0.576	0.583	0.588	0.592	0.595	0.597	0.599	0.6	0.601	0.601	0.602
2.5	0.492	0.53	0.551	0.565	0.575	0.583	0.588	0.592	0.595	0.597	0.599	0.6	0.601	0.601	0.602
2.6	0.491	0.53	0.551	0.565	0.575	0.582	0.588	0.592	0.595	0.597	0.598	0.6	0.601	0.601	0.602
2.7	0.491	0.53	0.551	0.565	0.575	0.582	0.588	0.592	0.595	0.597	0.598	0.599	0.6	0.601	0.602

BR	Reynolds number														
	1000	2000	3000	4000	5000	6000	7000	8000	9000	10000	11000	12000	13000	14000	15000
inf	3.22	2.626	2.347	2.179	2.068	1.99	1.934	1.894	1.863	1.841	1.824	1.811	1.8	1.792	1.785
0.3	2.594	2.127	1.91	1.782	1.701	1.648	1.613	1.591	1.579	1.572	1.571	1.572	1.575	1.58	1.585
0.4	2.737	2.242	2.01	1.874	1.786	1.728	1.688	1.662	1.646	1.636	1.63	1.629	1.629	1.631	1.633
0.5	2.827	2.313	2.073	1.931	1.839	1.777	1.735	1.706	1.687	1.675	1.668	1.664	1.662	1.662	1.663
0.6	2.888	2.363	2.117	1.971	1.876	1.811	1.767	1.736	1.715	1.702	1.693	1.687	1.684	1.683	1.682
0.7	2.933	2.398	2.148	1.999	1.902	1.836	1.79	1.758	1.736	1.721	1.711	1.704	1.7	1.698	1.697
0.8	2.968	2.426	2.172	2.021	1.922	1.854	1.807	1.774	1.751	1.735	1.725	1.717	1.713	1.71	1.708
0.9	2.995	2.447	2.191	2.038	1.938	1.869	1.821	1.787	1.763	1.747	1.735	1.727	1.722	1.719	1.716
1	3.016	2.464	2.206	2.052	1.95	1.881	1.832	1.798	1.773	1.756	1.744	1.736	1.73	1.726	1.723
1.1	3.034	2.478	2.218	2.063	1.961	1.891	1.841	1.806	1.781	1.763	1.751	1.742	1.736	1.732	1.728
1.2	3.049	2.49	2.229	2.072	1.97	1.899	1.849	1.813	1.788	1.77	1.757	1.748	1.741	1.737	1.733
1.3	3.062	2.5	2.237	2.08	1.977	1.906	1.855	1.819	1.794	1.775	1.762	1.753	1.746	1.741	1.737
1.4	3.073	2.509	2.245	2.087	1.983	1.912	1.861	1.825	1.798	1.78	1.766	1.757	1.75	1.744	1.74
1.5	3.083	2.517	2.252	2.093	1.989	1.917	1.866	1.829	1.803	1.784	1.77	1.76	1.753	1.748	1.743
1.6	3.091	2.523	2.257	2.098	1.994	1.921	1.87	1.833	1.806	1.787	1.773	1.763	1.756	1.75	1.746
1.7	3.099	2.529	2.263	2.103	1.998	1.925	1.874	1.837	1.81	1.79	1.776	1.766	1.759	1.753	1.748
1.8	3.105	2.535	2.267	2.107	2.002	1.929	1.877	1.84	1.813	1.793	1.779	1.769	1.761	1.755	1.75
1.9	3.111	2.539	2.271	2.111	2.005	1.932	1.88	1.842	1.815	1.796	1.781	1.771	1.763	1.757	1.752
2	3.116	2.543	2.275	2.114	2.008	1.935	1.883	1.845	1.818	1.798	1.783	1.773	1.765	1.759	1.754
2.1	3.121	2.547	2.278	2.117	2.011	1.937	1.885	1.847	1.82	1.8	1.785	1.774	1.766	1.76	1.755
2.2	3.126	2.551	2.281	2.12	2.014	1.94	1.887	1.849	1.822	1.802	1.787	1.776	1.768	1.762	1.757
2.3	3.13	2.554	2.284	2.123	2.016	1.942	1.889	1.851	1.824	1.803	1.789	1.778	1.769	1.763	1.758
2.4	3.134	2.557	2.287	2.125	2.018	1.944	1.891	1.853	1.825	1.805	1.79	1.779	1.771	1.764	1.759
2.5	3.137	2.56	2.289	2.127	2.02	1.946	1.893	1.855	1.827	1.806	1.791	1.78	1.772	1.765	1.76
2.6	3.14	2.562	2.291	2.129	2.022	1.947	1.894	1.856	1.828	1.808	1.793	1.781	1.773	1.766	1.761
2.7	3.143	2.564	2.293	2.131	2.024	1.949	1.896	1.857	1.829	1.809	1.794	1.782	1.774	1.767	1.762

C.4 Loss Data Extraction flow chart

The flow chart in this section outlines the process of taking the raw pressure and temperature data and details the steps followed to form the loss correlations used in this work.



Appendix D Camera Settings used for the Film-Cooling Effectiveness Experiments

Image settings:

- Palette: grey (white hot)
  - This was set to grey scale in order to simplify the image manipulation and results processing.
- Auto adjust: Off
  - This ensured consistency between both upstream and downstream images as well as between different test images.
- High value: 50 °C, Low value: 20 °C
  - The temperature range for which the camera would have to deal. The range was selected to keep it to a minimum in order to generate images with a high level of contrast.
- Force linear: On, Lock to: Temperature
  - This ensured there was a linear relationship between temperature and the gray scale value assigned in the image.
- At reboot: Keep range/scale
  - Ensured consistency between different tests on a day to day basis.
- Shutter period: Normal

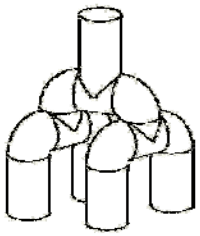
Object parameters:

- Emissivity: 0.8
  - The emissivity was established using a black can of known temperature (measured by a thermocouple). An emissivity of 0.8 produced a good match between the thermocouple and the camera readings at a temperature of 45°C. The camera reading was then verified again at a lower temperature of 25 °C.
- Distance: 0.5m
  - The distance of the test section to the camera lens, in this case the width of the wind tunnel.
- Temperature atmosphere: 22.5 °C
- Relative Humidity: 70%
  - Found using a dry bulb and wet bulb thermometer.
- External optics: On, Optics transmission: 0.98, Optics temperature: 22.5°C, Optics temperature source: Value
  - Adjusts the camera for viewing through the Zinc-Selenide window.

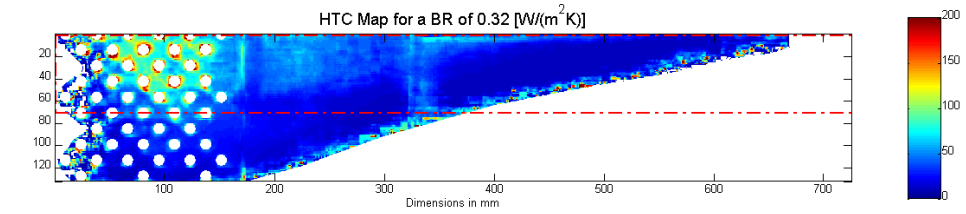
Appendix E Flat Plate Test Results

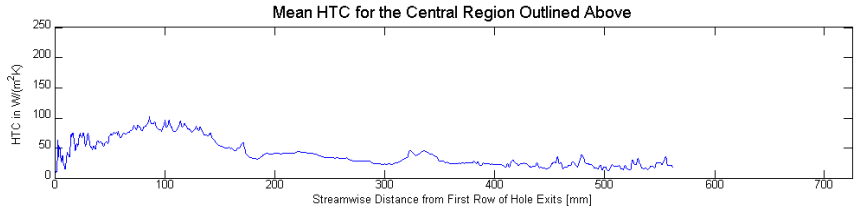
E.1 Results Acquired Using the Transient Technique

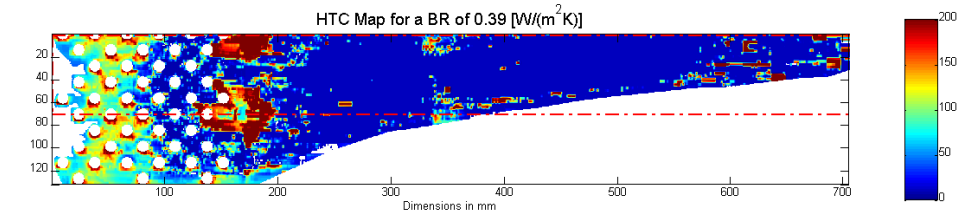
E.1.1 Circular Cross Section Dendrite

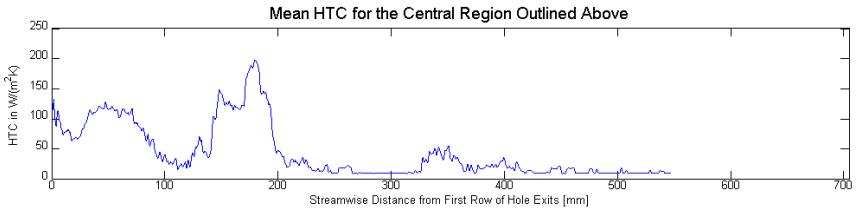


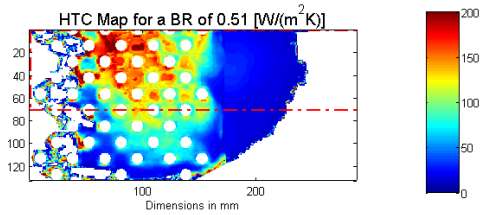
The results presented in this section relate to the heat transfer coefficient data for a 1-2-4 dendritic array with circular cross section passages. A single system from such an array is shown above.

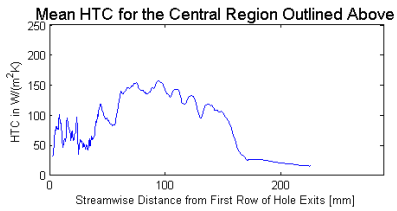


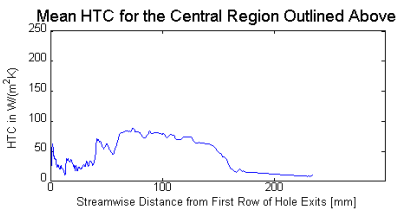


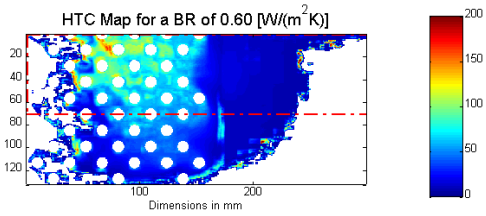


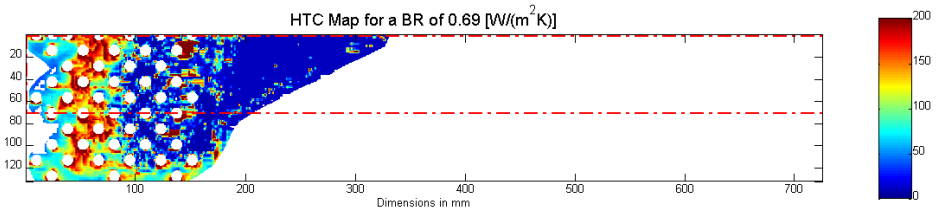


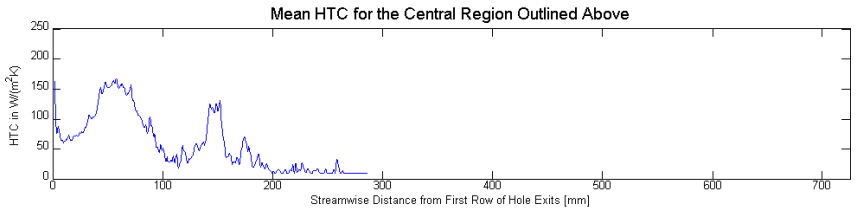

HTC Map for a BR of 0.51 [W/(m2K)]
Dimensions in mm

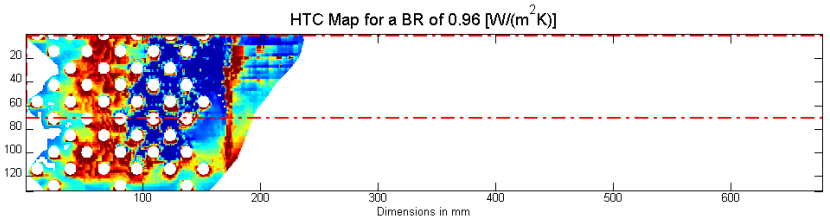

Mean HTC for the Central Region Outlined Above
HTC in W/(m2K)
Streamwise Distance from First Row of Hole Exits [mm]

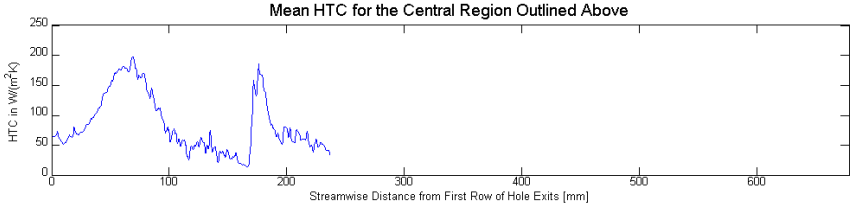

Mean HTC for the Central Region Outlined Above
HTC in W/(m2K)
Streamwise Distance from First Row of Hole Exits [mm]


HTC Map for a BR of 0.60 [W/(m2K)]
Dimensions in mm

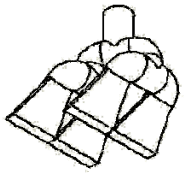

HTC Map for a BR of 0.69 [W/(m2K)]
Dimensions in mm


Mean HTC for the Central Region Outlined Above
HTC in W/(m2K)
Streamwise Distance from First Row of Hole Exits [mm]

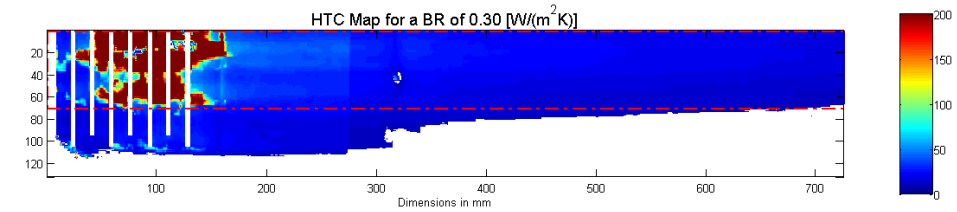

HTC Map for a BR of 0.96 [W/(m2K)]
Dimensions in mm

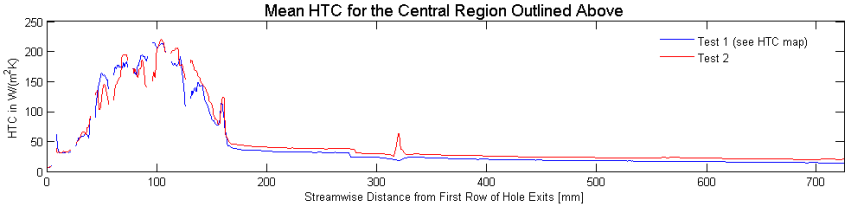

Mean HTC for the Central Region Outlined Above
HTC in W/(m2K)
Streamwise Distance from First Row of Hole Exits [mm]

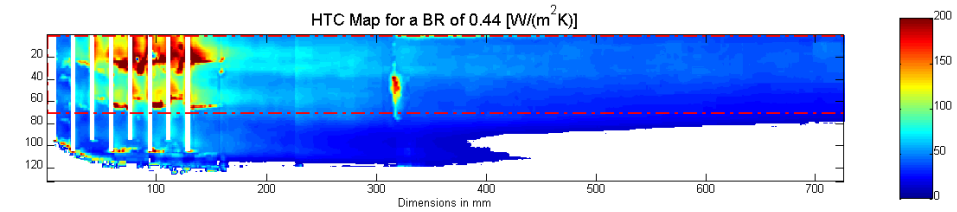
E.1.2 Slot Exit Dendrite

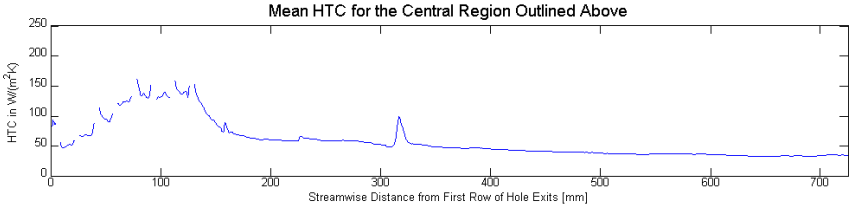


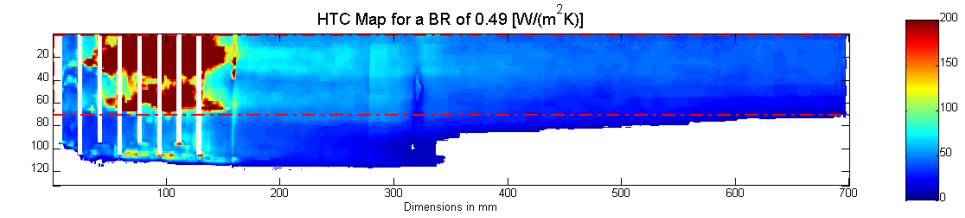
The results presented in this section relate to the heat transfer coefficient data for a 1-2-4 dendritic array with slot type exits. A single system from such an array is shown above.

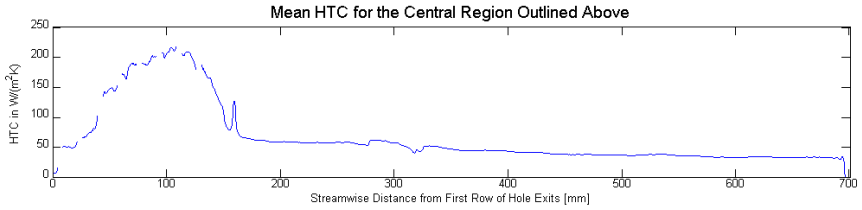


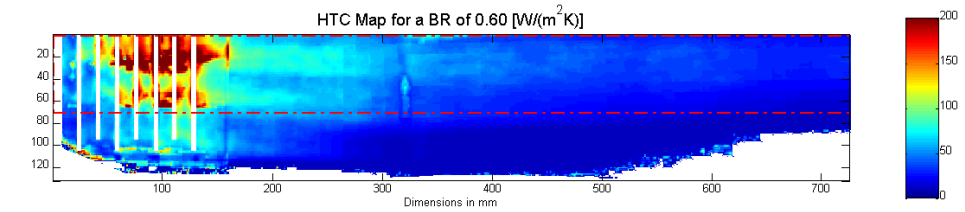


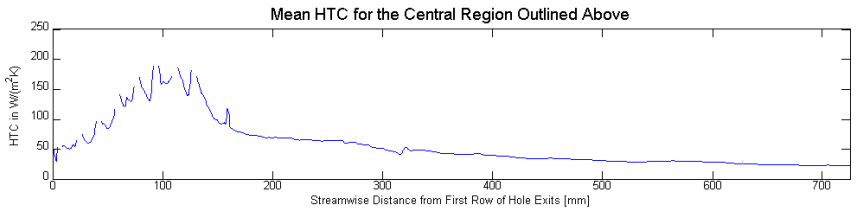






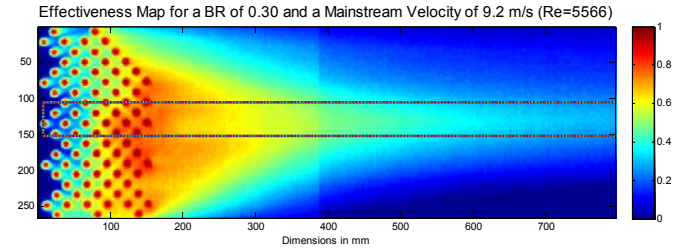


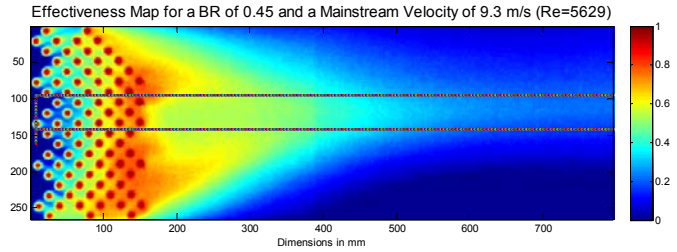


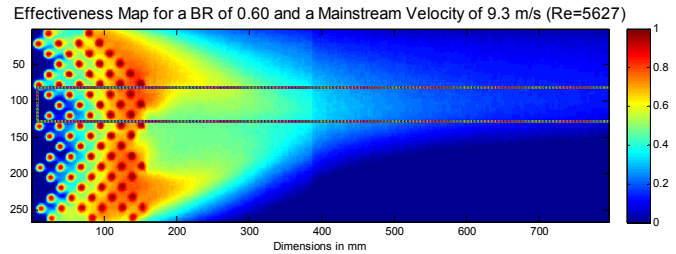


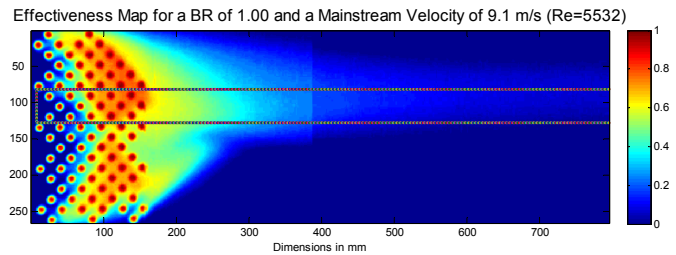
E.2 Results Acquired Using the Steady State Technique

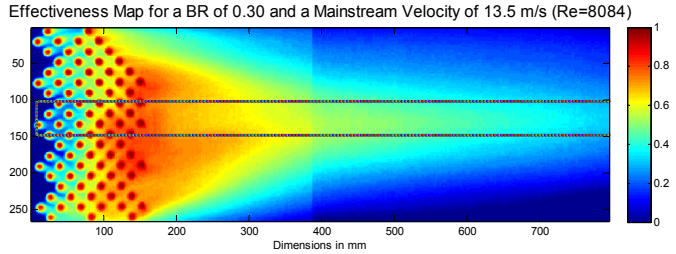
E.2.1 Straight Circular Cross Section Holes

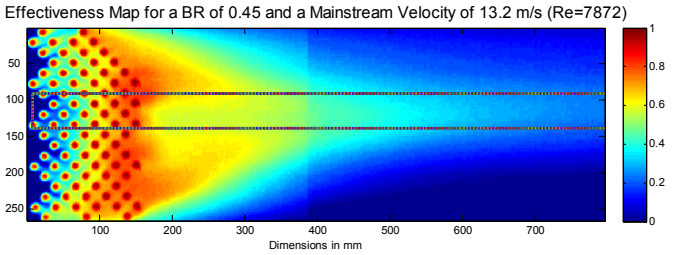




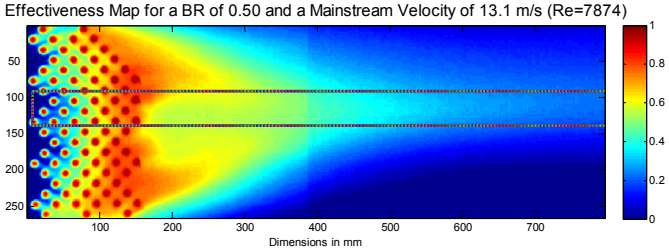




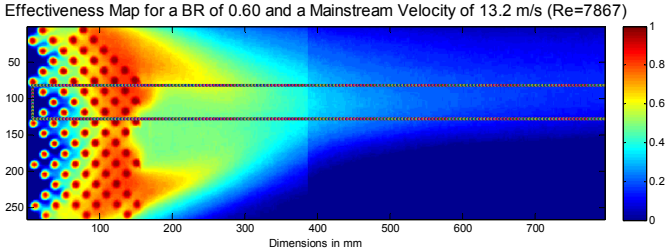




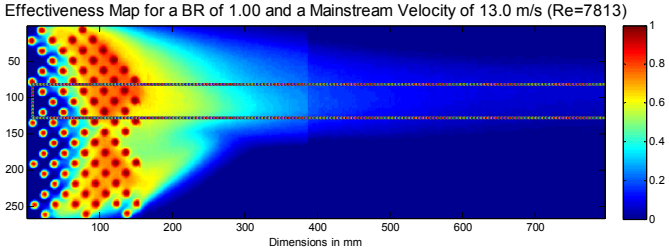
Effectiveness Map for a BR of 0.50 and a Mainstream Velocity of 13.1 m/s (Re=7874)



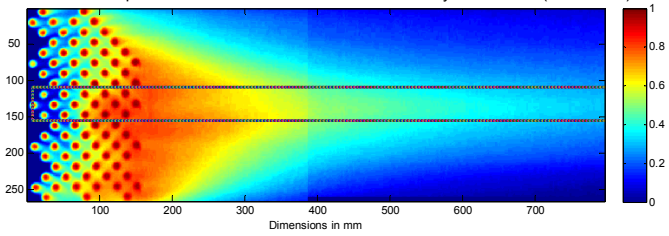
Effectiveness Map for a BR of 0.60 and a Mainstream Velocity of 13.2 m/s (Re=7867)



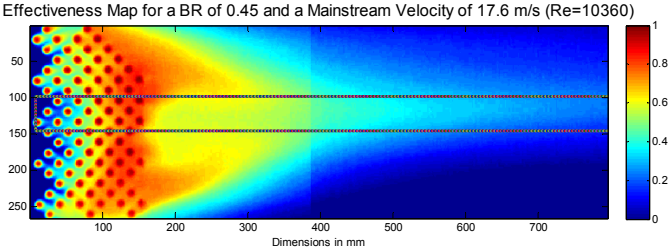
Effectiveness Map for a BR of 1.00 and a Mainstream Velocity of 13.0 m/s (Re=7813)



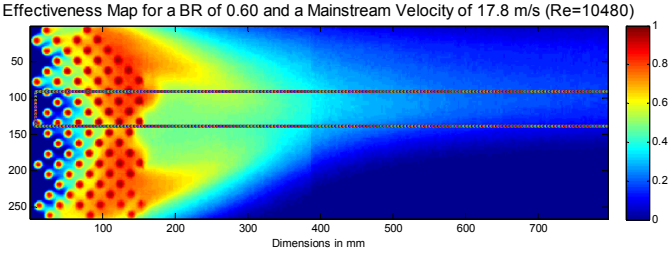
Effectiveness Map for a BR of 0.30 and a Mainstream Velocity of 17.5 m/s (Re=10297)



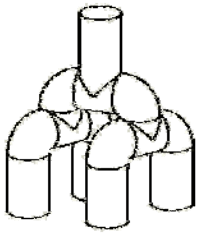
Effectiveness Map for a BR of 0.45 and a Mainstream Velocity of 17.6 m/s (Re=10360)



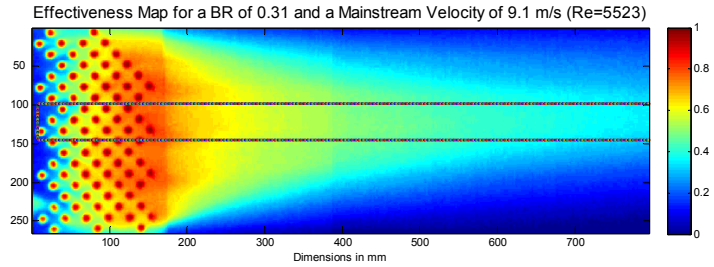
Effectiveness Map for a BR of 0.60 and a Mainstream Velocity of 17.8 m/s (Re=10480)

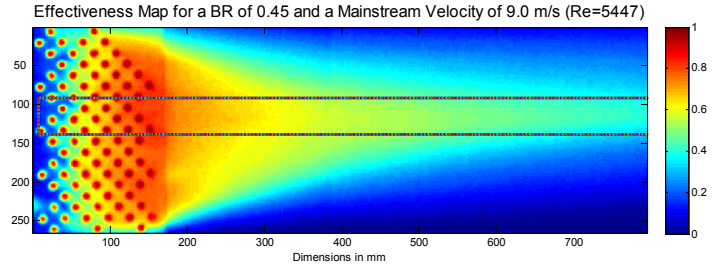


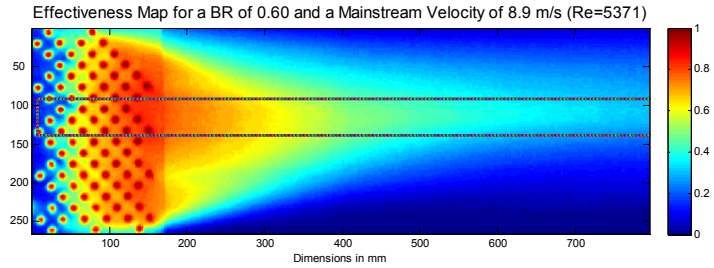
E.2.2 Circular Cross Section Dendrite

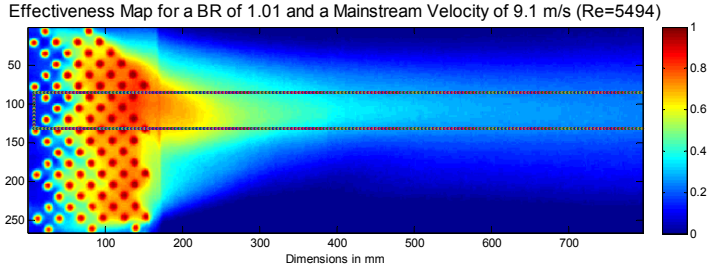


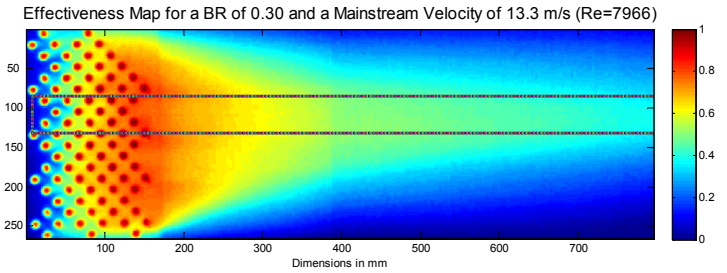
The results presented in this section relate to the heat transfer coefficient data for a 1-2-4 dendritic system with circular cross section passages. A single system from such an array is shown above.

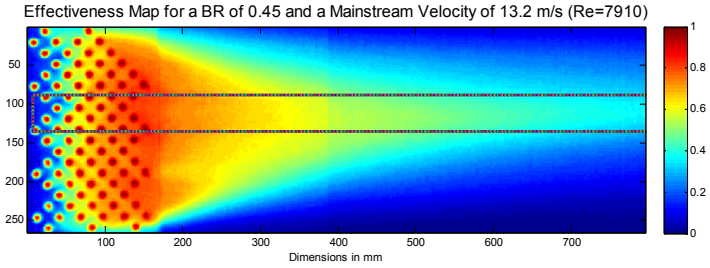


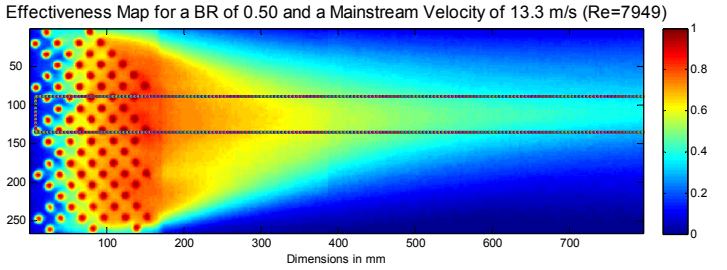


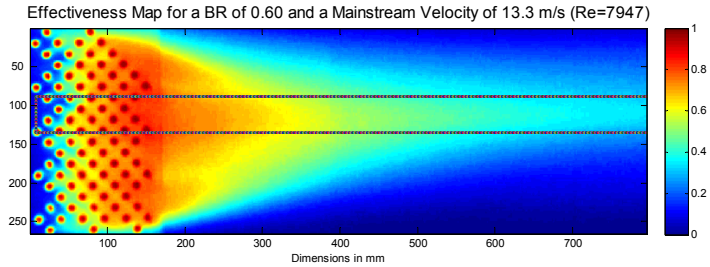


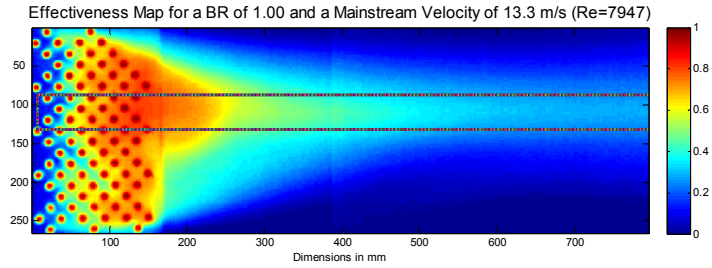


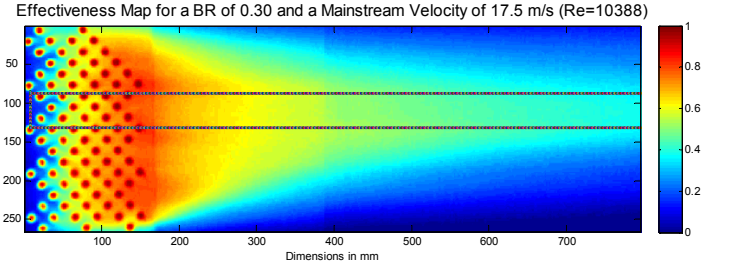

Effectiveness Map for a BR of 0.30 and a Mainstream Velocity of 13.3 m/s (Re=7966)
50
100
150
200
250
100
200
300
400
500
600
700
Dimensions in mm
1
0.8
0.6
0.4
0.2
0

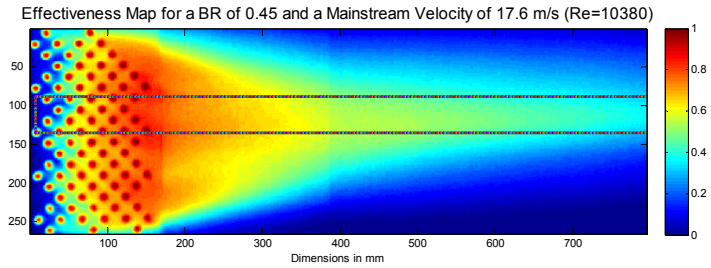

Effectiveness Map for a BR of 0.45 and a Mainstream Velocity of 13.2 m/s (Re=7910)
50
100
150
200
250
100
200
300
400
500
600
700
Dimensions in mm
1
0.8
0.6
0.4
0.2
0

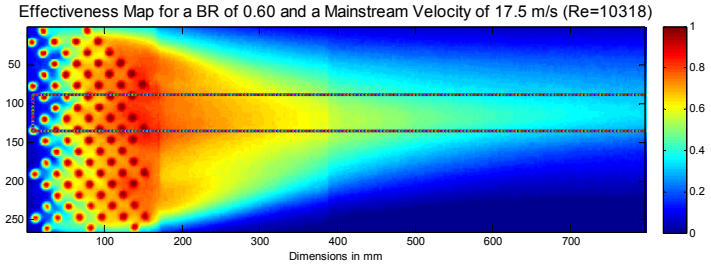

Effectiveness Map for a BR of 0.50 and a Mainstream Velocity of 13.3 m/s (Re=7949)
50
100
150
200
250
100
200
300
400
500
600
700
Dimensions in mm
1
0.8
0.6
0.4
0.2
0


Effectiveness Map for a BR of 0.60 and a Mainstream Velocity of 13.3 m/s (Re=7947)
50
100
150
200
250
100
200
300
400
500
600
700
Dimensions in mm
1
0.8
0.6
0.4
0.2
0

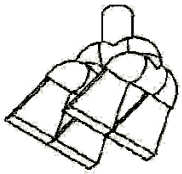

Effectiveness Map for a BR of 1.00 and a Mainstream Velocity of 13.3 m/s (Re=7947)
50
100
150
200
250
100
200
300
400
500
600
700
Dimensions in mm
1
0.8
0.6
0.4
0.2
0


Effectiveness Map for a BR of 0.30 and a Mainstream Velocity of 17.5 m/s (Re=10388)
50
100
150
200
250
100
200
300
400
500
600
700
Dimensions in mm
1
0.8
0.6
0.4
0.2
0

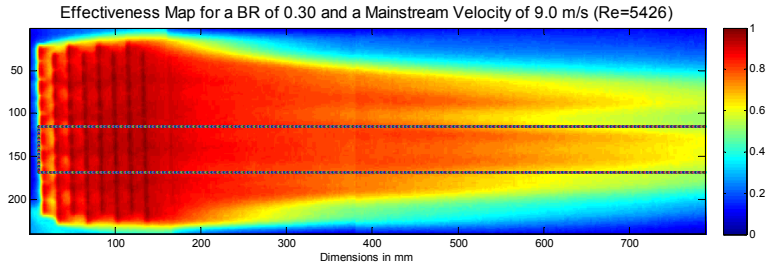


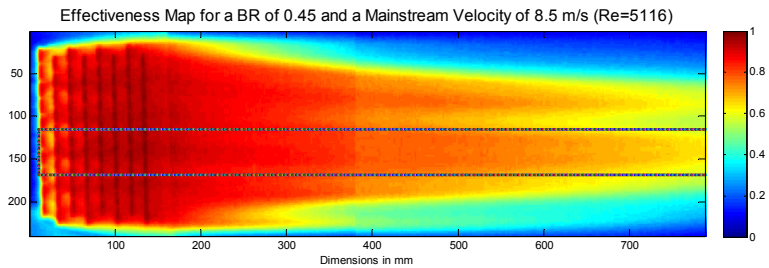


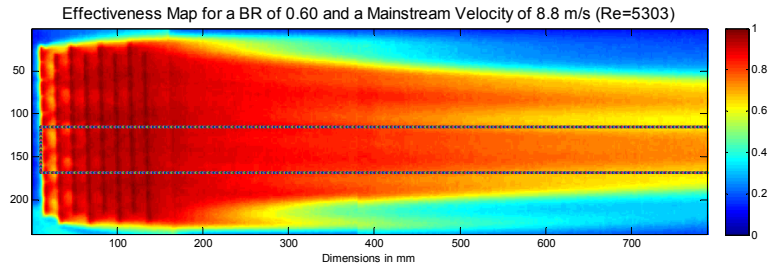
E.2.3 Slot Exit Dendrite

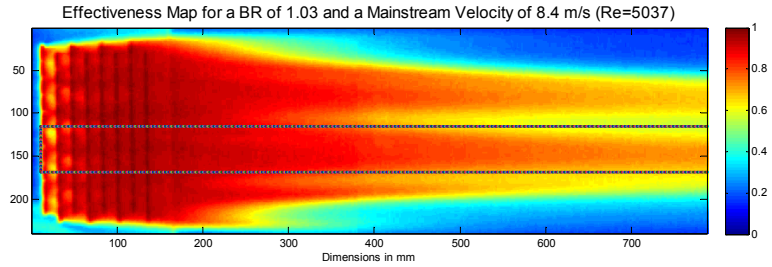


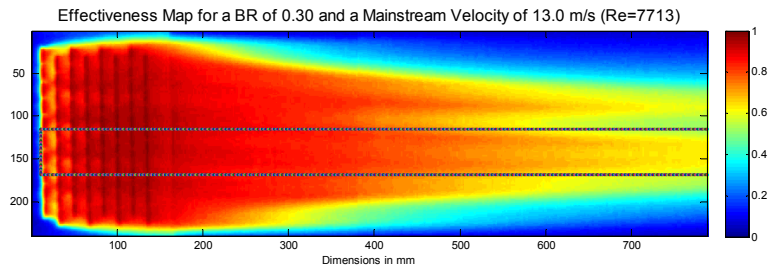
The results presented in this section relate to the heat transfer coefficient data for a 1-2-4 dendritic array with slot exits. A single system from such an array is shown above.

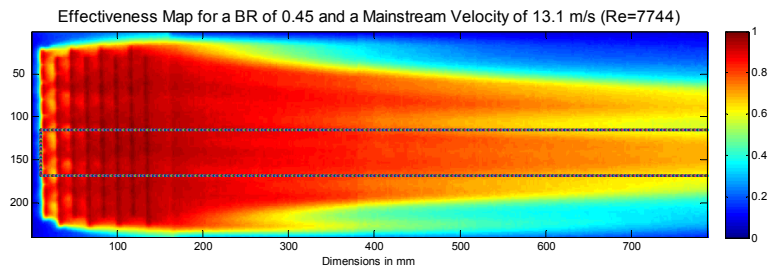


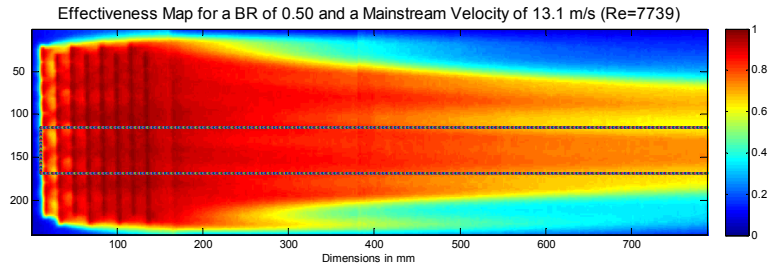


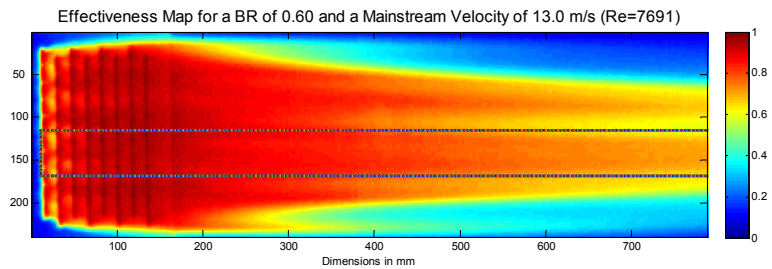

Effectiveness Map for a BR of 0.60 and a Mainstream Velocity of 8.8 m/s (Re=5303)
50
100
150
200
100
200
300
400
500
600
700
Dimensions in mm
1
0.8
0.6
0.4
0.2
0

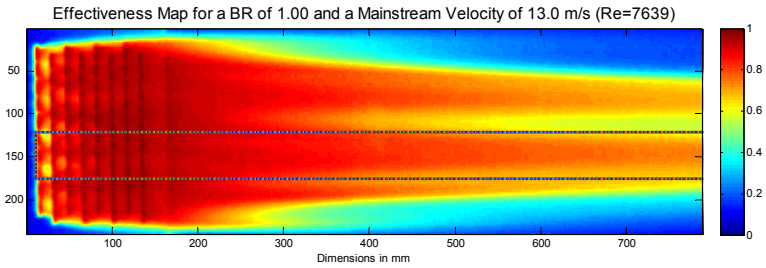

Effectiveness Map for a BR of 1.03 and a Mainstream Velocity of 8.4 m/s (Re=5037)
50
100
150
200
100
200
300
400
500
600
700
Dimensions in mm
1
0.8
0.6
0.4
0.2
0

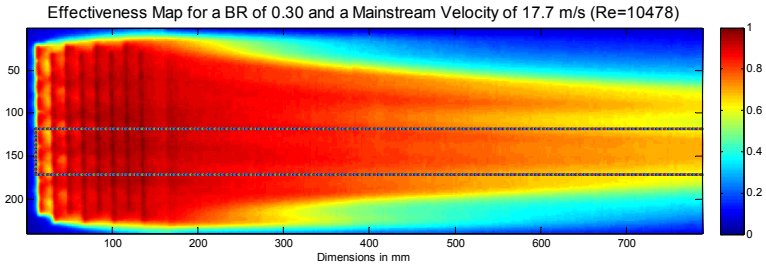

Effectiveness Map for a BR of 0.30 and a Mainstream Velocity of 13.0 m/s (Re=7713)
50
100
150
200
100
200
300
400
500
600
700
Dimensions in mm
1
0.8
0.6
0.4
0.2
0

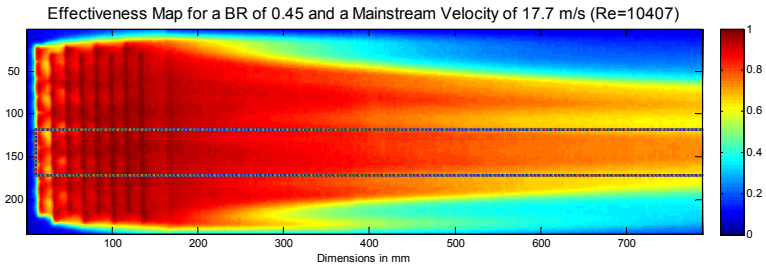

Effectiveness Map for a BR of 0.45 and a Mainstream Velocity of 13.1 m/s (Re=7744)
50
100
150
200
100
200
300
400
500
600
700
Dimensions in mm
1
0.8
0.6
0.4
0.2
0


Effectiveness Map for a BR of 0.50 and a Mainstream Velocity of 13.1 m/s (Re=7739)
50
100
150
200
100
200
300
400
500
600
700
Dimensions in mm
1
0.8
0.6
0.4
0.2
0


Effectiveness Map for a BR of 0.60 and a Mainstream Velocity of 13.0 m/s (Re=7691)
50
100
150
200
100
200
300
400
500
600
700
Dimensions in mm
1
0.8
0.6
0.4
0.2
0







Appendix F Rolls Royce Trent 500 Data

Trent 500 HP NGV Film Cooling Definition - RR-SI units
(Data presented for midheight only where required)

Surface	Row Id	Surface Length	%Surface Length	Hole Type	Diameter	No. of Holes	Surface Pitch	True Pitch	Surface Pitch/Diam.	Horiz. Surf. Angle	Radial Inclin'n	Row Flow area	Row Id
		mm	%		mm		mm	mm		°	°	mm²	
	6	13.28	15.85	3 into 1 laser	0.6 x 0.86	24 (19)	2.57 (3.23)	2.57	3.43 (4.31)	51.75	0	10.603 (8.394)	6
	5	10.76	12.84	3 into 1 laser	0.6 x 0.86	23 (18)	2.57 (3.23)	2.57	3.43 (4.31)	45.7	0	7.952 (10.161)	5
Suction	4	8.194	9.78	3 into 1 laser	0.6 x 0.86	24 (19)	2.57 (3.23)	2.57	3.43 (4.31)	46.39	0	10.603 (8.394)	4
Surface	3	5.626	6.71	2 into 1 laser	0.75	22	3.00	1.50	4.00	61.53	+/-60	9.719	3
	2	3.723	4.44	2 into 1 laser	0.75	23	3.00	1.50	4.00	75.05	+/-60	10.161	2
	1	1.862	2.22	2 into 1 laser	0.75	22	3.00	1.50	4.00	91.1	+/-60	9.719	1
Stagnation point													
	7	1.117	1.91	2 into 1 laser	0.75	22	3.00	1.50	4.00	99.03	+/-60	9.719	7
Pressure	8	4.26	7.29	2 into 1 laser	0.75	22	3.00	1.50	4.00	71.97	+/-60	9.719	8
Surface	9	11.407	19.53	3 into 1 laser	0.6 x 0.86	22	2.60	2.60	3.47	24.26	0	9.719	9
	11	23.667	40.53	3 into 1 laser	0.6 x 0.86	20	2.65	2.65	3.53	14.96	0	8.636	11
	12	34.501	59.08	3 into 1 laser	0.6 x 0.86	15	3.10	3.10	4.13	62.34	0	6.627	12

Surface	Row Id	Fan Width	Fan Inc. angle	Fan Width/diam.	Fan Area ratio	M/S Mn	Exhaust Pressure	Local Feed Pressure	Local Feed Temp.	Cd	Pc/pg	Mcpc	Blowing rate
		mm	°				kPa	kPa	K			%	
	6	1.85	32.00	2.47	2.35	0.463	3626.03	4257.09	980.5	0.915	1.174	1.525 (1.205)	1.694
	5	1.90	32.00	2.53	2.42	0.307	3907.51	4257.21	980.0	0.915	1.089	1.081 (0.847)	1.852
Suction	4	1.75	32.00	2.33	2.21	0.186	4056.49	4257.15	981.3	0.885	1.049	0.847 (0.674)	2.277
Surface	3	1.00"	8.00	1.33	1.42	0.116	4111.67	4258.60	991.6	0.785	1.036	0.627	3.148
	2	1.00"	8.00	1.33	1.42	0.079	4130.33	4258.59	992.6	0.775	1.031	0.595	4.278
	1	1.00"	8.00	1.33	1.42	0.047	4141.00	4258.43	988.6	0.775	1.028	0.556	6.899
Stagnation point													
	7	1.00"	8.00	1.33	1.42	0.022	4145.42	4258.66	1009.3	0.775	1.027	0.557	14.216
Pressure	8	1.00"	8.00	1.33	1.42	0.053	4139.16	4261.23	992.9	0.780	1.029	0.566	6.103
Surface	9	2.00	24.00	2.67	2.55	0.088	4126.32	4258.52	1002.9	0.865	1.032	0.661	3.898
	11	1.90	29.00	2.53	2.42	0.159	4080.95	4245.48	1002.6	0.910	1.040	0.717	2.423
	12	2.00	25.00	2.67	2.55	0.2866	3937.24	4245.29	1001.0	0.920	1.078	0.731	1.864

"estimate

Figures in brackets indicate the changes made for the "1640K" film cooling standard

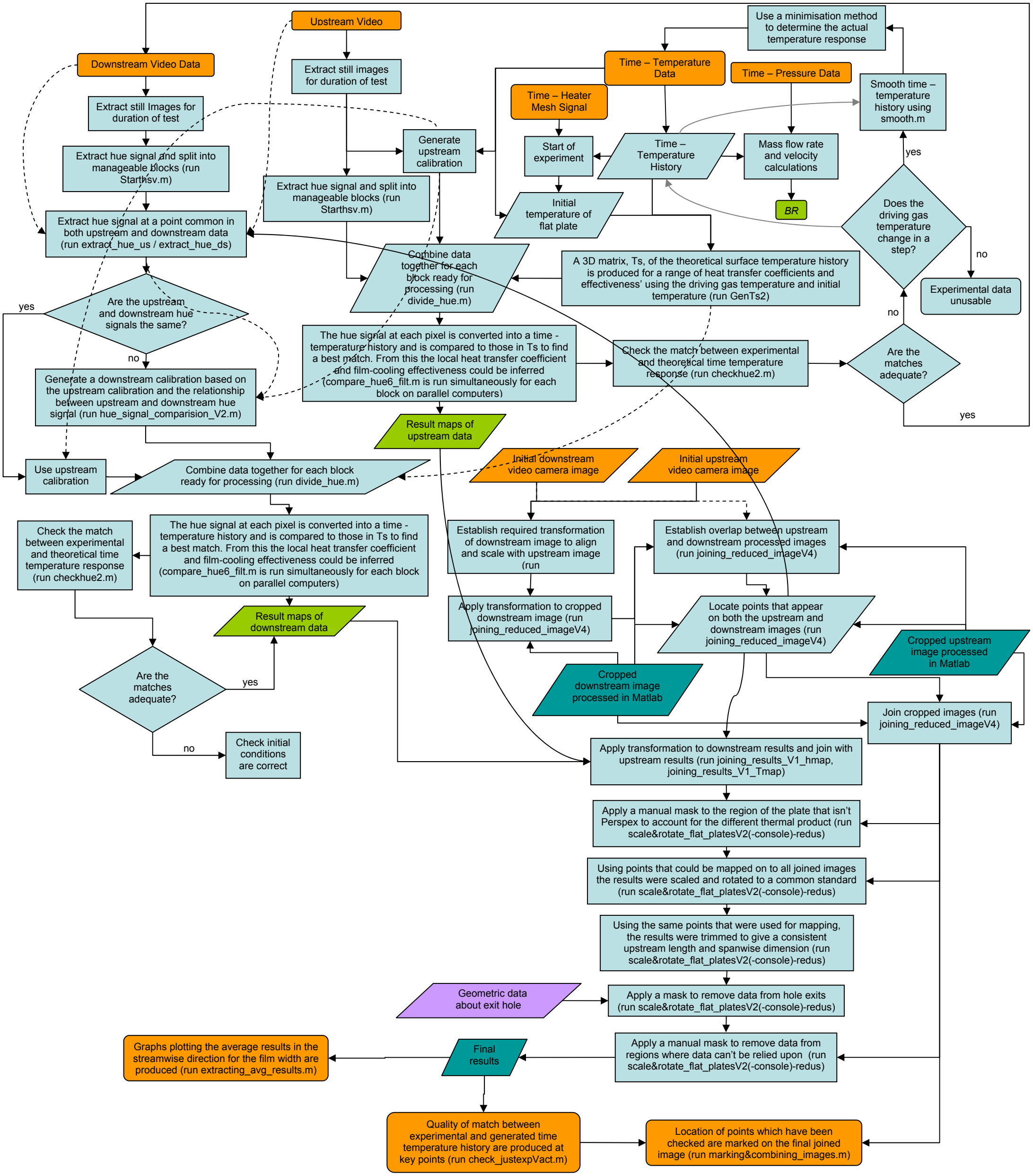
Figure 12

The data outlined above was provided by Rolls Royce PLC and are the maximum take of conditions as replicated in a Type Test under normal operating conditions.

Appendix G Processing Flow Charts

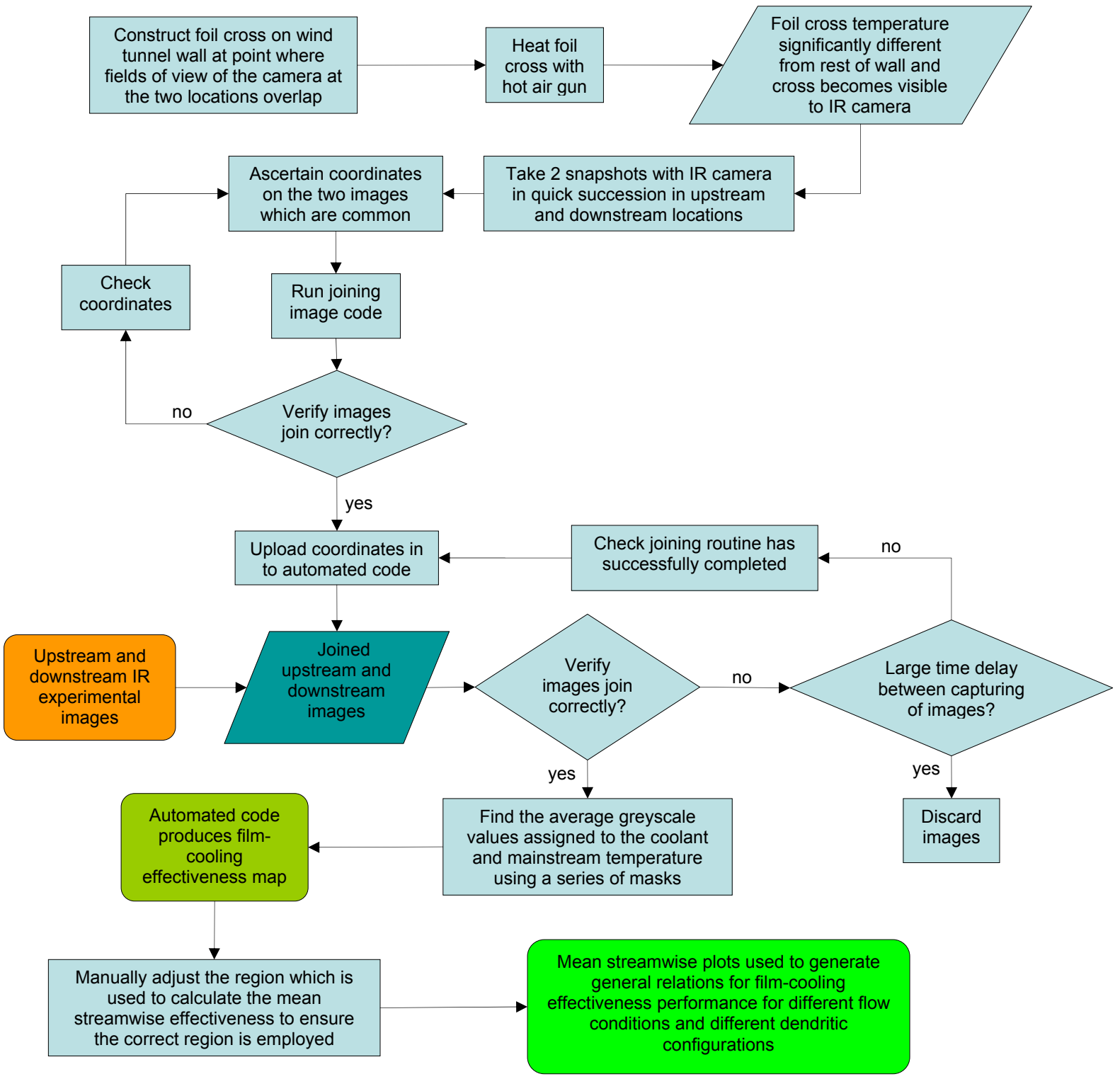
G.1 Heat Transfer Coefficient Map Generation

Flow chart explaining the processes involved in the generation of the transient flat plate results (orange – test inputs; lavender – prior geometric inputs; light blue – processes; dark green – intermediate output; lime green supplementary outputs, traffic light green – final output).



G.2 Film-cooling effectiveness Data Generation

Flow chart detailing and explaining the steps involved in the processing and generation of film-cooling effectiveness results from IR flat plate data using a combination of automated code and manual input to join, scale and extract useful information. (orange – test inputs; light blue – processes; dark green – intermediate output; lime green supplementary outputs, traffic light green – final output).



Appendix H Summary of Film Flow Visualisation Pictures

